OPTIMAL CONTROL OF WIND ENERGY CONVERSION SYSTEMS WITH DOUBLY-FED INDUCTION GENERATORS

by

CHERNGCHAI SOMPRACHA

A thesis submitted to The University of Birmingham for the degree of

DOCTOR OF PHILOSOPHY

School of Engineering

Department of Electronic, Electrical and Systems Engineering

The University of Birmingham, UK

January 2019

Abstract

Wind energy conversion systems (WECSs) have become the interesting topic over recent years for the renewable electrical power source. They are a more environmentally friendly and sustainable resource in comparison with the fossil energy resource. The WECS using a doubly-fed induction generator (DFIG) to convert mechanical power into electrical power has a significant advantage. This WECS requires a smaller power converter in comparison with a squirrel cage induction generator.

Efficiency of the DFIG-WECS can be improved by a suitable control system to maximise the output power from WECS. A maximum power point tracking (MPPT) controller such as tip-speed ratio (TSR)control and power signal feedback (PSF) control is use to maximise mechanical power from wind turbine and a model-based loss minimisation control (MBLC) is used to minimise electrical losses of the generator. However, MPPT and MBLC require the parameters of the wind turbine and the generator for generating the control laws like optimal generator speed reference and *d*-axis rotor current reference. The Efficiencies of the MPPT and MBLC algorithms deteriorate when wind turbine and generator parameters change from prior knowledge.

The field oriented control for a DFIG in the WECS is extended by introducing a novel control layer generating online optimal generator speed reference and *d*-axis rotor current reference in order to maximise power produced from the WECS under wind turbine and DFIG parameter uncertainties, which is proposed.

Abstract

The single input rule modules (SIRMs) connected fuzzy inference model is applied to the control algorithm for optimal power control for variable-speed fixed-pitch wind turbine in the whole wind speed range by generating an online optimal speed reference to achieve optimal power under wind turbine parameter uncertainties.

The proposed control combines a hybrid maximum power point tracking (MPPT) controller, a constant rotational speed controller for below-rated wind speed and a limited-power active stall regulation by rotational speed control for above-rated wind speed. The three methods are appropriately organised via the fuzzy controller based SIRMs connected fuzzy inference model to smooth transition control among the three methods.

The online parameter estimation by using Kalman filter is applied to enhance model-based loss minimisation control (MBLC). The *d*-axis rotor current reference of the proposed MBLC can adapt to the accurate determination of the condition of minimum electrical losses of the DFIG when the parameters of the DFIG are uncertain.

The proposed control algorithm has been verified by numerical simulations in Matlab/Simulink and it has been demonstrated that the energy generated for typical wind speed profiles is greater than that of a traditional control algorithm based on PSF MPPT and MBLC.

Acknowledgements

I wish to express my sincere gratitude to my supervisors Dr Pietro Tricoli and Dr Dilan Jayaweera for their invaluable advice, supervision and support throughout my study. I have greatly benefitted from their knowledge, experience and understanding of doubly-fed induction machine control, vector control system, wind energy conversion system and optimal control system. I am also grateful for their encouragement when I faced difficulties with my study and for their patience in helping me to improve my English.

I acknowledge the Ministry of Science and Technology of Thailand for providing financial support toward the cost of tuition fees and student general maintenance costs during my PhD study and also the Office of Educational Affairs, the Royal Thai Embassy, London for taking care of both education and welfare.

I am grateful to everybody at the Birmingham Centre for Railway Research and Education for their continuous help, support, encouragement and friendship.

Lastly, I would like to express my gratitude to everyone in my family for their understanding, sincere encouragement and never-ending support.

Table of Contents

List of Figures

List of Tables

List of Acronyms

Term	Explanation / Meaning / Definition
ACO	Ant Colony Optimisation
DFIG	Doubly Fed Induction Generator
DID	Dynamic Importance Degree
DSP	Digital Signal Processing
FLC	Fuzzy Logic Control
FSWT	Fixed Speed Wind Turbine
GA	Genetic Algorithm
GSC	Grid Side Converter
IGBTs	Insulated-Gate Bipolar Transistors
MBLC	Model-Based Loss Minimisation Control
MEL	Minimum Electric Loss
MPPT	Maximum Power Point Tracking
MRAS	Model Reference Adaptive System
OT	Optimal Torque
PLL	Phase Locked Loop
PMSG	Permanent Magnet Synchronous Generator
P&O	Perturb & Observe
PSF	Power Signal Feedback
PSO	Particle Swarm Optimisation
PWM	Pulse Width Modulation
RLS	Recursive Least Square
RSC	Rotor Side Converter

SCADA	Supervisory Control and Data Acquisition
SCIG	Squirrel Cage Induction Generator
SFO	Stator Flux Oriented
SIRMs	Single Input Rule Modules
SVO	Stator Voltage Oriented
TSR	Tip Speed Ratio
VSCs	Voltage Source Converters
VSFP	Variable Speed Fixed pitch
VSVP	Variable Speed Variable pitch
VSWT	Variable Speed Wind Turbine
WECS	Wind Energy Conversion System

Chapter 1 Introduction

1.1 Research Background and Significance

Wind power has a large potential for power generation due to its availability, high power density and low environmental impact. In the last two decades, the growth rate of large wind farms has increased continuously. A wind energy conversion system (WECS) is used to convert the kinetic energy of wind to electrical energy through a wind turbine, a generator and a controller.

In the late 1970s, fixed-speed WECSs were developed in Denmark using squirrel cage induction generators coupled to a fixed-speed variable-pitch (FSVP) wind turbine. However, the efficiency of the power extracted from the wind was unsatisfactory. Hence, variable-speed WECSs were developed to increase the amount of power extracted from the wind. The key of this technology is a power converter that can vary the amplitude and frequency voltage of the power supply of the electrical generator.

Doubly fed induction generators (DFIG) are attractive machines for WECS because they require a smaller power converter in comparison with squirrel cage induction generators (SCIG) and permanent magnet synchronous generators (PMSG) and operate as generators at both sub-synchronous speeds and super-synchronous speeds. The efficiency improvement of the variable-speed DFIG WECSs has become an interesting topic. Several control techniques have been proposed in the literature to optimise the efficiency of WECS with DFIG.

The control system of the variable-speed DFIG WECS is designed to optimise mechanical power extracted from the wind turbine. A maximum power point tracking (MPPT) controller is used to regulate the generator speed to maximise the power coefficient of the wind turbine below rated wind speed. For power limitation control, pitch control and stall control are two types of methods to limit the power extracted from the wind turbine above rated wind speed.

The majority of wind turbines used with variable-speed WECS are variable-speed, variable-pitch (VSVP). Pitch angle control is used to limit the extracted power from the turbine at its rated power to avoid damage to the blades, the generator and the power converter. To obtain low cost and high reliablility feature, it is preferable to use a variable-speed fixed-pitch (VSFP) wind turbine with an active stall control via speed regulation because this wind turbine does not require the pitch angle control mechanism.

Over recent years, MPPT controllers have been developed for variable-speed WECS, such as tip speed ratio (TSR) control, power signal feedback (PSF) control, optimal torque (OT) control, and perturb & observe (P&O).

Although the first three MPPT controllers give high efficiency and fast-response, all of them require the accurate knowledge of air density and parameters of the wind turbine. Furthermore, the air density varies with the location and the weather conditions. These problems lead to inaccurate determination of the maximum power operating point of the wind turbine and, hence, reduction of the electrical energy generated.

Another important aspect to improve the efficiency of WECS with DFIG is the control of the reactive power flow into the grid, as this affects the efficiency of the electrical generator as well as the cost of the power converter for the rotor.

The majority of the studies on reactive power flow management for DFIG set to zero the stator reactive power reference of the control loop on the rotor side converter. This method provided a high the copper losses on the DFIG. Model-based loss minimization control (MBLC) is used to solve this problem by controlling the reactive power circulating in system, resulting minimal copper losses on the DFIG. Although this technique provides fast-tracking, MBLC relies on the accurate knowledge of the parameters of the DFIG. Moreover, some DFIG parameters such as stator and rotor resistances are dependent on the temperature, while the magnetizing inductance is dependent on the level of saturation. This is a problem that affects the MBLC efficiency when the operating conditions are variable, such as those of WECS.

In this thesis, a novel MPPT algorithm is developed by using fuzzy control for hybrid MPPT combining PSF and P&O MPPT. The proposed MPPT algorithm is capable of reaching the maximum power operating point under wind turbine parameter and air density uncertainties. Also, the proposed MPPT algorithm will work well with wind turbines with large inertia and variable wind conditions.

For optimal efficiency power control, this research aims to design a power control algorithm for VSFP wind turbines to optimise the extracted mechanical power from the wind turbine for the whole wind speed range. Fuzzy control based SIRM uses the hybrid MPPT controller in a combination of PSF MPPT and P&O MPPT and active

stall control via speed regulation to generate an online speed reference trajectory for a speed control loop of the stator-flux oriented vector control on the rotor side converter. The proposed control has the objective to optimise the extracted energy of the WECS even in the presence of uncertainties in the wind turbine parameters.

Furthermore, the proposed controller tries to improve the electrical efficiency by minimising the electrical losses of the generator. For the DFIG in WECS' driven stator-flux oriented vector control, loss minimisation can be achieved through appropriate control of the reactive power flow through the control of the *d*-axis rotor current.

This research proposes a MBLC with online parameter estimation with a Kalman filter of the stator resistance, r_s, rotor resistance, r_r, stator leakage inductance, $L_{\sigma s}$, and mutual inductance, L_m. The main advantage of the Kalman filter is that it does not require test signals to estimate the machine parameters, thereby adding adaptive capabilities to the traditional MBLC.

1.2 Aims of the Research

The aim of the research is to study and design an optimal control algorithm to improve the efficiency of the wind energy conversion system with DFIG for VSFP wind turbines. This will be achieved by investigating the following objectives:

- To design an adaptive optimal power control to optimise the mechanical power extracted from the wind turbine even in the presence of a substantial inertia of the blades and the rotor and under wind turbine parameter uncertainties.

- To use an MPPT control to maximise the extracted power below the rated wind speed and a soft-stall control above the rated wind speed.
- To design an adaptive loss minimisation control to minimise copper losses of the DFIG in the presence of DFIG parameter uncertainties.

1.3 Methodology of the Research

- Fuzzy control based on SIRMs connected fuzzy inference model using the hybrid MPPT and active stall control via speed regulation is simulated with Matlab/Simulink to generate the speed reference for the vector control in DFIG generation system connected a VSFP wind turbine. The control is tested for realistic wind speed profiles and includes an error in the estimation of wind turbine parameters and air density.
- The simulation results are compared with those obtained by a traditional control method based on PSF MPPT control and active stall control.
- The MBLC is enhanced by online parameter estimation using the Kalman filter, which is simulated with Matlab/Simulink to generate the *d*-axis rotor current reference for the current loop of vector control. Simulations use realistic wind speed profiles and include an error in the estimation of four parameters of the DFIG: r_s, r_r, $L_{\sigma s}$, L_m.
- Simulation results are compared with those obtained by the traditional MBLC.
- The operation of the wind turbine controlled by the proposed optimal control algorithm, combining the fuzzy control based SIRM and the enhanced MBLC, is

simulated to analyse the annual extra electrical energy generated, taking into account the typical wind speeds over a year at Plymouth, UK in 2005.

This thesis proposes an optimal control algorithm to maximise the efficiency of DFIG wind generation system coupled with a VSPF wind turbine under DFIG and wind turbine parameter uncertainties. The stator-flux oriented vector control on the rotor converter side for generator speed reference, and *d*-axis rotor current reference will be extended by introducing new control layer generating an online optimal generator speed reference and *d*-axis rotor reference in order to optimise the energy production from the WECS for full range of wind speed. The fuzzy control based on SIRMs connected fuzzy inference model and enhanced MBLC by online parameter estimation using the Kalman filter are applied to generate two adaptive references.

1.4 Research Contribution

The main contributions of this thesis are as follows:

- Introduction of adaptivity to the fuzzy control based SIRM using hybrid MPPT control and active stall control via speed regulation. As a result, the proposed control algorithm can search for the maximum power of the wind turbine in the presence of uncertainties in control parameters, e.g. the air density and the wind turbine design. The fuzzy control based SIRM gives higher performance than traditional algorithms, such as PSF MPPT control.
- Introduction of adaptivity to the MBLC using the Kalman filter. As a result, the control can find the minimum copper loss of the DFIG even under parameter

uncertainties. Therefore, the proposed control algorithm gives higher performance than traditional MBLC.

- Simplification of the hardware and implementation, as the proposed control does not require wind speed sensors, motorised blades and pitch angle controls.
- Reduction of the number of rules of fuzzy control based SIRMs connected to the fuzzy inference model. The proposed fuzzy control gives an adaptive step size of speed reference, which leads to fast tracking.
- Improvement of the control response, as the proposed controller incorporates the PSF MPPT, which gives the correct direction to reach maximum operating point even in the presence of large inertia of the wind turbine and/or rapid wind change.

1.5 Organisation of the Thesis

The thesis consists of 7 chapters as follows:

- Chapter 1 presents the research background and significance, the motivation of the research, aims of the research, scope of the research, methodology in brief and the research contribution.
- Chapter 2 presents the variable-speed wind turbine wind energy conversion systems with a doubly-fed induction generator. The basic knowledge of the variable-speed wind turbines, the doubly-fed induction generator, the back-to-back voltage converter are studied. Furthermore, this chapter includes the efficiency evaluation of the variable-speed wind turbine wind energy conversion

systems and the literature review of the optimal effective control applied for variable-speed fixed-pitch wind turbines.

- Chapter 3 focuses on the vector control methodology driving the DFIG on the rotor side converter, the DFIG dynamic model: αβ model and dq model and stator-flux oriented vector control for DFIG on the rotor side converter are studied. In addition, this chapter includes the simulations of the stator-flux oriented vector control driven on the DFIG by Matlab/Simulink.
- Chapter 4 presents the optimum power control for variable-speed fixed pitch wind turbines. Also, the efficiency of the power control algorithm for variable-speed fixed pitch wind turbines under wind turbine parameter uncertainties is analysed. The fuzzy controller based on the SIRM connected fuzzy inference model for power control algorithm in the WECS for the fixed-pitch wind turbine is developed. Moreover, the fuzzy controller based on SIRM for the power control in WECS is tested under the wind turbine parameter uncertainties through simulation based on Matlab/Simulink.
- Chapter 5 presents robust copper loss minimisation control for DFIG. The efficiency of the model-based loss minimisation control under DFIG parameter uncertainties is analysed. Also, the basic knowledge of online parameter estimation of DFIG using the Kalman filter method is studied. The model-based loss minimisation control enhanced by the online parameter estimation is tested under the DFIG parameter uncertainties via simulation based on Matlab/Simulink.

- Chapter 6 analyses controller performance under parameter uncertainties. The performance of the fuzzy controller based on SIRM under air density and wind turbine parameter uncertainties and enhanced MBLC under DFIG parameter uncertainties is analysed.
- Chapter 7 concludes and presents possible future research.

Chapter 2 Wind Energy Conversion Systems for Variable-Speed Wind Turbines with DFIGs

2.1 Introduction

A wind energy conversion system (WECS) can is defined as a system that converts kinetic energy in the wind to rotational mechanical power via a wind turbine, then, this mechanical power is transformed into electrical power by an electrical generator [1],[2]. There are two kinds of WECSs: fixed-speed wind turbines (FSWT) and variable-speed wind turbines (VSWT) [3]. For the FSWT technique, an electrical generator, normally a squirrel cage induction generator (SCIG), is directly connected to the electrical power grid. Therefore, the SCIG coupled with the wind turbine must run at near synchronous speed to keep the terminal voltage of the generator at the same frequency as the power grid at 50 Hz or 60 Hz. However, when wind speed varies, the FSWT system has certain disadvantages such as poor efficiency of power extraction, high mechanical stress and high power fluctuation [4],[5].

The VSWT technique had been developed to overcome the drawbacks of the FSWT by using a back-to-back voltage converter connected between the generator and power grid. For this technique, the rotational speed of the wind turbine is adjusted when wind speed varies. Hence, the wind turbine can extract maximum power from the wind [6]. The VSWT technique becomes attractive in applications in the WECS. Three generators, the squirrel cage induction generator (SCIG), doubly-fed induction

generator (DFIG), and permanent magnet synchronous generator (PMSG), can be used in a variable speed wind generation system [7]. The DFIG-based WECS are most attractive due to using smaller power converters than other VSWT systems [8].

This chapter introduces the basic concepts of VSWT systems in terms of wind power generation, wind turbine aerodynamic model and electrical model. Next, the configuration of the VSWT WECS based on the DFIG is described each: DFIG; back-to-back converter; and control system. The efficiency of the VSWT-WECS based on the DFIG is evaluated by the active power flow. Finally, section 2.5 provides a literature review of the optimal effective control applied for VSFP wind turbines to improve both mechanical efficiency and electrical efficiency.

2.2 Variable-Speed Fixed-Pitch Wind Turbines

VSFP wind turbines are designed to regulate the mechanical power extracted from the wind by using only the control of the rotational speed of the rotor. This is achieved with a maximum power point tracking (MPPT) control and active stall control via speed regulation.

The following sub-sections explain the basic concepts of conversion of wind kinetic energy into mechanical energy, the wind turbine aerodynamic model and the power control.

2.2.1 Wind Power Fundamentals

The kinetic energy of a certain volume of wind can be expressed as [9],[10]:

$$E_w = \frac{1}{2} m V_w^2 \tag{2.1}$$

where m is the mass of air in the considered volume and V_w is the wind speed. Hence, the total power in the wind is given by the rate change of the kinetic energy [9],[10]:

$$P_w = \frac{1}{2} V_w^2 \frac{dm}{dt} \tag{2.2}$$

and wind can be analysed by fluid mechanics. Thus air flow is expressed in mass flow rate [9],[10]:

$$\frac{dm}{dt} = \rho A V_w \tag{2.3}$$

where ρ is the air density; and A is the surface area of the air stream. Substituting (2.3) into (2.2), the wind power is given by [9],[10]:

$$P_w = \frac{1}{2} \rho A V_w^3 \tag{2.4}$$

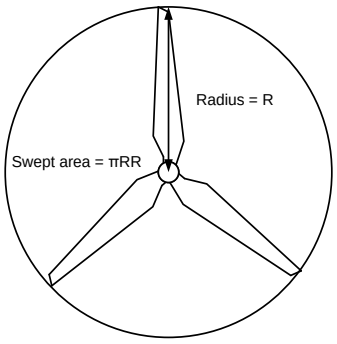

Figure 2.1: Wind turbine swept area [9]

2.2.2 Wind Turbine Aerodynamic Model

The swept area of the wind turbine is shown in Figure 2.1. This area can be calculated by using the formula of the area of a circle having as a radius the length of the blades:

$$A = \pi R^2 \tag{2.5}$$

According to wind turbine theory [11], the possible mechanical power that can be extracted by the wind turbine is [12]:

$$P_m = \frac{1}{2}\rho\pi R^2 V_w^3 C_p(\lambda,\beta) \tag{2.6}$$

where R is the radius of the wind turbine, and C_p is the power coefficient of the wind turbine. The power coefficient C_p represents the efficiency of the power extraction from the wind through the wind turbine. Theoretically, the possible maximum value of C_p is 59.3% as referred by the Betz Limit [3]. For practical wind turbines, typical values of C_p are between 0.4-0.5 [3].

The coefficient C_p is expressed as a function of the tip-speed ratio, λ, and the pitch angle, β [10],[13]–[15]. The tip speed ratio is defined as:

$$\lambda = \frac{\omega_T R}{V_w} \tag{2.7}$$

where ω_T is the wind turbine rotational speed. Typically, the pitch angle, β of the turbine blade is defined for small angle for the maximum power output of the wind turbine in below-rated wind speed.

The power coefficient C_p does not have an analytical closed-form, but its expression can be interpolated from experimental data. One example of this approximation is given by the following equation: [4], [7]:

$$C_p = a_1\left(\frac{a_2}{\lambda_i} - a_3\beta - a_4\right)e^{-a_5/\lambda_i} + a_6\lambda \tag{2.8}$$

where:

$$\frac{1}{\lambda_i} = \frac{1}{\lambda + b_1\beta} - \frac{b_2}{1+\beta^3} \tag{2.9}$$

and the coefficients a_1, a_2, a_3, a_4, a_5, a_6, b_1, and b_2 are calculated using curve fitting techniques.

The aerodynamic torque on the wind turbine is finally defined as [7]:

$$T_a = \frac{P_m}{\omega_T} = \frac{1}{2\lambda}\rho\pi R^3 V_w^2 C_p(\lambda,\beta) \tag{2.10}$$

2.2.3 Wind Turbine Characteristics

The power coefficient, C_p and coefficients, a_1-a_6 and b_1-b_2 in (2.8) and (2.9) are used to characterise the wind turbine through the C_p-λ curve. Figure 2.2 shows the power coefficient, C_p as a function of the tip-speed ratio for different pitch angle values. In this example, the coefficients of the wind turbine are: a_1 = 0.5176, a_2 = 116, a_3 = 0.4, a_4 = 5, a_5 = 21, a_6 = 0.0068, b_1 = 0.08 and b_2 = 0.035 which are derived from [4]. It can be observed that the optimum value of λ, called λ_{opt}, depends on the pitch angle. For a

pitch angle β = 0°, λ_{opt} is 8.1 and the maximum power coefficient, C_{pmax}, is 48%. When the pitch angle increases, the blade of the wind turbine is pitched out from the wind. Therefore, the mechanical power extracted from the wind also reduces.

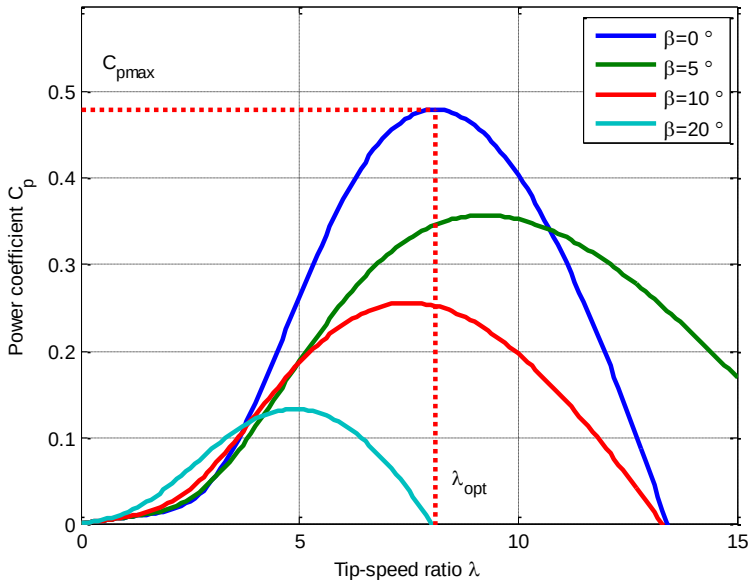

Figure 2.2: Characteristics of power coefficient versus tip-speed ratio for different blade pitch angles

The mechanical power can be calculated from (2.6). For example, a wind turbine designed for a wind speed of 10 m/s with a blade radius of 2.372 m, would generate 5 kW. If the gearbox ratio = 7, the rated generator rotational speed would be 2250 rpm (or $1.5\omega_s$, ω_s = 1500 rpm). Using the calculations from [16] relating the length of the blades to the power out of the wind turbine, the moment of inertia of the wind turbine would be 13.5 kg.m^2. Figure 2.3 shows the extracted mechanical power of the wind turbine with respect to the generator speed for various wind speeds and a pitch angle equal to zero. It can be observed that the maximum mechanical power is obtained by tracking the optimal generator speed when wind speed is below the rated value. If instead the wind

speed is above the rated value, the mechanical power must be limited to avoid damage to the turbine. This can be achieved by either pitch angle control or stall regulation.

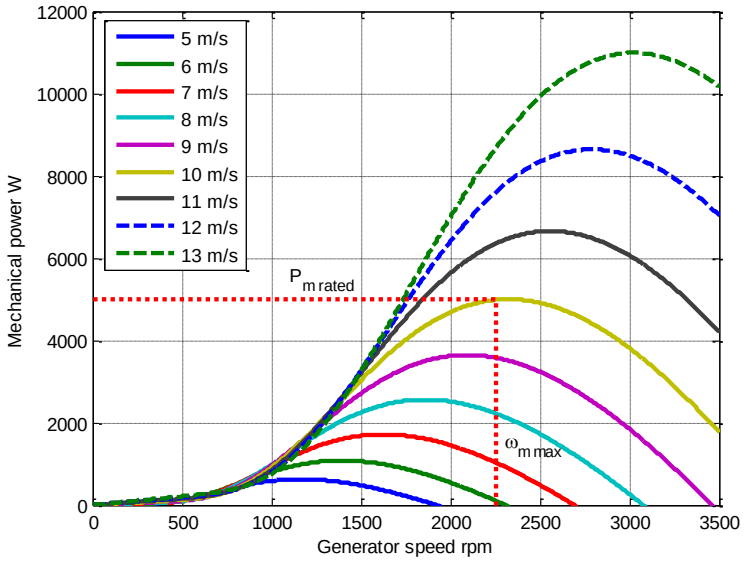

Figure 2.3: Characteristics of mechanical power versus generator speed for different wind speeds

2.2.4 Drive Train Model

When the wind turbine is connected to the electrical generator through a gearbox, the speed of the turbine ω_T is related to the speed of the generator ω_m through the gearbox ratio, G_r. The mechanical torque, T_m and machine speed, ω_m can be calculated as follows[7]:

$$T_m = \frac{T_a}{G_r} \tag{2.11}$$

$$\omega_m = G_r \omega_T \tag{2.12}$$

where T_a is aerodynamic torque on the wind turbine side. The drive train of the wind turbine is modelled by the following differential equation that takes into account the total moment of inertia [17]:

$$(J_G + \frac{J_T}{G_r^2})\frac{d\omega_m}{dt} = T_m - T_{em} \tag{2.13}$$

where T_{em} is the electromagnetic torque of the electrical generator, J_G is the inertia of the generator, and J_T is the inertia of the wind turbine.

The block diagram of the wind turbine model can be illustrated in Figure 2.4.

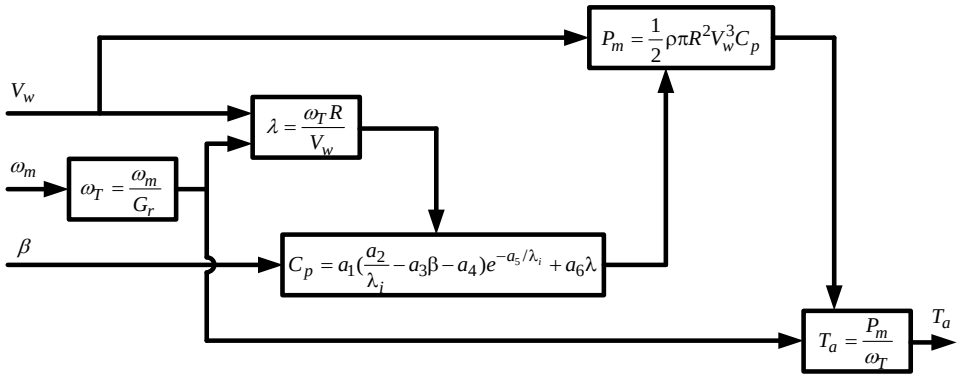

Figure 2.4: Wind turbine model block diagram

2.2.5 Control Objective of VSFP Wind Turbines

Control of the VSWT is classified into three modes as a function of the wind speed as shown in Figure 2.5 [18]–[20].

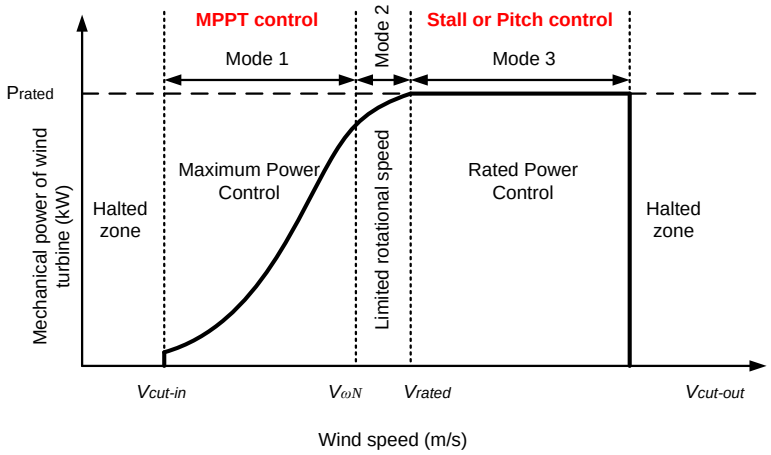

Figure 2.5: Variable speed wind turbine control [18]

1. Constant power coefficient at C_{pmax}
2. Constant rotational speed at its nominal value
3. Constant mechanical power at its nominal value, P_{rated}

The cut-in wind speed, $V_{cut\text{-}in}$, is the minimum wind speed for which the wind turbine is capable of sustaining a continuous generation. The cut-out wind speed, $V_{cut\text{-}out}$, is the maximum wind speed that does not cause damage to the blades, the generator and other components of the wind turbine. The rated wind speed, V_{rated}, is the minimum value of the wind speed for which the wind turbine provides the rated mechanical power, P_{rated}. The value $V_{\omega N}$ is the minimum value of the wind speed for which the wind turbine reaches the nominal rotational speed of the generator.

In mode 1, the objective of the control is to extract the maximum mechanical power from the wind turbine. The rotational speed is regulated to track λ_{opt} corresponding to the maximum power coefficient, C_{pmax}, also known as maximum power point tracking (MPPT) control. There are many methods for the MPPT, and the details are presented in following sections.

In mode 2, the objective of the control is to keep a constant rotational speed of the wind turbine at nominal value when the wind speed increase. This mode was called the transition region [18] because it is located between the maximum power control mode and the rated power control mode. The rotational speed reaches the nominal value while the output power of the turbine is less than the rated power value. However, mode 2 may not exist if the nominal rotational speed and the maximum power coefficient C_{pmax} meet at the rated wind speed V_{rated} as seen in [21]

In mode 3, the objective of the control is to limit the mechanical power to the rated value which, for fixed-pitch wind turbines, is achieved by the active stall control via speed regulation [18].

2.3 Wind Energy Conversion Systems with DFIGs

There are three main types of generators used in wind energy conversion systems for variable speed wind turbines: DFIG, SCIG, and PMSG [7]. The details of the generators are explained below.

2.3.1 Configuration of Wind Energy Conversion System based DFIG-VSWT

The electrical components of variable speed WECS consist of an electrical generator, a back-to-back converter, a control system and interconnection apparatus such as crowbar system and passive filters. Figure 2.6(a) depicts the configuration of the VSWT of PMSG, SCIG whereas Figure 2.6(b) indicates the configuration of DFIG [22]. The variable speed wind turbine with full-scale power converter configuration (total generated power to the grid through the power converter) is used with PMSG and SCIG, and the variable speed wind turbine with partial-scale power converter configuration (some of the total generated power to grid through the power converter) is used with DFIG.

The control system of WECS with either PMSG, SCIG or DFIG has two control levels as shown in Figure 2.6 [23],[24].

- **Control level 1** is used to control the active and reactive power that flows between the DFIG and the power grid using the RSC and the GSC, as explained in the previous sections.
- **Control level 2** is used to control the mechanical power in the full range of the wind speed by generating the references for control level 1 that achieve the maximum efficiency of the WECS. These references are the optimal speed reference to maximise the mechanical power and the optimal reactive power reference to minimise the electrical losses of the electrical generator.

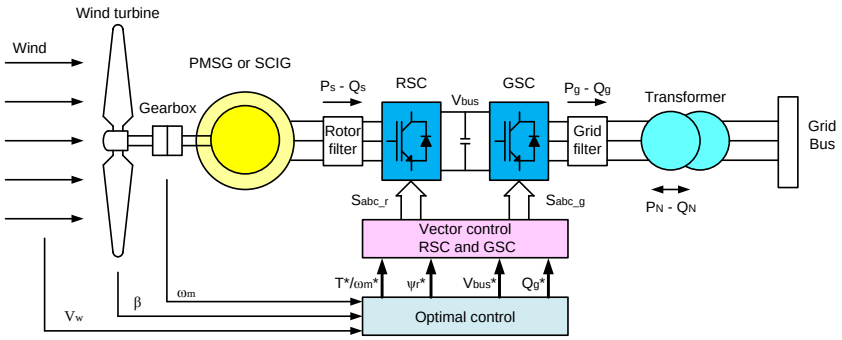

(a)

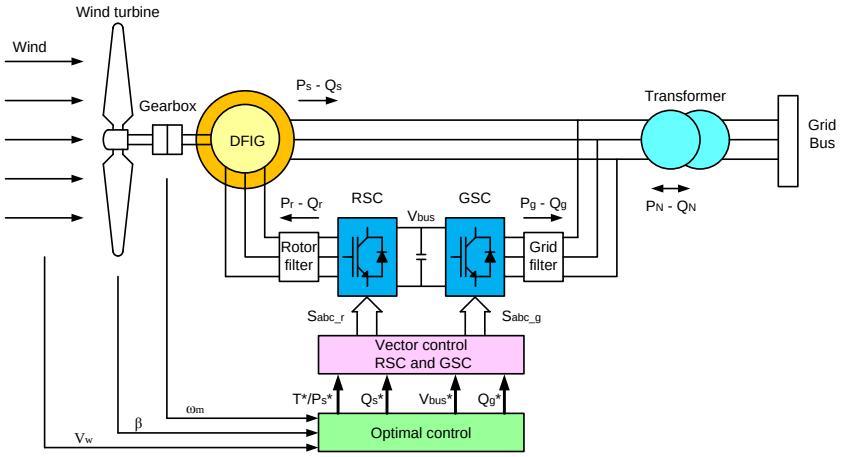

(b)

Figure 2.6: Configurations of the variable speed wind turbine with different generator: (a) based on PMSG or SCIG, (b) based on DFIG [4]

For the configurations of Figure 2.6(a) the stator terminals of either the PMSG or the SCIG are connected to the power grid through the power converter. The back-to-back power converter can control the generator speed independently on the frequency and voltage of power grid. Gearless concepts can also be used for this the wind turbine system with PMSG.

The variable speed generation system based on the PMSG or the SCIG have the following main characteristics:

- Full speed regulation.
- Reduce maintenance costs for the absence of slip-rings and brushes.
- Independent control of the output active and reactive powers.
- Full scale of the power converter.
- Gearbox required in the SCIG and possibility of gearless concept in the PMSG

Figure 2.6(b) shows the configuration of the variable speed wind turbine based on the DFIG. This configuration requires a gearbox but only a partial-scale power converter. The stator terminals of the DFIG are directly connected to the electrical power grid, while the rotor circuits are connected through a back-to-back power converter. The power converter controls the magnitude and phase of the rotor currents and, hence, the rotational speed, independently of the grid frequency and voltage. The power rating of DFIG power converters is only required 30% of the rated power and, consequently, a similar range of speed regulation can be obtained [22].

The variable speed generation system based on the DFIG has the following main characteristics:

- Decoupled control of the active and reactive powers by controlling on the rotor side converter within the rating of the power converters.
- Decoupled control of the DC-link voltage of the back-to-back converter and the power factor by controlling on the grid side converter.

- Speed range limited by the rating of the power converter, e.g. 0.7 – 1.3 per unit.
- Reduced converter cost and less switching losses as the power converter is rated only for a fraction of the total power.
- Need for slip-rings and brushes.
- Gearbox required.

The majority of generators used for WECS are DFIGs, as they represent a cost-effective solution, and reduced weight and size in comparison to other WECS [25]. Therefore, the operation of DFIG is explored more in details in the following sections.

2.3.2 Doubly-Fed Induction Generator (DFIG)

DFIGs convert the mechanical power from the wind turbine into electrical power. This section reviews the operating principle of DFIGs and the equations of the mathematical model. Steady-state operations are analysed by means of the equivalent electrical circuit. Then, the model is used to analyse the steady-state performance of the DFIG for various operating conditions.

2.3.2.1 Fundamental principles of doubly fed induction machines: Doubly-fed induction machines (DFIM) are characterised by a wound-rotor. The rotor windings are connected to an external AC source via slip-rings and brushes. The stator winding is similar to squirrel cage induction machines. Figure 2.7 shows the fundamental structure of the DFIM.

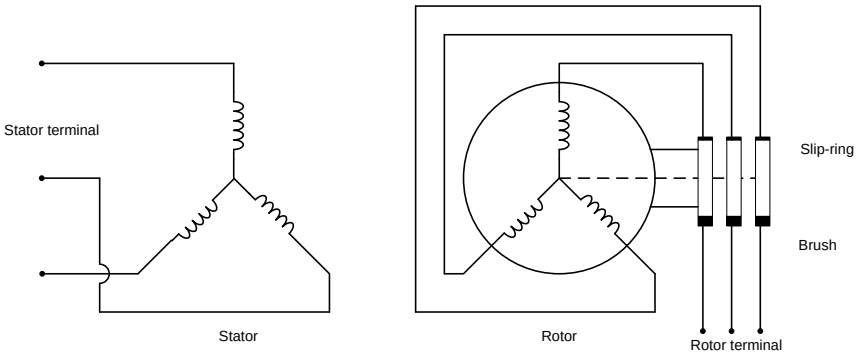

Figure 2.7: Configuration of doubly induction machines

The primary of operation of DFIM can be described as follows:

- The stator windings are supplied by a three-phase AC source having frequency f_s. This generates a stator magnetic field rotating at synchronous speed $2\pi f_s/p$, being p the number of pole pairs.
- The rotor windings are supplied via slip-rings with three phase voltages of a variable frequency and magnitude, which are dependent on the rotor mechanical speed. This results in a rotor magnetic field in the air gap, with the same spatial rotational speed as the stator flux.
- The stator magnetic field and the rotor magnetic field have a phase shift. Therefore, the electromagnetic torque is generated as the magnetic fields interact with each other.
- The synchronous speed, n_s, is a function of a number of poles of the DFIM, P, and frequency voltage supplied from the grid, f_s. The expression is [7]:

$$n_S = \frac{120\, f_S}{P} \tag{2.14}$$

- The difference between synchronous speed, n_s, and rotor speed, n, which can be calculated as a percentage of synchronous speed, is called the slip, s, as follows[7]:

$$s = \frac{n_s - n}{n_s} \tag{2.15}$$

- Three different operations of the machine that are classified by the slip's value

  $s > 0$; the DFIM is called sub-synchronous mode

  $s < 0$; the DFIM is called super-synchronous mode

  $s = 0$; the DFIM is called synchronous mode

- The frequency of voltage and current of the rotor depends on the slip[7]

$$f_r = sf_s \tag{2.16}$$

2.3.2.2 Characteristics of doubly fed induction machines: To study the behaviour of the DFIG, one-phase steady-state equivalent circuit of the DFIM is used to discuss the basic power and torque expression in the machine as shown in Figure 2.8 [7].

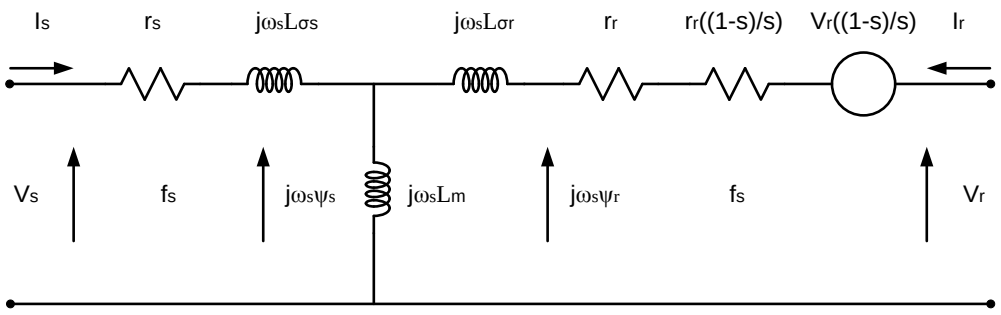

Figure 2.8: Per-phase equivalent circuit of DFIM [7][12]

From the diagram, the stator active power of the DFIM can be calculated by the following expression[7]:

$$P_s = 3\mathrm{Re}(V_s \cdot I_s^*) \tag{2.17}$$

The rotor active power is instead equal to:

$$P_r = 3\mathrm{Re}(V_r \cdot I_r^*) \tag{2.18}$$

The active power losses of the machine of the stator and rotor are given by:

$$P_{s\_CL} = 3r_s |I_s|^2 \tag{2.19}$$

$$P_{r\_CL} = 3r_r |I_r|^2 \tag{2.20}$$

The balancing active power equation of the DFIM can be written as follow:

$$P_s + P_r = P_{s\_CL} + P_{r\_CL} + P_{mech} \tag{2.21}$$

where P_{mech} is the mechanical power. Equation (2.21) allows the calculation of the mechanical power:

$$P_{mech} = 3r_r(\frac{1-s}{s})|I_r|^2 + 3(\frac{1-s}{s})\mathrm{Re}(V_r \cdot I_r^*) \tag{2.22}$$

The mechanical power is also related to the electromagnetic torque T_{em} and rotational speed by the equation:

$$P_{mech} = T_{em}\Omega_m = T_{em}\frac{\omega_m}{p} \tag{2.23}$$

The electromagnetic torque is calculated by using (2.22) and (2.23)

$$T_{em} = \frac{3r_r p}{\omega_m}\left(\frac{1-s}{s}\right)\left|I_r\right|^2 + \frac{3p}{\omega_m}\left(\frac{1-s}{s}\right)\mathrm{Re}(V_r \cdot I_r^*) \tag{2.24}$$

Finally, simplifying (2.24) the electromagnetic torque is obtained by the following equation:

$$T_{em} = 3pL_m \cdot \mathrm{Im}(I_r^* \cdot I_s) \tag{2.25}$$

The stator and rotor reactive powers are also expressed as:

$$Q_s = 3\,\mathrm{Im}(V_s \cdot I_s^*) \tag{2.26}$$

$$Q_r = 3\,\mathrm{Im}(V_r \cdot I_r^*) \tag{2.27}$$

The relation between stator active power and rotor active power is approximated by ignoring the copper losses on the stator and rotor. Using this hypothesis, it is possible to write that:

$$P_r \cong -sP_s \tag{2.28}$$

Therefore, the mechanical power can be expressed as:

$$P_{mech} \cong P_s - sP_s = (1-s)P_s \tag{2.29}$$

When the DFIM operates as a generator, the machine receives the mechanical power from the shaft ($P_{mech} < 0$). In the sub-synchronous mode, the rotor receives power from the grid, while the stator supplies power to the grid, i.e. part of the power is circulated through the generator. Conversely, in the super-synchronous mode, both rotor and stator supply power to the grid. In the synchronous mode, the stator supplies power to the grid while the rotor power is zero.

The active power flow of the DFIM in generator mode is summarised in Figure 2.9.

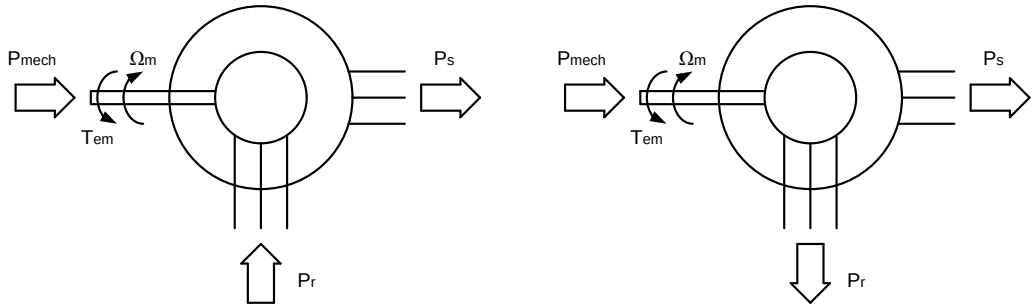

(a) (b)

Figure 2.9: Active power flow of DFIM in generator mode: (a) sub-synchronous speed (b) super-synchronous speed [7]

2.3.3 Bidirectional Back-to-Back Voltage Source Converter

The control of the DFIG in WECS is achieved by using a back-to-back PWM voltage source converter in the rotor circuit, using the vector control technique [7]. As the DFIG can operate in either sub-synchronous or super-synchronous mode, a bi-directional back-to-back converter is required to supply the rotor circuit. The bi-directional back-to-back converter consists of two PWM voltage source converters (VSCs) connected back-

to-back through a dc-link capacitor. Two-level converters with IGBTs are the most widely used topologies for variable speed wind-energy generation due to the low cost [7]. The schematic of the back-to-back converter is shown in Figure 2.10.

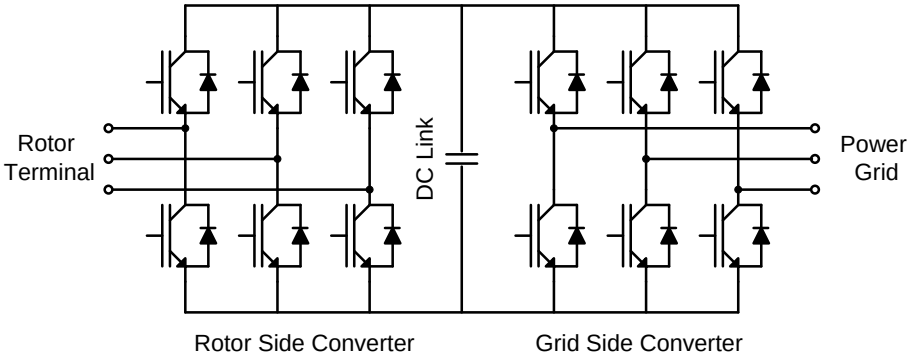

Figure 2.10: Schematic of back-to-back voltage source converter system [7]

The power converter connected to the rotor terminal of the DFIG is known as a rotor-side converter (RSC), while the power converter connected to the grid power is known as a grid-side converter (GSC).

The RSC functions to control the torque or the speed of the DFIG and also stator reactive power by generating a variable frequency and amplitude voltage to the rotor terminal. The RSC is usually controlled by a stator flux oriented vector control. According to the previous section, the rotor voltage frequency and rotor voltage amplitude can be expressed by the following equations[7]:

$$\omega_r = \omega_s - \omega_m \tag{2.30}$$

$$V_r = sV_s \tag{2.31}$$

The torque or speed of the DFIG and the stator reactive power are controlled by adjusting the amplitude, frequency and phase of the rotor voltage.

The rotor voltage control is depicted in Figure 2.11.

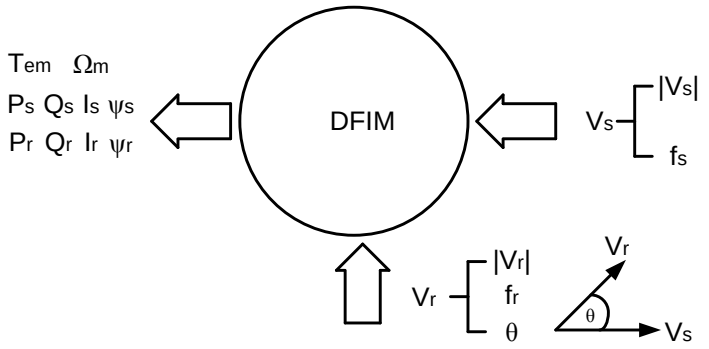

Figure 2.11: DFIM rotor voltage variation control[7]

The GSC functions to control a constant DC-link voltage regarding delivering and receiving the active rotor power. The GSC is operated at the grid frequency. In addition, the GSC can control reactive power exchanged with the grid.

In conclusion, the power converter for VSWT WECS with DFIG has the following properties:

- It handles bidirectional power flows.
- The RSC and GSC are two-level six switches converters.
- The RSC operates with low frequencies equal to the slip of the generator.
- The GSC operates with almost constant frequency equal to the grid frequency.
- The switching devices are usually insulated gate bipolar transistors (IGBT).

- Pulse width modulation (PWM) technique is used to generate the pulse to control the IGBTs.

2.4 Efficiency Evaluation of VSWT WECS

This section analyses the operating factors influencing the efficiency of variable-speed WECS with DFIG. The power losses of the WECS can be classified into three categories: aerodynamic, mechanical and electrical losses[26]. The power flow of the WECS is shown in Figure 2.12 [27].

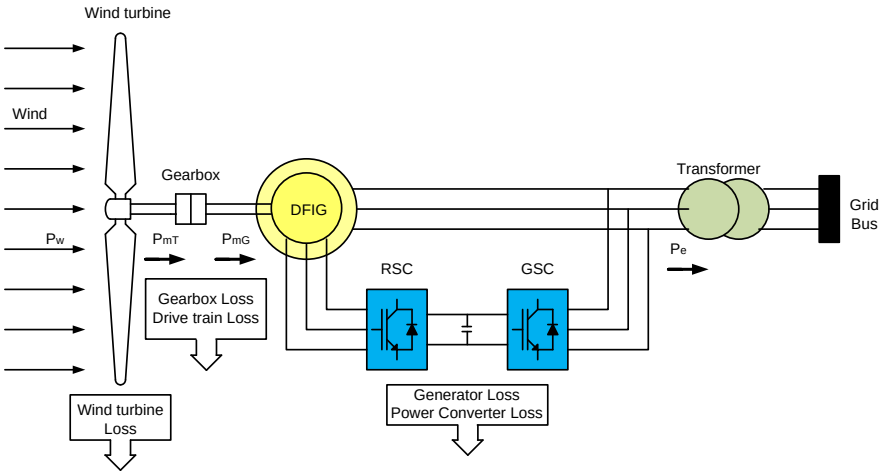

Figure 2.12: Power flow of variable-speed WECS

The aerodynamic power loss is caused by the conversion of the wind kinetic energy into mechanical power at the turbine blades. The efficiency of the wind turbine is defined by the power coefficient, C_p, as indicated in Eqn.(2.8). The aerodynamic power loss is the largest proportion of losses of WECS. The aerodynamic efficiency, η_T, is theoretically limited to 59%, known as the Betz Limit [7].

The mechanical power losses are generated in drive train and gearbox due to friction. The mechanical power is transferred from the wind turbine shaft at a low rotational speed to the generator shaft at a high rotational speed. The mechanical losses in WECS consist of the gear loss, bearing loss and windage loss The mechanical efficiency, η_m, is typically of a value of 96% at the generator rated power according to [28][29].

The electrical power losses are generated in the generator and the power converter. The generator losses consist of copper loss in stator and rotor windings, and core loss. The power converter losses consist of switching loss and conduction loss of IGBTs and diodes. The electrical efficiency, η_e, is typically of a value of 97% at the generator rated power according to [29].

Therefore, the power output at the point of connection of the WECS to the grid is given by:

$$P_g = \eta_t \eta_m \eta_e P_w \tag{2.32}$$

It is clear that the efficiency has a central part in the design and operations of WECS, as any improvement would lead to a higher annual energy yield and, consequently, a higher return on investment. The following chapter will explore in more detail how this can be achieved with a suitable control technique.

2.5 Currently Control Method and New Trends on WECS

The stator-flux oriented vector control is employed with the DFIG on RSC. The generator speed reference, ω_{m_ref}, and stator reactive power reference, Q_{s_ref} , will be extended by introducing a new control layer generating the optimal speed reference and stator reactive power reference in order to increase power, efficiency and reliability on the WECS.

In [30],[31], both mechanical and electrical efficiency of the WECS are improved by MPPT controller and minimum electric loss (MEL) controller, respectively. As a result, the maximum extracted power from the wind turbine and the minimum copper losses of the generator were obtained. However, the two optimal controllers require accurate knowledge of the air density, wind turbine parameters and generator parameters for control laws. In practical application, these parameters are obtained by the experimental tests of the wind turbine and generator. These experimental tests will give only rough parameters and are subject to change when the system gets older or weather conditions change.

Promising improvements could be obtained using adaptive optimal efficiency control algorithms, as the optimal operating conditions can be maintained by estimating the actual values of the parameters used in the calculations of the power flow maximisation.

2.5.1 Power Control Strategy for VSFP Wind Turbine

As reported in the literature [32]–[34][35], the majority of wind turbines used with variable-speed WECS are variable-speed variable-pitch as shown in Figure 2.13 for control desired output power from the wind turbine. When wind speed is below the rated value, the MPPT controller tracks the optimal operating point corresponding to the maximum output power of variable-speed wind turbine. When wind speed exceeds the rated value, the extracted power of the wind turbine is limited at the rated power to avoid damage to the blades, the generator and the power converter by keeping the generator speed at the rated value via pitch angle control. However, this is expensive and has a high maintenance cost [36].

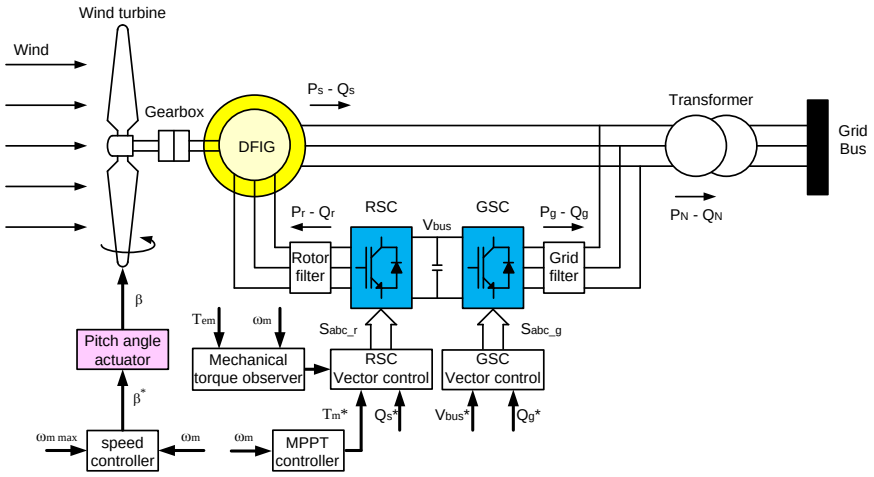

Figure 2.13: Variable-speed variable-pitch wind turbine control [7],[34]

The VSFP wind turbine can be replaced VSVP wind turbine for DFIG WECS to give more cost-effective and reliable [18]–[20]. The power limitation above rated wind speed is controlled by an active stall control via speed regulation.

The power control objective for a VSFP wind turbine is to maximise mechanical power extracted from the wind turbine for any wind speed and constrain generator speed and mechanical power of the turbine at its nominal values to prevent damage to the machine and power converter. Therefore, speed reference trajectory according to this control objective can be shown in a P_m-ω plane for the full range of wind speed in Figure 2.14. At the below-rated wind speed, control generates an optimal speed reference to maximise the mechanical power extracted from the wind turbine by using the MPPT controller. At the above-rated wind speed, control generates an optimal speed reference to limit the mechanical power at its rated value by using the active stall regulation. A MPPT control and a stall regulation are studied in this chapter. Details are given in the following subsections.

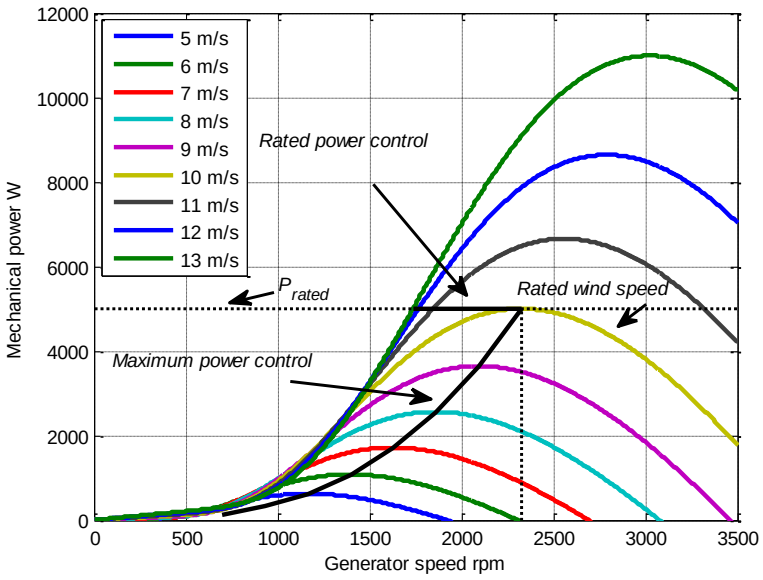

Figure 2.14: Speed reference trajectory in different wind speed

2.5.1.1 Maximum power point tracking (MPPT) control

The power coefficient of the wind turbine, C_p, is expressed as a function of the tip-speed ratio, λ, and the pitch angle, β as mentioned above. The power coefficient expression is defined by the manufacturer design. In this thesis, the power coefficient is written as [37]:

$$C_p = 0.5176\left(\frac{116}{\lambda_i} - 0.4\beta - 5\right)e^{-21/\lambda_i} + 0.0068\lambda \tag{2.37}$$

$$\frac{1}{\lambda_i} = \frac{1}{\lambda + 0.08\beta} - \frac{0.035}{1+\beta^3} \tag{2.38}$$

Figure 2.15 shows the relation between C_p and λ. It can be seen that the optimal tip-speed ratio, λ_{opt}, corresponds to the maximum power coefficient, C_{pmax}, when pitch angle β is zero. From (2.7), when the wind speed changes, the wind turbine speed also changes, to maintain optimal tip speed ratio constant.

From (2.5), the maximum mechanical power of the wind turbine can be calculated as:

$$P_{m\_\max} = \frac{1}{2}\rho\pi R^5 \frac{C_{p\max}}{\lambda_{opt}^3}\omega_m^3 \tag{2.39}$$

where $$k_{opt} = \frac{1}{2}\rho\pi R^5 \frac{C_{p\max}}{\lambda_{opt}^3}$$

$$P_{m\_\max} = k_{opt}\omega_m^3 \tag{2.40}$$

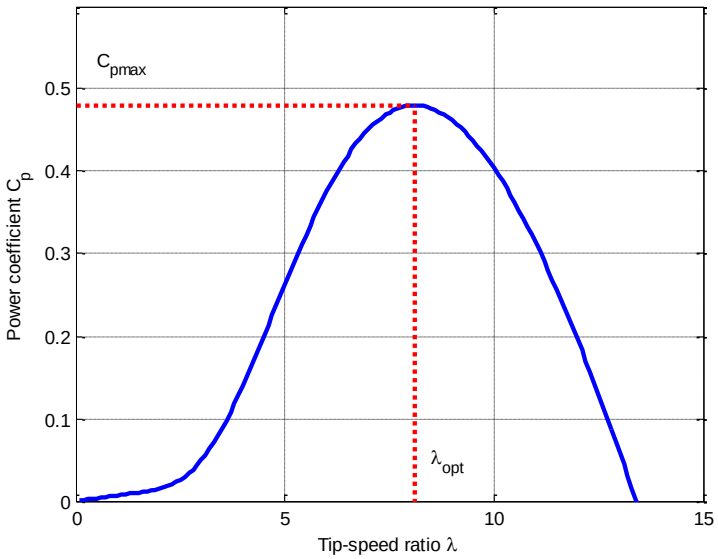

Figure 2.15: C_p-λ characteristics of three blade wind turbine

Four main MPPT controllers, TSR MPPT[38]–[40], PSF MPPT [41],[42], OT MPPT [43],[44] and P&O MPPT [21],[42][45], are widely used for the WECSs to extract the maximum output power from the wind turbine. The control methodologies of these MPPT controllers are explained as follows:

Tip-speed ratio (TSR) MPPT control: The TSP-MPPT control needs the λ_{opt}-V_w curve of the wind turbine and an anemometer for measuring accurate wind speed. The optimal speed reference can be expressed as[21]:

$$\omega_{m\_ref} = \frac{\lambda_{opt} V_w}{R} \tag{2.41}$$

The block diagram of the TSR-MPPT for the WECS can be shown in Figure 2.16

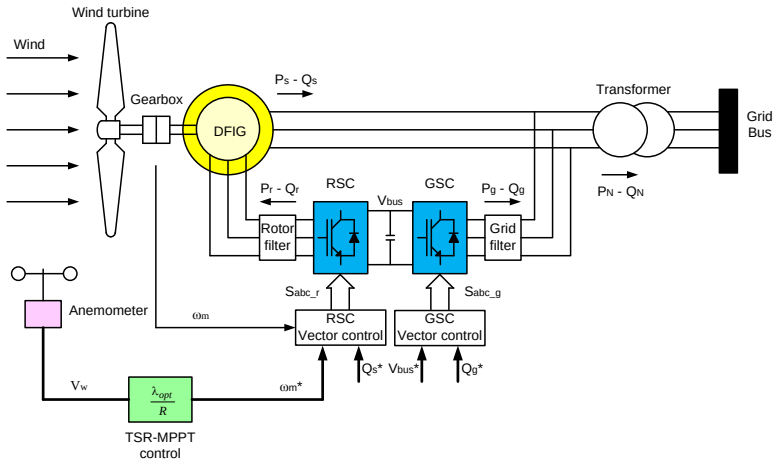

Figure 2.16: TSR-MPPT control for WECS

The technique of the TSR MPPT control is to regulate the generator speed to maintain λ at λ_{opt} which corresponds to maximum power extracted from the wind turbine as referred to in (2.7). This MPPT control requires an accurate wind speed sensor and a generator speed sensor including the design characteristics of the wind turbine at the optimal TSR, λ_{opt} [21],[46]. The advantages of TSR MPPT are high efficiency and fast-tracking, because the speed reference corresponding to the maximum power operating point can be directly calculated from the wind speed as expressed in (2.41) [44]. However, the wind speed sensor required for the TSR MPPT causes additional cost and reduces reliability [21].

Power signal feedback (PSF) MPPT control: the PSF-MPPT technique can extract the maximum mechanical power from the wind turbine by tracking the optimal power point at $\lambda = \lambda_{opt}$ and $C_p = C_{pmax}$. Thus, the optimal mechanical power reference can be calculated from (2.39) and (2.40) [21]. The block diagram of the PSF-MPPT for the WECS can be shown in Figure 2.17.

$$P_{m\_ref} = k_{opt}\omega_m^3 \tag{2.42}$$

and the optimal speed reference can also be expressed as:

$$\omega_{m\_ref} = \sqrt[3]{\frac{P_m}{k_{opt}}} \tag{2.43}$$

Optimal torque (OT) MPPT control: the OT-MPPT technique can extract the maximum mechanical power from the wind turbine by tracking the optimal mechanical torque point at $\lambda = \lambda_{opt}$ and $C_p = C_{pmax}$. Thus, the optimal mechanical torque reference can be expressed as [21]:

$$T_{m\_ref} = \frac{P_{m\_\max}}{\omega_m} = \frac{1}{2}\rho\pi R^5 \frac{C_{p\max}}{\lambda_{opt}^3}\omega_m^2 = k_{opt}\omega_m^2 \tag{2.44}$$

The block diagram of the OT-MPPT for the WECS can be shown in Figure 2.18.

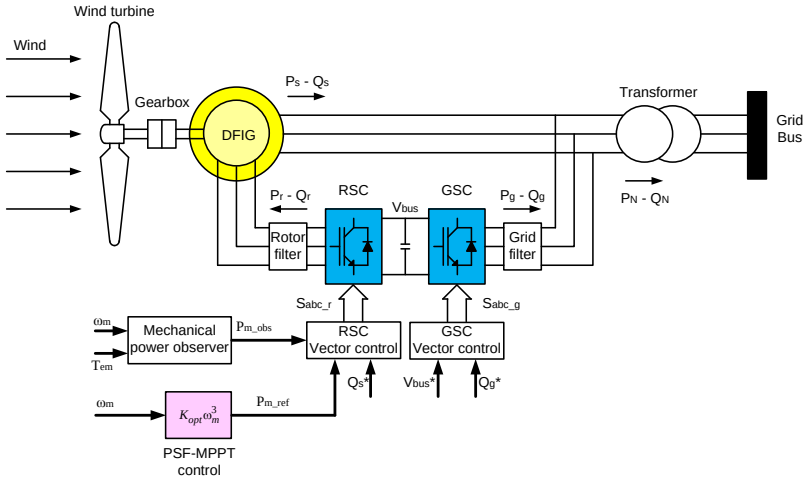

Figure 2.17: PSF-MPPT control for WECS

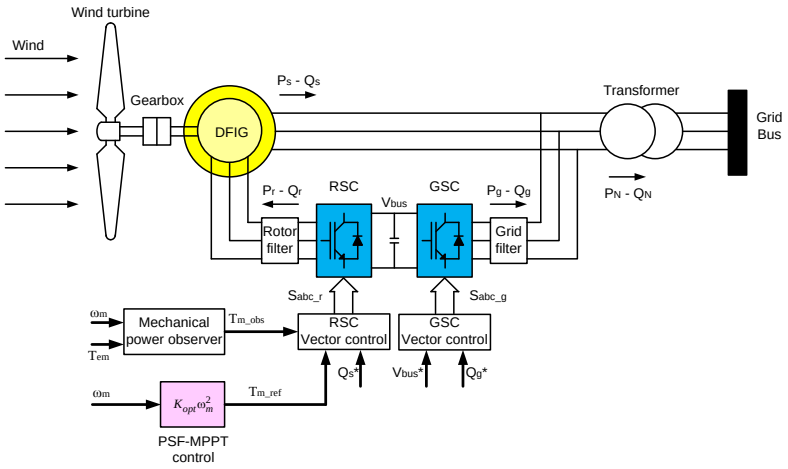

Figure 2.18: OT-MPPT control for WECS

PSF MPPT and OT MPPT control do not require a wind speed sensor. Calculation of optimal power reference and optimal torque reference corresponding to maximum power of the wind turbine are obtained by using as an input the wind turbine characteristic as the optimal TSR, λ_{opt}, and the maximum power coefficient, C_{pmax} and the air density where the turbine is installed [21] [47].

Although the first three MPPT controllers are widely used in the WECS because they are simple to use, and all of them require accurate knowledge of air density and parameters of the wind turbine. In practical applications, these parameters are only roughly known through experimental tests and are subject to change in the long-term [43],[23],[48],[49]. Furthermore, the air density varies with the location and the weather conditions. These problems lead to inaccurate determination of the maximum power operating point of the wind turbine and, hence, reduction of the electrical energy generated.

Perturb & Observe (P&O) MPPT control: P&O MPPT algorithm has been used to overcome the drawback of the previous three MPPT controls due to its capability to search the maximum power operating point of the wind turbine without a wind speed sensor and an accurate knowledge of wind turbine characteristics [50]. Figure 2.19 shows the principle of the P&O-MPPT algorithm for fixed step. The block diagram of the P&O-MPPT for the WECS can be shown in Figure 2.20.

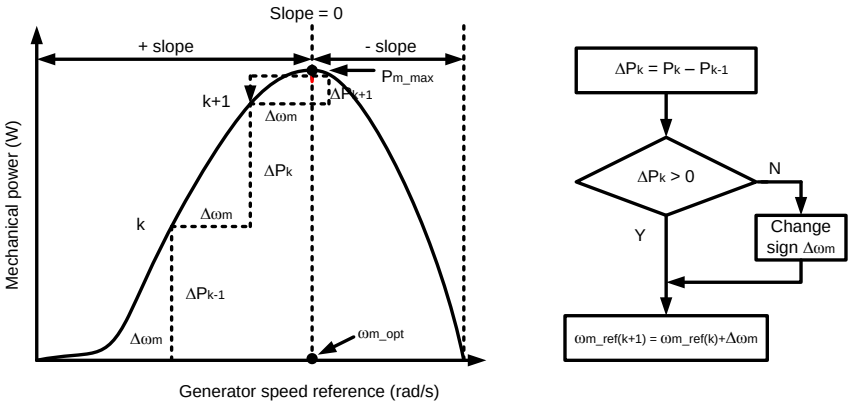

Figure 2.19: P&O-MPPT control principle[39]

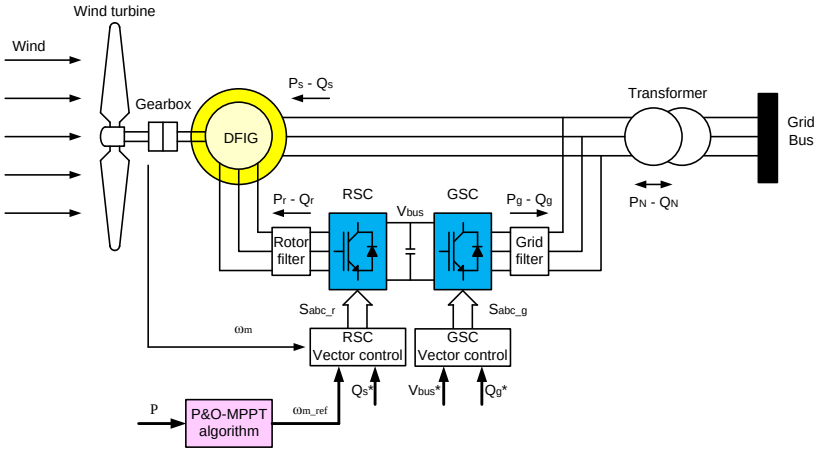

Figure 2.20: P&O-MPPT control for WECS[39]

The P&O MPPT algorithm searches the peak power based on perturbing the rotating speed in steps, such as $\Delta\omega$, and observes the change in output power, ΔP, to decide the direction of the next perturbation action. Then the speed reference is updated by iteration to reach the optimal speed reference according to maximum power from the wind turbine:

$$\omega_{m\_ref}(k+1) = \omega_{m\_ref}(k) + \Delta\omega_m \tag{2.45}$$

A peak point indicates when the slope becomes zero, $\Delta P/\Delta\omega = 0$ [51],[52]. The selection of the size of the step is a challenging topic for P&O MPPT algorithms. A small step gives more accurate results but slower tracking, while a large step gives faster tracking but fluctuates around the maximum power point.

This problem can be solved by a fuzzy logic control (FLC) applied to P&O MPPT [53],[54],[55],[56]. FLC does not require any mathematical model of the systems and is suitable for nonlinear systems [21]. The fuzzy controller provides adaptive step perturbation for P&O MPPT to search the maximum power point. Therefore, this MPPT algorithm provides a good balance between tracking speed and an accurate control [21]. The block diagram of a fuzzy-based MPPT controller is shown in Figure 2.21. From [53], the inputs of the fuzzy-based MPPT controller are the change of power, ΔP, and change of rotational speed, $\Delta\omega$. The updated speed reference is received by combining the change of speed reference, $\Delta\omega_{ref}$ from the fuzzy controller and the previous speed, $\omega_m(k\text{-}1)$.

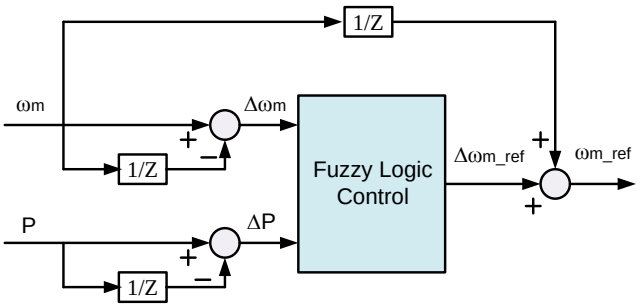

Figure 2.21: Fuzzy-based MPPT controller for WECS

However, fuzzy based MPPT algorithms [53],[54],[55],[56] have good performance only when the wind turbine inertia is small [57]. Additionally, a fuzzy-based MPPT algorithm may detect the wrong direction towards the maximum power operating point under rapid wind changes [21],[58].

Hybrid MPPT control: Hybrid MPPT algorithms have also been introduced to mitigate the problem of traditional controllers [59]. For example, the hybrid MPPT proposed in [59] are combined with the OT MPPT and the fixed step-size P&O MPPT. This hybrid MPPT has been used to improve the efficiency of the algorithm in the presence of either parameter changes, miscalculations of the OT MPPT, or wrong direction to search the maximum power point of the fixed step size P&O MPPT. However, the appropriate step perturbation of P&O MPPT is still difficult to design in the fixed step size P&O MPPT [21].

An advanced MPPT has been proposed in [58] combining three modes of operation. The training mode is used to calculate a k_{opt} via the P&O MPPT controller. When the P&O MPPT controller reached the maximum power operating point, the maximum

power output and optimal generator speed are measured to calculate k_{opt} as the following equation:

$$k_{opt} = \frac{P_{\max}}{\omega_{opt}} \tag{2.46}$$

The recording mode is used to calculate the maximum power operating point through PSF MPPT for constant wind speed as in (2.43); the updating mode is used to update k_{opt} when the wind speed changes. This MPPT algorithm can deal with uncertainties in air density and wind turbine parameters and has fast-tracking. However, it cannot reach the maximum power operating point exactly as k_{opt} is changed for different wind speeds. In addition, it is more complex than the other MPPT algorithms.

2.5.1.2 Stall control

When the mechanical power extracted from the wind turbine exceeds the rated power in the above-rated wind speed, stall regulation is used to maintain the power of the turbine at its rated value, P_{m_rated}. The power coefficient, C_p, is reduced by forcing the wind turbine into a stall operation by decreasing the tip-speed ratio, λ, through the generator speed. The optimal speed reference is given by:

$$\omega_{m\_ref} = \frac{P_{m\_rated}}{\hat{T}_m} \tag{2.47}$$

where mechanical torque, $\hat{T}_m$, is received from the observer algorithm which is detailed in Fig. 2.23.

2.5.1.3 Traditional power control for VSFP wind turbines

The overall block diagram of the traditional power control of WECS coupled with VSFP wind turbines is shown in Figure 2.22 [20]. In the below-rated wind speed, the PSF-MPPT controller is used to track the maximum power operating point of the wind turbine as mentioned above. However, the mechanical power of the wind turbine cannot be measured directly. This problem is solved by the observer design. The closed-loop mechanical power observer structure is shown in Figure 2.23. Electromagnetic torque and generator speed are input signals of the observer block. The estimated mechanical torque is generated by the PI controller, adapting the estimated mechanical torque until the estimated and real generator speed is equal. Therefore, the mechanical power is obtained by multiplying the observed speed and observed torque. In transition region, constant rotational speed control at rated speed is applied to the system. In this control mode, the PSF-MPPT controller has given a larger speed reference than rated speed of the wind turbine and the wind turbine has extracted a smaller mechanical power than the rated value.

In the above-rated wind speed, the active stall control is used to limit the mechanical power extracted from the wind turbine at the rated value, P_{m_rated}, by reducing the generator speed to the stall region. To keep the power constant at the rated value, a rated mechanical power controller is added to the PSF-MPPT control. It provides the compensation speed term via the PI controller to subtract from the speed reference of the PSF-MPPT to regulate the mechanical power at rated value [20].

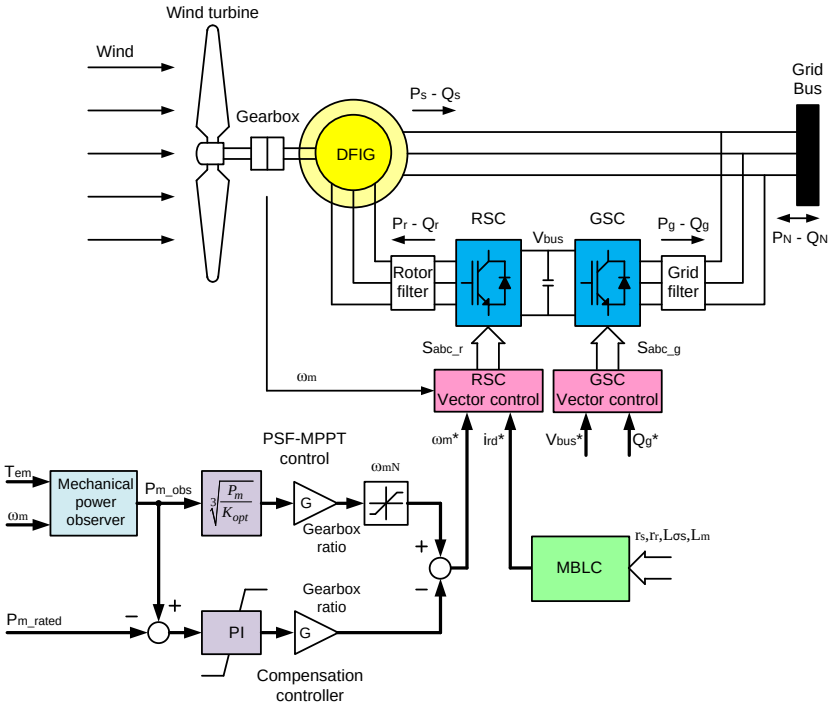

Figure 2.22: Traditional power control for VSFP wind turbines

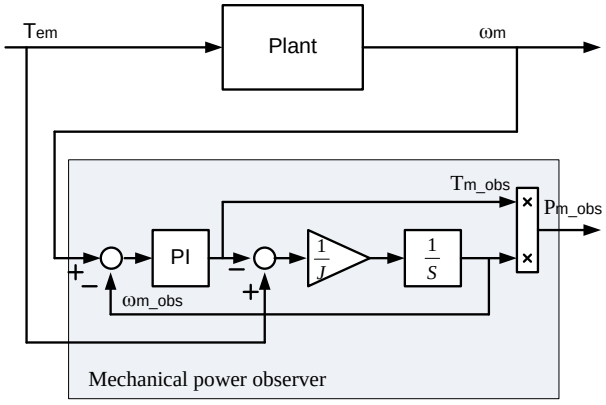

Figure 2.23: Mechanical power observer block diagram[20]

2.5.1.4 Advanced power control for VSFP wind turbines

In [18], fuzzy logic control for VSFP wind turbines has been proposed with the main objective to optimise operations for the full range of wind speed. Figure 2.24 shows the block diagram fuzzy-based power control for the variable-speed fixed-pitch wind

turbine. Six inputs of the FLC in [18] consist of E_{be}, E_{ab}, T_a, ΔT_a, ω_t and $\Delta\omega_t$. For more detail of each input, please see [18]. In below-rated wind speed, three inputs, $E_{be,}$ $\Delta\omega_t$, and T_a are used in the fuzzy logic control algorithm to generate ΔT_g to track the optimal torque reference that corresponds to the maximum power output of the wind turbine. In above-rated wind speed, five inputs E_{ab}, T_a, ΔT_a, ω_t and $\Delta\omega_t$ are used in the fuzzy logic control algorithm to generate ΔT_g to track the optimal torque reference to limit power output at rated value. The algorithm has fast-tracking in the below-and above-rated wind speed and a low power fluctuation in the above-rated wind speed, because the fuzzy controller can generate the optimal torque reference. However, the implementation of the conventional fuzzy control has a complex software implementation due the large number of fuzzy rules (with 140 rules in [18]), resulting in a large memory storage of the control programme [18].

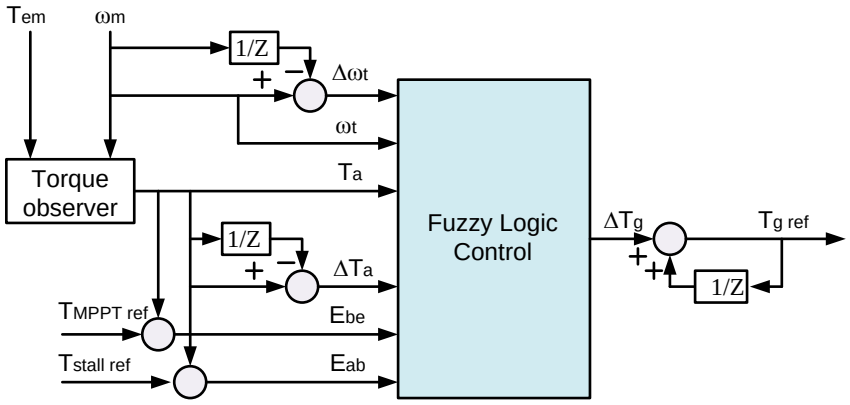

Figure 2.24: Fuzzy-based power control wind turbine block diagram [18]

This problem can be solved by fuzzy control based on single input rule modules (SIRMs) connected fuzzy inference model. In conventional fuzzy controllers, IF-THEN rules for fuzzy inference model are produced by using all the input variables of the

system to be placed in the condition of either "and" or "or" into the antecedent part of each fuzzy rule [60]. For example, two inputs fuzzy rules of the conventional model are shown in Table 2.1. The relationship between x_1 and x_2 for Δy can be designed fuzzy rules for 9 rules [61].

Table 2.1: Fuzzy rules of the conventional model corresponding membership functions N (Negative), Z (Zero) and P (Positive)[61]

Δy		**x_2**		
		N	**Z**	**P**
x_1	**N**	-1.0	-1.0	0.0
	Z	-1.0	0.0	1.0
	P	0.0	1.0	1.0

A "IF-THEN" fuzzy rule can be expressed as:

Rule 1 **IF** x_1 is N and x_2 is N **THEN** Δy is -1.0

"**x_1 is N and x_2 is N**" is called "antecedent" part and "**Δy is -1.0**" is called "consequent" part. Hence, the number of fuzzy rules and the number of parameters will increase and the design and adjustment of fuzzy rules will become difficult work [61]. Instead, the SIRMs connected fuzzy inference model [62],[63],[64],[65] uses a single input rule module for each input variable. Therefore, each input rule has only one single input variable in the antecedent part, reducing the number of fuzzy rules dramatically. In the same case, two inputs for the SIRMs connected fuzzy inference model are shown in Table 2.2. The fuzzy rule of x_1 and x_2 for Δy can be designed for 6 rules[61].

Table 2.2: Fuzzy rules of SIRMs corresponding membership functions N, Z and P[61]

x_i (i = 1,2)	Δy_i (i = 1,2)
N	-1.0
Z	0.0
P	+1.0

Fuzzy controls based on the SIRMs-connected fuzzy inference model has been widely applied to control first and second-order dynamic systems [61], stabilisation control of inverted pendulum systems [64], and trajectory tracking control of unconstrained objects [66].

2.5.2 Model-Based Loss Minimisation Control (MBLC)

Another important aspect to improve the efficiency of WECS with DFIG is the control of the reactive power flow to the grid, as this affects the efficiency of the electrical generator as well as the cost of the power converter for the rotor.

Model-based loss minimisation controllers have been presented to derive the optimal control law for minimising electrical losses in the WECS such as using a copper loss model of DFIG [67],[68], an iron and copper loss model of DFIG [27], and a loss model of DFIG, the filter and the power converter [69]. All these loss minimisation control methods require accurate models and knowledge of the parameters of the DFIG, the filter and the power converter for generating the optimal control law.

On the *dq* model of DFIG driven stator-flux oriented vector control, the electromagnetic torque, T_{em}; stator active power, P_s; and stator reactive power, Q_s can be expressed as [7]:

$$T_{em} = -\frac{3}{2} p \frac{L_m}{L_s} \psi_{sd} i_{rq} \tag{2.48}$$

$$P_s = -\frac{3}{2} \omega_s \frac{L_m}{L_s} \psi_{sd} i_{rq} \tag{2.49}$$

$$Q_s = -\frac{3}{2} \omega_s \frac{L_m}{L_s} \psi_{sd} (i_{rd} - \frac{\psi_{sd}}{L_m}) \tag{2.50}$$

where i_{rd} is the rotor current in *d*-axis; i_{rq} is the rotor current in *q*-axis; L_m is the mutual inductance; L_s is the total stator inductance; ω_s is the supply angular speed; p is the number of pole pairs of the DFIG; ψ_{sd} is the stator flux linkage in *d*-axis, assuming $\psi_{sd} = |\psi_s| = |v_s|/\omega_s$. v_s is the stator voltage [70].

It can be observed that the electromagnetic torque and the stator active power can be controlled by the *q*-axis rotor current component, i_{rq}, while the stator reactive power can be controlled by the *d*-axis rotor current component, i_{rd}.

For a normal control strategy, the stator reactive power, Q_s, is set to zero by $i_{rd} = \frac{\psi_{sd}}{L_m}$ or $i_{rd} = i_{ms}$ [71],[67]. Thus, the stator current does not have any reactive current component, $i_{sd} = 0$ [72]. The reactive power control on the grid side converter is not active. However, this control of the reactive current causes extra copper losses in the rotor winding [72].

Model-based loss minimisation control (MBLC) for variable-speed DFIG WECS has been presented in [68],[4],[67]. For this control method, the *d*-axis rotor current reference is obtained by the equivalent circuit of the DFIG and its parameters for minimum copper losses of the generator. The control law of the MBLC relies on copper losses of the DFIG as a function of current and resistance[67]:

$$P_{ss\_cu} = \frac{3}{2}(i_{sd}^2 + i_{sq}^2) r_s + \frac{3}{2}(i_{rd}^2 + i_{rq}^2) r_r \tag{2.51}$$

where i_{sd} is the stator current in *d*-axis; i_{sq} is the stator current in *q*-axis; r_s is the stator resistance; and r_r is the rotor resistance.

Under the stator-flux oriented vector control, copper losses of the DFIG can be expressed as[67]:

$$P_{ss\_cu} = \frac{3}{2}(r_r + \frac{L_m^2}{L_s^2} r_s) i_{rq}^2 + \frac{3}{2}\frac{\psi_{sd}^2}{L_s^2} r_s - \frac{3\psi_{sd} L_m r_s}{L_s^2} i_{rd} + \frac{3}{2}(r_r + \frac{L_m^2}{L_s^2} r_s) i_{rd}^2 \tag{2.52}$$

As i_{rq} and ψ_{sd} have been assumed constant, the minimum copper losses as a function of i_{rd} can be expressed by the following equation[67]:

$$\frac{\partial P_{ss\_cu}}{\partial i_{rd}} = -\frac{3L_m r_s \psi_{sd}}{L_s^2} + 3(r_r + \frac{L_m^2}{L_s^2} r_s) i_{rd} = 0 \tag{2.53}$$

and, hence, the optimal i_{rd} reference to minimise copper losses of the DFIG is[67]:

$$i_{rd\_ref} = \frac{L_m r_s \psi_{sd}}{L_m^2 r_s + L_s^2 r_r} \tag{2.54}$$

The optimal stator reactive power regulated optimal copper loss level is obtained by substituting (2.54) into (2.50) as expressed:

$$Q_{s\_ref} = -\frac{3}{2}\omega_s \frac{L_m}{L_s}\psi_{sd}\left(\frac{L_m r_s \psi_{sd}}{L_m^2 r_s + L_s^2 r_r} - \frac{\psi_{sd}}{L_m}\right) \tag{2.55}$$

Substituting DFIG parameters which are provided in Appendix A to (2.54), i_{rd_ref} value corresponding to the minimum copper loss is 5.2626A referred on the stator (or 5.2626*u = 2.8418A referred on the rotor). The optimal i_{rd_ref} value is proved by the graph of relation between copper losses and i_{rd} from (2.52) for any constant i_{rq} as shown in Figure 2.25.

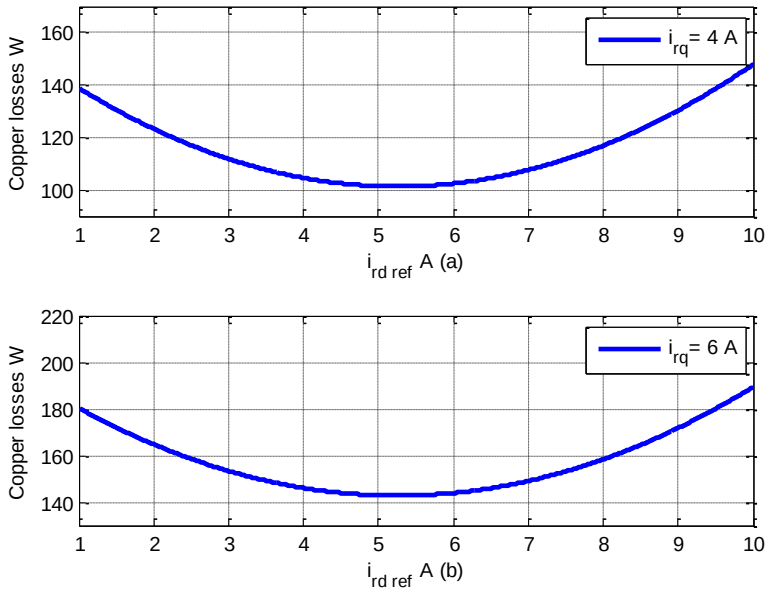

Figure 2.25: Copper losses on DFIG on i_{rd_ref} variation a) i_{rq} = 4 A b) i_{rq} = 6 A.

Although this technique gives a fast-tracking, MBLC relies on the accurate knowledge of the parameters of the DFIG. In practical applications, these parameters are only roughly known via the no-load test and the locked rotor test [73]. Moreover, some of

them, such as stator and rotor resistances are dependent on temperature [74], while the magnetising inductance is dependent on the level of saturation. This is a problem that affects the MBLC efficiency when the operating conditions are variable, such as those of WECS.

Online parameter estimation algorithms have been used to solve the drawbacks of MBLC. The principle of online parameter estimation is that a parameterization of the plant model is run in parallel with the process plant model and then generating and updating the parameter vector estimated by proposed algorithms for minimal output error of the two plant model [75]. Many techniques of the parameter estimation of DFIG have been reported in the literature. In [76], an online parameter estimation for the DFIG based on recursive least square (RLS) algorithm was presented. This method was implemented in discrete time, and the estimated parameters were recursively computed for minimizing the quadratic error [77]. Other studies suggest a model reference adaptive systems (MRAS) algorithm [78] for which the estimated parameter vector was updated by an adaptive law using input and output data [77].

This research proposes a MBLC with the online parameter estimation with a Kalman filter of the stator resistance, r_s, rotor resistance, r_r, stator leakage inductance, $L_{\sigma s}$, and mutual inductance, L_m. The main advantage of the Kalman filter is that it does not require test signals to estimate the machine parameters[73], thereby adding adaptive capabilities to the traditional MBLC.

2.6 Summary

This chapter has provided the basis of knowledge and background of variable speed wind energy conversion systems. It has been reviewed how wind kinetic energy is converted into mechanical power and different control objectives when the wind speed is below or above the rated wind speed. The review of the state of the art and the current diffusion for practical application suggested that focusing on DFIG would produce the best benefit in terms of energy generated by wind. Therefore, the main components of DFIG-based variable speed wind-energy generation were reviewed and the basic control methods analysed.

This chapter also reviews the optimal control of the WECS with a DFIG to increase the efficiency. The power control for VSFP wind turbine and the loss minimisation control of the DFIG are the two topics that are reviewed. The MPPT controller and active stall control via speed regulation were used to control power extracted from the wind turbine in below-rated wind speed and above-rated wind speed, respectively. The objectives of MPPT controller and active stall regulation are maximisation and limitation of extracted power from the wind turbine. Meanwhile, the loss minimisation method was used to minimise the electrical losses of the DFIG. However, the MPPT controllers, such as TSR-MPPT, PSF-MPPT and OT-MPPT, and the loss minimisation control such as MBLC require accurate knowledge of the air density, wind turbine parameters and generator parameters for control laws. In practical application, these parameters are obtained by the experimental test of the wind turbine and generator. These experimental tests will give only rough parameters and are subject to change when the system gets

older or weather conditions change. As a result, the efficiency of those MPPT controllers, and loss minimisation control were reduced. An adaptive optimal efficiency control algorithm will be used to solve this problem.

Chapter 3 Converter Control of DFIG for Wind Turbines

3.1 Introduction

In Chapter 2, the control system for DFIGs for WECS was divided into two levels. Control level 1 regulates the power flow between the DFIG and the power grid by using a rotor back-to-back converter. Control level 2 calculates the optimal references for control level 1 to improve the performance of the WECS.

This chapter focuses on control level 1, for which the main control variables are shown in Figure 3.1. The vector control of the RSC is reviewed to show how the control of the stator reactive power and the generator speed can be decoupled. It is also shown that the vector control of the GSC provides a decoupled control for the DC-link voltage and the grid reactive power. As the latter is well covered in the literature [8], the GSC vector control will not be further considered in this thesis.

Section 3.2 illustrates the three-phase dynamic model of the DFIG, which is first written using a space vector model in the stationary and rotating reference frames. Then, the principles of vector control are analysed with a focus on the stator flux oriented (SFO) technique of the vector control in section 3.3. Finally, the performances of the SFO vector control are analysed by the simulation results in the Matlab/Simulink software package.

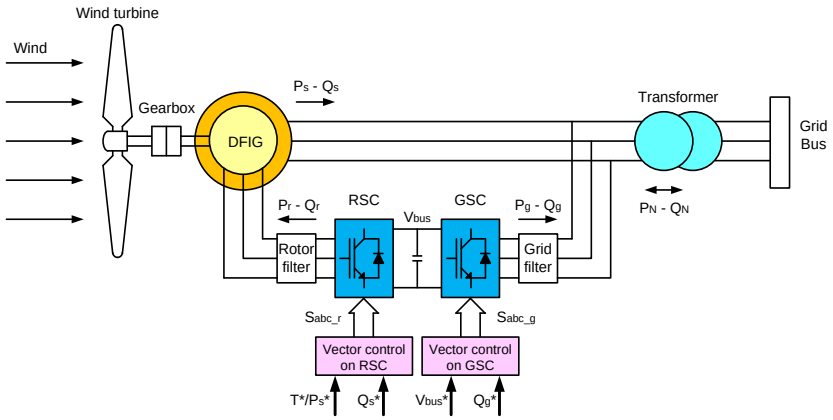

Figure 3.1: Schematic diagram of DFIG-based wind energy conversion system

3.2 DFIG Dynamic Model

The dynamic model of DFIG is needed to develop control of the RSC. At steady-state, the dynamic model of the DFIG can be represented by the equivalent circuit mentioned in Chapter 2, which is used to explain the relationships between active powers, reactive powers, voltages and currents for different operating conditions.

3.2.1 Basic Machine Configuration

Figure 3.2 shows the basic configuration of a three-phase DFIG. The Kirchhoff voltage laws applied to the stator and rotor windings are given by the following set of equations [79]:

$$\begin{cases} v_{sa} = r_s i_{sa} + \dfrac{d\psi_{sa}}{dt} \\ v_{sb} = r_s i_{sb} + \dfrac{d\psi_{sb}}{dt} \\ v_{sc} = r_s i_{sc} + \dfrac{d\psi_{sc}}{dt} \end{cases} \tag{3.1}$$

$$\begin{cases} v_{ra} = r_r i_{ra} + \dfrac{d\psi_{ra}}{dt} \\ v_{rb} = r_r i_{rb} + \dfrac{d\psi_{rb}}{dt} \\ v_{rc} = r_r i_{rc} + \dfrac{d\psi_{rc}}{dt} \end{cases} \tag{3.2}$$

where v_{sa}, v_{sb} and v_{sc} are the phase stator voltages; v_{ra}, v_{rb} and v_{rc} are the phase rotor voltages; i_{sa}, i_{sb} and i_{sc} are the phase stator currents; i_{ra}, i_{rb} and i_{rc} are the phase rotor currents; ψ_{sa}, ψ_{sb} and ψ_{sc} are the stator flux linkages and ψ_{ra}, ψ_{rb} and ψ_{rc} are the rotor flux linkages.

The stator equations are written in the stationary reference frame, while the rotor equations are written in the rotating reference frame synchronous to the rotor.

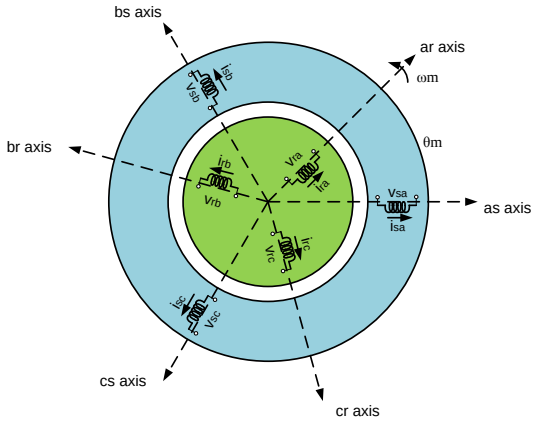

Figure 3.2: Three-phase DFIG winding circuit [7]

3.2.2 Space Vector Definition and Projection

The three-phase quantities of a DFIG such as voltages, currents and flux linkages, can be represented using the space vector form [7]. The space vector of a generic quantity,

$\vec{x}_s$, can be defined by the three-phase instantaneous magnitude of the same quantity, x_{sa}, x_{sb} and x_{sc} as follows:

$$\vec{x}_s = \frac{2}{3}(x_{sa} + x_{sb}e^{j(2\pi/3)} + x_{sc}e^{-j(2\pi/3)}) \tag{3.3}$$

The space vector can be represented on the complex plane as the sum of the three individual components, oriented along three axis forming mutual angles of 120 degrees, For example, Figure 3.3 shows how the space vector can be obtained as a vector sum of the three individual components.

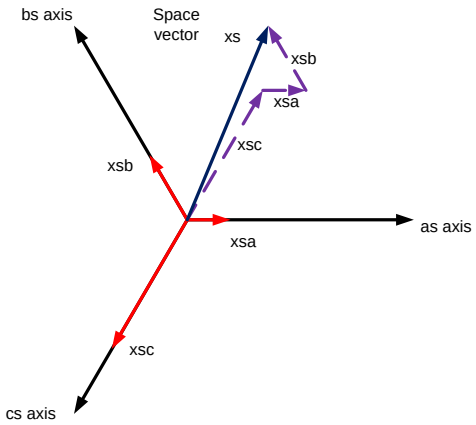

Figure 3.3: Stator current space vector and projection [7]

Therefore, the DFIG dynamic model in (3.1) and (3.2) can be rearranged in space vector form:

$$\vec{v}_s^{\,s} = r_s\vec{i}_s^{\,s} + \frac{d\vec{\psi}_s^{\,s}}{dt} \tag{3.4}$$

$$\vec{v}_r^{\,r} = r_r\vec{i}_r^{\,r} + \frac{d\vec{\psi}_r^{\,r}}{dt} \tag{3.5}$$

where $\vec{v}_s^s$, $\vec{i}_s^s$ and $\vec{\psi}_s^s$ are the stator voltage space vector; the stator current space vector and the stator flux linkages space vector in the stator reference frame, respectively. $\vec{v}_r^r$, $\vec{i}_r^r$ and $\vec{\psi}_r^r$ are the rotor voltage space vector; the rotor current space vector and the rotor flux linkages space vector in the rotor reference frame, respectively.

The stator and rotor total flux linkages are dependent on the stator and rotor current space vectors according to the following equations:

$$\vec{\psi}_s^s = L_s\vec{i}_s^s + L_m\vec{i}_r^s \tag{3.6}$$

$$\vec{\psi}_r^r = L_m\vec{i}_s^r + L_r\vec{i}_r^r \tag{3.7}$$

where $\vec{i}_r^s$ is the referred rotor current space vector in the stator reference frame; $\vec{i}_s^r$ is the referred stator current space vector in the rotor reference frame; L_s is the total stator inductance; L_r is the total rotor inductance and L_m is mutual inductance. The superscripts *s* and *r* indicate the space vectors referring to stator or rotor reference frame.

The advantage of the space vector is that it can be transformed into the two-phase quantities in any arbitrary complex plane. The two quantities, x_d and x_q, in the direct and quadrature axis can be expressed as:

$$\begin{cases} x_d = |\vec{x}_s|\cos\theta \\ x_q = j|\vec{x}_s|\sin\theta \end{cases} \tag{3.8}$$

where θ is the angle between the direct axis of a complex plane and space vector

3.2.3 DFIG Model in an Arbitrary Reference Frame

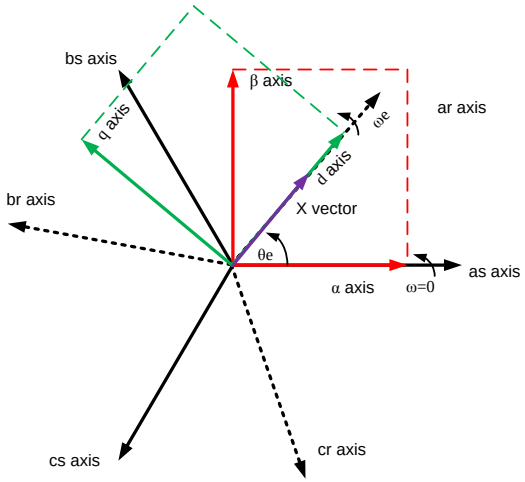

Figure 3.4: Relation between *abc*, αβ and *dq* reference frame [7]

As (3.1) and (3.2) are referred to different reference frames, it is useful to refer them to the same reference frame to eliminate one of the equations from the model. There are two types of common reference frames used to model DFIG: the stationary and the rotating reference frames. The stationary reference frame, known as the αβ reference frame, has angular speed equal to zero ($\omega = 0$). The α-axis is aligned with the magnetic axis of phase *a* of the stator winding. The rotating reference frame, known as the *dq* reference frame, forms an angular position, θ_e, with the α-axis, and has angular speed equal to ω_e. The *d* axis is aligned with an arbitrary space vector dependent on the chosen control technique. Typical choices are the phase *a* of the rotor winding, the stator flux linkage space vector and the rotor flux linkage space vector, as shown in Figure 3.4.

Basically, the three-phase quantities of the stator winding are transformed into the two-phase quantities in the stator reference frame, (αβ complex plane); the three-phase quantities of the rotor winding are transformed into the two-phase quantities in the rotor reference frame, (*DQ* complex plan) rotating at speed $p\omega_m$ where ω_m is the mechanical rotor speed and *p* is the number of the pole pairs of the DFIG. Therefore, the two phase DFIG dynamic model can be expressed in terms of space vector components as [7]:

$$\begin{cases} v_{s\alpha} = r_s i_{s\alpha} + \dfrac{d\psi_{s\alpha}}{dt} \\ v_{s\beta} = r_s i_{s\beta} + \dfrac{d\psi_{s\beta}}{dt} \end{cases} \tag{3.9}$$

$$\begin{cases} v_{rD} = r_s i_{rD} + \dfrac{d\psi_{rD}}{dt} \\ v_{rQ} = r_s i_{rQ} + \dfrac{d\psi_{rQ}}{dt} \end{cases} \tag{3.10}$$

where $v_{s\alpha}$, $v_{s\beta}$, $i_{s\alpha}$, $i_{s\beta}$, $\psi_{s\alpha}$ and $\psi_{s\beta}$ are the stator voltages; the stator currents and the stator flux linkages in αβ reference frame, respectively. v_{rD}, v_{rQ}, i_{rD}, i_{rQ}, ψ_{rD} and ψ_{rQ} are the rotor voltages; the rotor currents and the rotor flux linkages in *DQ* reference frame, respectively.

3.2.3.1 DFIG αβ model: In this section, the model of the DFIG is presented in the stationary reference frame (αβ plane). Therefore, the components of space vector in the rotor frame (*DQ* plane) are transformed into the components in the stator frame (αβ plane) using the rotational conversion factor $e^{j\theta m}$ as follows[7]:

$$\begin{bmatrix} x_{r\alpha} \\ x_{r\beta} \end{bmatrix} = \begin{bmatrix} \cos\theta_m & -\sin\theta_m \\ \sin\theta_m & \cos\theta_m \end{bmatrix} \begin{bmatrix} x_{rD} \\ x_{rQ} \end{bmatrix} \tag{3.11}$$

where θ_m can be calculated from:

$$\theta_m = \int p\omega_m \, dt \tag{3.12}$$

Applying (3.11), the voltages (v_{rD}, v_{rQ}), currents (i_{rD}, i_{rQ}) and flux linkages (ψ_{rD}, ψ_{rQ}) in the rotor frame are transformed into the stator frame., Therefore the dynamic model of the DFIG in the stationary reference frame is given by [7]:

$$\begin{cases} v_{s\alpha} = r_s i_{s\alpha} + \dfrac{d\psi_{s\alpha}}{dt} \\ v_{s\beta} = r_s i_{s\beta} + \dfrac{d\psi_{s\beta}}{dt} \end{cases} \tag{3.13}$$

$$\begin{cases} v_{r\alpha} = r_s i_{r\alpha} + \dfrac{d\psi_{r\alpha}}{dt} + p\omega_m \psi_{r\beta} \\ v_{r\beta} = r_s i_{r\beta} + \dfrac{d\psi_{r\beta}}{dt} - p\omega_m \psi_{r\alpha} \end{cases} \tag{3.14}$$

$$\begin{cases} \psi_{s\alpha} = L_s i_{s\alpha} + L_m i_{r\alpha} \\ \psi_{s\beta} = L_s i_{s\beta} + L_m i_{r\beta} \end{cases} \tag{3.15}$$

$$\begin{cases} \psi_{r\alpha} = L_m i_{s\alpha} + L_r i_{r\alpha} \\ \psi_{r\beta} = L_m i_{s\beta} + L_r i_{r\beta} \end{cases} \tag{3.16}$$

The schematic of the αβ model of the DFIG can be illustrated by the equivalent circuit in Figure 3.5 [7].

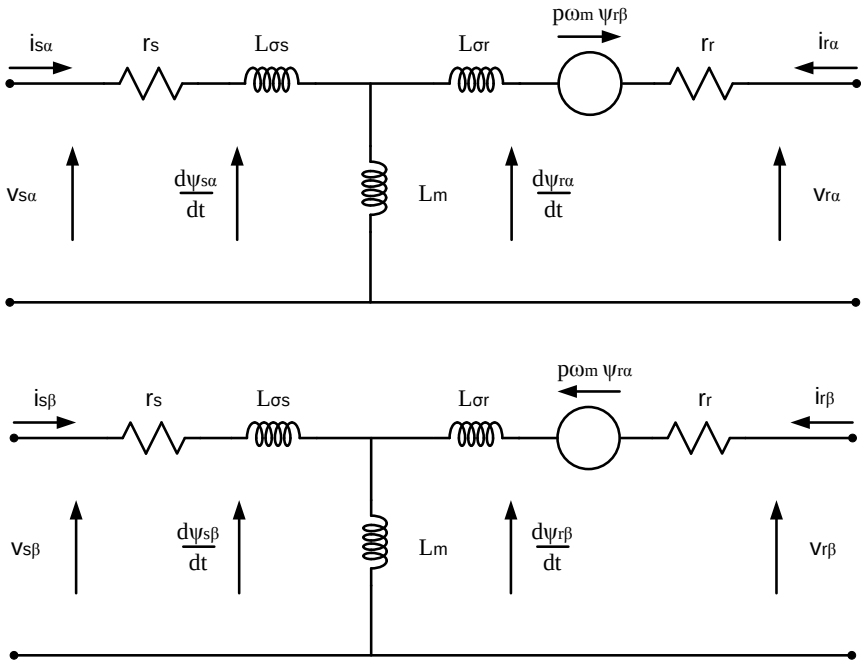

Figure 3.5: Schematic of αβ model of the DFIG[7]

From the circuit in Figure 3.5, the active powers of the stator and rotor windings can be calculated as follows [7]:

$$P_s = \frac{3}{2}(v_{s\alpha} i_{s\alpha} + v_{s\beta} i_{s\beta}) \tag{3.17}$$

$$P_r = \frac{3}{2}(v_{r\alpha} i_{r\alpha} + v_{r\beta} i_{r\beta}) \tag{3.18}$$

and the reactive powers of the stator and rotor windings can be calculated as follows:

$$Q_s = \frac{3}{2}(v_{s\beta} i_{s\alpha} - v_{s\alpha} i_{s\beta}) \tag{3.19}$$

$$Q_r = \frac{3}{2}(v_{r\beta} i_{r\alpha} - v_{r\alpha} i_{r\beta}) \tag{3.20}$$

The electromagnetic torque of the DFIG is expressed as a function of the rotor flux linkages and the rotor currents as [7]:

$$T_{em} = \frac{3}{2} p(\psi_{r\beta} i_{r\alpha} - \psi_{r\alpha} i_{r\beta}) \tag{3.21}$$

By eliminating $i_{s\alpha}$, $i_{s\beta}$, $i_{r\alpha}$ and $i_{r\beta}$ in (3.13) and (3.14) using (3.15) and (3.16), the state-space dynamic equations of the DFIG in αβ frame is finally equal to [7]:

$$\begin{cases} \dfrac{d\psi_{s\alpha}}{dt} = -\dfrac{r_s \psi_{s\alpha}}{\sigma L_s} + \dfrac{r_s L_m \psi_{r\alpha}}{\sigma L_s L_r} + v_{s\alpha} \\ \dfrac{d\psi_{s\beta}}{dt} = -\dfrac{r_s \psi_{s\beta}}{\sigma L_s} + \dfrac{r_s L_m \psi_{r\beta}}{\sigma L_s L_r} + v_{s\beta} \\ \dfrac{d\psi_{r\alpha}}{dt} = \dfrac{r_r L_m \psi_{s\alpha}}{\sigma L_s L_r} - \dfrac{r_r \psi_{r\alpha}}{\sigma L_r} - p\omega_m \psi_{r\beta} + v_{r\alpha} \\ \dfrac{d\psi_{r\beta}}{dt} = \dfrac{r_r L_m \psi_{s\beta}}{\sigma L_s L_r} + p\omega_m \psi_{r\alpha} - \dfrac{r_r \psi_{r\beta}}{\sigma L_r} + v_{r\beta} \\ \dfrac{d\omega_m}{dt} = \dfrac{T_{em}}{J} - \dfrac{T_m}{J} \end{cases} \tag{3.22}$$

where $\sigma = 1 - L_m^2/L_s L_r$ is a coefficient that takes into account the rotor and stator leakage flux; J is the total moment of inertia of the rotor and other equipment coupled with rotor, and T_m is the mechanical torque.

3.2.3.2 DFIG *dq* model: In this section, the model of the DFIG is written in the rotating reference frame (*dq* plane). The components of space vectors in the stator frame (αβ plane) are transformed into the components in the arbitrary rotating reference frame using the transformation factor $e^{j\theta s}$ as follows [7]:

$$\begin{bmatrix} x_{sd} \\ x_{sq} \end{bmatrix} = \begin{bmatrix} \cos\theta_s & \sin\theta_s \\ -\sin\theta_s & \cos\theta_s \end{bmatrix} \begin{bmatrix} x_{s\alpha} \\ x_{s\beta} \end{bmatrix} \tag{3.23}$$

where θ_s is the angular position between the direct axis of the stationary frame and rotating frame. The components of the space vector in the rotor frame (*DQ* plane) are transformed into vectors in the arbitrary rotating reference frame by [7]:

$$\begin{bmatrix} x_{rd} \\ x_{rq} \end{bmatrix} = \begin{bmatrix} \cos(\theta_s - \theta_m) & \sin(\theta_s - \theta_m) \\ -\sin(\theta_s - \theta_m) & \cos(\theta_s - \theta_m) \end{bmatrix} \begin{bmatrix} x_{rD} \\ x_{rQ} \end{bmatrix} \tag{3.24}$$

Applying to the voltages ($v_{s\alpha}$, $v_{s\beta}$), currents ($i_{s\alpha}$, $i_{s\beta}$) and flux linkages ($\psi_{s\alpha}$, $\psi_{s\beta}$) of the stator winding and to the voltages (v_{rD}, v_{rQ}), currents (i_{rD}, i_{rQ}) and flux linkages (ψ_{rD}, ψ_{rQ}) of the rotor winding, the dynamic model of the DFIG in the arbitrary rotating frame (*dq*) is given by [7]:

$$\begin{cases} v_{sd} = r_s i_{sd} + \dfrac{d\psi_{sd}}{dt} - \omega_s \psi_{sq} \\ v_{sq} = r_s i_{sq} + \dfrac{d\psi_{sq}}{dt} + \omega_s \psi_{sd} \end{cases} \tag{3.25}$$

$$\begin{cases} v_{rd} = r_s i_{rd} + \dfrac{d\psi_{rd}}{dt} - (\omega_s - p\omega_m)\psi_{rq} \\ v_{rq} = r_s i_{rq} + \dfrac{d\psi_{rq}}{dt} + (\omega_s - p\omega_m)\psi_{rd} \end{cases} \tag{3.26}$$

$$\begin{cases} \psi_{sd} = L_s i_{sd} + L_m i_{rd} \\ \psi_{sq} = L_s i_{sq} + L_m i_{rq} \end{cases} \tag{3.27}$$

$$\begin{cases} \psi_{rd} = L_m i_{sd} + L_r i_{rd} \\ \psi_{rq} = L_m i_{sq} + L_r i_{rq} \end{cases} \tag{3.28}$$

The *dq* model of the DFIG can be represented by the equivalent circuit shown in Figure 3.6 [7].

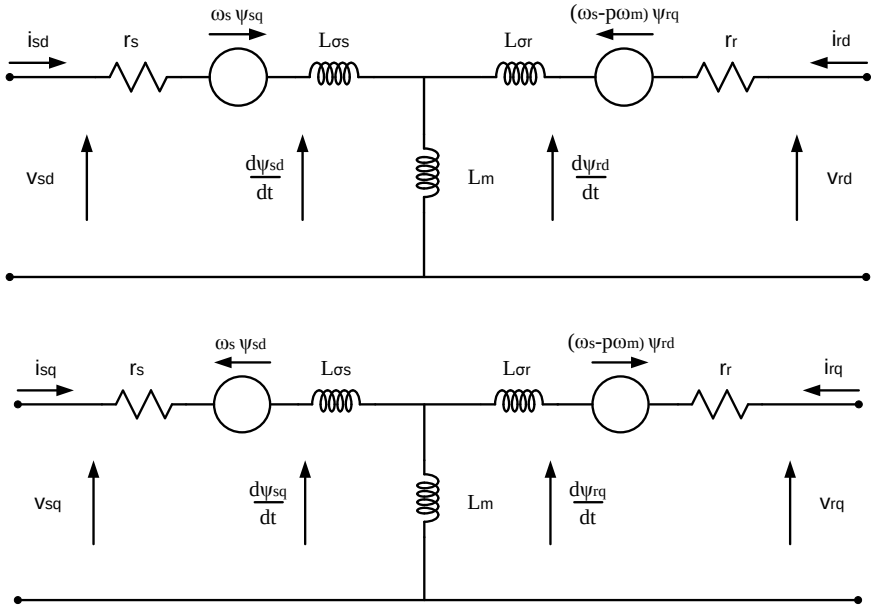

Figure 3.6: Schematic of *dq* model of the DFIG[7]

From the circuit in Figure 3.6, the active powers of the stator and rotor windings can be calculated as follows [7]:

$$P_s = \frac{3}{2}(v_{sd} i_{sd} + v_{sq} i_{sq}) \tag{3.29}$$

$$P_r = \frac{3}{2}(v_{rd} i_{rd} + v_{rq} i_{rq}) \tag{3.30}$$

and the reactive powers of the stator and rotor windings can be calculated as follows:

$$Q_s = \frac{3}{2}(v_{sq} i_{sd} - v_{sd} i_{sq}) \tag{3.31}$$

$$Q_r = \frac{3}{2}(v_{rq} i_{rd} - v_{rd} i_{rq}) \tag{3.32}$$

The electromagnetic torque of the DFIG can be expressed as a function of the stator flux linkages and the rotor currents as [7]:

$$T_{em} = \frac{3}{2} p \frac{L_m}{L_s}(\psi_{sq} i_{rd} - \psi_{sd} i_{rq}) \tag{3.33}$$

The state-space dynamic equations of the DFIG in *dq* frame and the rotor dynamics can be written as [7]:

$$\begin{cases} \dfrac{d\psi_{sd}}{dt} = -\dfrac{r_s \psi_{sd}}{\sigma L_s} + \omega_s \psi_{sq} + \dfrac{r_s L_m \psi_{rd}}{\sigma L_s L_r} + v_{sd} \\ \dfrac{d\psi_{sq}}{dt} = -\omega_s \psi_{sd} - \dfrac{r_s \psi_{sq}}{\sigma L_s} + \dfrac{r_s L_m \psi_{rq}}{\sigma L_s L_r} + v_{sq} \\ \dfrac{d\psi_{rd}}{dt} = \dfrac{r_r L_m \psi_{sd}}{\sigma L_s L_r} - \dfrac{r_r \psi_{rd}}{\sigma L_r} + (\omega_s - p\omega_m)\psi_{rq} + v_{rd} \\ \dfrac{d\psi_{rq}}{dt} = \dfrac{r_r L_m \psi_{sq}}{\sigma L_s L_r} - (\omega_s - p\omega_m)\psi_{rd} - \dfrac{r_r \psi q}{\sigma L_r} + v_{rq} \\ \dfrac{d\omega_m}{dt} = \dfrac{T_{em}}{J} - \dfrac{T_m}{J} \end{cases} \tag{3.34}$$

3.3 DFIG Stator Flux Oriented Vector Control on RSC

This section shows how the equations derived in the previous section can be manipulated to control the active and reactive powers of the DFIG independently of the control of the RSC current.

Two techniques of the vector control on RSC have been reported in the literature: the stator flux oriented (SFO) technique [8],[80],[81] and the stator voltage oriented (SVO) technique [82]–[85]. In SFO vector control, the DFIG is controlled in a rotating reference frame *dq*, with the *d* axis oriented along the stator flux space vector position. The electromagnetic torque and stator reactive power can be controlled independently by i_{rq} and i_{rd}.

In SVO vector control, the DFIG is controlled in a rotating reference frame *dq*, with the *d* axis oriented along the stator voltage space vector position. The electromagnetic torque and stator reactive power can be controlled independently by i_{rd} and i_{rq}.

In this thesis, the SFO vector control principle is studied due to it being the standard method used for control of the DFIG[86]. Three-phase voltages, currents and fluxes of stator and rotor of the DFIG are transformed into the rotating reference frame for which the *d*-axis is aligned with the stator flux space vector. Then, a cascaded control is used for tracking the stator reactive power and the generator reference speed. The PI controllers of these control loops generate the rotor current command to the inner current loops. Tracking current commands are provided in inner control loops by generating rotor voltage references to the PWM unit of the RSC, as explained below.

3.3.1 Estimation of Stator Flux Space Vector Position

Stator flux space vector position, θ_s, is used to transform the space vector components in the stator reference frame ($\alpha\beta$) and the rotor reference frame (*DQ*) into the space vector components in the rotating reference frame (*dq*) which rotate along with the stator flux space vector, ψ_s. Figure 3.7 shows the space vectors of the DFIG and three reference frames: stator ($\alpha\beta$), rotor (*DQ*) and rotating (*dq*) frame. Under the SFO vector control, all space vectors of the DFIG are transformed into the rotating reference frame for which the *d*-axis is aligned with the stator flux space vector. The angle θ_s can be calculated by (3.35):

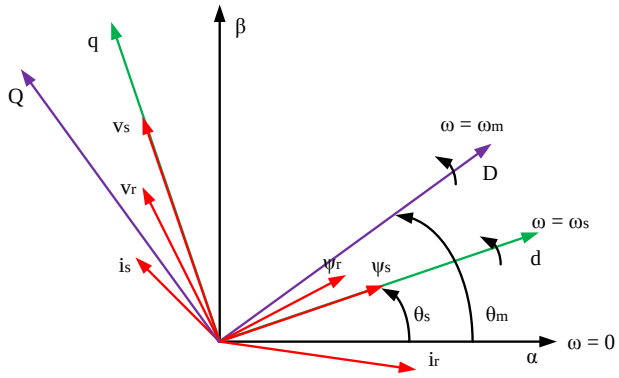

Figure 3.7: Space vector of DFIG and three different reference frames

$$\theta_s = \tan^{-1}\frac{\psi_{s\beta}}{\psi_{s\alpha}} \tag{3.35}$$

In practical applications, the stator flux linkage cannot be measured directly. Therefore, the angle θ_s has to be estimated using a phase locked loop (PLL), as shown in Figure 3.8 [84]. Under the SFO vector control, when the *d*-axis of the rotating frame is aligned

with stator flux linkage space vector, the stator voltage space vector, v_s, is aligned with the *q*-axis rotating reference frame. That means $v_{sq} \approx |v_s|$ and $v_{sd} \approx 0$. To get the correct angle θ_s, the three-phase stator voltages measured from the DFIG are transformed into *dq* coordinate system using the estimated θ_s, while the v_{sd} command is set to zero. Then, the PLL controller modifies the estimated θ_s until the actual component v_{sd} becomes zero.

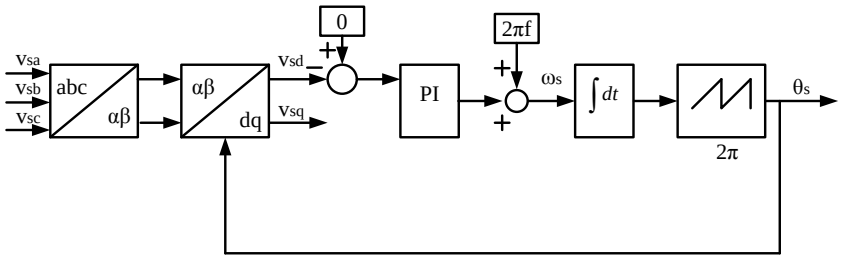

Figure 3.8: Closed-loop PLL block diagram [7],[84]

3.3.2 Speed and Reactive Power Control

When the *d*-axis of the rotating reference frame is aligned to the stator flux linkage space vector, the stator flux linkages in the *dq* coordinate system are expressed as follows:

$$\begin{cases} \psi_{sd} = |\psi_s| \\ \psi_{sq} = 0 \end{cases} \tag{3.36}$$

Under the hypothesis of small stator resistance and constant magnetising current [9], the stator voltages in *dq* coordinate system are obtained from (3.25):

$$\begin{cases} v_{sd} \approx & 0 \\ v_{sq} \approx & \omega_s \psi_{sd} \end{cases} \tag{3.37}$$

For the DFIG of wind-energy systems, the stator windings are directly connected to the grid, which can be assumed to have constant voltage. Therefore, the stator flux linkage of the DFIG can also be assumed as a constant. Substituting (3.36) into (3.33), the electromagnetic torque in the *dq* coordinate system becomes [87]:

$$T_{em} = -\frac{3}{2} p \frac{L_m}{L_s} \psi_{sd} i_{rq} \tag{3.38}$$

Substituting (3.36) into (3.27), the stator currents in *dq* coordinate system become:

$$\begin{cases} i_{sd} = \dfrac{\psi_{sd}}{L_s} - \dfrac{L_m}{L_s} i_{rd} \\ i_{sq} = -\dfrac{L_m}{L_s} i_{rq} \end{cases} \tag{3.39}$$

under (3.37) and (3.39), the stator active and reactive power equations in (3.29) and (3.31) become [87]:

$$P_s = -\frac{3}{2} \omega_s \frac{L_m}{L_s} \psi_{sd} i_{rq} \tag{3.40}$$

$$Q_s = -\frac{3}{2} \omega_s \frac{L_m}{L_s} \psi_{sd} (i_{rd} - \frac{\psi_{sd}}{L_m}) \tag{3.41}$$

These equations show that with the stator flux oriented vector control the electromagnetic torque and the stator reactive power can be independently controlled by the rotor current. In particular, the electromagnetic torque and the stator active power

can be controlled by the quadrature axis rotor current component, i_{rq}, while the stator reactive power can be controlled by the direct axis rotor current component, i_{rd}.

From (3.38) and (3.41), the rotor current commands for the inner current control can be generated by two outer feedback loops as shown in Figure 3.9. In the first loop, the *d*-axis rotor current reference, i_{dr}, is generated by a PI regulator having as its input the difference between the reactive power command and the actual reactive power. The *q*-axis rotor current reference, i_{rq}, is instead generated by a PI regulator having as its input the difference between the speed command and the actual speed.

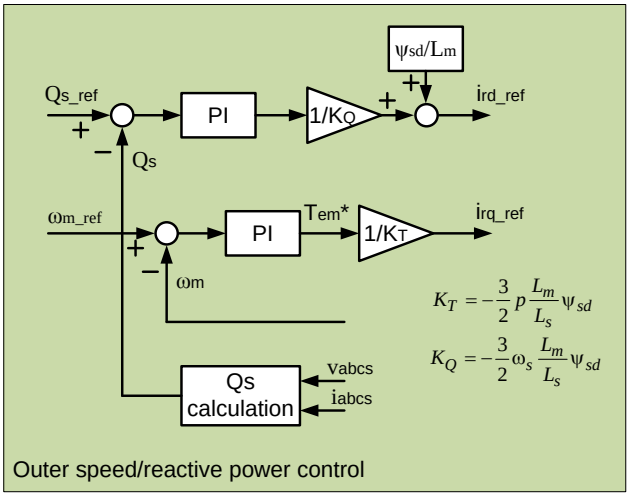

Figure 3.9: Generator speed and reactive power outer control loops [81]

3.3.3 Inner Current Control

For the inner current control, the plant model has the rotor voltages as inputs and the rotor currents as outputs.

Feedback control with PI regulators can be used to generate the rotor voltage signals for the PWM control of the RSC to track the rotor current references.

More specifically, using the stator flux oriented reference frame, (3.26) can be rearranged as a function of i_{rd} and i_{rq} by using (3.28) and (3.39). The rotor voltage equations in the *dq* coordinate system become:

$$\begin{cases} v_{rd} = r_s i_{rd} + \sigma L_r \dfrac{di_{rd}}{dt} - (\omega_s - p\omega_m)(\sigma L_r i_{rq}) \\ v_{rq} = r_s i_{rq} + \sigma L_r \dfrac{di_{rq}}{dt} + (\omega_s - p\omega_m)(\sigma L_r i_{rd} + \dfrac{L_m}{L_s}\psi_{sd}) \end{cases} \tag{3.42}$$

A feedforward control can be used to provide a decoupled control of the direct and quadrature axis rotor current component. Therefore, by introducing two new modified voltages:

$$\begin{cases} u_{crd} = v_{rd} + (\omega_s - p\omega_m)(\sigma L_r i_{rq}) \\ u_{crq} = v_{rq} - (\omega_s - p\omega_m)(\sigma L_r i_{rd} + \dfrac{L_m}{L_s}\psi_{sd}) \end{cases} \tag{3.43}$$

and substituting (3.43) into (3.42), the rotor voltage equations can be written as:

$$\begin{cases} u_{crd} = r_s i_{rd} + \sigma L_r \dfrac{di_{rd}}{dt} \\ u_{crq} = r_s i_{rq} + \sigma L_r \dfrac{di_{rq}}{dt} \end{cases} \tag{3.44}$$

where it can be noticed that the two equations are now decoupled. Two first-order transfer function models of the rotor voltage equation can be obtained from (3.44):

$$\frac{I_{rd}(s)}{U_{crd}(s)} = \frac{1}{r_s + \sigma L_r s} \tag{3.45}$$

$$\frac{I_{rq}(s)}{U_{crq}(s)} = \frac{1}{r_s + \sigma L_r s} \tag{3.46}$$

These transfer functions can be used to design the PI regulators. There are many techniques for PI controller tuning presented in the literature, e.g. the pole placement method[86][17][88], the Ziegler-Nichols method[89][90] and the bode plot method[91]. The inner current control is shown in Figure 3.10.

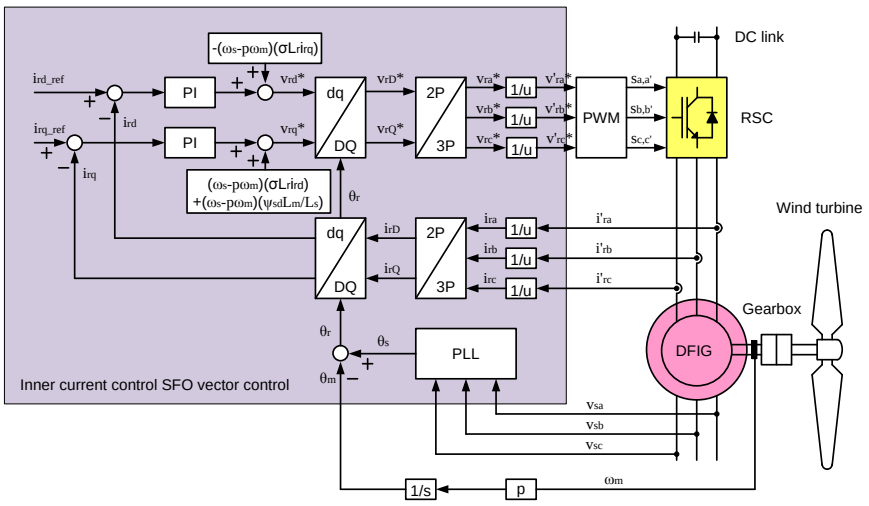

Figure 3.10: Inner current control based on stator flux oriented vector control [81]

The inner current control of the SFO vector control can be explained its operation in following steps:

- The three-phase rotor currents on terminal are referred from rotor to stator by turn ratio between stator and rotor windings, called the *u* factor.
- The three-phase rotor currents referred on the stator are transformed into *DQ*-coordinate system in the rotor reference frame.
- The *DQ* rotor currents are transformed into *dq*-coordinate system in the stator flux rotating reference frame by using the different position value between rotor and stator flux rotating reference frame, θ_r.
- The rotor voltages in direct and quadrature axis (v_{rd}, v_{rq}) are generated independently by the feedback control for tracking the current command in the PI controller manner.
- The rotor voltages in the *dq* coordinate system are added with the cancellation terms for a decoupled control of the active and reactive rotor current (i_{rd}, i_{rq}).
- The *dq* rotor voltages are inversely transformed into a *DQ*-coordinate system in the rotor reference frame by θ_r.
- The *DQ* rotor voltages are transformed into the three-phase rotor voltages
- The three-phase rotor voltages are referred from the stator to the rotor by *u* factor.
- The three-phase rotor voltages are reference signal in the PWM for generating a switching signal to the RSC.

Finally, the complete vector control of the DFIG is shown in Figure 3.11 combining the outer and inner control loops.

In order to obtain suitable operations of the controller, the current loops should be faster than the outer loop. The rotor current control design and the generator speed/stator reactive power design can be undertaken separately if the following assumptions are satisfied.

- The current control is sufficiently fast that the generator speed and stator reactive power can be considered constant for the design of the current regulators.
- For the design of the generator speed and stator reactive power controller it can be considered that the currents instantaneously track the commands.

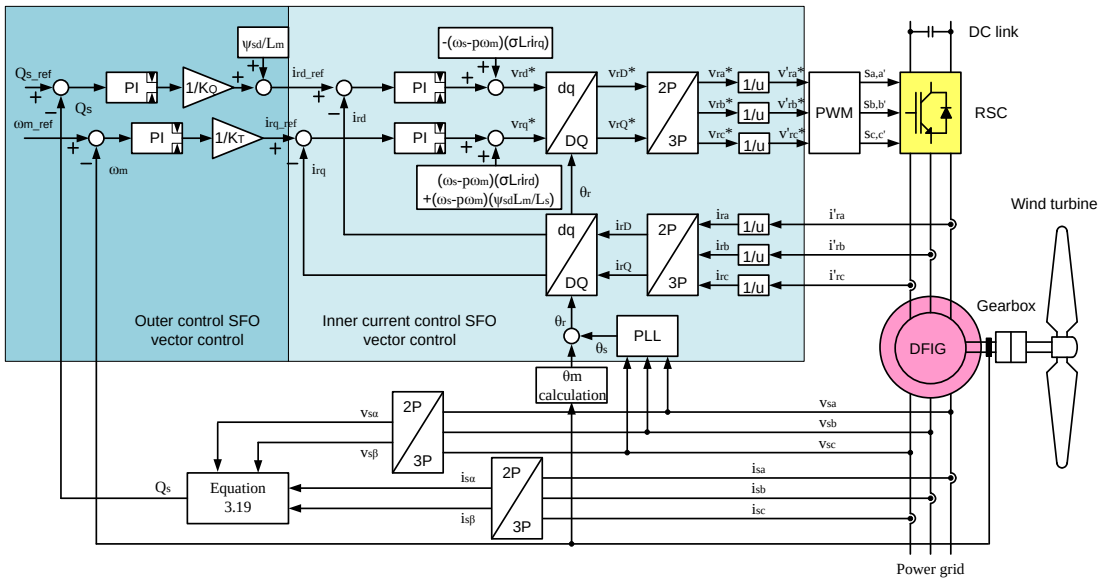

Figure 3.11: Stator flux oriented vector control for rotor side converter [81]

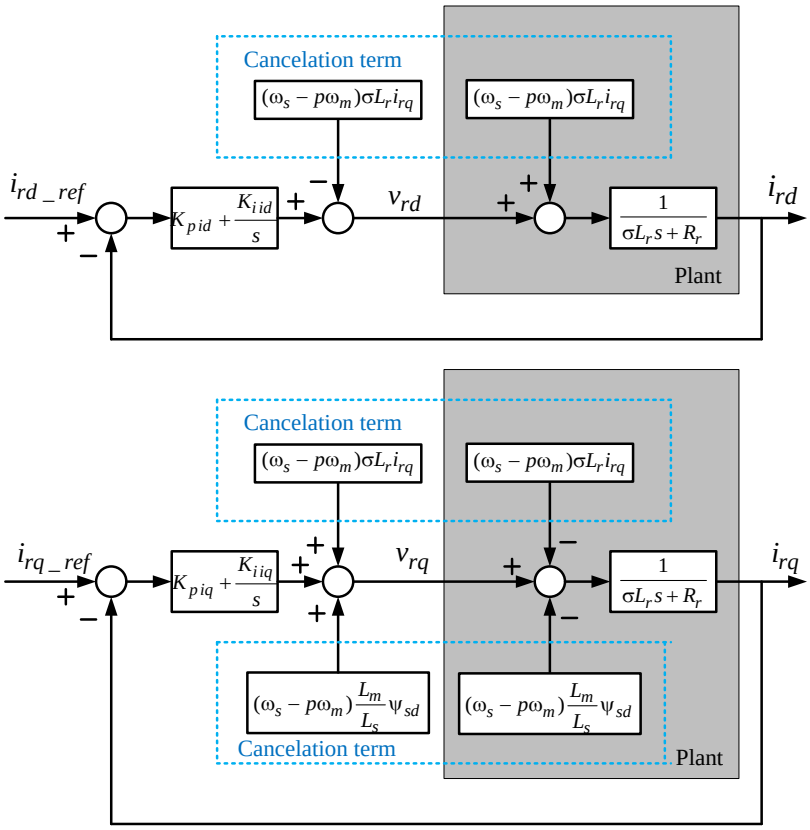

Figure 3.12: Current control loops of DFIG RSC [92]

3.3.4 PI Controller Design on DFIG RSC

This subsection shows how to select the appropriate gains of the PI controllers for the RSC of the DFIG.

3.3.3.1 PI controller design for the inner current control loop: Using (3.42), the closed loop current control can be represented by the block diagrams in Figure 3.12.

Taking the Laplace transforms of the quantities in the figure, the closed loop transfer function of the two inner current control loops can be expressed as:

$$\frac{I_{rd}(s)}{I_{rd\_ref}(s)} = \frac{I_{rq}(s)}{I_{rq\_ref}(s)} = \frac{\frac{K_p s}{\sigma L_r} + \frac{K_i}{\sigma L_r}}{s^2 + \frac{(K_p + r_r)s}{\sigma L_r} + \frac{K_i}{\sigma L_r}} \tag{3.47}$$

where K_p is the proportional gain and K_i is the integral gain of the PI controllers. The transfer function in (3.47) can be equal as a standard second-order system by assuming $K_p << K_i$, then [92]:

$$\frac{I_{rd}(s)}{I_{rd\_ref}(s)} = \frac{I_{rq}(s)}{I_{rq\_ref}(s)} = \frac{\frac{K_i}{\sigma L_r}}{s^2 + \frac{(K_p + r_r)s}{\sigma L_r} + \frac{K_i}{\sigma L_r}} = \frac{\omega_n^2}{s^2 + 2\zeta\omega_n s + \omega_n^2} \tag{3.48}$$

where ζ is the damping ratio and ω_n is the natural frequency of the transfer function. In general, the performance of the closed-loop control of the second-order system can be evaluated from the transient response by determining the percent overshoot, *%OS*, and the settling time, t_s. The percent overshoot and the settling time can be calculated by [93],[86]:

$$\%OS = 100 \cdot \exp\left\{\frac{-\zeta\pi}{\sqrt{1-\zeta^2}}\right\} \tag{3.49}$$

$$t_s = \frac{4}{\zeta\omega_n} \tag{3.50}$$

For a second-order system, the percent overshoot should be less than 25% which can be only determined via ζ as seen in (3.49). In general, an optimal damping ratio of the standard second-order system is designed to be 0.707, which the percent overshoot is

less than 5% with suitable settling time [94]. In addition, the settling time requires the time of transient response to reach and remain within 2% of the steady-state value which can be determined though ζ and ω_n as seen in (3.50) [92]. The value of ω_n impacts the settling time, such that a high ω_n gives a fast response. However, the gains of the PI controller are also increasing with ω_n, reducing the stability of the closed-loop system. One method to obtain specified performance from the system is to design the gains of the PI controller of the current control loop through the pole placement method:

$$\begin{cases} K_p = 2\zeta\omega_n(\sigma L_r) - r_r \\ K_i = \omega_n^2(\sigma L_r) \end{cases} \tag{3.51}$$

In this thesis, the damping ratio in current control is selected as $\zeta = 1$ for the critically damped system, which returns a percent overshoot lower than 5% due to two poles of the system being real numbers. The optimal ω_n can be calculated from (3.50) as a function of the settling time t_s and damping ratio ζ.

Once the value ω_n has been designed from the desired dynamic performance of the current control loops, the optimal gains of the PI controller are tuned by using (3.51) according to the desired percent overshoot and settling time.

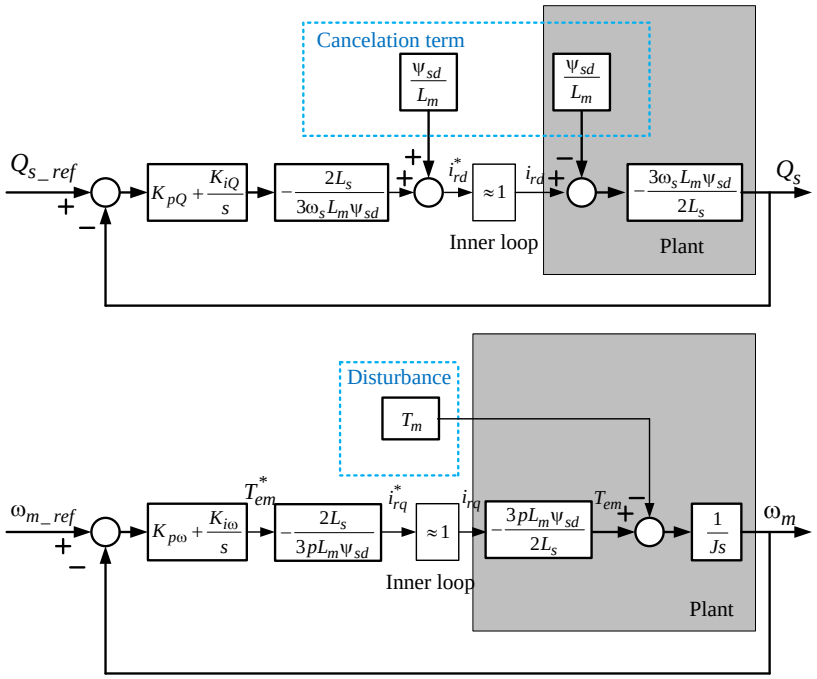

Figure 3.13: Stator reactive power and speed loops of DFIG RSC [92]

3.3.3.2 PI controller design for outer control loop: As indicated previously, the design of the outer loop assumes that the current control loops can track the constant commands of the outer loops. In practical applications, the stator reactive power and generator speed control loops are at least four times slower than the current control loops. Hence, when outer control loops are in progress, the actual currents of inner control loop are assumed to be equal their reference suddenly as $i_{rd\_ref} = i_{rd}$ and $i_{rq\_ref} = i_{rq}$ [92],[86]. The closed-loop control of the reactive power and generator speed are shown in the block diagram in Figure 3.13.

Taking the Laplace transform of the quantities indicated in Figure 3.13, the transfer function of the stator reactive power is:

$$\frac{Q_s(s)}{Q_{s\_ref}(s)} = \frac{\frac{K_p s}{K_i} + 1}{(\frac{1}{K_i} + \frac{K_p}{K_i})s + 1} \tag{3.52}$$

Note that the transfer function of the reactive power in (3.52) can be approximated to the standard first-order system by assuming $K_p << K_i$, then [92]:

$$\frac{Q_s(s)}{Q_{s\_ref}(s)} = \frac{1}{(\frac{1}{K_i} + \frac{K_p}{K_i})s + 1} \approx \frac{1}{\tau s + 1} \tag{3.53}$$

Therefore, the time constant of the stator reactive power control only depends on K_i. Then, K_i of the stator reactive power control loop can be designed as follows:

$$K_i = \frac{1}{\tau - K_p / K_i} \tag{3.54}$$

On the other hand, the transfer function of the generator speed is:

$$\frac{\omega_m(s)}{\omega_{m\_ref}(s)} = \frac{K_p s + K_i}{s^2 J + K_p s + K_i} \tag{3.55}$$

The transfer function in (3.55) can be reduced to a standard second-order system by assuming $K_p << K_i$:

$$\frac{\omega_m(s)}{\omega_{m\_ref}(s)} = \frac{\frac{K_i}{J}}{s^2 + \frac{K_p s}{J} + \frac{K_i}{J}} = \frac{\omega_n^2}{s^2 + 2\zeta\omega_n s + \omega_n^2} \tag{3.56}$$

Therefore, the gains of the PI controller of the speed control loop can be designed again through the pole placement method:

$$\begin{cases} K_p = (2\zeta\omega_n J) \\ K_i = (\omega_n^2 J) \end{cases} \tag{3.57}$$

The gains of the PI controller are tuned in the same way of the inner current control loop, although the settling time of the speed control loop should be larger than the inner control loop at least 4 times [92].

3.3.5 Limitation of Current and Voltage References

The current and voltage references from the PI controllers are limited within the rated values to avoid damage to the DFIG and power converter from overcurrent and overvoltage in the rotor [7]. The limitations of the current and voltage references are defined by:

$$\begin{cases} \sqrt{(i_{rd\_ref})^2 + (i_{rq\_ref})^2} \le (i_{r\_rated\_phase}\sqrt{2}) \\ \sqrt{(v_{rd\_ref})^2 + (v_{rq\_ref})^2} \le (v_{r\_rated\_phase}\sqrt{2}) \end{cases} \tag{3.58}$$

From (3.58), the space vector of the current and voltage reference are manipulated in terms of their magnitude within the nominal value. The priority limitation method is provided when the space vector of the current reference exceeds the nominal value. For instance, the speed tracking is much more important than stator reactive power tracking, i_{rd_ref} is reduced first to keep current reference space vector at the nominal value, and if the current reference space vector is still exceeded, i_{rq_ref} is reduced later.

Figure 3.14 shows block diagram of PI stator reactive power controller and PI speed controller that generates i_{rd_ref} and i_{rq_ref}. The references in direct and quadrature axis are maintained within the rated current value by the current reference limitation block. In addition, the anti-windup is provided in PI controllers through limited integrator when the actuators are saturated [95]

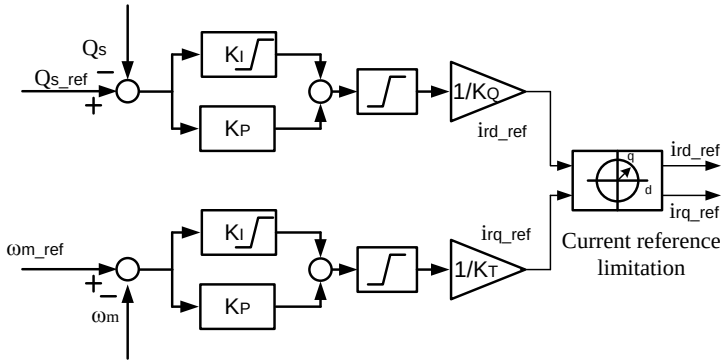

Figure 3.14: Current reference limitation and anti-windup

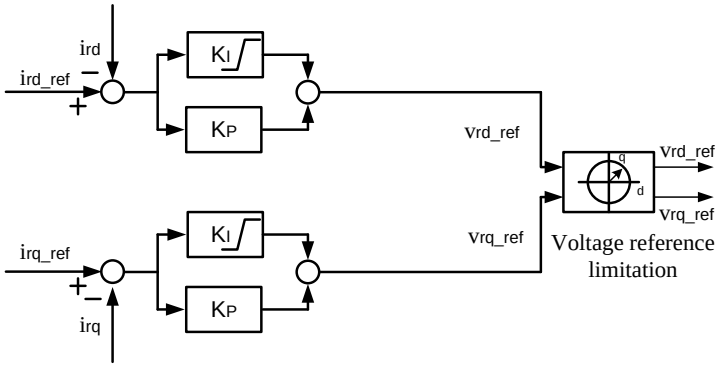

Figure 3.15: Voltage reference limitation and anti-windup

Similarly, Figure 3.15 shows the block diagram of PI current controllers that generate v_{rd_ref} and v_{rq_ref}. The references in direct and quadrature axis are maintained within the

rated rotor voltage value by the voltage reference limitation block before supplying their rotor voltage to the power converter.

3.4 Performance of RSC Vector Control for DFIG

In this section, the SFO vector control of the RSC has been verified by numerical simulations in Matlab/Simulink. The control system diagram used for the simulation is shown in Figure 3.11.

The characteristics of the 5-kW DFIG used for the simulations are reported in Appendix A. The values of all parameters and quantities are referred to the stator winding.

3.4.1 DFIG Model Simulation

The numerical simulator uses the two-phase DFIG αβ model developed in section 3.2.3.1. This machine model has as inputs the stator voltages, $v_{s\alpha}$ and $v_{s\beta}$, the rotor voltages, $v_{r\alpha}$ and $v_{r\beta}$, and the mechanical torque, T_m; the outputs are the stator flux linkages, $\psi_{s\alpha}$ and $\psi_{s\beta}$, the rotor flux linkages, $\psi_{r\alpha}$ and $\psi_{r\beta}$, and the mechanical speed, ω_m. The electromagnetic torque in (3.21) can be rearranged as a function of stator and rotor flux linkages by [7]:

$$T_{em} = \frac{3}{2}\frac{L_m}{\sigma L_s L_r} p(\psi_{r\alpha}\psi_{s\beta} - \psi_{r\beta}\psi_{s\alpha}) \tag{3.59}$$

The stator and rotor currents can be rearranged from (3.15) and (3.16) as a function of stator and rotor flux linkages[7]:

$$\begin{cases} i_{s\alpha} = \dfrac{\psi_{s\alpha}}{\sigma L_s} + \dfrac{L_m \psi_{r\alpha}}{\sigma L_s L_r} \\ i_{s\beta} = \dfrac{\psi_{s\beta}}{\sigma L_s} + \dfrac{L_m \psi_{r\beta}}{\sigma L_s L_r} \\ i_{r\alpha} = \dfrac{\psi_{r\alpha}}{\sigma L_r} + \dfrac{L_m \psi_{s\alpha}}{\sigma L_s L_r} \\ i_{r\beta} = \dfrac{\psi_{r\beta}}{\sigma L_r} + \dfrac{L_m \psi_{s\beta}}{\sigma L_s L_r} \end{cases} \tag{3.60}$$

The αβ DFIG model in (3.22) can be provided to be compatible with the real three-phase system as shown in Figure 3.16. Transformation blocks are required.

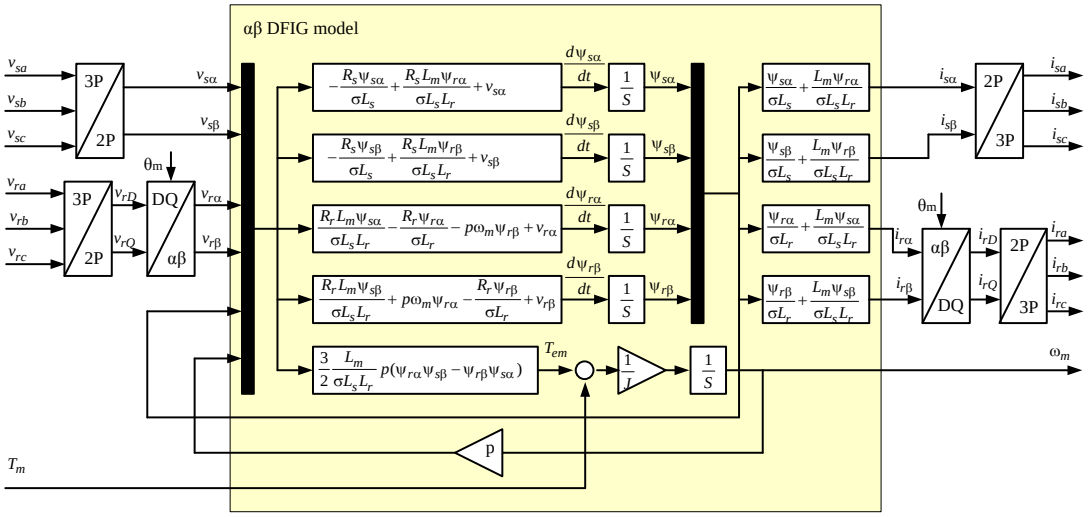

Figure 3.16: DFIG model simulation block diagram [7]

Suitable transformation blocks, described in section 3.4.2, allow the transformation of the variables from the stationary to the rotating reference frame and vice versa.

3.4.2 Transformation Block

Transformation blocks are used to represent the space vector notation of voltages, currents and fluxes of the DFIG in two-phase magnitude in different reference frames.

The reference frames used for the simulation are the stator reference frame (αβ), the rotor reference frame (*DQ*) and the synchronous reference frame (*dq*). The components of a generic space vector, $\vec{x}$ in the αβ, *DQ* and *dq* reference frames can be calculated as shown in Figure 3.17 [7].

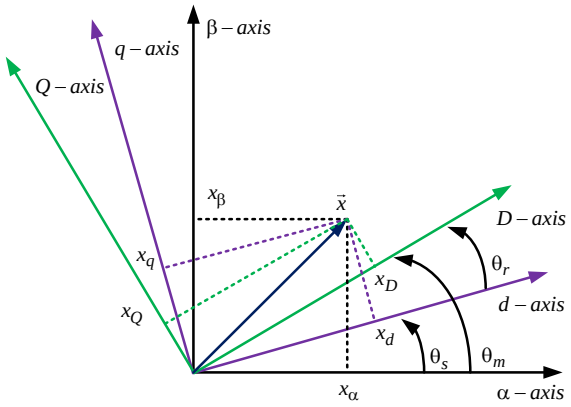

Figure 3.17: Space vector in three reference frame [7]

3.4.2.1 3P to 2P transformation block: this block is used to transform the real three-phase components into the two-phase components in the same reference frame. The projections, the transformation blocks and simulations of the stator and the rotor frame are shown in Figure 3.18. The two-phase components can be calculated by [7]:

$$\begin{bmatrix} x_\alpha \\ x\beta \end{bmatrix} = \frac{2}{3}\begin{bmatrix} 1 & -\frac{1}{2} & -\frac{1}{2} \\ 0 & \frac{\sqrt{3}}{2} & -\frac{\sqrt{3}}{2} \end{bmatrix}\begin{bmatrix} x_a \\ x_b \\ x_c \end{bmatrix} \tag{3.61}$$

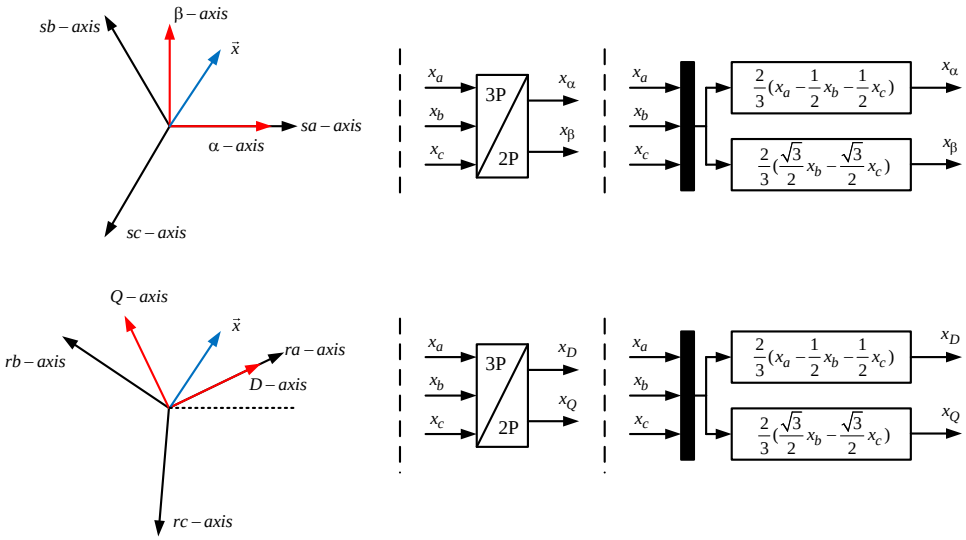

Figure 3.18: 3-phase to 2-phase transformations [7]

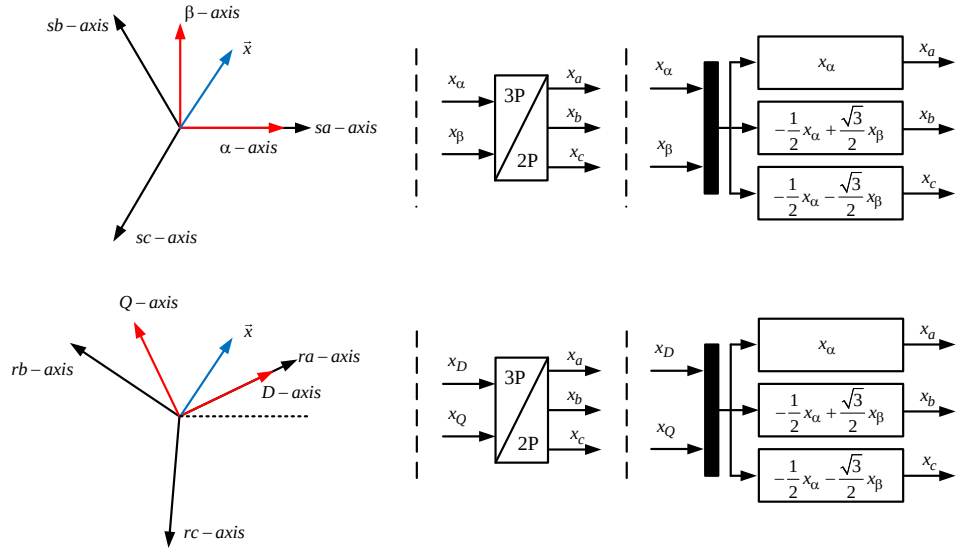

Figure 3.19: 2-phase to 3-phase transformations [7]

3.4.2.2 2P to 3P transformation block: this block is used to transform the two-phase components into the three-phase components in the same reference frame. The projections, the transformation blocks and simulations of the stator and the rotor frame are shown in Figure 3.19. The real three-phase components can be calculated by [7]:

$$\begin{bmatrix} x_a \\ x_b \\ x_c \end{bmatrix} = \begin{bmatrix} 1 & 0 \\ -\frac{1}{2} & \frac{\sqrt{3}}{2} \\ -\frac{1}{2} & -\frac{\sqrt{3}}{2} \end{bmatrix} \begin{bmatrix} x_\alpha \\ x_\beta \end{bmatrix} \tag{3.62}$$

3.4.2.3 *DQ* to αβ transformation block: this block is used to transform the two-phase components into the *DQ* reference frame to the αβ reference frame. θ_m is the position between the αβ reference frame and the *DQ* reference frame as shown in Figure 3.17. Therefore, the transformation equation is:

$$\begin{bmatrix} x_\alpha \\ x_\beta \end{bmatrix} = \begin{bmatrix} \cos\theta_m & -\sin\theta_m \\ \sin\theta_m & \cos\theta_m \end{bmatrix} \begin{bmatrix} x_D \\ x_Q \end{bmatrix} \tag{3.63}$$

The projections, the transformation blocks and simulations are shown in Figure 3.20.

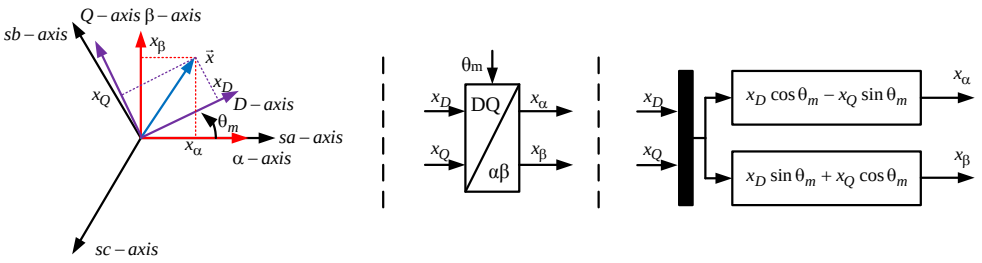

Figure 3.20: *DQ* frame to αβ frame transformations [7]

3.4.2.4 αβ to *DQ* transformation block: this block is used to transform the two-phase components into the αβ reference frame to the *DQ* reference frame. θ_m is the position between the αβ reference frame and the *DQ* reference frame. Therefore, the transformation equation is [7]:

$$\begin{bmatrix} x_D \\ x_Q \end{bmatrix} = \begin{bmatrix} \cos\theta_m & \sin\theta_m \\ -\sin\theta_m & \cos\theta_m \end{bmatrix} \begin{bmatrix} x_\alpha \\ x_\beta \end{bmatrix} \tag{3.64}$$

The projections, the transformation blocks and simulations are shown in Figure 3.21.

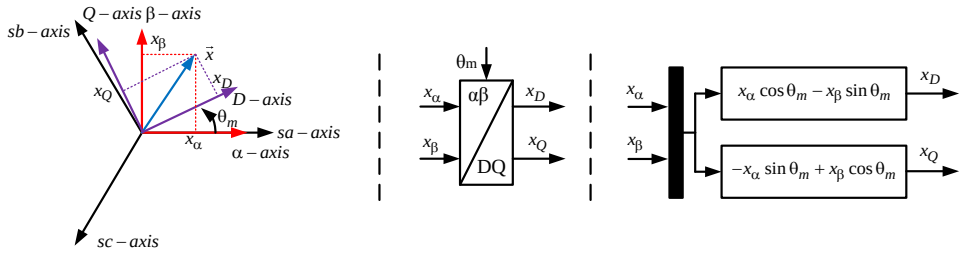

Figure 3.21: αβ frame to *DQ* frame transformations [7]

For other transformations that refer to the position in Figure 3.17, the transformation from αβ coordinates to *dq* coordinates can be conducted in the same way as above, by using θ_s and the transformation from *DQ* coordinates to *dq* coordinates can be done by using θ_r, respectively.

3.4.3 Position Calculation Block

This section reviews how the rotor position and the stator flux linkage position can be calculated.

3.4.3.1 Electrical angular position of the rotor, θ_m: The θ_m can be calculated from (3.12). The block diagram of the θ_m calculation is shown in Figure 3.22. The θ_m value is denoted between 0 and 2π. The practical measurement of the rotor position requires either a position or a speed sensor with sufficient resolution. Typical sensors used are rotary incremental encoders or resolvers[96]. For the simulation in this thesis, the sensing delays of sensors are neglected.

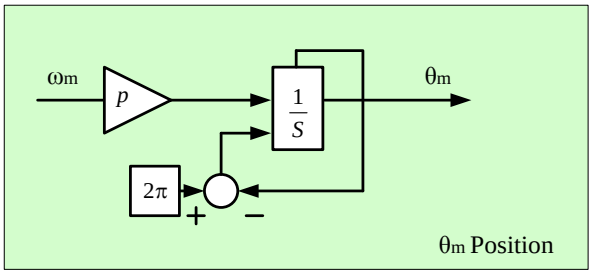

Figure 3.22: Electrical angular position of the rotor simulation [7]

3.4.3.2 Stator flux space vector position, θ_s (PLL): Under assumptions of stator flux oriented vector control, the stator voltage, v_{sd}, in *d*-axis is zero as indicated by (3.37). The PLL estimate θ_s by tracking the quantity v_{sd} using the $\alpha\beta$ to *dq* transformation block as shown in Figure 3.23.

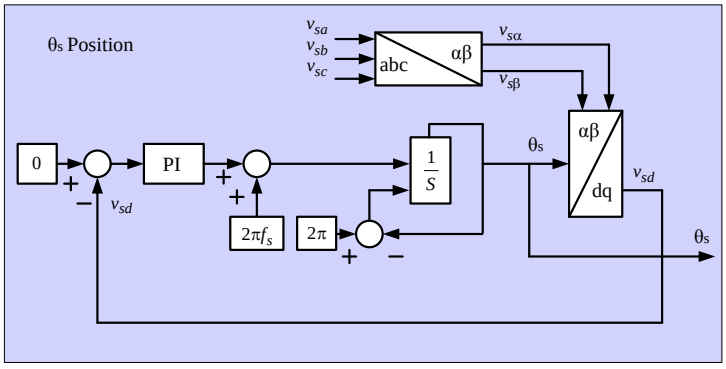

Figure 3.23: Stator flux linkage space vector calculation block diagram [7]

Therefore, the position of the stator flux linkage space vector in the rotor reference frame is $\theta_r = \theta_s - \theta_m$, as shown in Figure 3.24.

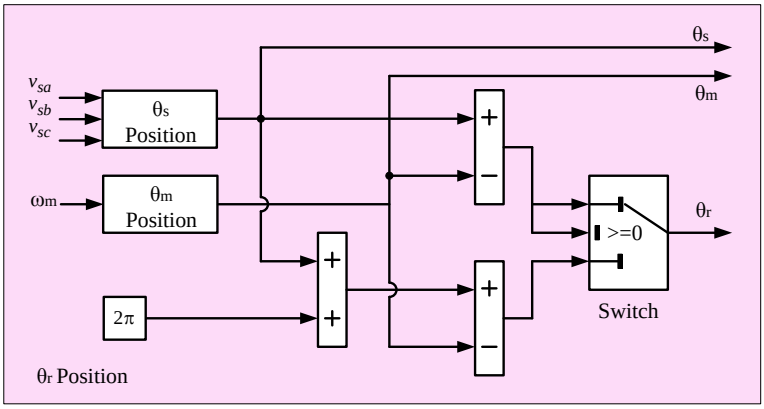

Figure 3.24: θ_r position calculation block diagram

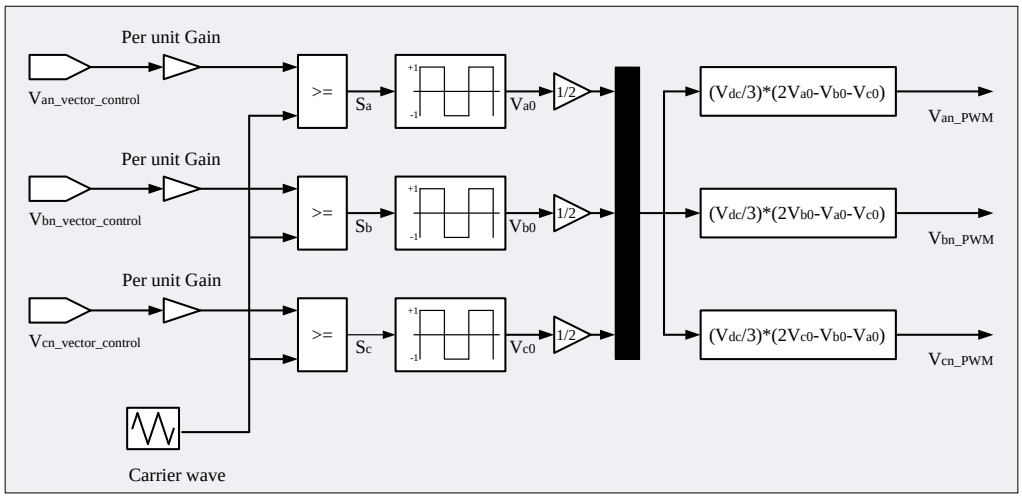

Figure 3.25: Two-level three-phase converter simulation

3.4.4 Two-Level Three-Phase PWM Converter Block

A model of the two-level three-phase RSC has been built and simulated in Matlab/Simulink, assuming, for simplicity, a constant DC link voltage, as shown in Figure 3.25, The reference voltages obtained from the current control are used for a

pulse-width modulation (PWM) block to generate the gate signals of the converter switches.. The three-phase reference voltages are normalised in a range of [-1 1] and compared with a triangular carrier to generate the switching signals for phases *a*, *b* and *c*: S_a, S_b and S_c. The switching signals fed the two-level converter block to generate PWM voltages to the rotor terminals of the DFIG.

3.4.5 Simulation Results on the Control Performance of DFIGs

The simulation results of the control of the DFIG are used to validate the performance of the SFO vector control on the sample case of a 5 kW generator. The 5-kW DFIG parameters are provided in Appendix A. All gains of the PI controller are designed by section 3.3.3. For the current control loops, the settling time at 2% is defined as $t_s = 3.5$ which should be less than the time constant of model in (3.45) for four times and damping ratio is $\zeta = 1$. ω_n is calculated via (3.50) to be 1143 rad/s. PI gains of the current control loop is calculated by (3.51) to be $K_{Prd} = K_{Prq} = 25$ and $K_{Ird} = K_{Irq} = 14671$ [V/A]. PI gains of the speed control loop can be calculated for $t_s = 0.4$ s, $\zeta = 1$ and $\omega_n = 10$ rad/s via (3.50) to be $K_{P\omega} = 6.08$ and $K_{I\omega} = 30.40$ [Nm/rad.s^{-1}]. PI gains of the stator reactive power control loop can be calculated for $\tau = 0.1$ and $K_P/K_I = 0.01$ via (3.54) to be $K_{PQ} = 0.1111$ and $K_{IQ} = 11.11$ [A/Var]. The mechanical torque for the DFIG has been set constant as $-0.2*T_{em\_rated}$. All the PI gains obtained above are used as beginning values for control system. However, PI gains are retuned in appropriate values for better performance for both steady-state and dynamic responses.

The simulations have been repeated for different generator speed and stator reactive power references. The control performance of the DFIG is evaluated on the basis of the tracking effectiveness of the generator speed and stator reactive power both for steady-state and dynamic responses.

3.4.5.1 Ideal vector control: Initially, the vector control on the RSC has been tested without the three-phase PWM converter block. Therefore, the three-phase output voltages from the SFO vector control are supplied directly to the rotor terminals of the DFIG using ideal voltage sources.

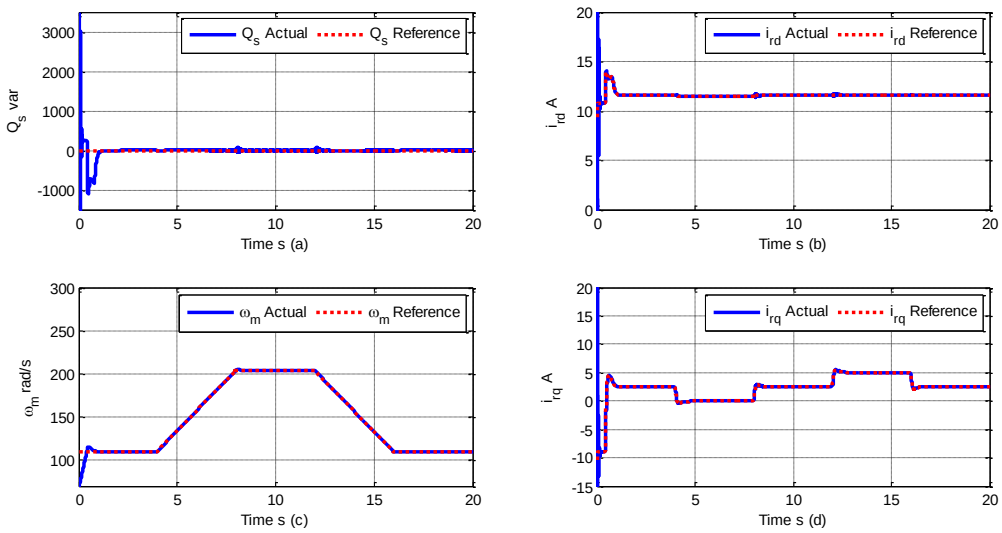

Figure 3.26: SFO control performance for DFIG in generator speed tracking and stator reactive power tracking ($Q_s = 0$)

Figure 3.26 shows a simulation where the generator speed reference is varied from 110 to 204 rad/s, which is equivalent to a rotor slip variation from 30% to -30%, while the stator reactive power reference is set at zero. As the torque is constant, the diagram of

the speed also represents the diagram of the mechanical power input, scaled by the value of the torque.

Figure 3.26(a) shows that the stator reactive power settles to the reference signal in around 1.5 seconds. It looks like a slow response due to i_{rd} is limited at rated rotor current in start-up state. This start-up state in which stator of DFIG was connected to the grid gave the large transient of current and electromagnetic torque and should not be used in reality. The start-up state of the wind turbine system has been simplified in these simulations by ignoring the stator overcurrent occurring during the first few cycles. The generator speed reference steps up at below 30% of synchronous speed, 110 rad/s, until t = 4, and then is gradually increased to 204 rad/s at t = 8 to reach 30% above the synchronous speed. At 12 seconds, the reference is linearly decreased to 110 rad/s. Figure 3.26(c) shows that the actual speed follows the reference quite well. The rotor currents and their references in the rotating reference frame are shown in Figure 3.26(b) and (d), respectively. The *d*-axis rotor current reference is generated by the stator reactive power control loop and the *q*-axis rotor current reference is produced by the speed control loop. When the start-up state is ignored, the speed response gave 20% of the percent overshoot, 0.7 seconds of settling time, no steady-state error and good speed-tracking. For stator reactive power response, it gave a high control performance when i_{rd} is below the rated rotor current and vice versa. It can be seen that the stator reactive power and generator speed can be controlled independently by using i_{rd} and i_{rq}, respectively.

Figures 3.27 and 3.28 show the voltages and currents of the stator and the rotor winding when the speed reference varies according to Figure 3.26(c) and the stator reactive power reference is set to zero.

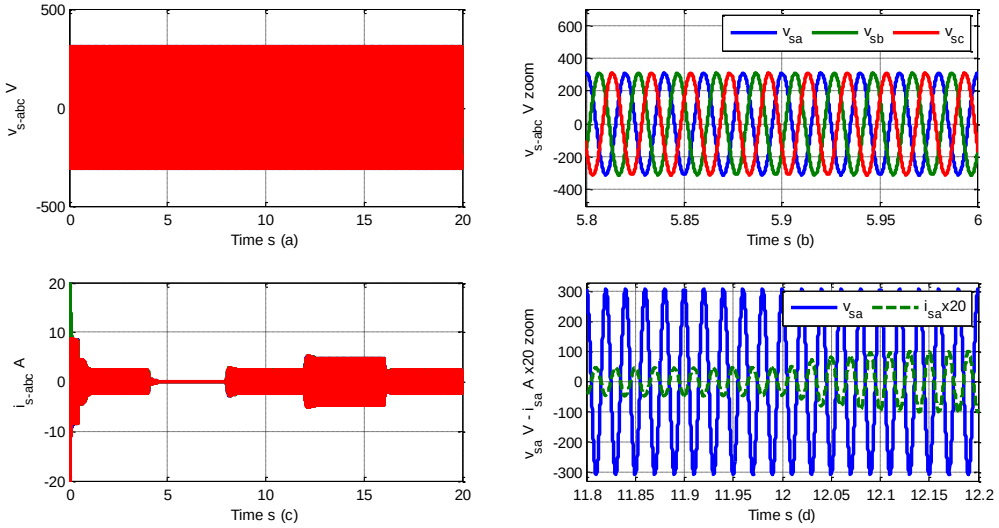

Figure 3.27: SFO control performance for DFIG of stator voltages and stator currents in generator speed tracking and stator reactive power tracking ($Q_s = 0$)

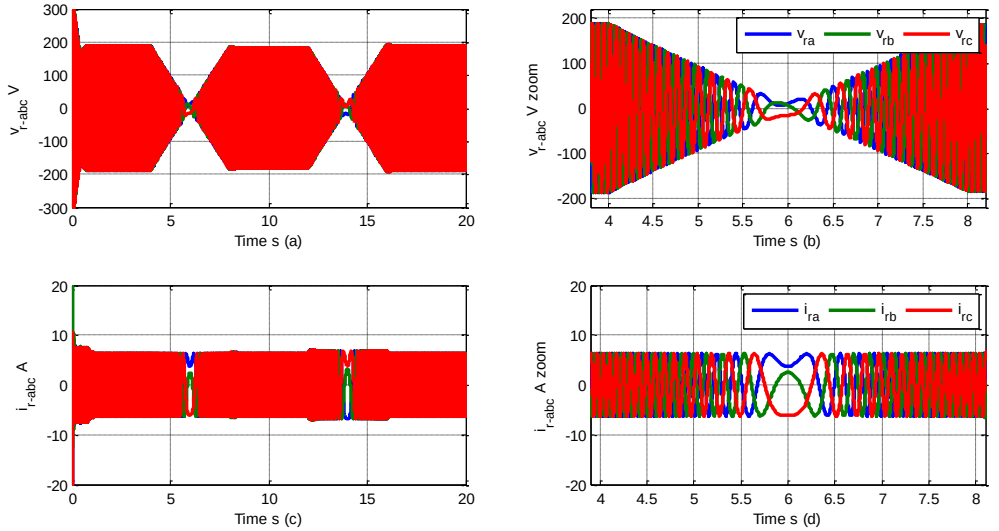

Figure 3.28: SFO control performance for DFIG of rotor voltages and rotor currents in generator speed tracking and stator reactive power tracking ($Q_s = 0$)

Figure 3.27(a) shows the three-phase stator voltages, which have constant amplitude of 380 V_{rms} phase-to-phase and frequency of 50 Hz. A zoomed figure of the voltage is shown in Figure 3.27(b). Figure 3.27(c) shows the three-phase stator currents, whose amplitude varies according to the active power supplied to the grid. The phase angle between the stator voltage and stator current is equal to 180 degrees as better shown in Figure 3.27(d), which means that the stator reactive is equal to 0. When i_{sd} is zero, the stator flux linkage is produced by i_{rd} only, as predicted by (3.25).

Figure 3.28 shows the three-phase rotor voltages and currents of the RSC. The rotor voltage and zoomed rotor voltage are shown in Figures 3.28(a) and (b), respectively. Figure 3.28(c) shows the rotor current. The phase angle of voltage and current in the rotor is shown in Figure 3.28(d). The figures show that the magnitude and frequency of the required rotor voltages vary according to the slip of the DFIG.

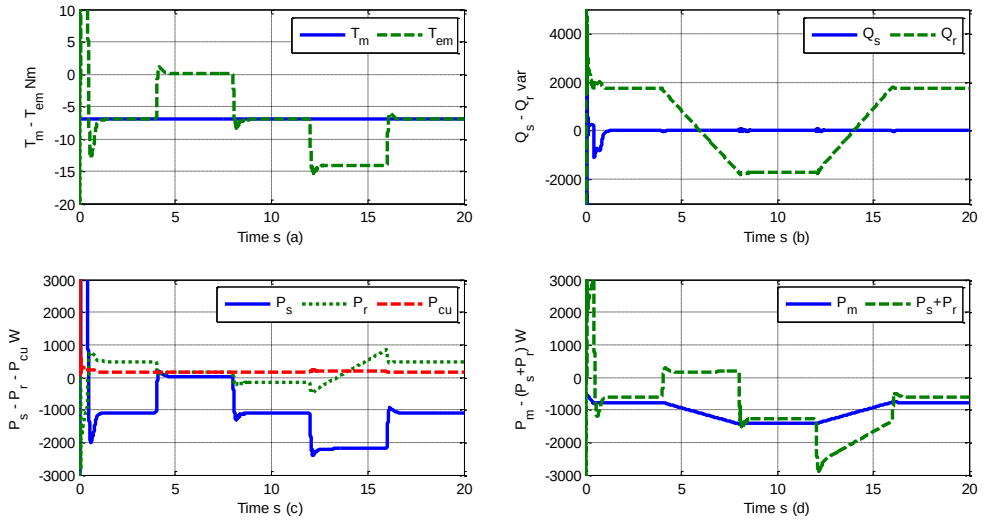

Figure 3.29: SFO control performance for DFIG in torque, reactive power and active power in generator speed tracking and stator reactive power tracking (Q_s = 0)

The mechanical torque, T_m, and electromagnetic torque, T_{em}, are shown in Figure 3.29(a). The mechanical torque is constant at -7 Nm.(0.2*T_{rated}). The electromagnetic torque is equal to the mechanical torque value only at the steady-state and is within the limits when the rotor speed has to be modified. The stator reactive power, Q_s, and rotor reactive power, Q_r, are shown in Figure 3.29(b). The stator reactive power Q_s is maintained at zero while the rotor reactive power Q_r varies with the generator speed. It can be seen that the rotor active power P_r varies from positive to negative between sub-synchronous and super-synchronous operations. Then, the phase sequence of the rotor current is reversed when the generator speed crosses the synchronous speed. As a result, the rotor reactive power Q_r change from positive to negative and vice versa. Figure 3.29(c) shows the stator active power, P_s, the rotor active power, P_r and the copper losses, P_{cu}. For sub-synchronous speed operations, the stator generates active power, but a fraction of it is recirculated by the rotor. In super-synchronous speed operations, both the stator and rotor generate active power to the electrical grid. The copper losses are always positive as a function of currents and resistances in the stator and rotor. The copper losses affect the DFIG efficiency from P_s+P_r = P_{cu}+P_m. Finally, the mechanical power, P_m and total electrical active power produced from the DFIG, P_e =P_s+P_r are shown in Figure 3.29(d). In steady-state, the electrical active power P_e of the DFIG increases according to the generator speed because the rotor active power P_r changes from positive to negative between sub-synchronous and super-synchronous operations, while the stator active power P_s is constant in whole operations with constant torque.

In the transient state, during the acceleration of the rotor, the mechanical power extracted from the wind turbine P_m is higher than the electrical power from the DFIG P_e. The difference in power between P_m and P_e is used to increase kinetic energy in the wind turbine. In contrast, the kinetic energy is restored during the deceleration of the rotor. Consequently, the electrical power from the DFIG P_e is higher than the mechanical power P_m [97].

In the following simulation, the generator speed reference is the same as Figure 3.26, but the reactive power reference has a step-change at 12 seconds from 0 to 2000 Var.

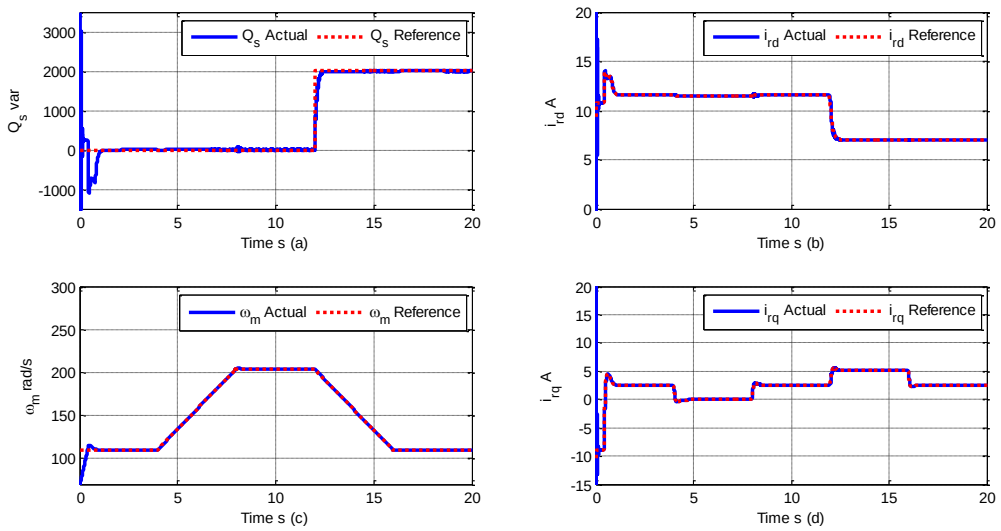

Figure 3.30: SFO control performance for DFIG in speed tracking and stator reactive power tracking (Q_s = step-changing)

Figure 3.30 shows that the actual stator reactive power is tracked within 0.7 seconds in agreement with the control specifications. The same performance is observed for the *d*-axis rotor current, the generator speed and the *q*-axis rotor current. The simulation

proves that the stator reactive power and generator speed can be independently controlled using i_{rd} and i_{rq} even when both references change simultaneously.

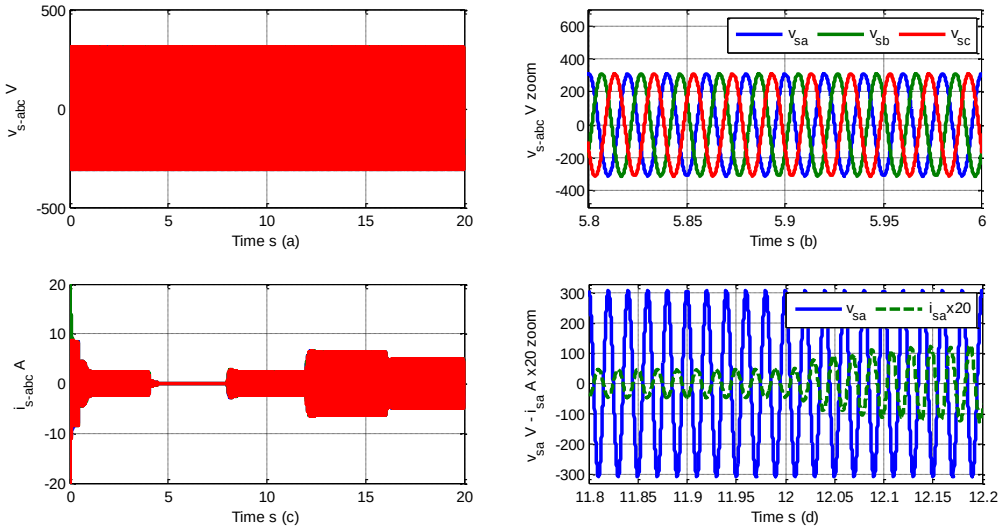

Figure 3.31: SFO control performance for DFIG of stator voltages and stator currents in speed tracking and stator reactive power tracking (Q_s = step-changing)

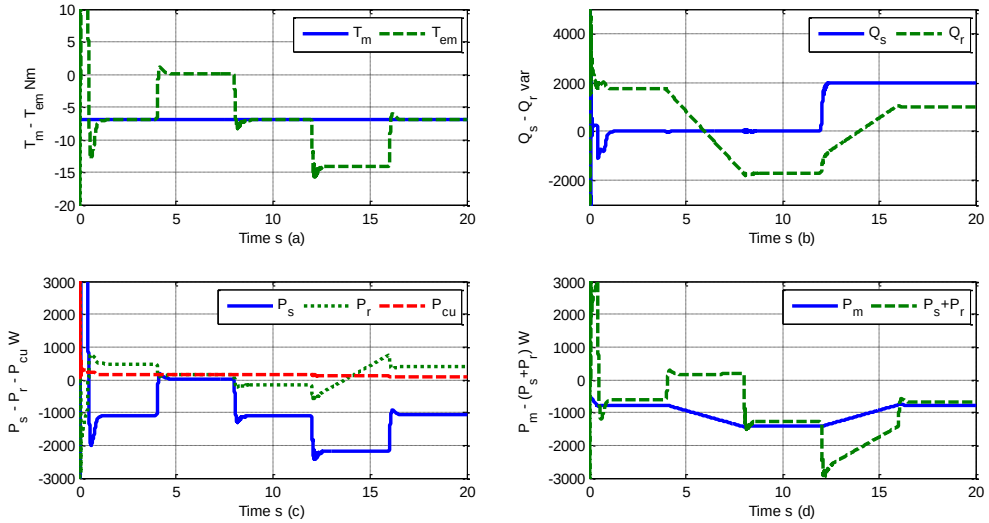

Figure 3.32: SFO control performance for DFIG in torque, reactive power and active power in speed tracking and stator reactive power tracking (Q_s = step-changing)

Figure 3.31 shows the three-phase voltages and currents in the stator terminals of the DFIG under stator-flux oriented vector control. The voltages, zoomed voltages and currents are shown in Figure 3.31(a), (b) and (c), respectively. It can be observed that the power factor on the stator changes from unity at time = 12 seconds because the stator reactive power changes from 0 to 2000 Var.

Figure 3.32 shows the quantities of torque, active power and reactive power of the DFIG in stator flux oriented control when a speed reference varies from sub-synchronous speed to super-synchronous speed and stator reactive power reference is applied with step-changing. It can be observed that, while the torque and the reactive power diagrams remain substantially unchanged, the variation of the reactive power reference has an influence on copper losses. In comparison with Fig. 3.28, the copper losses decrease from 164 to 88 W. This means that a suitable choice of the reactive power reference increases the efficiency of the DFIG. The simulations have been repeated for various references, and the optimal value has been found to be equal to 2800 Var. That means that the efficiency increases by 13.53 %, from 606 to 688 W, compared to the simple case of setting the reactive power reference to 0.

3.4.5.2 Vector control with three-phase PWM converter: The vector control of the RSC has been tested with the two-level three-phase PWM converter block. The switching frequency of the converter and DC link voltage have been set to 1 kHz and 550 V, respectively. The PI gains of inner control loop and outer control loop and other parameters are defined as the same as the previous case.

The simulation results are performed to compare between the ideal SFO vector control to the DFIG and the SFO vector control with three-phase PWM converter to DFIG. The vector control and the power converter were tested with the same speed diagram and mechanical torque input.

Figure 3.33 to 3.39 show the control performance of the stator reactive power tracking, the generator speed tracking, the stator voltage, the stator current, the rotor voltage, the rotor current, the electromagnetic torque and the active power in the stator and rotor generated by the two methods, respectively.

It can be seen that the ideal vector control generates pure sinusoidal voltage waveforms for the rotor terminals as shown in Figure 3.36(a) and (c). Therefore, the rotor and stator currents are also sinusoidal waveforms and the electromagnetic torque is smooth.

The vector control with power converter is instead shown for comparison in Figure 3.36(b) and 3.36(d). The figures 3.35(d) and 3.37(d) show a ripple for both the stator current and rotor current equal to 83.82% and 14.93%, respectively. The electromagnetic torque in the machine is settled around -7 Nm and varies between -9 and -3.3 Nm. Therefore, the electromagnetic torque has a ripple of 81.42%, as shown in Figure 3.38(d) although it does not substantially affect the effectiveness of the control loops.

These simulations give confidence that the simplification of using an ideal converter does not substantially alter the validity of the results of the various methods of controlling the wind turbine with the objective of maximising the energy extracted from the wind, which is the ultimate goal of this thesis. The main advantage of using an ideal converter is the possibility of using a larger time step of the simulation, which then enables significantly longer simulation times with the same computational resource. For these reasons, in this thesis, the vector control is simulated with an ideal power converter for the simulations of Chapter 4, 5 and 6 focusing on the analysis of the efficiency of the wind energy conversion system over a long time period.

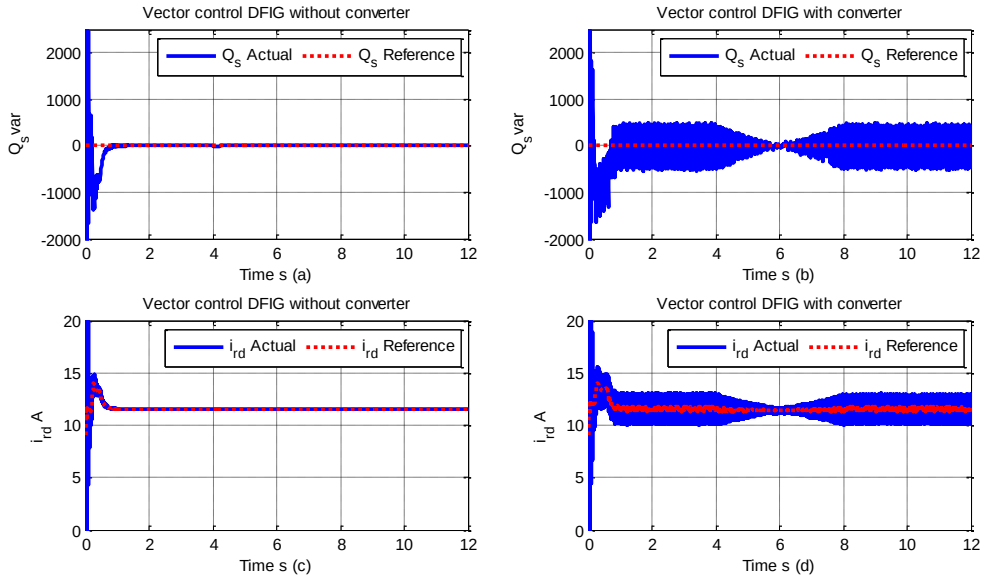

Figure 3.33: Comparison of SFO control performance for DFIG in stator reactive power tracking with and without a converter in the system

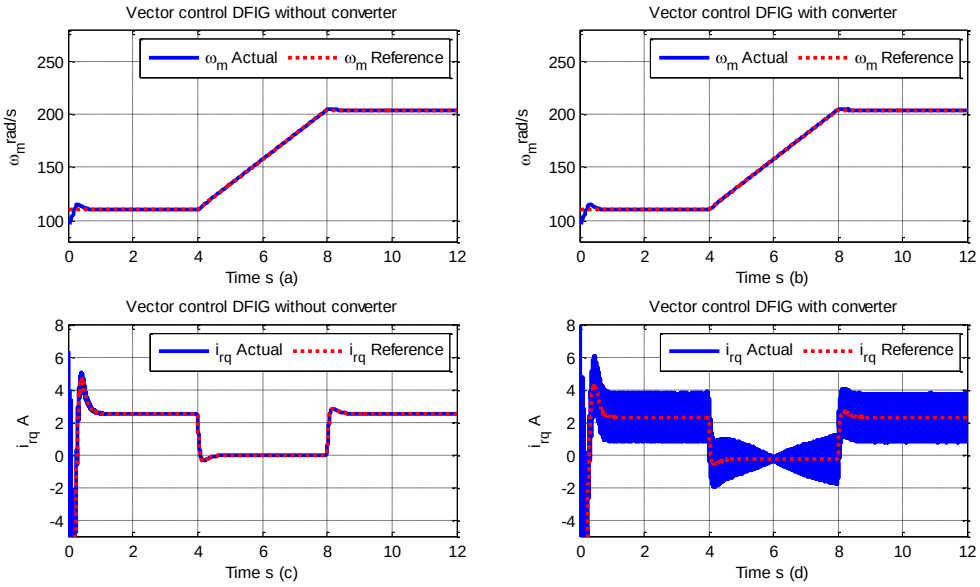

Figure 3.34: Comparison of SFO control performance for DFIG in generator speed tracking with and without a converter in the system

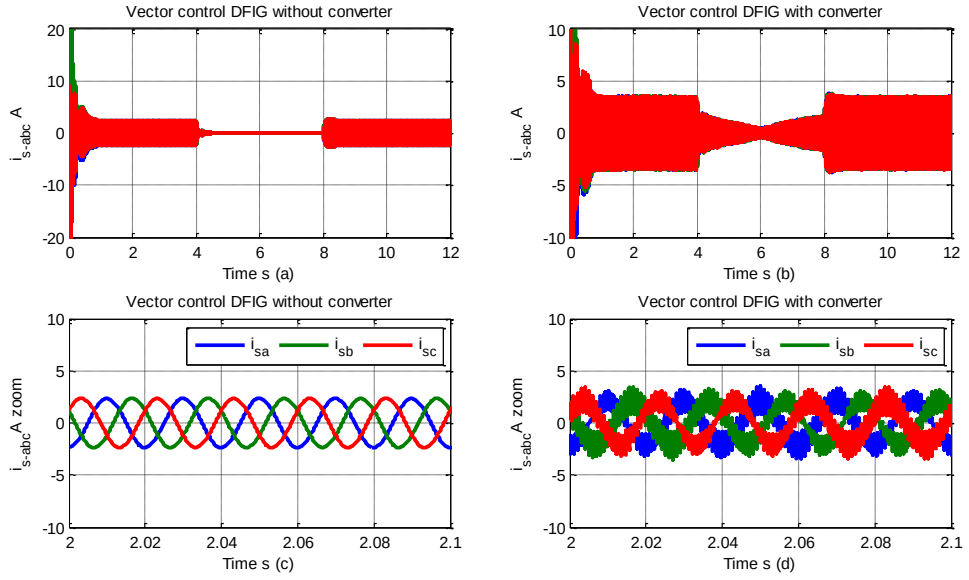

Figure 3.35: Comparison of SFO control performance for DFIG of stator current in generator speed tracking and stator reactive power tracking with and without a converter in the system

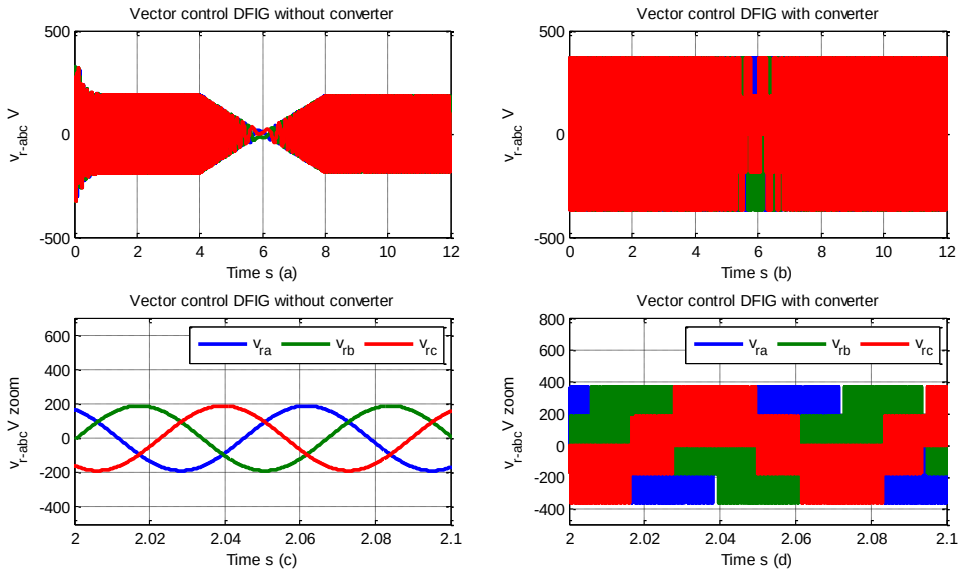

Figure 3.36: Comparison of SFO control performance for DFIG of rotor voltage in generator speed tracking and stator reactive power tracking with and without a converter in the system

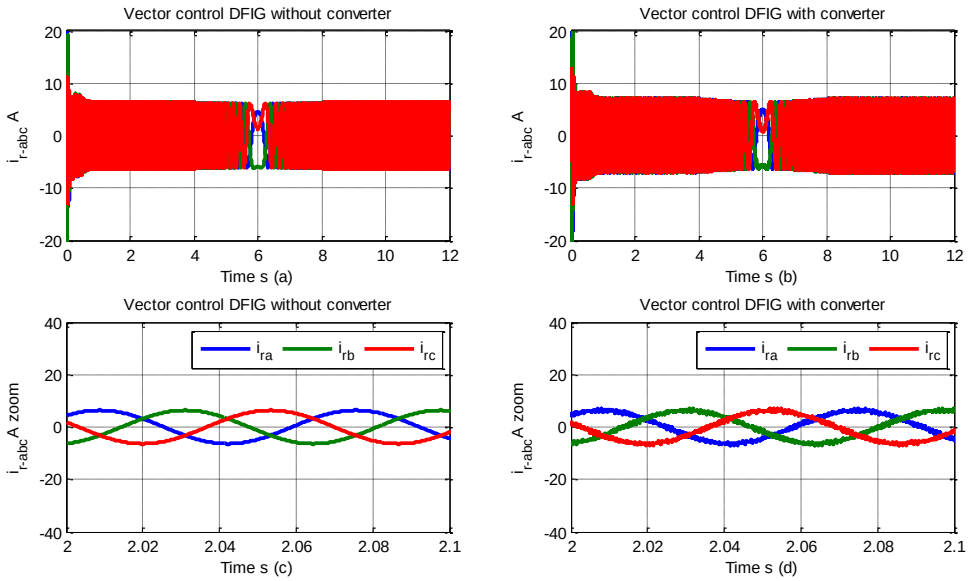

Figure 3.37: Comparison of SFO control performance for DFIG of rotor current in generator speed tracking and stator reactive power tracking with and without a converter in the system

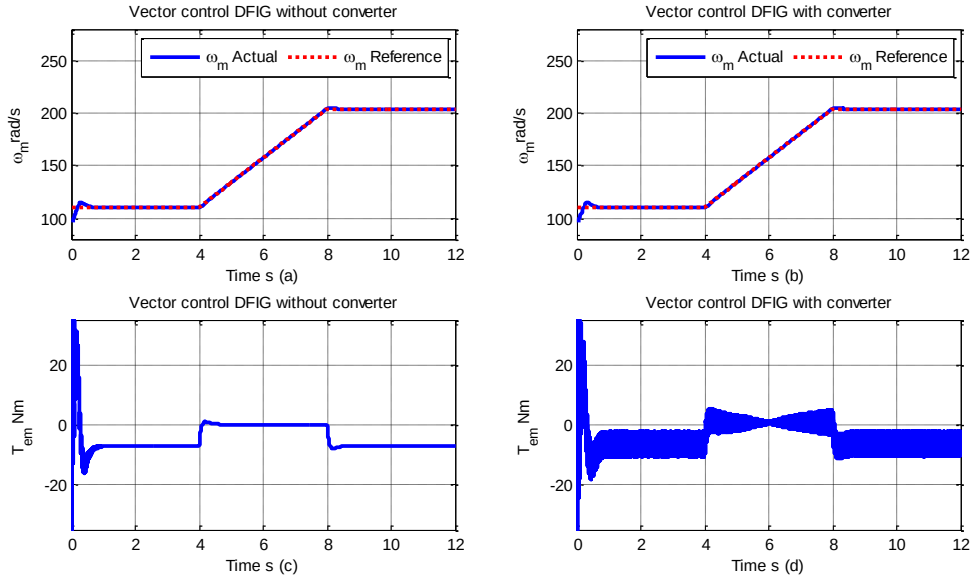

Figure 3.38: Comparison of SFO control performance for DFIG of electromagnetic torque in generator speed tracking and stator reactive power tracking with and without a converter in the system

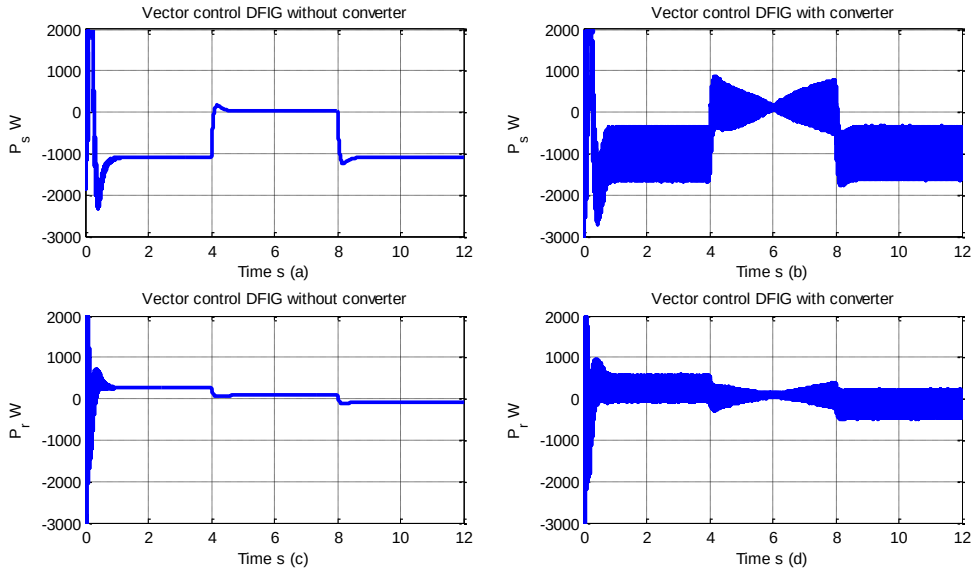

Figure 3.39: Comparison of SFO control performance for DFIG of stator active power and rotor active power in generator speed tracking and stator reactive power tracking with and without a converter in the system

3.4.6 Validation of the Simulation Model

In this section, the SFO vector control for the DFIG is simulated with a 7.5 kW DFIG to validate the experimental results in [98]. The parameters of the 7.5kW DFIG used in the experiment in [98] are shown in Table 3.1. The DC link voltage and the switching frequency of the converter are set at 500 V and 1 kHz, respectively. The PI gains of the inner control loop and the outer control loop have been tuned to match the dynamic performance of the DFIG of [13].

In the first simulation, the vector control and the converter were tested by running the DFIG at the sub-synchronous speed of 109.9 rad/s with a load drawing 2 kW at unity power factor. The vector control performance of the generator speed tracking and the stator reactive power tracking are shown in Figure 3.40.

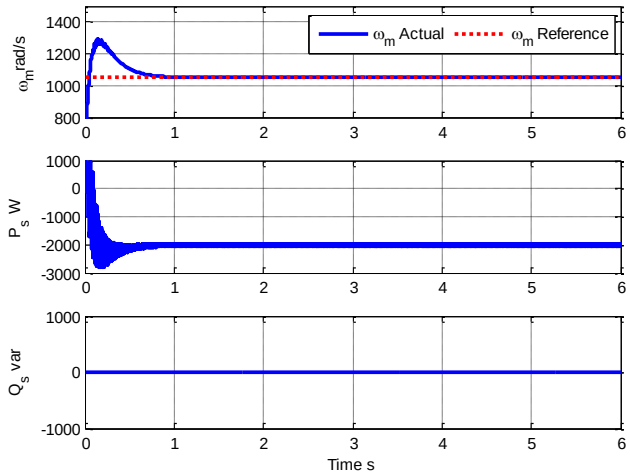

Figure 3.40: Control performance of generator speed at sub-synchronous speed (1050 rpm) and stator reactive power (unity power factor)

The simulation results have been validated with the experimental results shown in Figure 3.41 and 3.42. Figure 3.41 shows the stator voltage and stator current of phase *a* under the stated condition. It can be seen that the results of the simulation from the proposed model and the experiments are in good agreement. Figure 3.42 shows the rotor current of phase *a* in the simulation result and experimental result from [98]. It can be seen that both results produce a rotor current frequency of 15 Hz and a peak value of around 18 A. The waveform of the simulation does not present any distortion because the ideal converter model has been used.

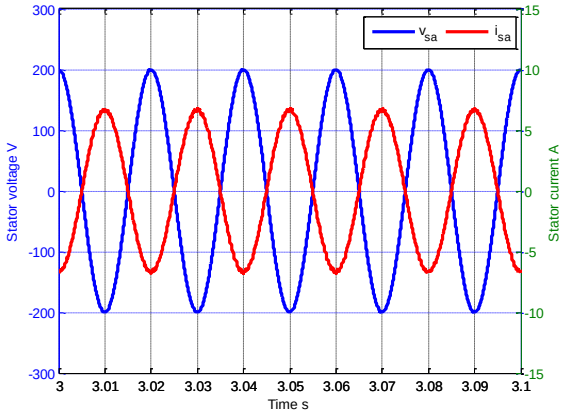

(a)

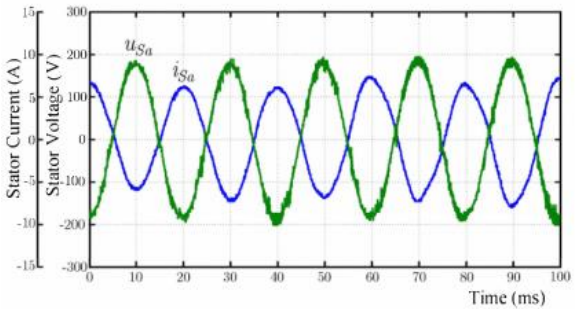

(b)

Figure 3.41: Control performance validation of stator voltage and stator current of phase *a* at sub-synchronous speed a) Simulation result. b) Experimental result [98]

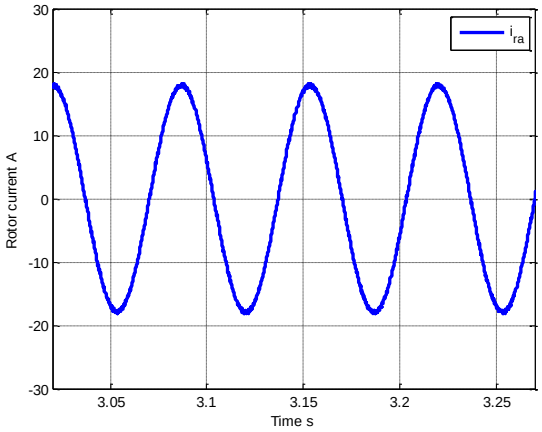

(a)

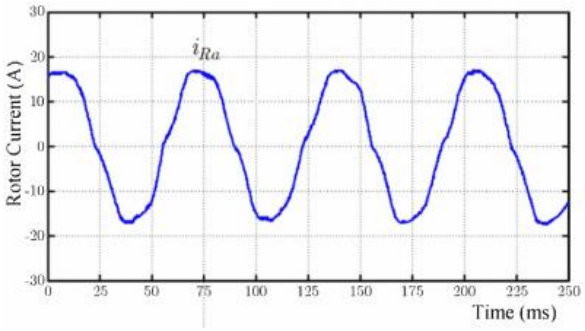

(b)

Figure 3.42: Control performance validation of rotor current of phase *a* at sub-synchronous speed a) Simulation result. b) Experimental result [98]

In a second comparison, the simulated vector control has been tested with a speed ramp including a transition from sub-synchronous to super-synchronous speed. Figure 3.43 shows the simulation result and experimental result of [98] of the generator speed and the phase *a* of the rotor current. Both the simulation and experimental results are in very good agreement. It can be observed that the frequency of the rotor current is reduced to zero when the speed is close to the synchronous speed.

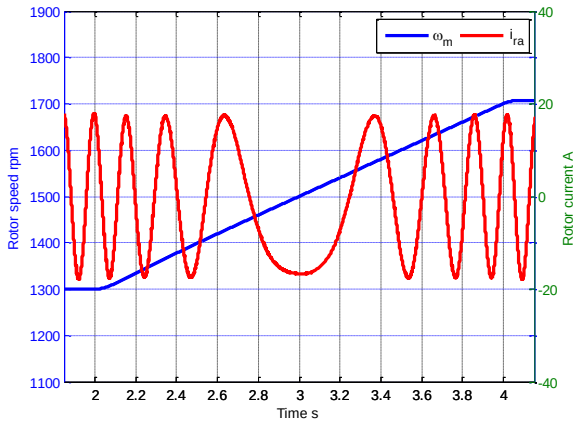

(a)

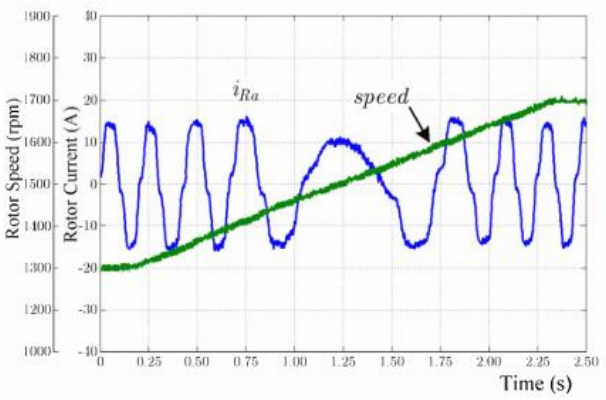

(b)

Figure 3.43: Control performance validation of variation of DFIG speed from sub-synchronous to super-synchronous speed. a) Simulation result. b) Experimental result[98]

From the comparison, it can be concluded that the model developed in this thesis is an accurate representation of a DFIG for a wind turbine and, hence, the control strategies proposed in Chapter 4 and 5 can be successfully implemented on a practical system.

Table 3.1: DFIG characteristics used in the experiment in [98]

Characteristics	**Value**	**Unit**
Power	7.5	kW
Rated speed	1425	rpm
Stator voltage	220/380	V
Rate stator current	28.2/16.3	A
Rotor voltage	180	V
Rated rotor current	27	A
Frequency	50	Hz
Number of poles	4	poles
Stator : Rotor turns ratio	2.1 : 1	-
Stator connection	Δ/Y	-
Rotor connection	Y	-
r_s	0.60	Ω
r_r	0.164	Ω
L_s	97	mH
L_r (refer to stator)	21.8	mH
L_0 (refer to stator)	43.6	mH

3.5 Summary

This chapter dealt with the dynamic modelling and control of the RSC of the DFIG. The mathematical model is written in terms of space vectors, and it has been shown how the stator and rotor equations can be written in three different reference frames, i.e. the stationary reference frame ($\alpha\beta$), the rotor reference frame (DQ), and the rotating reference frame (dq).

The SFO vector control technique is chosen in the thesis, so the control of stator reactive power and generator speed can be decoupled by controlling the direct and quadrature components of the rotor current. The transfer functions of the controllers of the stator reactive power and generator speed have been analytically derived. It has been shown that these transfer functions can be used for the design of the PI regulator once specific performance levels have been set.

The SFO vector control of the RSC has been simulated in Matlab/Simulink to verify that the transient response and the steady-state errors of the stator reactive power and generator speed are within the limits given by the design. In addition, it has been verified that the ideal model of the RSC does not affect significantly the control performance compared to the case of an accurate model of the RSC.

Finally, the SFO vector control model has been fully validated by comparing the simulation results with the experimental results presented in [98].

Chapter 4 Optimal Power Control for VSFP Wind Turbines

4.1 Introduction

The stator-flux oriented vector control is used to control the DFIG through the RSC in the WECS, as it provides a decoupled control of the generator speed and the stator reactive power. The generator speed is adjusted to the optimal point according to the any wind speed to maximise the mechanical power extracted from the wind turbine. This chapter focusses on the design of the control strategy to optimise the power output of the wind turbine.

In particular, section 4.2 summarises the control performance and limits in terms of efficiency of traditional power control methods for VSFP wind turbines [99] when wind turbine parameter uncertainties are taken into account.

Section 4.3 proposed a new fuzzy controller based on single input rule modules (SIRMs) that could overcome the main shortcoming of traditional controllers. The proposed fuzzy controller is designed to track the maximum power point of the wind turbine for the below-rated wind speed and the rated power for the above-rated wind speed even if the knowledge of the system parameters is not accurate.

Simulation results are shown in section 4.4 using the validated software simulated presented in Chapter 3 to compare the control performance between the SIRM-based fuzzy controller and the traditional power control using realistic wind speed profiles.

4.2 Efficiency of Traditional Power Control Considering Wind Turbine Parameter Uncertainties

In this section, the efficiency of the traditional power control for VSFP wind turbine is analysed both in terms of maximisation of extracted mechanical power by the MPPT controller and the limitation of the power by active stall control. The study specifically considers the effect of uncertainty on the knowledge of air density, ρ, and C_p-λ curve via λ_i in (2.9) [57],[100],[101].

4.2.1 Typical Problems of PSF-MPPT Control

The efficiency of the traditional MPPT control, using a PSF-MPPT method, is negatively affected when the air density and the C_p-λ curve are different from those obtained via experimental tests [57], as the control scheme does not adapt to changes of the wind turbine parameters.

Generally, the air density according to the ideal gas law is varied by the atmospheric pressure and temperature as following expression[102]:

$$\rho = \frac{p}{RT} \tag{4.1}$$

where p is the absolute pressure in Pa, R is the specific gas constant for dry air, 287.058 J/(kg.K), and T is the absolute temperature in °K.

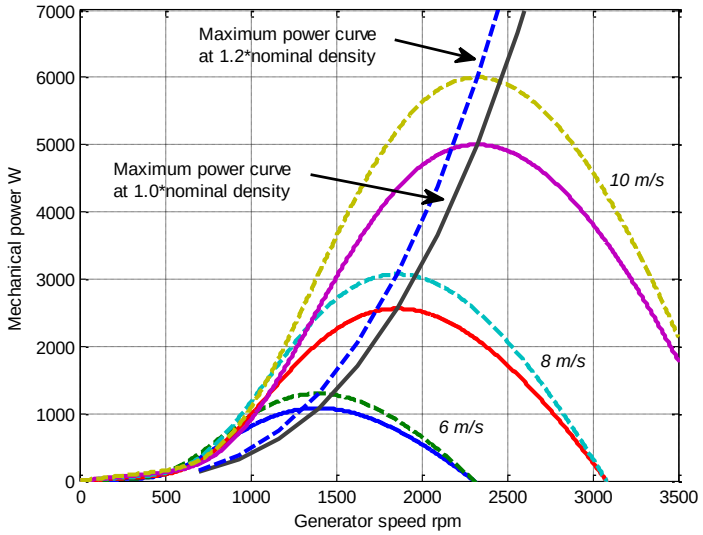

Figure 4.1: Maximum power curve under uncertainty of air density

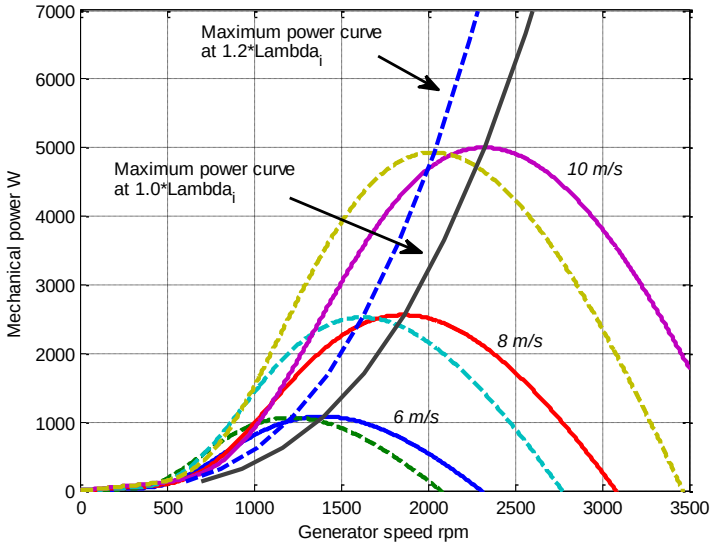

Figure 4.2: Maximum power curve under uncertainty of C_p-λ curve

The reference value of the air density is 1.225 kg/m^3 at 101,325 Pa and 15 °C. According to (4.1), the air density is increased by 20%, if the pressure increases by 10% and the temperature decreases by 10%. Figure 4.1 shows the influence of the air density on the mechanical power curve. When the air density increases by 20% of its nominal value, the maximum mechanical power calculated from (2.5) is significantly larger than the real power and the maximum power point is shifted by 20% of the nominal value.

The C_p-λ curve of this thesis is derived from (2.37) and (2.38). When the pitch angle is equal to zero, C_{pmax} and λ_{opt} are 0.48 and 8.1, respectively. The power coefficient charateristic is derived from the wind turbine manufacturers. To analyse the effect of the C_p-λ curve uncertainty, λ_i has been increased by 20% of its nominal value [57], shifting the estimated power curves to the left side of the real power curves. Hence, its maximum power curve (dashed line) also is shifted from the real maximum power curve as shown in Figure 4.2.

For this analysis, it can be seen that the use of (2.43) for the calculation of the speed reference can lead to substantial errors in the individuation of the correct speed and, hence, reduced efficiency of the MPPT algorithm and the energy generated by the wind turbine.

4.2.2 Simulation Results

The DFIG-WECS for a VSFP wind turbine, shown in Figure 2.22, has been analysed by numerical simulation in Matlab/Simulink environment to evaluate the performance of the system. The wind energy generation consists of a 5-kW DFIG and a 5-kW wind

turbine. The parameters of the DFIG and the wind turbine used for the simulations are given in Appendix A. In this thesis, the three reference parameters of the wind turbine via experimental tests are $\rho = 1.225$, $\lambda_{opt} = 8.11$ and $C_{pmax} = 0.48$, then $k_{opt} = 0.1186$. The pitch angle is $\beta = 0°$ for all the simulations to satisfy the requirement of a fixed pitch.

The wind turbine model and the DFIG model driven by the stator-flux oriented vector control were simulated according to the block diagram in Chapter 2 and Chapter 3, respectively, and the hypotheses on the power converters of Chapter 3.

The first simulation shows the control performance of the ideal MPPT control compared to the traditional power control based on PSF MPPT and active stall under uncertain aerodynamic conditions, i.e. the air density and C_p-λ curve by λ_i. The generation system is tested under a step-change of the wind speed.

The DFIG is always regulated in generation mode in the simulation. With this control strategy, during the acceleration of the rotor, the electromagnetic torque, T_{em} of the DFIG is limited at maximum value, $T_{em} = 0$, while the electromagnetic torque is limited at the minimum value, $T_{em} = -T_{rated}$ during deceleration.

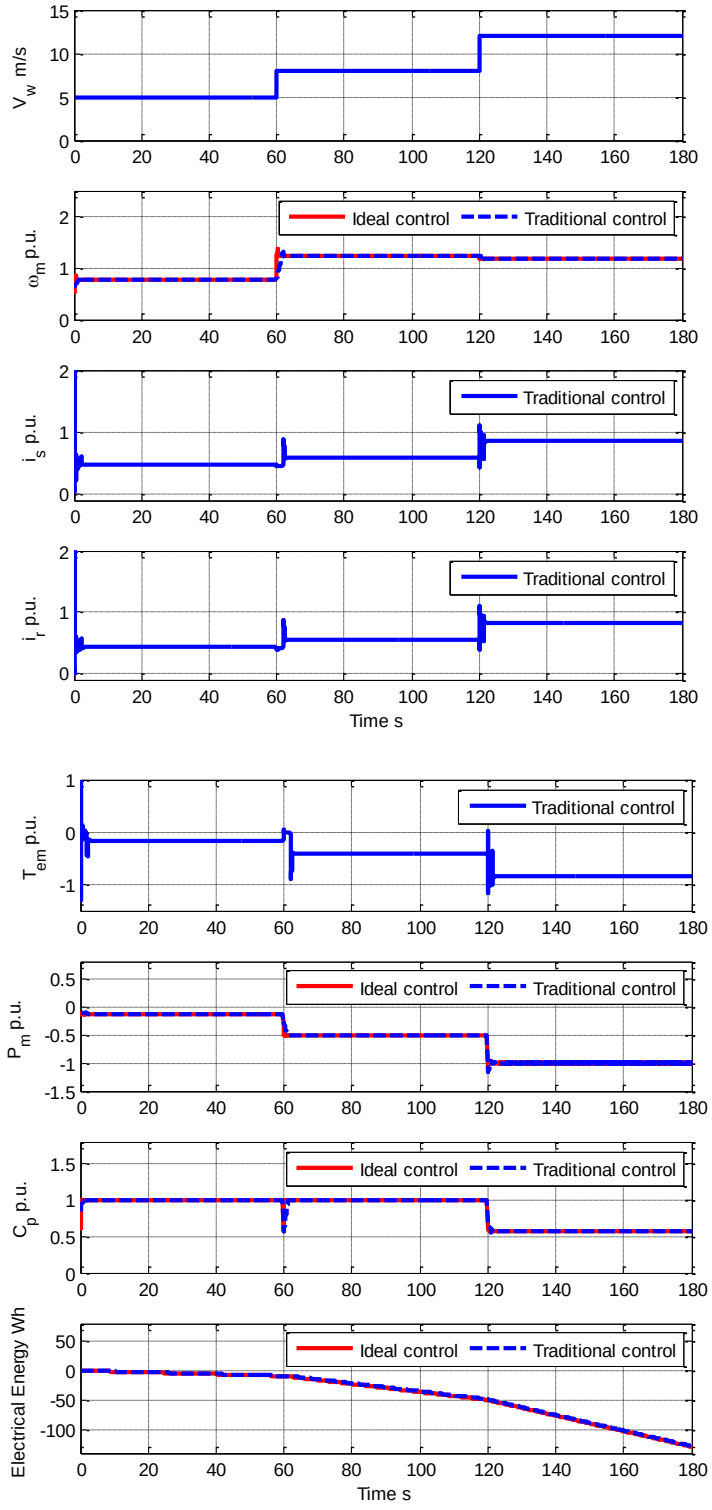

Figure 4.3: WECS performance for step-changing wind speed with no error on the estimation of air density and λ_i

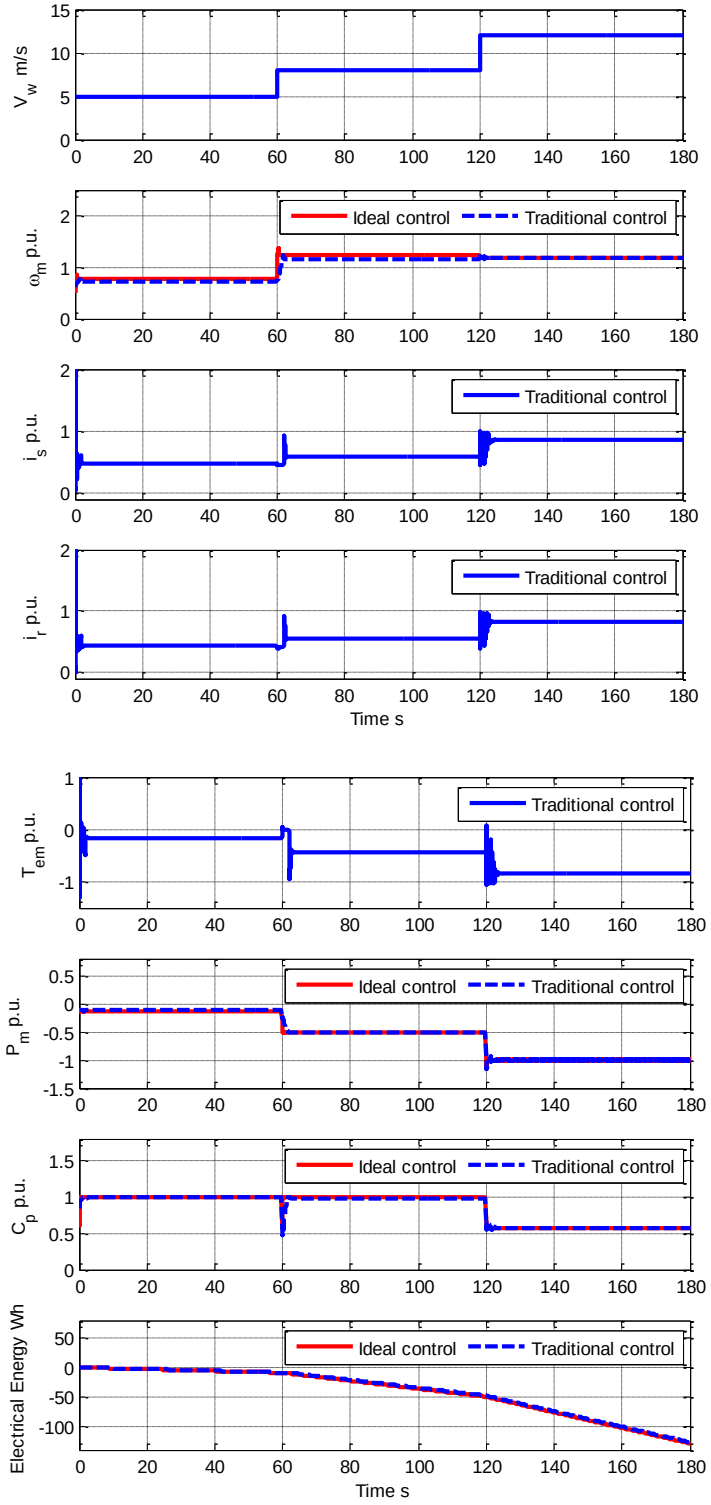

Figure 4.4: WECS performance for step-changing wind speed with an error of +20% on the estimation of air density

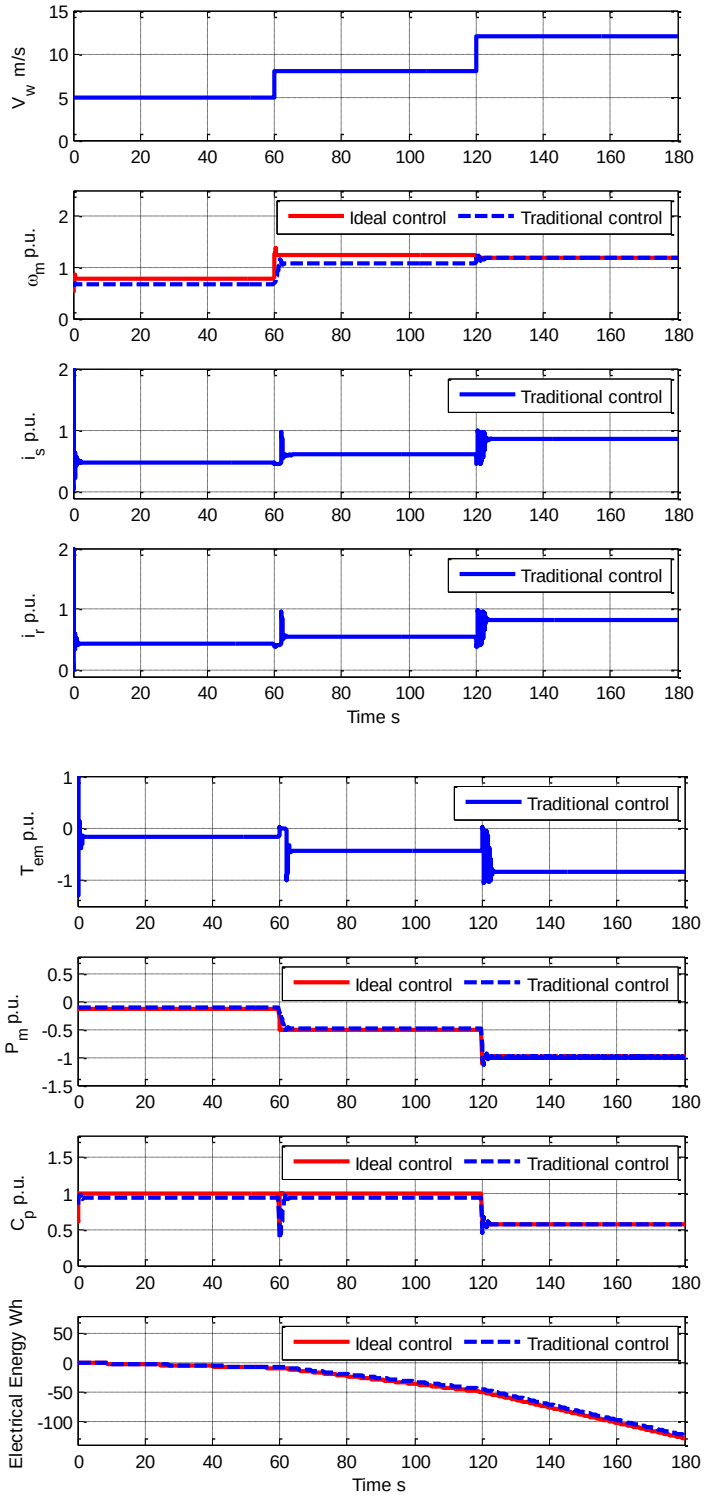

Figure 4.5: WECS performance for step-changing wind speed with an error of +20% on the estimation of λ_i

Figure 4.3 to 4.5 show the dynamic response of the system with a step-change of the wind speed from 5 to 8 m/s and then from 8 to 12 m/s produced by the ideal control applying small the inertia as 0.024 kg.m^2 and the traditional control applying inertia of the turbine referred to generator side and inertia of the DFIG as 0.304 kg.m^2. Figure 4.3 to 4.5 report the following diagrams: the wind speed, V_w, the generator speed, ω_m, the magnitude of the stator current, i_s, the magnitude of the rotor current, i_r, the electromagnetic torque, T_{em}, the mechanical power extracted from the turbine, P_m, the power coefficient, C_p and the generated electrical energy.

Remark: the start-up state of the wind turbine system has been simplified in these simulations by ignoring the stator overcurrent occurring during the first few cycles. This is because the verification of the start-up of the generator is beyond the scope of this thesis. A practical DFIG would include a correct start-up procedure using one of the various methods useful to reduce the initial overcurrent, i.e. connection of a stator reactor, reduction of the stator voltage using a VARIAC or a TRIAC, etc.

Figure 4.3 shows the case with no errors. The PSF MPPT control generates speed references of 121.8 rad/s (0.775 p.u.) and 194.9 rad/s (1.241 p.u.) when the wind speed is 5 and 8 m/s, respectively. That corresponds to a maximum power coefficient, C_{pmax} of 0.48 (1 p.u.).The traditional power control has a slightly slower response than the ideal control due to the inertia of the wind turbine which T_{em} reaches to zero under acceleration for 2 seconds. When the wind speed changes from 8 to 12 m/s, the power limitation kicks in, as the wind speed is higher than the rated value of 10 m/s. The traditional power control generates speed references of 194.9 rad/s (1.241 p.u.) and

184.9 rad/s (1.177 p.u.). The last speed reference corresponds to the rated power point of the wind turbine, i.e., 5 kW.

As the limitation of current and voltage references are provided for PI controller in section 3.3.5, the current of the rotor converter and the stator winding have been plotted to verify that they do not exceed its nominal value.

The delay of the controller in reaching the optimal speed leads to a reduction of the electrical energy generated compared to the ideal control. In the case of perfect knowledge of the aerodynamic parameters, the energy generated is 0.85% less than the ideal case.

Figure 4.4 shows the dynamic response of the same 5-kW WECS when the estimation of the air density has an error of +20% of its nominal value, while λ_i has no error. Considering the error, the real k_{opt} changes from the nominal value of 0.1186 to 0.1418 (+20%). Therefore the PSF MPPT cannot generate the correct speed reference when the wind speed is below the rated value. Specifically, the actual value of C_p achievable by the controller achieves decreases to 0.475. Therefore, the electrical energy generated when the speed is lower than the rated value decreases by 1.48% compared to the ideal power control. When wind speed is above the rated wind speed, the traditional power control generates the correct speed reference that gives the rated mechanical power by the active stall control. The rated power, P_{m_rated} and observed power, P_{m_obs} are used in the power limitation process. The air density does not affect power control in this region and, hence, there is no reduction of the energy generated.

Figure 4.5 show again the dynamic response when the estimation of λ_i has an error of +20% of its nominal value, while the air density has no error. In this case, k_{opt} changes from 0.1186 to 0.1750 (+47.55%). The PSF MPPT control cannot generate the correct speed reference also for this situation and the power coefficient, C_p, decreases to 0.45. Therefore, the electrical energy when the wind speed is below the rated value is 3.88% lower than the ideal control. The traditional power control can still generate the correct speed reference when the wind speed is above the rated value, as the active stall regulation is not affected by the estimation of λ_i.

Under the assumptions of the DFIG operation in this thesis, the electromagnetic torque, T_{em}, the mechanical power extracted from the turbine, P_m, and the generated electrical energy are given negative sign to define the operation of the machine as a generator in simulation results. The machine receives the mechanical power through the shaft and supplies the electrical enregy to the power grid.

The second simulation shows the performance of PSF MPPT control for realistic wind speed profiles with uncertain aerodynamic conditions. In this thesis, wind speed model is used to generate different real-wind speed profiles for the wind turbine which can generate easily by simulation. The realistic wind speed model consists of a linear combination of a slowly varying mean value, $\bar{v}_w$, and a turbulent component composed of a finite number of sinusoidal terms within the typical frequency range of fast wind variations [103]. These sinusoidal terms are characterised by amplitude, A_i, at each discrete frequency, ω_i, and by random phases, ϕ_i [57]:

$$v_w(t) = \bar{v}_w + \sum_{i=0}^{N} A_i \cos(\omega_i t + \phi_i) \tag{4.2}$$

The amplitudes, A_i, are based on a spectral density function, $S(\omega_i)$, which is fitted to the wind turbulence. In this thesis, the von Karman distribution [57],[104] is used to express the spectral density function with the following equation:

$$S(\omega_i) = \frac{0.475\sigma^2 (L/\bar{v}_w)}{[1+(\omega_i L/\bar{v}_w)^2]^{5/6}} \tag{4.3}$$

where $\bar{v}_w$ is the mean wind speed, L is the roughness of the surrounding landscape and σ is the standard deviation of the wind speed distribution. All parameters can be obtained from on-site measured data to calibrate the spectral density function. In this thesis, L = 180 and σ = 0.25* $\bar{v}_w$ have chosen for application in this thesis [57]. Hence, the amplitudes A_i can be calculated for each discrete frequency ω_i from the area under the spectral density function over a certain interval of frequency, for example every 0.0065 rad/s (0 to 6.5 rad/s) [57]:

$$A_i(\omega_i) = \frac{2}{\pi}[\frac{1}{2}(S(\omega_i) + S(\omega_{i+1}))(\omega_{i+1} - \omega_i)]^{1/2} \tag{4.4}$$

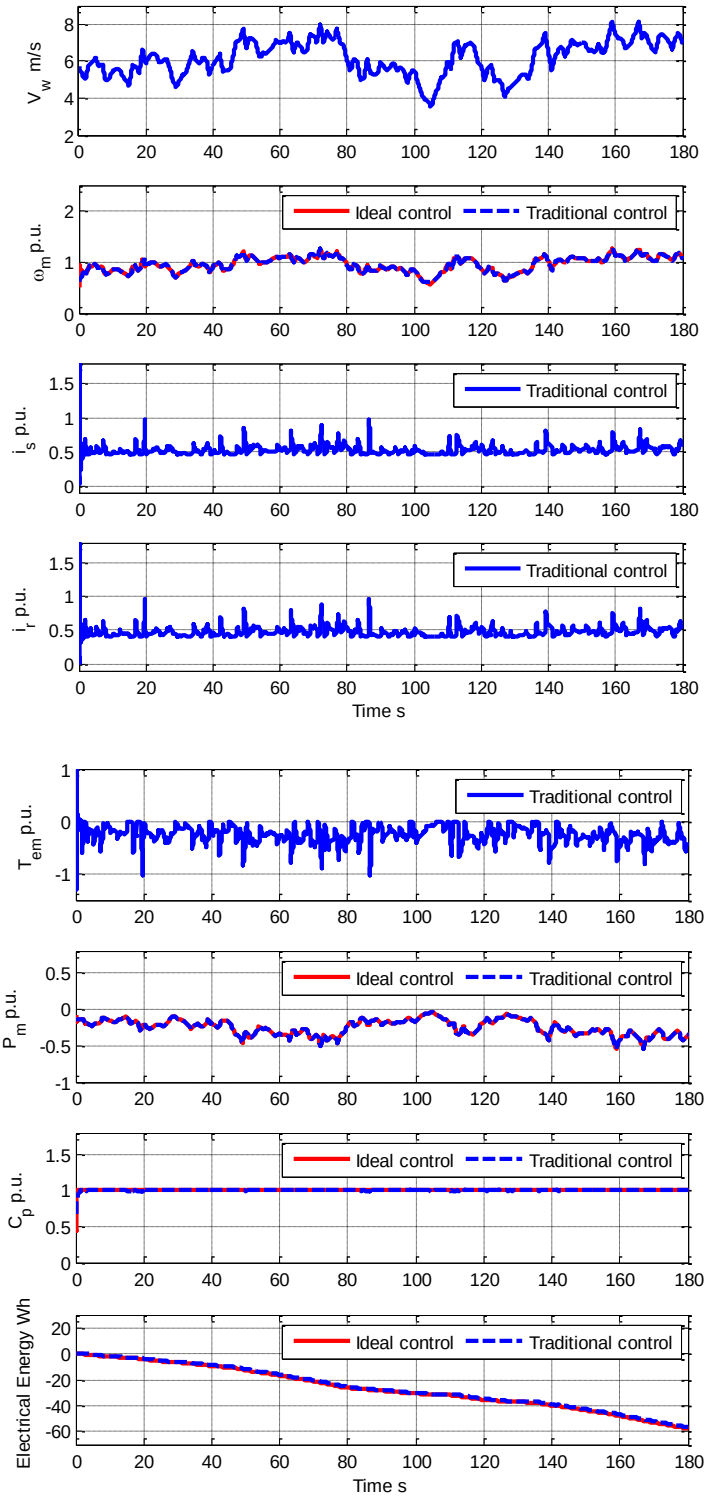

Figure 4.6: WECS performance for realistic wind speed of $\bar{v}_w$ = 6 m/s with no error on the estimation of air density and λ_i

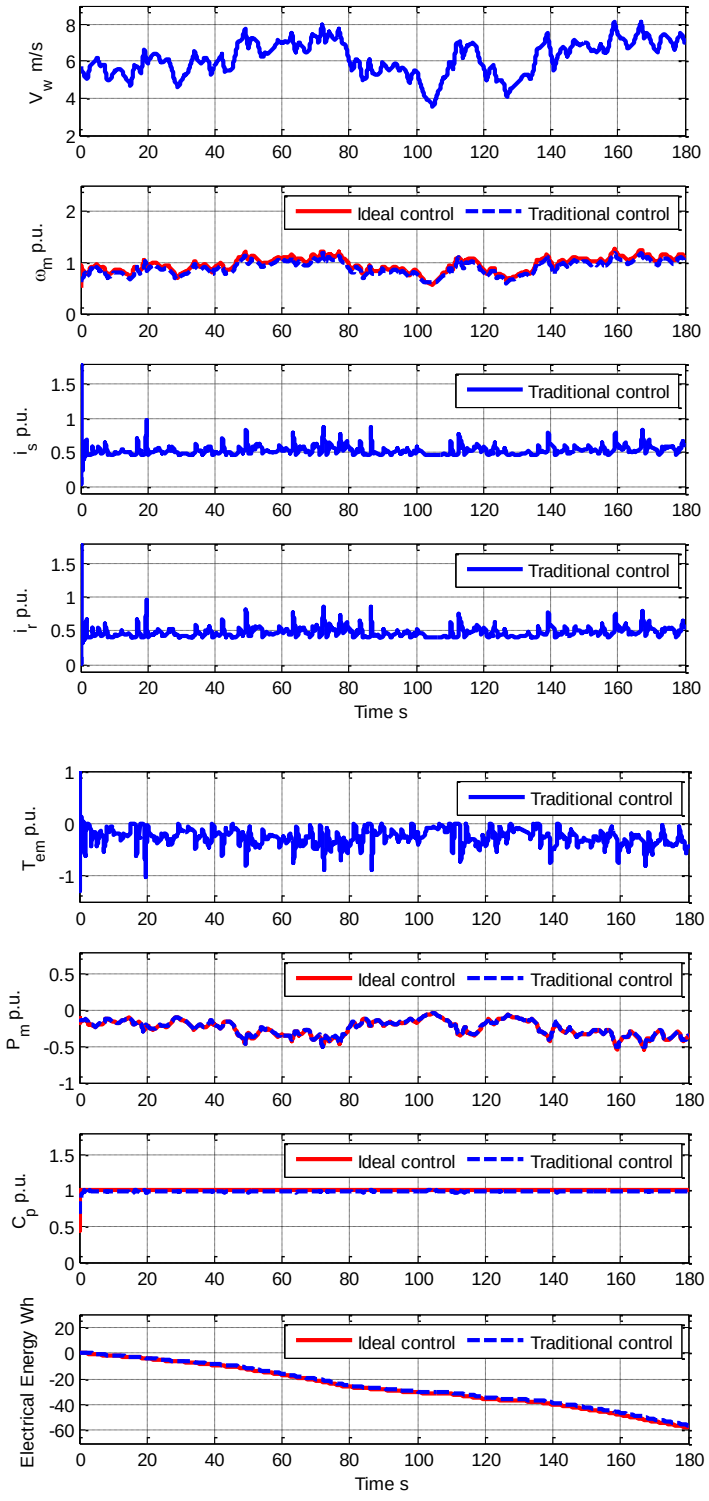

Figure 4.7: WECS performance for realistic wind speed of $\bar{v}_w$ = 6 m/s with an error of +20% on the estimation of air density

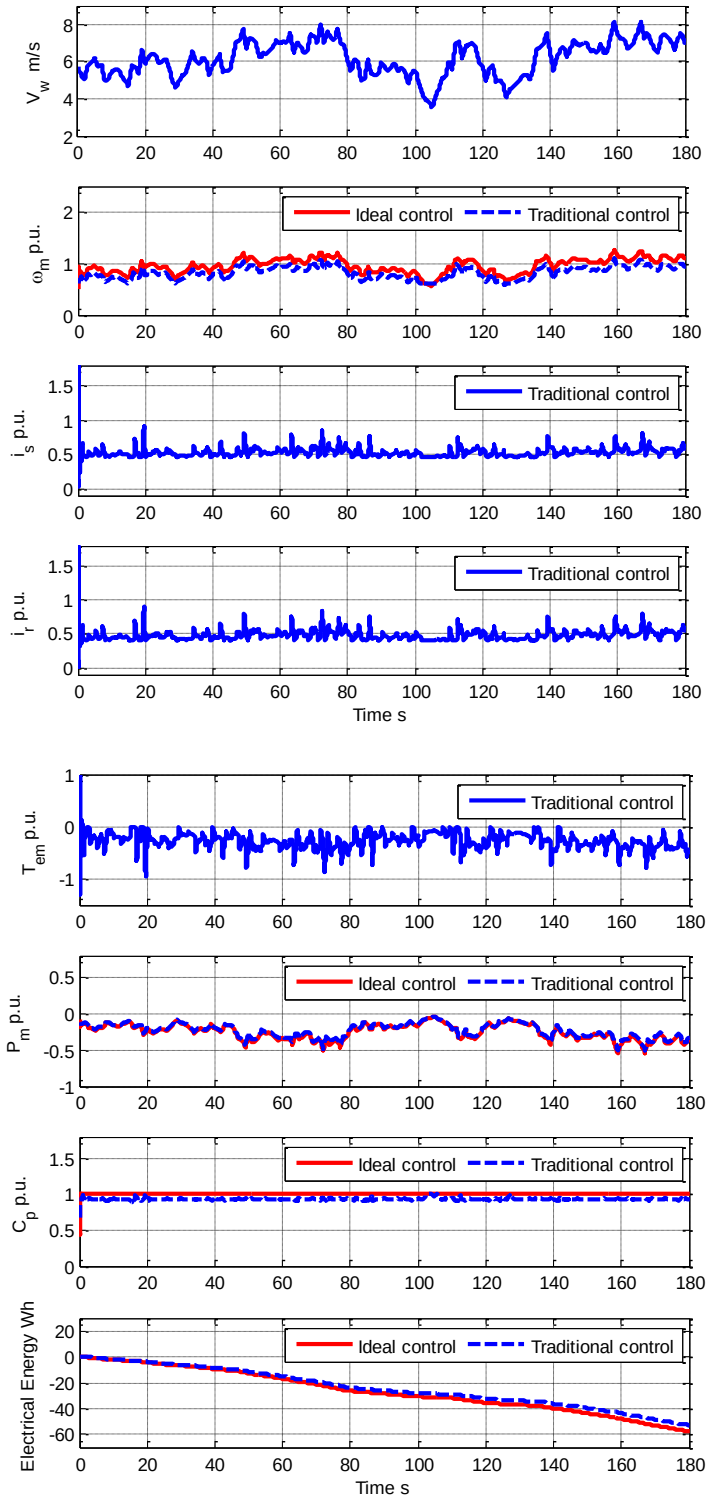

Figure 4.8: WECS performance for realistic wind speed of $\bar{v}_w$ = 6 m/s with an error of +20% on the estimation of λ_i

For the location selected, the average wind speed is $\bar{v}_w$ = 6 m/s. The simulations have been then repeated for the same types of uncertainties of the air density and λ_i and the results are shown in Figure 4.6 to 4.8. The diagrams in the simulations are the same as those of the previous figures.

Figure 4.6 shows the case where there is no error in the estimation of the parameter. The wind speed varies in practice between 4 and 8 m/s and has an average of $\bar{v}_w$ = 6 m/s.

The PSF MPPT control does not have difficulty in tracking the correct optimal rotational speed, and the small difference is only due to the inertia of the wind turbine.

Figure 4.7 shows the dynamic response when the estimated air density is +20% larger than its nominal value, while λ_i is correctly identified. As the maximum estimated power coefficient is lower than the actual one, the PSF MPPT control generated 1.83 Wh less than the ideal control (-3.16%).

Figure 4.8 shows the dynamic response when the estimation on λ_i has an error of +20% of its nominal value, while the air density has no error. Consequently, the correct speed reference cannot be identified and, as the difference is more substantial, the PSF MPPT control generated 5.02 Wh less electrical energy than the ideal control (-8.68%).

The impact of the error in the estimation of the air density and λ_i on the PSF MPPT efficiency has been analysed by Table 4.1 and 4.2, respectively. The analysis of the tables reveals that the error on the estimation of λ_i has a much larger impact than the

error on the air density. Due to the non-linearity of the power curve, the loss of energy is not symmetric for a positive and negative error.

Table 4.1: Electrical energy decrease in WECS with an error in the estimation of ρ for a simulation of 3 minutes, with $\bar{v}_w$ = 6 m/s (comparison with ideal control: -57.82 Wh.)

Estimation error of ρ from its nominal value	**k_{opt} estimation**	**Electrical energy (Wh)**	**Loss energy of PSF MPPT**
-20%	0.0945	-55.75	-3.58%
-10%	0.1063	-56.50	-2.28%
0%	0.1186	-56.74	-1.87%
+10%	0.1300	-56.55	-2.20%
+20%	0.1418	-55.99	-3.16%

Table 4.2: Electrical energy decrease in WECS with an error in the estimation of λ_i for a simulation of 3 minutes, with $\bar{v}_w$ = 6 m/s (comparison with ideal control: -57.82 Wh.)

Estimation error of λ_i from its nominal value	**k_{opt} estimation**	**Electrical energy (Wh)**	**Loss energy of PSF MPPT**
-20%	0.0754	-53.17	-8.04%
-10%	0.0952	-55.81	-3.48%
0%	0.1186	-56.74	-1.87%
+10%	0.1447	-55.80	-3.49%
+20%	0.1750	-52.80	-8.68%

4.3 Fuzzy Control based SIRM for VSFP Wind Turbines

Fuzzy logic control has received significant attention over the last few years for WECS due to its capabilities of effectively controlling non-linear systems, providing robust control against parameter uncertainties and providing fast-tracking [105]. In [50], an MPPT algorithm is built upon a fuzzy controller where the change of power and rotational speed are the two inputs used to construct the set of 25 fuzzy rules for generating the desired rotational speed step change. This fuzzy-based MPPT relies on P&O MPPT to find operating point given the maximum output power of the turbine below rated wind speed. However, the disadvantage of this MPPT is that its performance is decreased during rapid wind variation [21],[58] because it maybe gave the wrong direction of speed reference to the maximum power point.

In [18], PSF MPPT control and active stall regulation for a VSFP wind turbine are built upon a fuzzy logic controller having six inputs to create the set of 140 fuzzy rules for generating the reference torque step change. However, the results of these papers have shown that the presence of a large number of fuzzy rules leads to slow dynamic response of the controller due to the high computational burden of the four stages present in a fuzzy algorithm [106]. Also, its MPPT efficiency is decreased under the wind turbine parameter uncertainties as shown in the simulation results above.

The hybrid MPPT combining between PSF MPPT and P&O MPPT has been used to solve the two problems above. The advantage of one MPPT overcomes the disadvantages of the other as mentioned in Chapter 2.

For ambition of thesis, the hybrid MPPT control and active stall control for a VSFP wind turbine are built upon a fuzzy logic control. As a result, the number of input of the fuzzy system is increased. For a conventional fuzzy inference model, all inputs are placed into the antecedent part of each fuzzy rule. If number of input variables of the fuzzy controller is increased, the number of fuzzy rules also exponentially increase which lead to the problem of designing the fuzzy rules in the large system [61].

A SIRMs connected fuzzy inference model has been used to overcome the drawback of the conventional fuzzy inference model. Each input of the new fuzzy controller consists of a SIRM and a dynamic importance degree (DID). When each SIRM required only one input, each fuzzy rule in SIRM uses one input in the antecedent part. As a result, the number of fuzzy rules in the proposed fuzzy controller is strongly reduced and design of the fuzzy rules becomes easy [61],[63],[64]. The example had shown in chapter 2 already. Also, the dynamic importance degree is used to indicate the significance of each input and changes automatically with control conditions.

4.3.1 SIRMs Connected Fuzzy Inference Model

In this subsection, the fuzzy controller based on a SIRMs connected fuzzy inference model is explained in order to understand the basic concepts of the control.

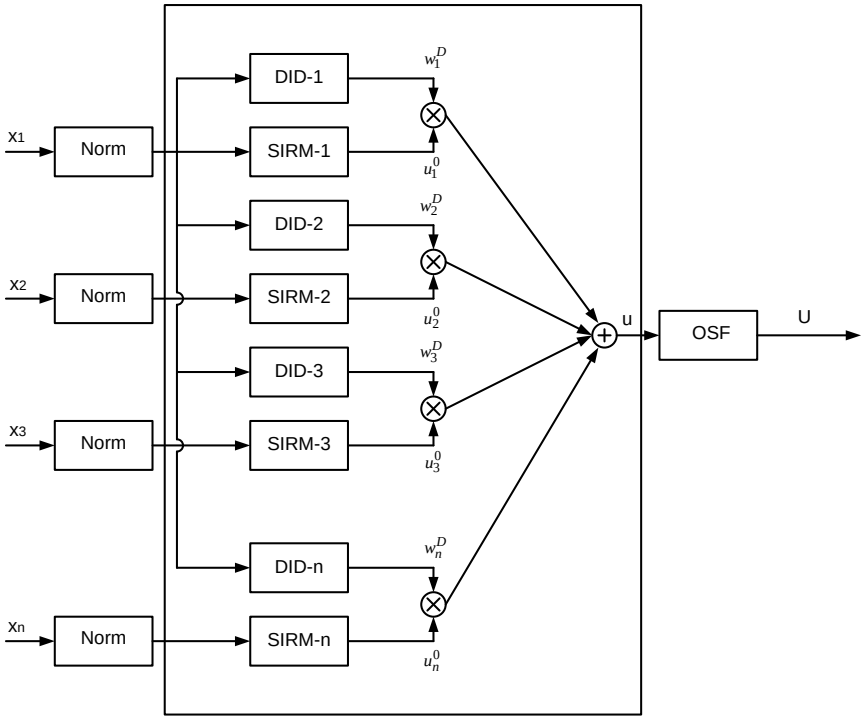

Figure 4.9: SIRM fuzzy control structure

The fuzzy controller based on the SIRM connected fuzzy inference model is a system with *n* input variables and one output variable, as shown by the block diagram in Figure 4.9. Each input, x_1, $x_{2\ldots,}$ x_n, of the fuzzy controller based SIRM is normalised in a range of [-1.0, +1.0] called the universe of discourse by their scaling factor and feed to the SIRM of each input, SIRM-1, SIRM-2…, SIRM-*n*. The fuzzy rules of each SIRM are expressed as follows [107]:

$$\begin{aligned} &SIRM-1 \ : \{R_1^j : if\ x_1 = A_1^j\ then\ u_1 = C_1^j\}_{j=1}^{m_1} \\ &SIRM-2 \ : \{R_2^j : if\ x_2 = A_2^j\ then\ u_2 = C_2^j\}_{j=1}^{m_2} \\ &SIRM-n \ : \{R_n^j : if\ x_n = A_n^j\ then\ u_n = C_n^j\}_{j=1}^{m_n} \end{aligned} \tag{4.5}$$

where *SIRM-i* is the SIRM of i^{th} input variable, R_i^j is the j^{th} fuzzy rule in the SIRM-i, x_i is the i^{th} input variable put into the antecedent part of the SIRM, u_i is the i^{th} output variable as consequent part of fuzzy rules, A_i^j is the membership functions of x_i in the j^{th} rule of the SIRM-i, C_i^j is the membership function of u_i in the j^{th} rule of the SIRM-i. Further, $i = 1, 2, \ldots, n$ is the index number of the SIRMs, and $j = 1, 2, \ldots, m_i$ is the index number of the rules in the SIRM-i [64].

The fuzzy inference result, u_i^0, of the consequent variable, u_i, is calculated by using the simplified fuzzy reasoning method [108]. Since the membership function of the consequent variable is defined as a singleton, the expression of the fuzzy inference result of each the SIRM is given by [61]:

$$u_i^0 = \frac{\sum_{j=1}^{m_i} A_i^j(x_i) C_i^j}{\sum_{j=1}^{m_i} A_i^j(x_i)} \tag{4.6}$$

Generally, each input variable has a different impact on the system performance. Some input variables strongly contribute to it while the others are weakly correlated. Therefore, if all variable are considered of the same importance, the control may lead to reduced performance of the system [61],[64]. To avoid that, each input variable of a SIRM based fuzzy control is defined with a different weight according to the experience of the control designer. A dynamic importance degree (DID), w_i^D, is introduced to determine the significance level of each input variable according to its contribution to

the system performance. The dynamic importance degree of each input variable can be expressed as [64]:

$$w_i^D = w_i + B_i \times \Delta w_i^0 \tag{4.7}$$

where w_i is called the base value: $B_i \times \Delta w_i^0$ is called dynamic value: B_i is the breadth value and Δw_i^0 is the fuzzy inference result from the dynamic variable Δw_i. The base value w_i and the breadth value B_i are constant values derived from experimental tests. The dynamic variable Δw_i can be obtained by fuzzy rules defined like SIRM in (4.5).

The output signal, u, of the SIRM based fuzzy control is obtained from the summation of the products of the fuzzy inference result of each SIRM and the dynamic importance degree [64]:

$$u = \sum_{i=1}^{n} w_i^D u_i^0 \tag{4.8}$$

where n is number of the input variables. The control signal in (4.8) operates on the range of the universe of discourse which does not necessarily match the practical range of the inputs to control the real system. An output scale factor (OSF) is used to adjust the magnitude of the output signals to levels compatible with the real system.

It can be summarised that each fuzzy rule in the SIRM and DID corresponds to an input on a "IF-THEN" form.

4.3.2 SIRM Fuzzy Controller Design for VSFP Wind Turbines

The SIRM-based fuzzy control algorithm has been applied to the WECS with DFIG to optimise the output power in the presence of uncertainties of wind turbine parameters and during rapid wind variation.

The fuzzy controller based on SIRM algorithm is used to generate the optimal speed reference to maximise the extracted power of the wind turbine in the full range of wind speed.

4.3.2.1 Maximum power point tracking zone: At below-rated wind speeds, the hybrid MPPT strategy structure consists of the PSF and adaptive P&O MPPT is applied for tracking the maximum output power of the wind turbine from the mechanical power versus generator speed characteristics.

The PSF MPPT strategy requires the knowledge of the wind turbine especially C_{pmax} and λ_{opt} to calculate the generator speed reference as follows:

$$P_{m\_\max} = \frac{1}{2}\rho\pi R^5 \frac{C_{p\max}}{\lambda_{opt}^3}\omega_m^3 = K_{opt}\omega_m^3 \tag{4.9}$$

$$\omega_{m\_ref}^{be} = \sqrt[3]{\frac{P_m}{K_{opt}}} \tag{4.10}$$

The adaptive P&O MPPT strategy uses the perturb and observe method to track the maximum power point without the knowledge of the wind turbine characteristics and the presence of a wind speed sensor. The input variables of the adaptive P&O MPPT are

the generator speed change, $\Delta\omega_m$, and the mechanical power change, ΔP_m; the output variable is the reference speed change, $\Delta\omega_{m\_ref}$ at the k^{th} iteration, as shown in (4.11), (4.12), and (4.13). The maximum power point of the adaptive P&O is identified by the derivative of the $\Delta P_m/\Delta\omega_m = 0$. The speed reference is updated by (4.14):

$$\Delta\omega_m(k) = \omega_m(k) - \omega_m(k-1) \tag{4.11}$$

$$\Delta P_m(k) = P_m(k) - P_m(k-1) \tag{4.12}$$

$$\Delta\omega_{m\_ref}^{be}(k) = M\frac{\Delta P_m(k)}{\Delta\omega_m(k)} \tag{4.13}$$

$$\omega_{m\_ref}^{be}(k+1) = \omega_{m\_ref}^{be}(k) + \Delta\omega_{m\_ref}^{be}(k) \tag{4.14}$$

where M is the positive definite gain. In the proposed SIRM fuzzy model, the four input variables are the error between the speed reference of the PSF MPPT and the actual speed, called x_1, the change of x_1, called x_2, the derivative of $\Delta P_m/\Delta\omega_m$, called x_3, and the change of x_3, called x_4. The dynamic importance degree (DID) is used to define the relative significance of the PSF MPPT and the adaptive P&O MPPT, which automatically change depending on the actual situation. The main objective of the design of the dynamic importance degree (DID) is to set priority the advantage of the P&O MPPT to find the maximum output power without any knowledge of the system, with the advantage of PSF MPPT to correct the direction of change of the rotational speed for a sudden change of the wind speed.

4.3.2.2 Rated power point tracking zone: At above-rated wind speed, the active stall control structure is used to limit the mechanical power of the wind turbine at its rated value. The speed reference in rated power control zone can be calculated by:

$$\omega_{m\_ref}^{ab} = \frac{P_{m\_rated}}{\hat{T}_m} \tag{4.15}$$

The fuzzy controller for limiting the output power of the wind turbine at its rated value is also based on the SIRMs connected fuzzy inference model. The two input variables are the error between the speed reference of the active stall control and actual speed, called x_5, and the change of x_5, called x_6.

The last input of the fuzzy system is the observed mechanical power, $\hat{P}_m$ called x_7 as shown in Figure 2.23. This input is used as the dynamic importance degree (DID) is to set significance between the hybrid MPPT control below rated wind speed zone and the active stall control above rated wind speed zone.

4.3.2.3 Fuzzy controller based SIRMs rules: Considering that the two main objectives of the control design are the maximum power tracking at below-rated wind speeds and the rated power tracking at above-rated wind speeds, seven input variables of the fuzzy controller based on the SIRMs are:

- $x_1(k)$ is the error between the speed reference of the PSF MPPT from (4.10) and the actual speed at the sampling time k defined in (4.16). The mechanical power, P_m, is derived by the observer.

$$x_1(k) = \omega_{m\_ref}^{be}(k) - \omega_m(k) \tag{4.16}$$

- $x_2(k)$ is the variation of the error $x_1(k)$, and it is defined as:

$$x_2(k) = x_1(k) - x_1(k-1) \tag{4.17}$$

- $x_3(k)$ is a derivative of the mechanical power with respect to ω_m and, according to the adaptive P&O MPPT algorithm, it is defined as:

$$x_3(k) = \frac{P_m(k) - P_m(k-1)}{\omega_m(k) - \omega_m(k-1)} \tag{4.18}$$

- $x_4(k)$ is a variation of the error $x_3(k)$, and it is defined as:

$$x_4(k) = x_3(k) - x_3(k-1) \tag{4.19}$$

- $x_5(k)$ is an error between the speed reference of the rated power control zone, given by (4.15), and the actual speed and it is defined as:

$$x_5(k) = \omega_{m\_ref}^{ab}(k) - \omega_m(k) \tag{4.20}$$

- $x_6(k)$ is the variation of the error $x_5(k)$, and it is defined as:

$$x_6(k) = x_5(k) - x_5(k-1) \tag{4.21}$$

- $x_7(k)$ is the mechanical power which is received by an observer as defined by:

$$x_7(k) = \hat{P}_m \tag{4.22}$$

The output variable is the change of speed reference, $\Delta\omega_{m\_ref}(k)$. The fuzzy rules of the SIRM of each input variable can be summarised according to Table 4.3. For the fuzzy rules of each SIRM, a corresponding input variable $x_i(k)$ (i = 1, 2, 3, 4, 5, 6) is placed into the antecedent part and $\Delta\omega_{im\_ref}(k)$ is its consequent part. The membership functions of input are defined as triangular and trapezoidal membership functions in the range of [-1.0, +1.0]. The fuzzy sets of input are defined in linguistic terms: negative big (NB), negative small (NS), zero (ZE), positive small (PS) and positive big (PB) as shown in Figure 4.10. The consequent variables of fuzzy rules are defined as singleton membership functions, which is suitable to the simplified fuzzy reasoning inference as shown in Figure 4.11. The membership function, μ of each fuzzy set is between 0 to 1.

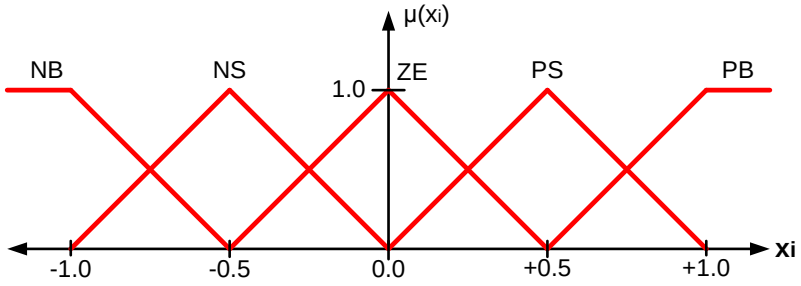

Figure 4.10: Inputs membership functions of SIRM

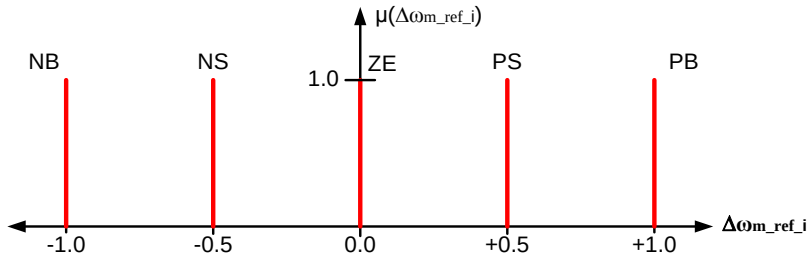

Figure 4.11: Output membership function of SIRM

Table 4.3: SIRM of each input variable

Antecedent Variable $x_i(k)$	**Consequent Variable** $\Delta\omega_{m\_ref\_i}$
NB	-1.0
NS	-0.5
ZE	0.0
PS	0.5
PB	1.0

Therefore, the fuzzy rules of six SIRMs which are defined by the inputs and output membership functions in Figure 4.10 and 4.11 can be expressed as follows:

SIRM-1: Rule 1 IF x_1 = NB THEN $\Delta\omega_{m\_ref\_1}$ = -1.0

Rule 2 IF x_1 = NS THEN $\Delta\omega_{m\_ref\_1}$ = -0.5

Rule 3 IF x_1 = ZE THEN $\Delta\omega_{m\_ref\_1}$ = 0.0

Rule 4 IF x_1 = PS THEN $\Delta\omega_{m\_ref\_1}$ = +0.5

Rule 5 IF x_1 = PB THEN $\Delta\omega_{m\_ref\_1}$ = +1.0

SIRM-2: Rule 6 IF x_2 = NB THEN $\Delta\omega_{m\_ref\_2}$ = -1.0

Rule 7 IF x_2 = NS THEN $\Delta\omega_{m\_ref\_2}$ = -0.5

Rule 8 IF x_2 = ZE THEN $\Delta\omega_{m\_ref\_2}$ = 0.0

Rule 9 IF x_2 = PS THEN $\Delta\omega_{m\_ref\_2}$ = +0.5

Rule 10 IF x_2 = PB THEN $\Delta\omega_{m\_ref\_2}$ = +1.0

SIRM-3:	Rule 11	IF x_3 = NB	THEN	$\Delta\omega_{m\_ref\_3}$ = -1.0
	Rule 12	IF x_3 = NS	THEN	$\Delta\omega_{m\_ref\_3}$ = -0.5
	Rule 13	IF x_3 = ZE	THEN	$\Delta\omega_{m\_ref\_3}$ = 0.0
	Rule 14	IF x_3 = PS	THEN	$\Delta\omega_{m\_ref\_3}$ = +0.5
	Rule 15	IF x_3 = PB	THEN	$\Delta\omega_{m\_ref\_3}$ = +1.0
SIRM-4:	Rule 16	IF x_4 = NB	THEN	$\Delta\omega_{m\_ref\_4}$ = -1.0
	Rule 17	IF x_4 = NS	THEN	$\Delta\omega_{m\_ref\_4}$ = -0.5
	Rule 18	IF x_4 = ZE	THEN	$\Delta\omega_{m\_ref\_4}$ = 0.0
	Rule 19	IF x_4 = PS	THEN	$\Delta\omega_{m\_ref\_4}$ = +0.5
	Rule 20	IF x_4 = PB	THEN	$\Delta\omega_{m\_ref\_4}$ = +1.0
SIRM-5:	Rule 21	IF x_5 = NB	THEN	$\Delta\omega_{m\_ref\_5}$ = -1.0
	Rule 22	IF x_5 = NS	THEN	$\Delta\omega_{m\_ref\_5}$ = -0.5
	Rule 23	IF x_5 = ZE	THEN	$\Delta\omega_{m\_ref\_5}$ = 0.0
	Rule 24	IF x_5 = PS	THEN	$\Delta\omega_{m\_ref\_5}$ = +0.5
	Rule 25	IF x_5 = PB	THEN	$\Delta\omega_{m\_ref\_5}$ = +1.0
SIRM-6:	Rule 26	IF x_6 = NB	THEN	$\Delta\omega_{m\_ref\_6}$ = -1.0
	Rule 27	IF x_6 = NS	THEN	$\Delta\omega_{m\_ref\_6}$ = -0.5
	Rule 28	IF x_6 = ZE	THEN	$\Delta\omega_{m\_ref\_6}$ = 0.0
	Rule 29	IF x_6 = PS	THEN	$\Delta\omega_{m\_ref\_6}$ = +0.5
	Rule 30	IF x_6 = PB	THEN	$\Delta\omega_{m\_ref\_6}$ = +1.0

4.3.2.4 Dynamic importance degree: the optimal power control of VSFP wind turbine for full range of wind speed is controlled by using the SIRMs and DIDs in (4.8). The roles of the input variables are weighted according to the difference control situations to achieve a high dynamic performance of the control. The dynamic importance degree in (4.7) is applied with the SIRM to weight each input variable.

In the maximum power control zone, the PSF MPPT controller and P&O MPPT controller are used to tracking the maximum power operating point of the turbine. As appropriate hybrid MPPT control, if wind speed changes suddenly, the PSF MPPT should have a higher priority than the P&O MPPT to give the correct direction of speed reference, and the P&O MPPT should be done after the speed reference has moved towards the correct direction to search accurately for the maximum power point. The amplitude of the dynamic importance degrees is used to set significance each SIRM of PSF MPPT and P&O MPPT in different control conditions.

The priority order of the PSF MPPT controller relies on the two dynamic importance degrees of x_1 and x_2 and priority order of the P&O MPPT controller relies on the two dynamic importance degrees of x_3 and x_4. The dynamic variable Δw_i from (4.7) is derived from the fuzzy rules.

$|x_1|$ is used to set priority order of the hybrid MPPT controller. If $|x_1|$ is large, the PSF MPPT controller has domination over the P&O MPPT controller. The P&O MPPT controller has domination over the PSF MPPT controller when $|x_1|$ is small. The fuzzy rules of the dynamic variable Δw_i are considered only $|x_1|$ in the antecedent part. The membership functions of input of each dynamic variable (Δw_1, Δw_2, Δw_3, Δw_4) are

defined as trapezoidal membership functions in the range of [0.0, +1.0]. The fuzzy sets of input are defined in linguistic terms: PSF MPPT controller (PSF) and P&O MPPT controller (P&O) as shown in Figure 4.12. The consequent variables of fuzzy rules are defined as singleton membership functions as a real number: 0.0 and 1.0.

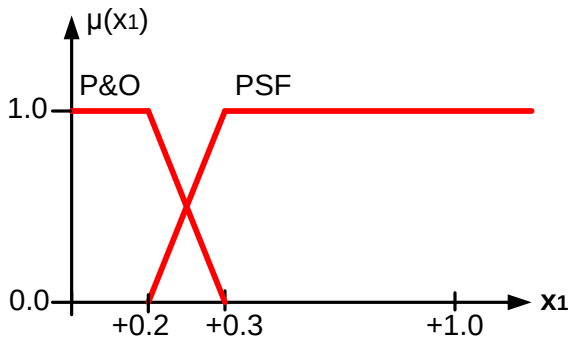

Figure 4.12: Inputs membership functions of dynamic importance degree

The fuzzy rules of the dynamic variable in dynamic importance degrees for x_1 and x_2 are shown in Table 4.4, and the fuzzy rules of the dynamic variable in dynamic importance degrees for x_3 and x_4 are shown in Table 4.5. When $|x_1|$ is big located in PSF fuzzy set in Figure 4.12, Δw_1, and Δw_2 is 1.0 and Δw_3 and Δw_4 is 0.0. As a result, the PSF MPPT controller has domination over the P&O MPPT controller and vice versa.

Table 4.4: Rules for dynamic variable of x_1 and x_2

Antecedent Variable $\|x_1\|$	**Consequent Variable** $\Delta w_i (i = 1,2)$
P&O	0.0
PSF	1.0

Table 4.5: Rules for dynamic variable of x_3 and x_4

Antecedent Variable $\|x_1\|$	**Consequent Variable** $\Delta w_i (i = 3,4)$
P&O	1.0
PSF	0.0

Therefore, the fuzzy rules of the dynamic variable according to Table 4.4 and 4.5 can be expressed as follows:

DID-1: Rule 1 IF $|x_1|$ = P&O THEN $\Delta w_1 = 0.0$

Rule 2 IF $|x_1|$ = PSF THEN $\Delta w_1 = 1.0$

DID-2: Rule 3 IF $|x_1|$ = P&O THEN $\Delta w_2 = 0.0$

Rule 4 IF $|x_1|$ = PSF THEN $\Delta w_2 = 1.0$

DID-3: Rule 5 IF $|x_1|$ = P&O THEN $\Delta w_3 = 1.0$

Rule 6 IF $|x_1|$ = PSF THEN $\Delta w_3 = 0.0$

DID-4: Rule 7 IF $|x_1|$ = P&O THEN $\Delta w_4 = 1.0$

Rule 8 IF $|x_1|$ = PSF THEN $\Delta w_4 = 0.0$

However, the dynamic variables provided by the fuzzy rules above are insufficient to complete the control priority of the hybrid MPPT. Each dynamic importance degree also consists of control parameters: base value and breadth. The optimal base values w_i and breadth values B_i can be tuned by trial and error and are reported in Table 4.6.

Table 4.6: Base value and breadth value of input variable

Input variable	Base value	Breadth value
x_1	0.0	1.00
x_2	0.0	0.45
x_3	0.0	1.00
x_4	0.0	0.40

When the mechanical power extracted from the wind turbine exceed the rated value, the power control of the wind turbine will switch from the hybrid MPPT controller to the active stall controller. The dynamic importance degree is required to define the weight of the input variable as x_1, x_2, x_3, x_4, x_5 and x_6 for exchange between the hybrid MPPT controller and the active stall controller.

$|x_7|$ is used to set priority order of the hybrid MPPT controller and active stall controller. If $|x_7|$ is small, the hybrid MPPT controller has domination over the active stall controller, giving the maximum power operating point of the speed reference. The active stall controller has domination over the hybrid MPPT controller when $|x_7|$ is large, giving the rated power operating point of the speed reference. The fuzzy rules of the dynamic variable are considered for $|x_7|$ in the antecedent part. The membership functions of input of each dynamic variable (Δw_{MPPT} and Δw_{STR}) are defined as trapezoidal membership functions in the range of [0.0, +1.0]. The fuzzy sets of input are defined in linguistic terms: hybrid MPPT controller (MPPT) and active stall controller (STR) as shown in Figure 4.13. The consequent variables of fuzzy rules are defined as singleton membership functions as real number: 0.0 and 1.0.

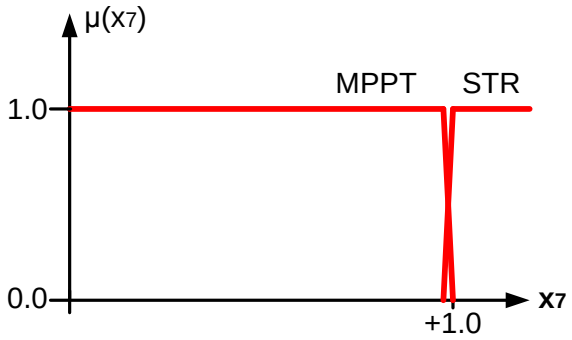

Figure 4.13: Inputs membership functions of dynamic importance degree

The fuzzy rules of the dynamic variable in dynamic importance degrees for x_1, x_2, x_3, and x_4 are shown in Table 4.7, and the fuzzy rules of the dynamic variable in dynamic importance degrees for x_5 and x_6 are shown in Table 4.8. When $|x_7|$ is less than 0.8 located in MPPT fuzzy set in Figure 4.13, Δw_{MPPT} is 1.0 and Δw_{STR} is 0.0. As a result, the hybrid MPPT controller has domination over the active stall controller and vice versa.

Table 4.7: Rules for dynamic variable of x_1, x_2, x_3 and x_4

Antecedent Variable $\|x_7\|$	**Consequent Variable** Δw_{MPPT}
MPPT	1.0
STR	0.0

Table 4.8: Rules for dynamic variable of x_5 and x_6

Antecedent Variable $\|x_7\|$	**Consequent Variable** Δw_{STR}
MPPT	0.0
STR	1.0

Therefore, the fuzzy rules of the dynamic variable, according to Table 4.7 and 4.8 can be expressed as follows:

DID-MPPT: Rule 1 IF $|x_7|$ = MPPT THEN $\Delta w_{MPPT} = 1.0$

Rule 2 IF $|x_7|$ = STR THEN $\Delta w_{MPPT} = 0.0$

DID-STR1: Rule 3 IF $|x_7|$ = MPPT THEN $\Delta w_{STR1} = 0.0$

Rule 4 IF $|x_7|$ = STR THEN $\Delta w_{STR1} = 1.0$

DID-STR2: Rule 5 IF $|x_7|$ = MPPT THEN $\Delta w_{STR2} = 0.0$

Rule 6 IF $|x_7|$ = STR THEN $\Delta w_{STR2} = 1.0$

The optimal base w_i values and breadth values B_i, tuned by trial and error according to [61], are given in Table 4.9.

Table 4.9: Base value and breadth value of input variable

Input variable	Base value	Breadth value
x_1,x_2,x_3, x_4	0.0	1.00
x_5	0.0	1.00
x_6	0.0	0.40

4.3.2.5 Fuzzy inference with simplified fuzzy reasoning method: the simplified fuzzy reasoning method has been proposed by [108]. This method is less complex than the product-sum-gravity method [109] as demonstrated in [108]. Initially, the fuzzy rules for the simplified fuzzy reasoning method can be obtained as follows:

Rule 1: A_1 and B_1 then z_1

Rule 2: A_2 and B_2 then z_2

…… (4.23)

Rule n: A_n and B_n then z_n

where A_i and B_i are the fuzzy sets of inputs placed into the antecedent part of fuzzy rules represented in triangular membership functions and z_i are fuzzy sets in the consequent part of fuzzy rules represented in singleton membership functions. x_0 and y_0 are the input variables in the antecedent part of fuzzy rules, and z_0 is the output derived from the proposed fuzzy inference result. The fuzzy inference with the simplified fuzzy reasoning method can be visually described by Figure 4.14. The degree of fitness, h_i, can be calculated by multiplying the degree of the membership function of x_0 in the fuzzy set, A_i $\mu_{A_i}(x_0)$ and the degree of the membership function of y_0 in the fuzzy set, B_i $\mu_{B_i}(y_0)$ as follows:

$$h_i = \mu_{A_i}(x_0) \cdot \mu_{B_i}(y_0) \tag{4.24}$$

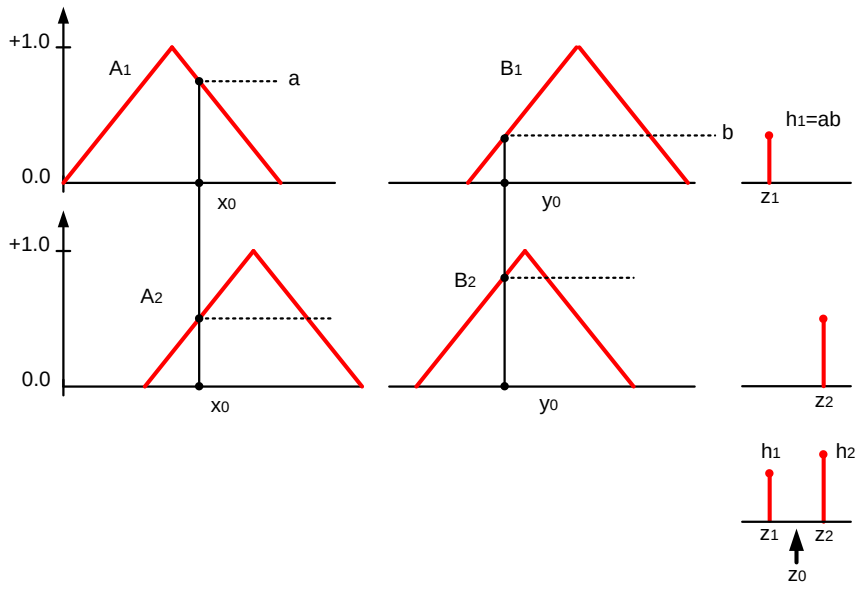

Figure 4.14: Simplified fuzzy reasoning method [108]

For n fuzzy rules, the proposed fuzzy inference result, z_0, is calculated by using the weighted average as [108]:

$$z_0 = \frac{h_1 \cdot z_1 + h_2 \cdot z_2 + ... + h_n \cdot z_n}{h_1 + h_2 + ... + h_n} \tag{4.25}$$

where h_1 is the degree of fitness derived from the input x_0 and y_0 from fuzzy rule 1 and z_1 is the output from fuzzy rule 1, and h_2,…, h_n and z_2,…, z_n are derived from rule 2 to rule n, respectively.

The simplified fuzzy reasoning method is employed for the fuzzy controller based the SIRM. For each SIRM, only one input variable is taken into the antecedent part of each fuzzy rule, therefore, the degree of fitness, h_i, is simply expressed as the degree of the membership function of the input each fuzzy rule. For example, the change of the speed reference, $\Delta\omega_{m\_ref\_1}$, of the SIRM-1 which x_1 is an only input variable can be expressed by five fuzzy rules indicated below:

SIRM-1:

Rule 1	IF	x_1 = NB	THEN	$\Delta\omega_{m\_ref\_1}$ = -1.0
Rule 2	IF	x_1 = NS	THEN	$\Delta\omega_{m\_ref\_1}$ = -0.5
Rule 3	IF	x_1 = ZE	THEN	$\Delta\omega_{m\_ref\_1}$ = -0.0
Rule 4	IF	x_1 = PS	THEN	$\Delta\omega_{m\_ref\_1}$ = +0.5
Rule 5	IF	x_1 = PB	THEN	$\Delta\omega_{m\_ref\_1}$ = +1.0

From fuzzy rules above, the fuzzy sets of input are defined in linguistic terms: negative big (NB), negative small (NS), zero (ZE), positive small (PS) and positive big (PB) with

triangular and trapezoidal membership functions. The output is defined by singleton membership functions as shown in Figure 4.15.

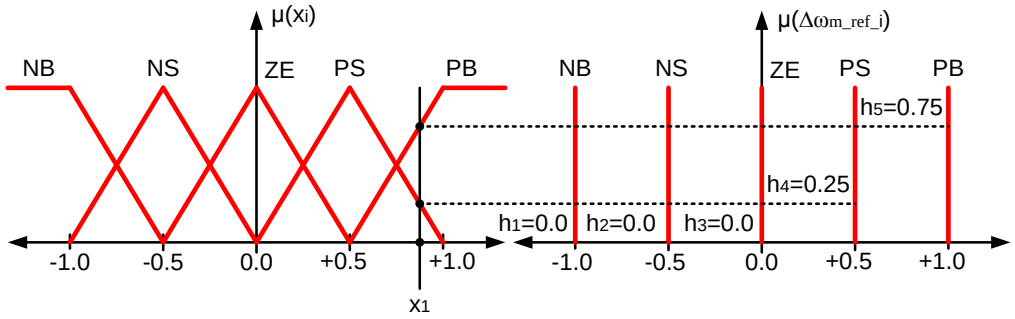

Figure 4.15: Simplified fuzzy reasoning method in SIRM

From Figure 4.15, when input x_1 is equal to 0.9, in rule 1, $\mu(x_1)$ of fuzzy set NB is 0, h_1 = 0.0, in rule 2 $\mu(x_1)$ of fuzzy set NS is 0, h_2 = 0.0, in rule 3, $\mu(x_1)$ of fuzzy set ZE is, h_3 = 0.0, in rule 4, $\mu(x_1)$ of fuzzy set PS is 0.25, h_4 = 0.25 and in rule 5 $\mu(x_1)$ of fuzzy set PB is 0.75, h_5 = 0.75. Thus, the final change of the speed reference, $\Delta\omega^0_{m\_ref\_1}$ is obtained by the fuzzy inference result with the simplified fuzzy reasoning from (4.25) as follows:

$$\Delta\omega^0_{m\_ref\_1} = \frac{h_1 \cdot \Delta\omega_{m\_ref1,1} + h_2 \cdot \Delta\omega_{m\_ref1,2} + h_3 \cdot \Delta\omega_{m\_ref1,3} + h_4 \cdot \Delta\omega_{m\_ref1,4} + h_5 \cdot \Delta\omega_{m\_ref1,5}}{h_1 + h_2 + h_3 + h_4 + h_5} \tag{4.26}$$

$$\Delta\omega^0_{m\_ref\_1} = \frac{0.0 \cdot (-1.0) + 0.0 \cdot (-0.5) + 0.0 \cdot (0.0) + 0.25 \cdot (0.5) + 0.75 \cdot (1.0)}{0.0 + 0.0 + 0.0 + 0.25 + 0.75} = 0.875$$

From (4.26), the fuzzy inference result obtained by the simplified fuzzy reasoning method is simple. Therefore, this fuzzy inference is employed in the fuzzy controller based on the SIRM for the simulations of this thesis.

4.4 Numerical Simulation of SIRM-Based Fuzzy Controller for VSFP Wind Turbines

4.4.1 Block Diagram of SIRM-Based Fuzzy Controller

The block diagram of the SIRM-based fuzzy controller for a VSFP wind turbine is shown in Figure 4.16. The voltages, currents and the generator speed are measured from the DFIG, then sent to the power observer to estimate the mechanical power extracted from the wind turbine. The seven inputs of the SIRM-based fuzzy controller have been discussed in the previous sections. All inputs fed to the SIRM-based fuzzy controller are normalised in a range of [-1.0,+1.0] by suitable scaling factor.

The input variables x_i (i = 1, 2, 3, 4, 5, 6) are fed to the SIRM-i block to generate the output variable $\Delta\omega_{m\_ref\_i}$ using a base of 30 rules. The absolute value of the input x_1 is fed to the dynamic importance degree block: DID-1, DID-2, DID-3, and DID-4 to generate the weight of x_1, x_2, x_3 and x_4 in the hybrid MPPT algorithm with a base of 8 rules. The absolute value of the input x_7 is fed to the dynamic importance degree block, MPPT, STR1, and STR2, to generate the weight of the input of the maximum power control as x_1, x_2, x_3 and x_4 and the rated power control as x_5 and x_6 with a base of 6 rules. Each output and weight of the SIRM block and the dynamic importance degree block are obtained by the simplified fuzzy reasoning method. The change of speed reference, $\Delta\omega_{m\_ref}$ of the fuzzy controller can be defined by (4.27) as the summation of the products of the output of each SIRM block and dynamic importance degree block. The output scaling factor (OSF) block is used to adjust the manipulated variable of the fuzzy

controller based SIRM to the actual speed reference. The updated speed reference, ω_{m_ref} can be calculated by (4.28). The speed reference generated by the SIRM-based fuzzy controller is limited at the nominal value, ω_{mN} as $1.5*\omega_s$.

$$\Delta\omega_{m\_ref}(k) = (u_1^0 \cdot w_1^D + u_2^0 \cdot w_2^D + u_3^0 \cdot w_3^D + u_4^D \cdot w_4^D) \cdot w_{MPPT}^D + (u_5^0 \cdot w_{STR1}^D + u_6^0 \cdot w_{STR2}^D) \quad (4.27)$$

$$\omega_{m\_ref}(k) = \omega_{m\_ref}(k-1) + \Delta\omega_{m\_ref}(k) \quad (4.28)$$

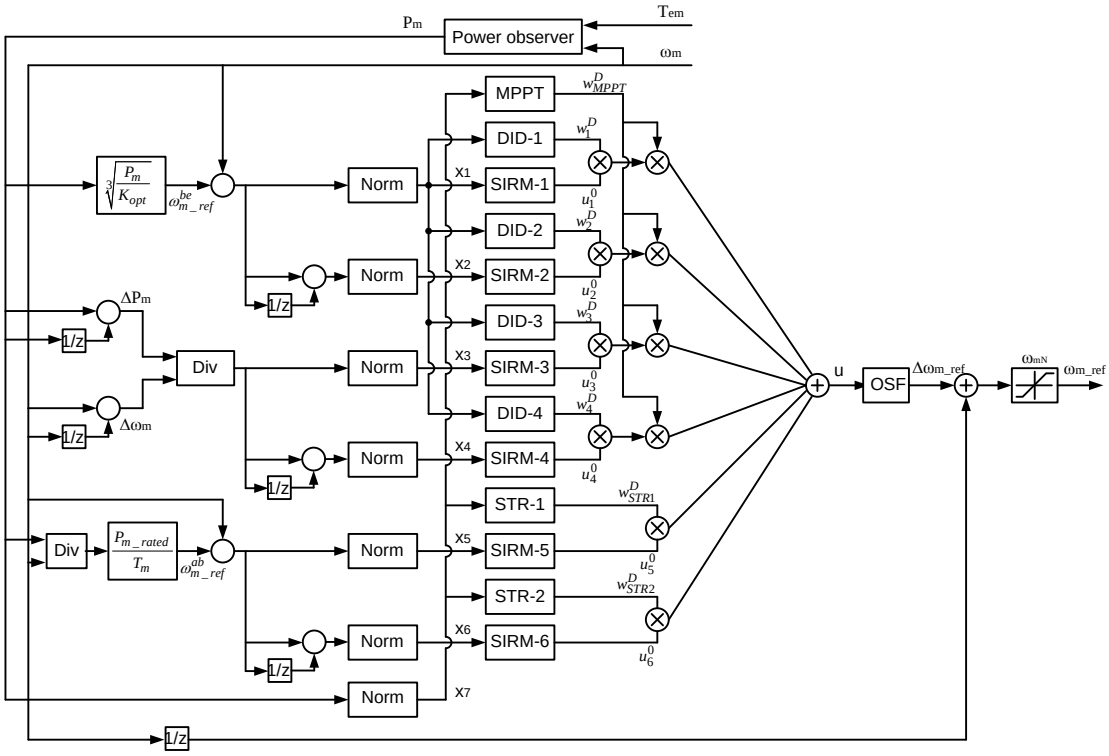

Figure 4.16: Block diagram of SIRM-based fuzzy controller for VSFP wind turbine

It can be seen that since each of SIRM block and dynamic importance degree block has only 1 input and 1 output, the proposed fuzzy controller is simpler than traditional fuzzy controllers and, as such, it has an easier hardware implementation.

4.4.2 Simulation Results

The SIRM-based fuzzy controller has been verified with the 5-kW DFIG-WECS with fixed-pitch shown in Figure 2.22 using the membership functions, fuzzy rules of SIRMs, and dynamic importance degree given in subsection 4.3.2. Therefore, for all simulations, it has been assumed that $\beta = 0°$.

The wind turbine model and the DFIG model driven by the stator-flux oriented vector control were simulated according to the block diagram of Chapter 2 and Chapter 3, respectively with the same parameters of the wind turbine

In the first simulation, the ideal MPPT controller and the SIRM-based fuzzy controller have been compared considering uncertain aerodynamic conditions as a step.

Figure 4.17 to 4.19 show the dynamic responses when the wind speed changes as a step from 5 to 8 m/s and then from 8 to 12 m/s.

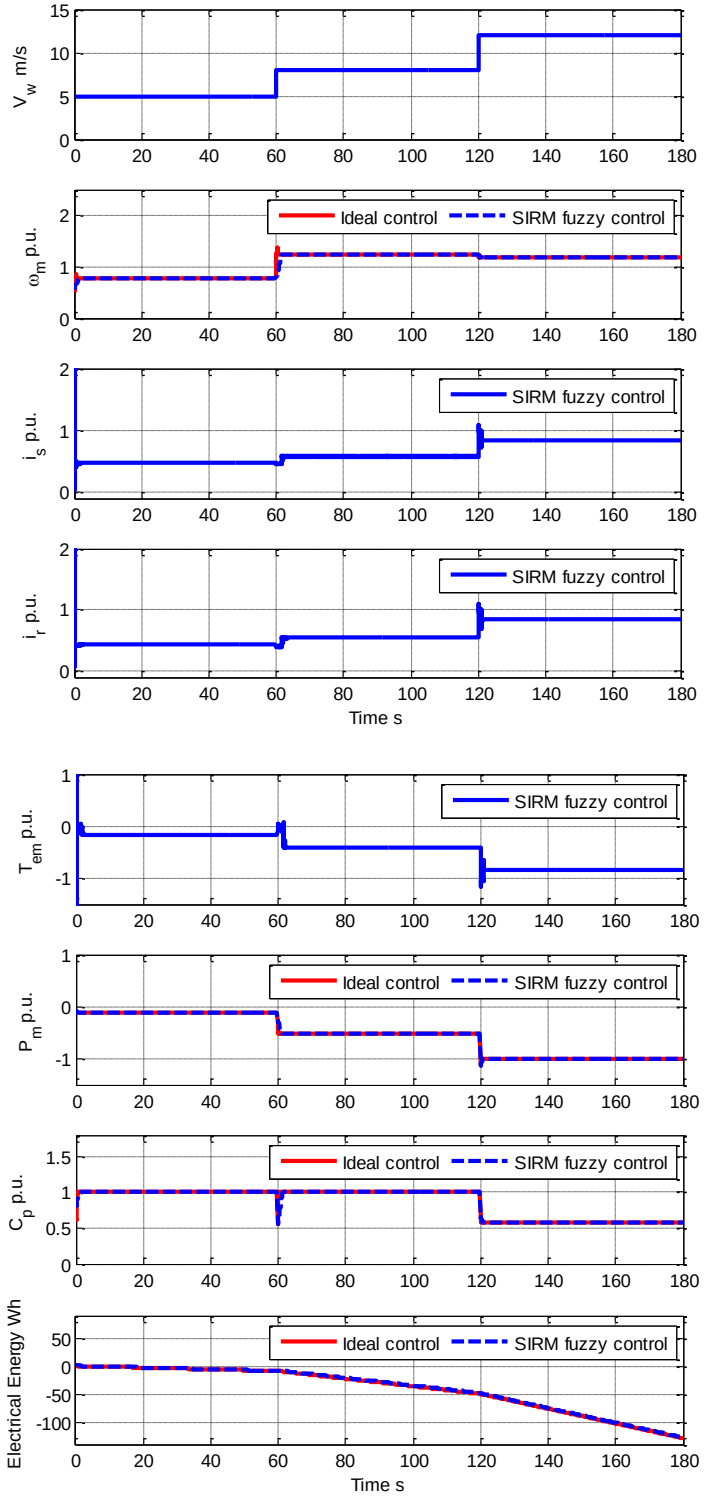

Figure 4.17: WECS performance for step-changing wind speed with no error on the estimation of air density and λ_i

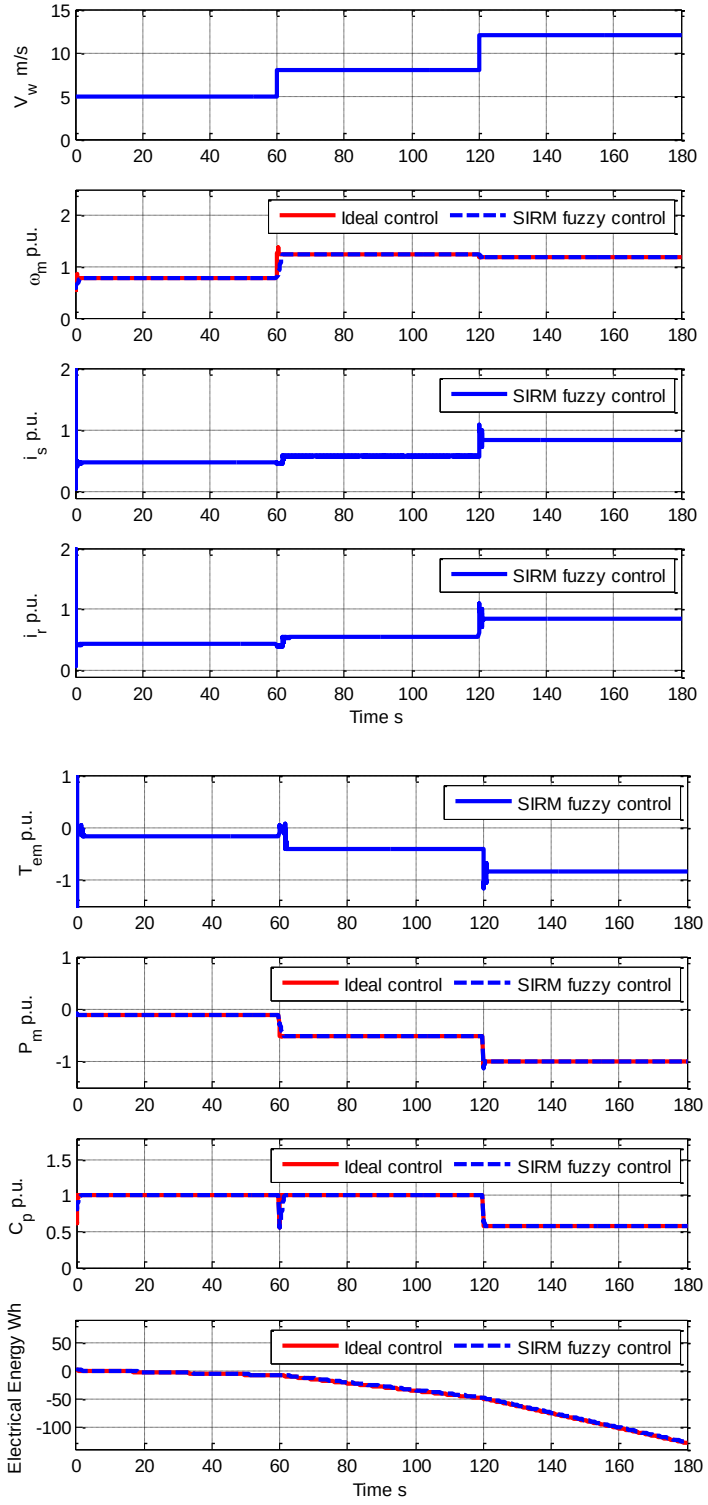

Figure 4.18: WECS performance for step-changing wind speed with an error of +20% on the estimation of air density

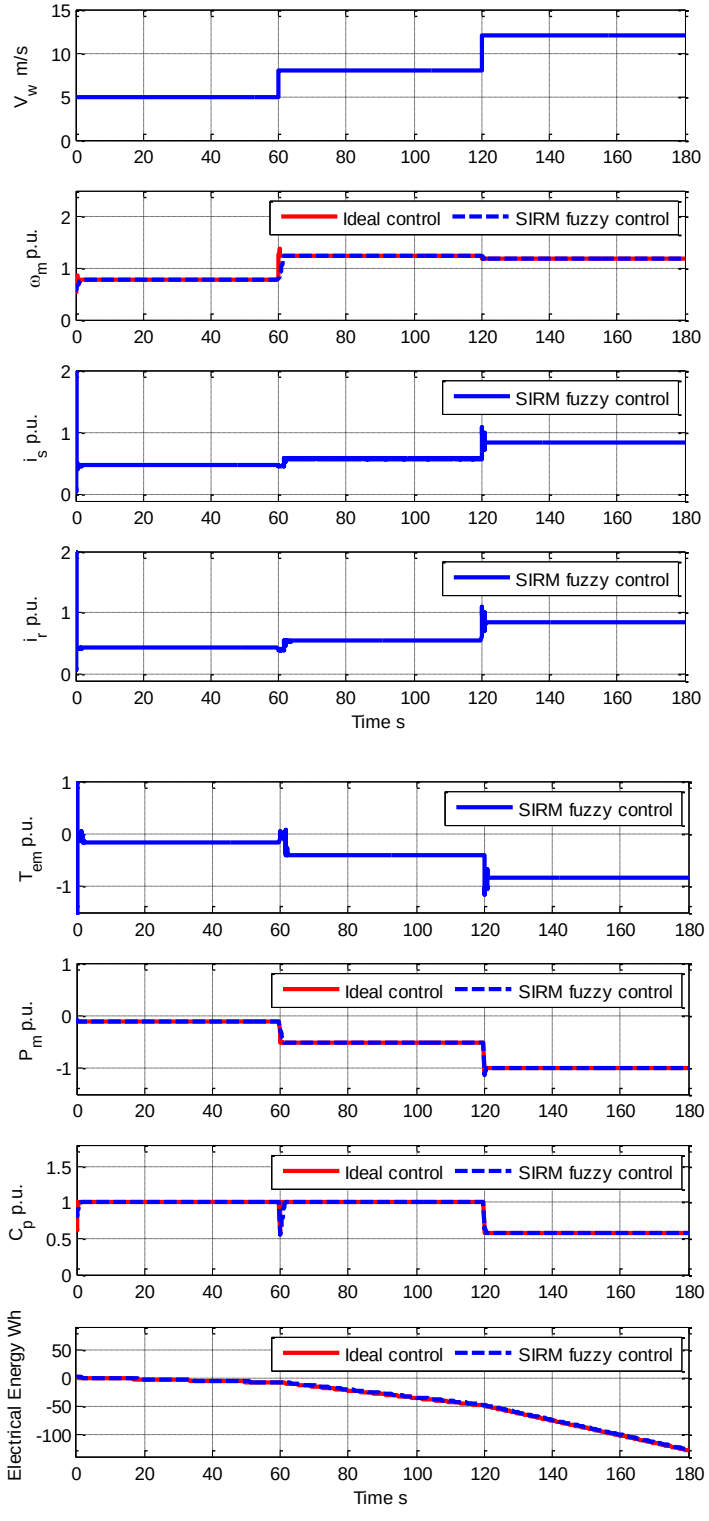

Figure 4.19: WECS performance for step-changing wind speed with an error of +20% on the estimation of λ_i

Figure 4.17 shows the case where the estimation on the air density and λ_i has no error. The SIRM-based fuzzy controller generates the correct speed references of 0.775 p.u. and 1.241 p.u. when the wind speed is 5 and 8 m/s, respectively, corresponding to the maximum power coefficient, C_{pmax} of 0.48. The fuzzy controller has a slightly slower response than the ideal control due to the inertia of the wind turbine which T_{em} reaches to zero under acceleration for 2.2 seconds. Similarly, the fuzzy controller generates the correct speed reference of 1.177 p.u. when wind speed changes to 12 m/s, which corresponds to the rated power of the wind turbine. The generator speed cannot decrease quickly to the value required for the active stall mode, because the electromagnetic torque reaches to $-T_{rated}$ under deceleration for 0.8 seconds.

The simulations show that SIRM-based fuzzy controllers have a fast response and accurate steady-state estimation of the maximum power thanks to their adaptive step size.

Figure 4.18 shows the transient response when the estimation of air density has an error of +20% of its nominal value, while λ_i has no error. This means that the actual parameter k_{opt} changes from 0.1186 to 0.1418 (+20%). The SIRM-based fuzzy controller adapts itself to generate the optimal speed reference corresponding to the actual maximum power coefficient, C_{pmax} of 0.48 even in the presence of this error regardless of the wind speed value and for operations below and above the rated wind speed.

Figure 4.19 shows the dynamic response when the estimation on λ_i has an error of +20% of its nominal value, while the air density has no error. In this case, the parameter k_{opt} increases from 0.1186 to 0.1750 (+47.55%). Also, in this case, the SIRM-based fuzzy controller generates the correct speed reference, and there is no error in tracking the maximum power point below and above the rated wind speed.

In the second simulation, the SIRM-based fuzzy controller has been tested with the wind speed diagram presented in the previous sections.

The simulation tests have considered the same case studies of uncertainty on the air density and uncertainty of C_p-λ curve affected by the knowledge of the value λ_i. The simulations have been repeated for three different average speeds, corresponding to a scenario of low, medium and high wind. The levels of wind are classified by the average wind speed, $\bar{v}_w$, as 4 to 6 m/s for low wind, 7 to 10 m/s for medium wind, and 11 to 14 m/s for high wind [110].

Case study 1: uncertainty of air density

In this case study, the error of the estimation of the air density has been varied between -20% and +20% of the nominal value [57], while C_{pmax} and λ_{opt} are correctly estimated. Consequently, the parameter k_{opt} of the PSF MPPT varies between 0.0945 and 0.1418.

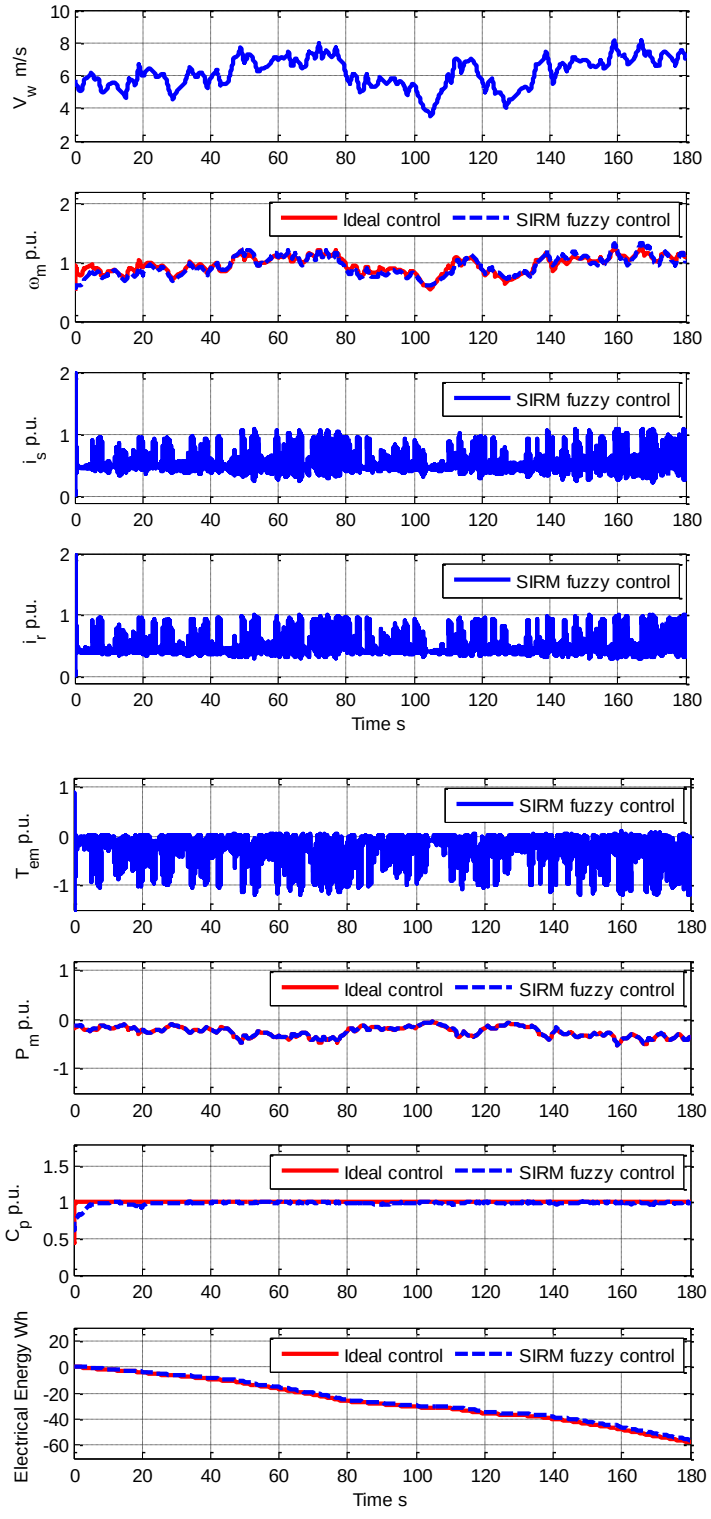

Figure 4.20: WECS performance for realistic wind speed of $\bar{v}_w$ = 6 m/s with an error of +20% on the estimation of air density

Figure 4.20 shows the dynamic response of the 5-kW WECS controlled by both the SIRM-based fuzzy controller and the ideal power controller with an average wind speed $\bar{v}_w$ = 6 m/s. The actual wind speed varies between 4 and 8 m/s, so the two power control algorithms operate in the maximum power control mode. The diagrams of the figures show the wind speed, V_w, the generator speed, ω_m, the magnitude stator current, i_s, the magnitude rotor current, i_r, the electromagnetic torque, T_{em}, the mechanical power, P_m, the power coefficient, C_p and the electrical energy generated by the DFIG

The fuzzy controller based on SIRM is capable of tracking the optimal speed reference to a value close to the ideal power control.

Table 4.10: Electrical energy decrease in WECS with fuzzy controller based SIRM with an error in the estimation of ρ for a simulation of 3 minutes, with $\bar{v}_w$ = 6 m/s (comparison with ideal control: -57.82 Wh.)

Error in estimation ρ of its nominal value	**k_{opt} estimation**	**Electrical energy (Wh)**	**Loss energy of proposed control**
-20%	0.0945	-56.00	-3.13%
-10%	0.1063	-56.06	-3.04%
0%	0.1186	-56.03	-3.09%
+10%	0.1300	-56.01	-3.13%
+20%	0.1418	-55.99	-3.16%

Table 4.10 shows the impact of the electrical energy generated by the DFIG by the SIRM-base fuzzy logic controller for various errors in the estimation of the air density and average wind speed $\bar{v}_w$ = 6 m/s. It can be seen that the algorithm is not substantially affected by this error and the slightly lower energy produced compared to the ideal case is only due to the inertia of the turbine. For comparison, the loss of energy of the fuzzy controller based SIRM is -3.13% when the error is -20% and -3.16% when the error is +20%.

Figure 4.21 shows the dynamic response for an average wind speed $\bar{v}_w$ = 8 m/s when the estimation of the air density is +20% of the nominal value, respectively. The actual wind speed changes between 6 and 10 m/s, so it is always below the rated value. The SIRM-based fuzzy control is capable of satisfactorily tracking the maximum power point of the wind turbine also in this situation, although the speed difference compared to the ideal case increases to 4.35% at time = 100 second.

The proposed power control can produce less electrical energy from the DFIG than the ideal power control around 2.45% over a period of 3 minutes.

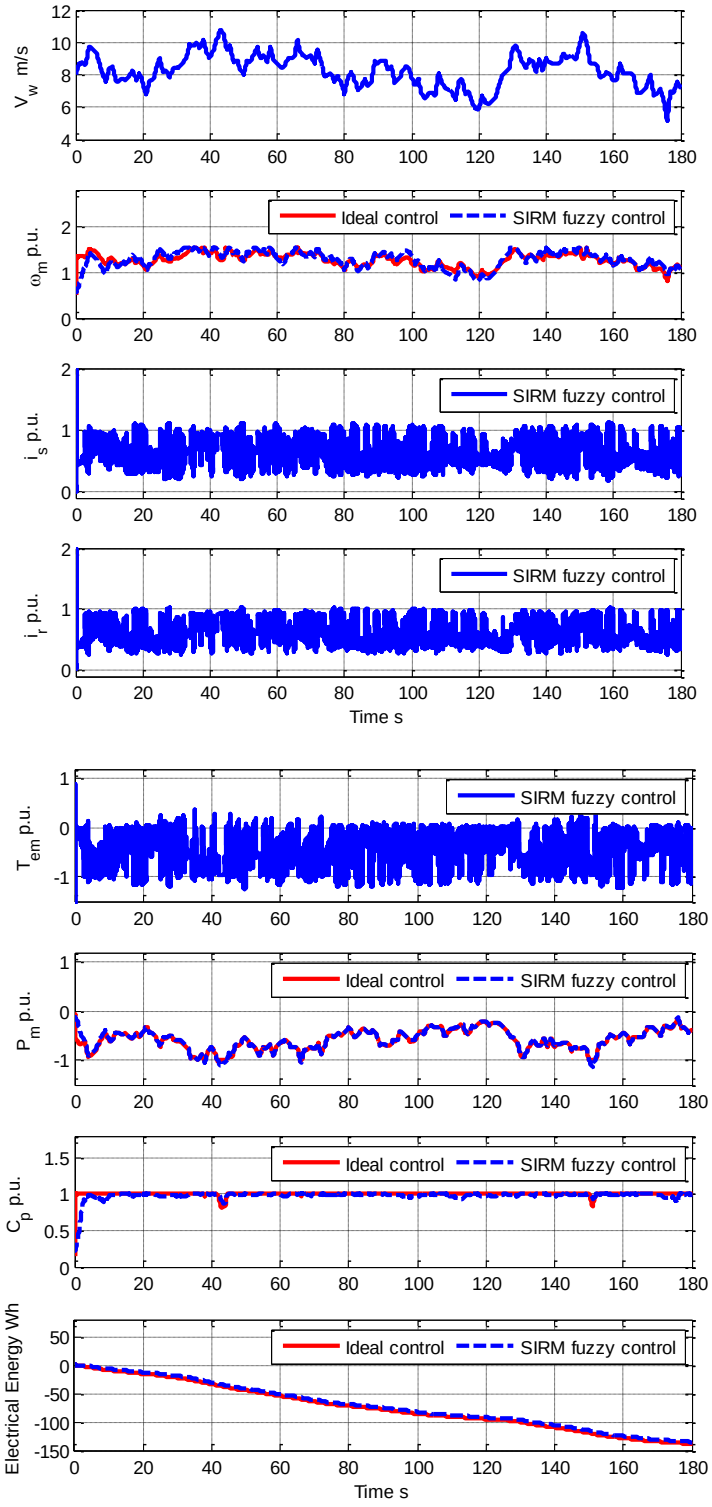

Figure 4.21: WECS performance for realistic wind speed of $\bar{v}_w$ = 8 m/s with an error of +20% on the estimation of air density

Table 4.11: Electrical energy decrease in WECS with fuzzy controller based SIRM with an error in the estimation of ρ for a simulation of 3 minutes, with $\bar{v}_w$ = 8 m/s (comparison with ideal control: -138.8 Wh.)

Error in estimation ρ of its nominal value	**k_{opt} estimation**	**Electrical energy (Wh)**	**Loss energy of proposed control**
-20%	0.0945	-135.3	-2.52%
-10%	0.1063	-135.3	-2.52%
0%	0.1186	-135.1	-2.66%
+10%	0.1300	-135.3	-2.52%
+20%	0.1418	-135.4	-2.45%

Table 4.11 shows the electrical energy generated by the DFIG in this case, and again the difference from the ideal case is less than 2.66%.

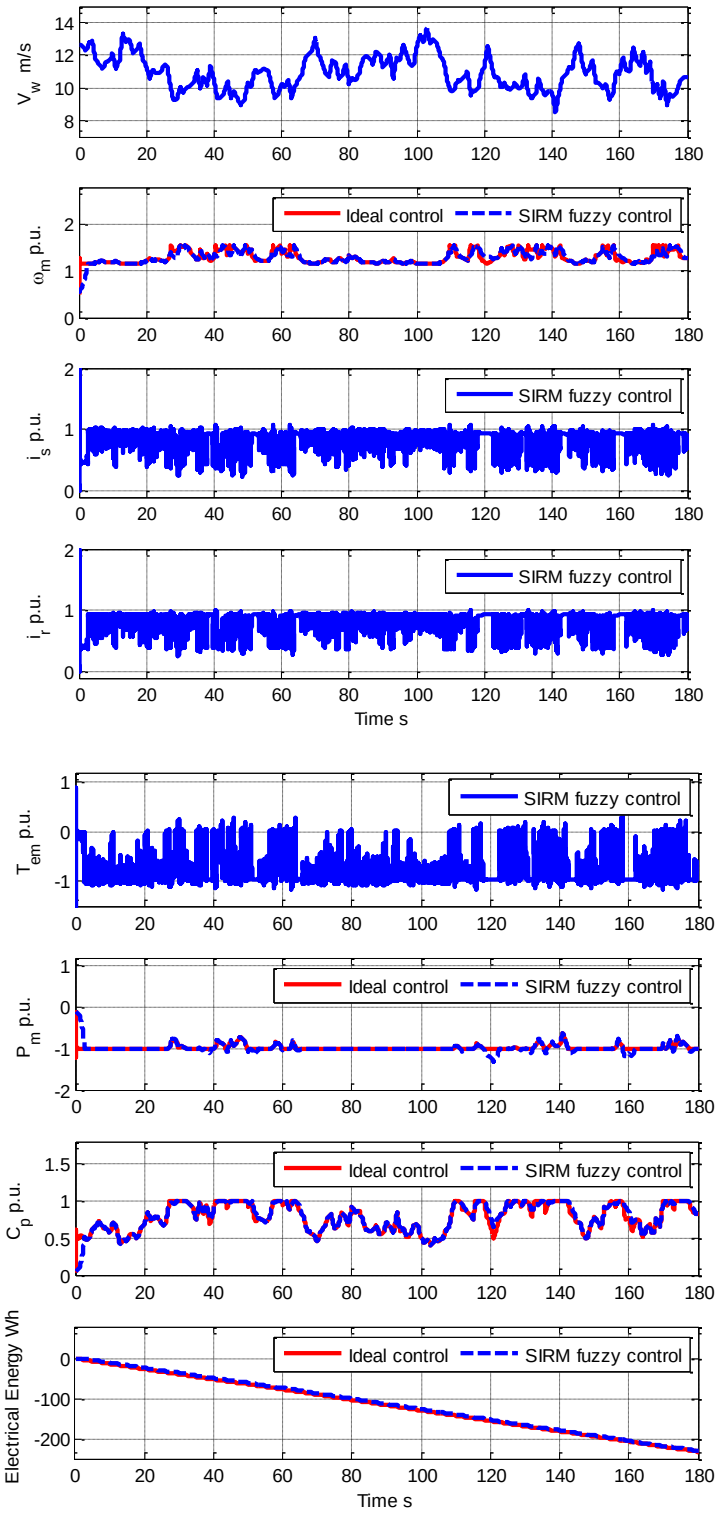

Figure 4.22: WECS performance for realistic wind speed of $\bar{v}_w$ = 11 m/s with an error of +20% on the estimation of air density

Figure 4.22 shows the transient response for an average wind speed $\bar{v}_w$ = 11 m/s when the error on the estimation of the air density is +20% of its nominal value. The diagram of the wind speed shows in this case operations both below and above the rated speed. Therefore, the SIRM-based fuzzy logic controller switches from the MPPT to the limitation of the mechanical power with active stall controller. In particular, for the transition from the MPPT control to active stall regulation, the generator speed cannot decrease quickly because the electromagnetic torque is limited to the rated value of the DFIG. Therefore, the mechanical power is temporarily over-rated power, The rated power, P_{m_rated}, in this thesis is defined as 5 kW so that this DFIG can produce sufficient electromagnetic torque under deceleration to the stall. In [8], the DFIG having over-torque capability is provided to overcome this problem. The rotor current is kept not to exceed the rated value in over-rated power to save the power converter as seen in Figure 4.22. The higher mechanical power input also means that the DFIG generates more electrical energy than the ideal power control, as shown in Figure 4.22(b). It can be observed that the SIRM-based fuzzy controller also gives a smooth speed reference trajectory in the transition between the MPPT and active stall control due to the fuzzy set of the dynamic importance degree which weights roles both controllers via the observed mechanical power.

Table 4.12 shows the impact of the electrical energy generated by the DFIG for errors on the estimation of the air density variable between -20% and +20% of the rated value when the average wind speed is $\bar{v}_w$ = 11 m/s.

It can be seen that for all the situations, the proposed control produces less electrical energy than the ideal power control of around 0.69% over a period of 3 minutes.

Table 4.12: Electrical energy decrease in WECS with fuzzy controller based SIRM with an error in the estimation of ρ for a simulation of 3 minutes, with $\bar{v}_w$ = 11 m/s (comparison with ideal control: -232.4 Wh.)

Error in estimation ρ of its nominal value	**k_{opt} estimation**	**Electrical energy (Wh)**	**Loss energy of proposed control**
-20%	0.0945	-230.8	-0.69%
-10%	0.1063	-230.8	-0.69%
0%	0.1186	-230.8	-0.69%
+10%	0.1300	-230.8	-0.69%
+20%	0.1418	-230.8	-0.69%

Case study 2: uncertainty of C_p-λ curve via λ_i

In this case, an error in the estimation of the λ_i has been assumed and varied between -20% and +20% of the nominal value [57], while the air density has been considered constant and equal to the nominal value. Consequently, the k_{opt} of the PSF MPPT corresponding to λ_i changes between 0.0754 and 0.1750.

Figure 4.23 to 4.25 show the transient response for an average wind speed of $\bar{v}_w$ = 6 m/s, 8m/s and 11 m/s when the estimation of λ_i has an error of +20% of its nominal value.

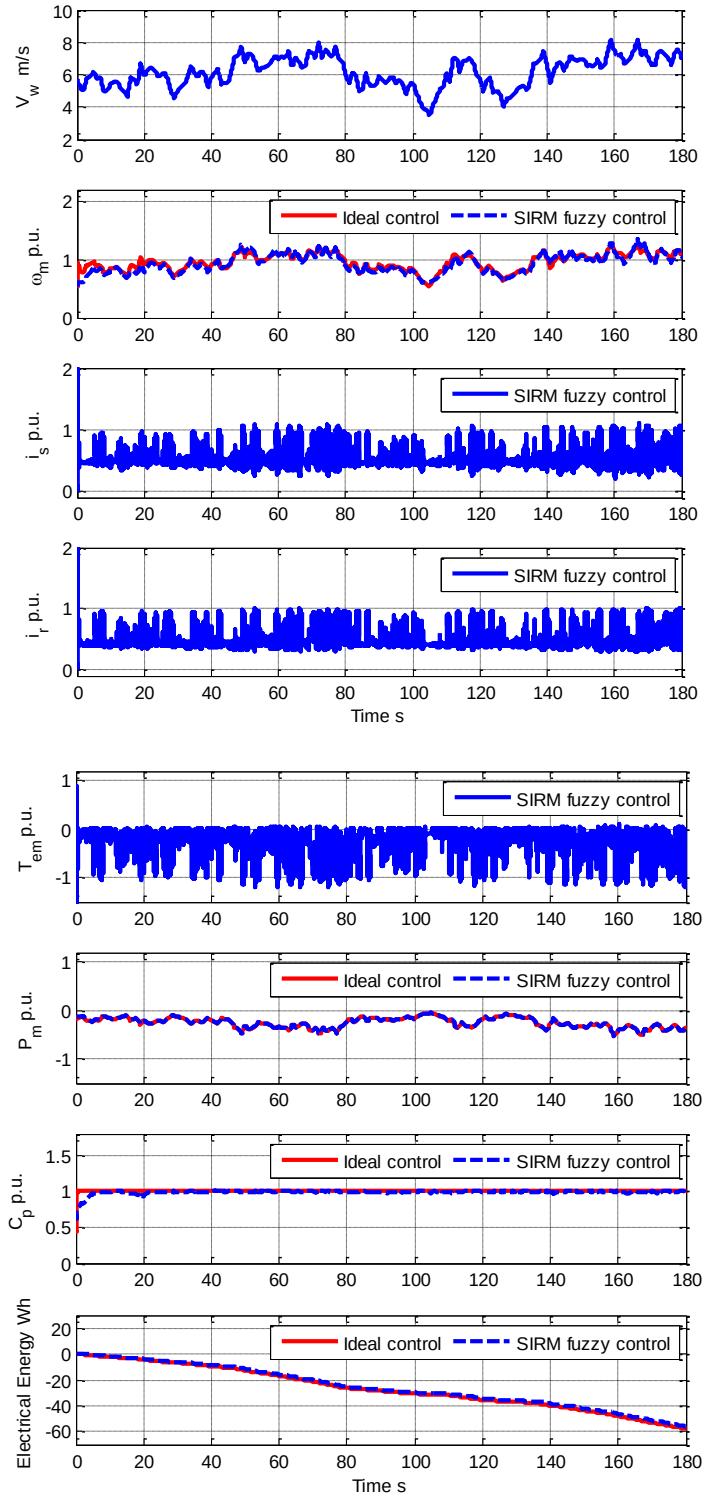

Figure 4.23: WECS performance for realistic wind speed of $\bar{v}_w$ = 6 m/s with an error of +20% on the estimation of λ_i

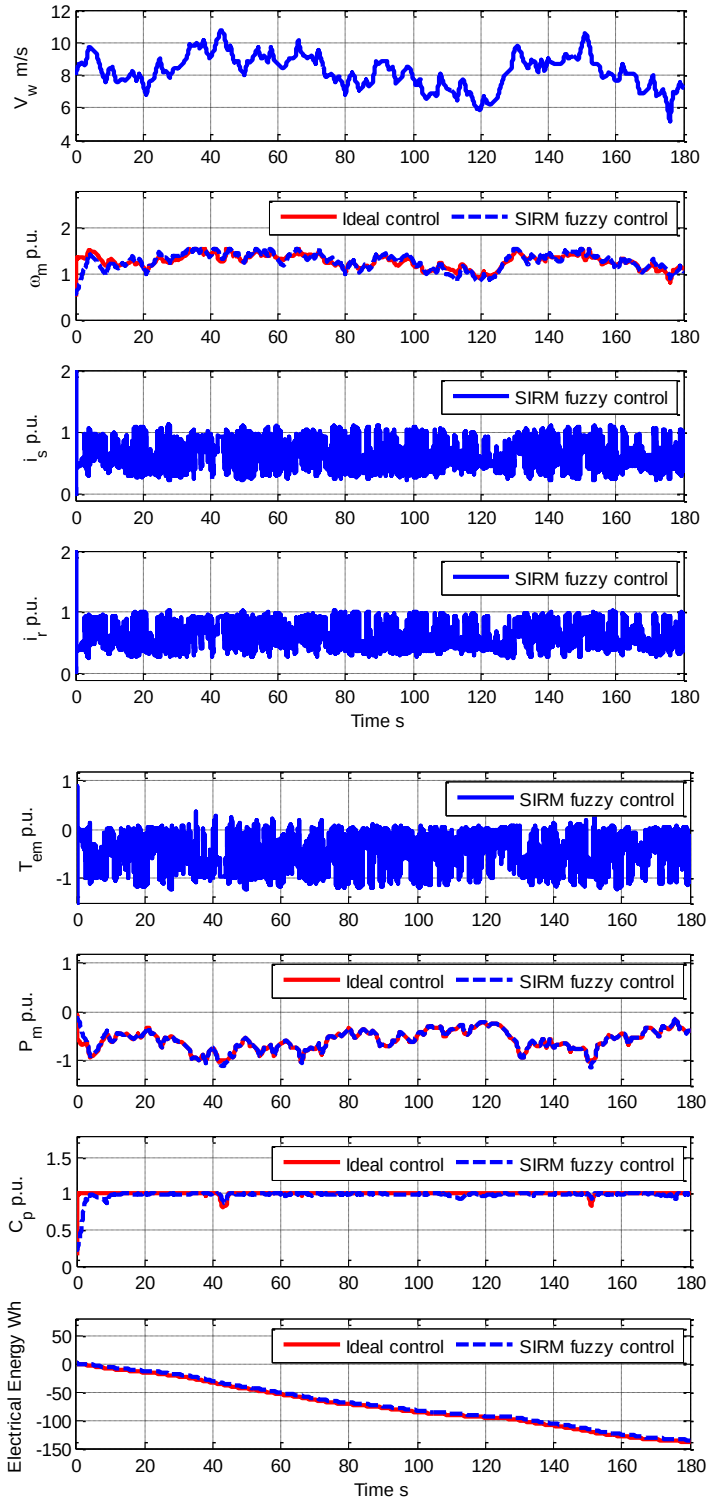

Figure 4. 24: WECS performance for realistic wind speed of $\bar{v}_w$ = 8 m/s with an error of +20% on the estimation of λ_i

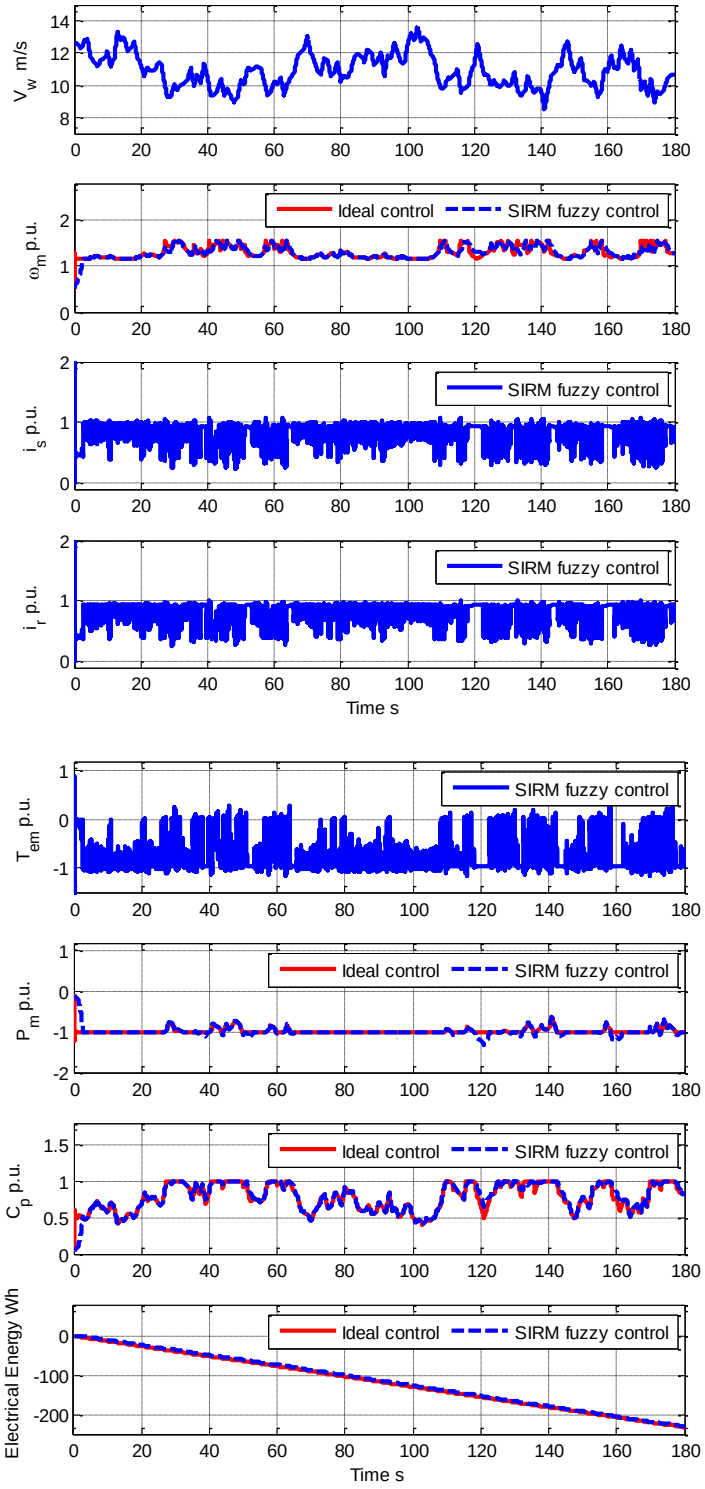

Figure 4.25: WECS performance for realistic wind speed of $\bar{v}_w$ = 11 m/s with an error of +20% on the estimation of λ_i

The proposed control provides good adaptation capabilities against the uncertainties of λ_i when the wind speed is always below the rated value

When instead the average wind speed is 11 m/s, the proposed power control gives a slower response than the ideal power control due to the inertia of the wind turbine. Consequently, the proposed control generates less electrical energy than the ideal power control below the rated wind speed and more electrical energy above the rated wind speed. Also, in this case, it is necessary to consider the DFIG having overtorque ability to overcome the large torque of the turbine during wind speed variation from the MPPT to stall control. However, the overtorque will result in increased drive train fatigue which an issue will merit investigation.

The effect on the error on the estimation of λ_i has been analysed in Table 4.13 and 4.14 for the low and medium average wind speeds of $\bar{v}_w$ = 6 and 8 m/s, respectively. It can be observed that the proposed control can generate the same energy value around 56 Wh for low wind speed and 135 Wh for medium wind speed when the error in the estimation of λ_i between -20% and +20% of the nominal value, with a different smaller than 3.15% compared to the ideal situation.

Table 4.13: Electrical energy decrease in WECS with fuzzy controller based SIRM with an error in the estimation of λ_i for a simulation of 3 minutes, with $\bar{v}_w$ = 6 m/s (comparison with ideal control: -57.82 Wh.)

Error in estimation λ_i of its nominal value	**k_{opt} estimation**	**Electrical energy (Wh)**	**Loss energy of proposed control**
-20%	0.0754	-56.08	-3.01%
-10%	0.0952	-56.01	-3.13%
0%	0.1186	-56.03	-3.10%
+10%	0.1447	-56.00	-3.15%
+20%	0.1750	-56.01	-3.13%

Table 4.14: Electrical energy decrease in WECS with fuzzy controller based SIRM with an error in the estimation of λ_i for a simulation of 3 minutes, with $\bar{v}_w$ = 8 m/s (comparison with ideal control: -138.8 Wh.)

Error in estimation λ_i of its nominal value	**k_{opt} estimation**	**Electrical energy (Wh)**	**Loss energy of proposed control**
-20%	0.0754	-135.6	-2.31%
-10%	0.0952	-135.4	-2.45%
0%	0.1186	-135.1	-2.67%
+10%	0.1447	-135.4	-2.45%
+20%	0.1750	-135.7	-2.23%

Table 4.15 reports the energy generated for an average wind speed of $\bar{v}_w$ = 11 m/s. It can be seen that the proposed control produces less electrical power than the ideal power control around 0.69% over a period of 3 minutes.

Table 4.15: Electrical energy decrease in WECS with fuzzy controller based SIRM with an error in the estimation of λ_i for a simulation of 3 minutes, with $\bar{v}_w$ = 11 m/s (comparison with ideal control: -232.4 Wh.)

Error in estimation λ_i of its nominal value	**k_{opt} estimation**	**Electrical energy (Wh)**	**Loss energy of proposed control**
-20%	0.0754	-230.8	-0.69%
-10%	0.0952	-230.8	-0.69%
0%	0.1186	-230.8	-0.69%
+10%	0.1447	-230.8	-0.69%
+20%	0.1750	-230.8	-0.69%

4.5 Summary

This chapter has presented the main characteristics of SIRM-based fuzzy controllers for WECS with VSFP wind turbines and DFIGs. The main advantage of this control is the capabilities of compensating for errors in the estimation of the turbine parameters. The new fuzzy controller is constructed as a SIRM for each input variable. Therefore, the proposed fuzzy controller has a smaller number of rules and parameters compared with a conventional fuzzy control. For this thesis, the fuzzy controller based SIRM is designed with 30 fuzzy rules for six SIRMs and 14 fuzzy rules for the dynamic importance degree.

The simulation results have shown that the control reacts well to uncertainties on the estimation of the air density and the parameter λ_i even when the wind changes as a stochastic process and for various average wind speeds. Critical operations have been

found in the transition across the rated wind speed, for which the power limitation has a response slower than the ideal case due to the inertia of the wind turbine and the limitation on the resistant torque offered by the DFIG. This situation leads to a temporary exceeding rated power of the turbine, although the nominal power is defined for 5 kW so that 5-kW DFIG can produce sufficient electromagnetic torque to decrease speed in the active stall control. Therefore, the V_{cut_out} is determined at 14 m/s to limit instantaneous torque of the wind turbine less than the available electromagnetic torque of the DFIG. It has been seen that there is no overload on the power converter, which is instead much more sensitive than the machine.

Chapter 5 Robust Loss Minimisation Control for DFIG

5.1 Introduction

Chapter 4 has presented the optimal power control for a VSFP wind turbine based on a hybrid MPPT. This chapter focusses on the control strategy to minimise the copper losses of the DFIG using the model-based loss minimisation control (MBLC).

The basic concept of traditional MBLC for minimising DFIG copper losses and the impact of parameter uncertainties are studied in section 5.2. The online parameter estimation with a Kalman filter is explained in section 5.3, where an enhanced MBLC is proposed. The simulation results based on Matlab/Simulink aimed at comparing the performance between the standard and the enhanced MBLC as shown in section 5.4.

5.2 Traditional MBLC for DFIG and its Efficiency

5.2.1 Problem of Model-Based Loss Minimisation Control

A MBLC generates an optimal *d*-axis rotor current, i_{rd}, reference to the vector control on the rotor-side converter to regulate the reactive power to reach the condition for which power losses are minimum.

As in can be seen from (2.54), the MBLC relies on the accurate knowledge of the parameters of the DFIG for generating the optimal control law. If the parameters are not

exactly known, the algorithm forces the DFIG to operate in a point different from the actual minimum of copper losses. This problem is happening in practice because:

- The parameters of the DFIG are only roughly known by using the no-load test and the locked rotor test [73]. Often, the leakage inductance and the resistances are assumed to be equal as there is no easy way to split them accurately, unavoidably leading to errors. Therefore, obtaining parameters with a higher degree of accuracy is difficult.
- During operations, some of the parameters may change their value due to the influence of environmental and operational conditions as shown in Figure 5.1[7].

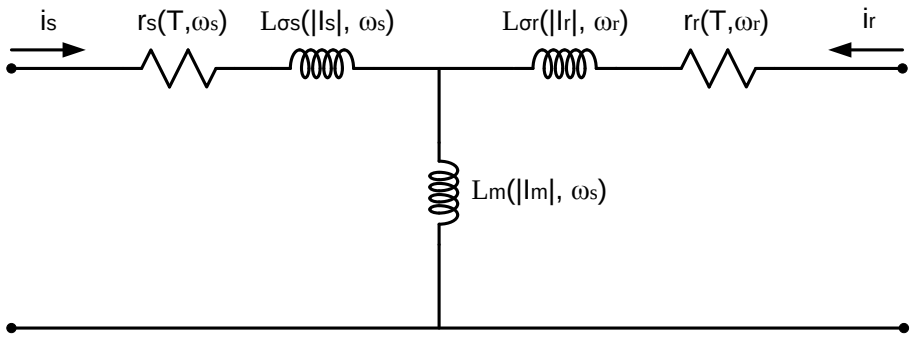

Figure 5.1: Parameter variation of DFIG steady-state model

1. Stator resistance, r_s: its value may change due to temperature (T) and stator current frequency (ωs) [7]:

$$r_s = f(T, \omega_s) \tag{5.1}$$

A resistance value (Ω) can be expressed with a function of a temperature variation (°C) as follows:

$$r_T = r_x \frac{(1+kC_T)}{(1+kC_x)} \tag{5.2}$$

where r_x is the known resistance value at temperature $C_{x,}$ and r_T is the corrected resistance value at temperature $C_{T,}$ and k is the temperature coefficient of resistivity (a typical value for copper at 0 °C may be 0.00427 Ω/Ω°C). For example, The effect of the resistance of the DFIG with the winding temperature is shown in Figure 5.2. Considering that for typical insulation classes of DFIGs are F or H, the maximum temperature is between 145°C and 180°C, so the rotor resistance, which at 35 °C is assumed equal to 0.75 Ω, it would increase at 180 °C by 53.86%.

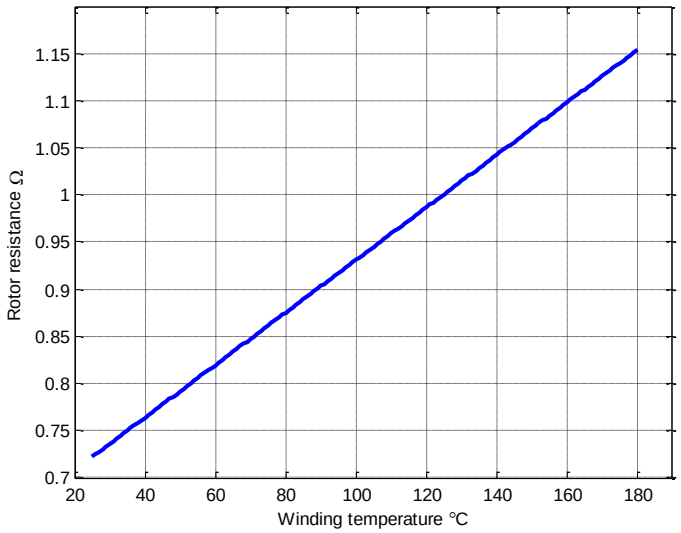

Figure 5.2: Rotor resistance variation as a function of winding temperature

The variation of the stator resistance with the frequency is instead much more modest, as the grid frequency can diverge only up to 0.1% of the nominal value.

2. Rotor resistance, r_r: the behaviour of rotor resistance is similar to the stator resistor. Its value may change due to temperature (T) and rotor current frequency (ω_r) that flows [7]:

$$r_r = f(T, \omega_r) \tag{5.3}$$

In [111], The rotor resistance may increase by 50% with the winding temperature rise. The variation with the frequency is instead more evident, as the distribution of the current is uniform when the slip is zero and begins to be more and more asymmetric when the slip increases with the skin effect. The skin effect caused by increasing slip affects the rotor resistance variation around 2-3 times of the nominal value [111].

3. Stator leakage inductance, $L_{\sigma s}$: Its value may change due to the amplitude and frequency of the stator current [7]:

$$L_{\sigma s} = f(|I_s|, \omega_s) \tag{5.4}$$

The variation with stator current, i_s can be expressed as follows [112]:

$$L_{\sigma s}(i_s) = \begin{cases} L_{\sigma s} & i_s < i_{ssat} \\ K_{\sigma s}(i_s) \cdot L_{\sigma s} & i_s \geq i_{ssat} \end{cases} \tag{5.5}$$

where i_{ssat} is the threshold of the stator current which can change the stator leakage inductance from its nominal value. It is defined as $1.8 i_{s\_rated}$ [113]. $K_{\sigma s}$ is the saturation coefficient which can be calculated by [112]:

$$K_{\sigma s}(i_s)=\begin{cases}1 & i_s < i_{ssat}\\ \frac{2}{\pi}(\arcsin(\frac{i_{ssat}}{i_s})+0.5\sin(2\arcsin(\frac{i_{ssat}}{i_s}))) & i_s \geq i_{ssat}\end{cases} \quad (5.6)$$

According to (5.5) and (5.6), $L_{\sigma s}$ is decreased from its nominal value when i_s is above i_{ssat}, causing the leakage flux saturation [112]. In practical application on WECS, the $L_{\sigma s}$ is nearly constant because the stator current is maintained not to exceed its nominal value.

4. Rotor Leakage inductance, $L_{\sigma r}$: the behavior of rotor leakage inductance is similar to the stator leakage inductance. Its value may change due to the amplitude and frequency of the rotor current that flows [7]:

$$L_{\sigma r} = f(|I_r|, \omega_r) \quad (5.7)$$

5. Mutual inductance, L_m: Its value may change due to the amplitude and frequency of the magnetising current due to the saturation of the main magnetic circuit of the machine [7]:

$$L_m = f(|I_m|, \omega_s) \quad (5.8)$$

The variation with the magnetising current, i_m can be expressed as follows [112]:

$$L_m(i_m)=\begin{cases}L_m & i_m < i_{msat}\\ K_{ms}(i_m)\cdot L_m & i_m \geq i_{msat}\end{cases} \quad (5.9)$$

where i_{msat} is the threshold of the magnetising current which can change the mutual inductance from its nominal value. It is defined as $0.7i_{s\_rated}$ [113]. K_{ms} is the saturation coefficient which can be calculated by [112]:

$$K_{ms}(i_m) = \begin{cases} 1 & i_m < i_{msat} \\ \frac{2}{\pi}(\arcsin(\frac{i_{msat}}{i_m}) + 0.5\sin(2\arcsin(\frac{i_{msat}}{i_m}))) & i_m \geq i_{msat} \end{cases} \quad (5.10)$$

According to (5.9) and (5.10), L_m is decreased from its nominal value when i_m is above i_{msat}, causing the mutual flux saturation [112]. For wind energy generation with the DFIG, the stator terminals of the machine are directly connected to a power grid with substantially constant voltage amplitude and frequency. It means that the L_m is maintained nearly constant in normal operation.

5.2.2 Simulation Results on the Impact of Parameter Uncertainty on MBLC

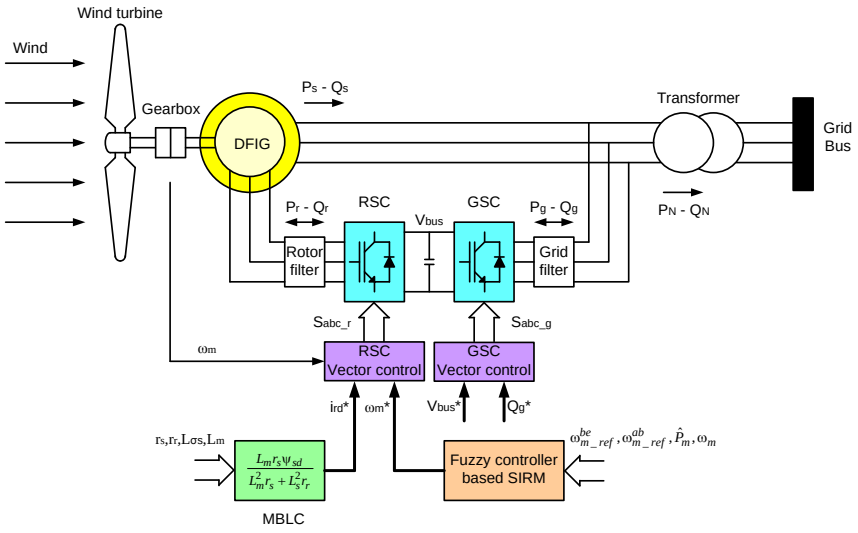

Figure 5.3: Block diagram of MBLC for WECS

To study the influence on the error in the estimation of DFIG parameters on the MBLC, the model of DFIG-WECS presented in Chapter 2 and shown in Figure 5.3 has been used. From Figure 5.3; the generator speed reference is provided by the fuzzy controller based SIRM while the i_{rd} reference is generated by the traditional MBLC method. The wind speed has been assumed constant at 6 m/s and the error in the estimation of r_s, r_r, $L_{\sigma s}$ and L_m between -50% and +50% of the nominal values.

Considering an error of -50% for r_s, r_r, $L_{\sigma s}$ and L_m, Figure 5.4-5.8 show the dynamic response of the following quantities: *d*-axis rotor current reference, i_{rdref}; the electrical power generated by the DFIG, P_e, and the extracted electrical energy in Wh from the DFIG.

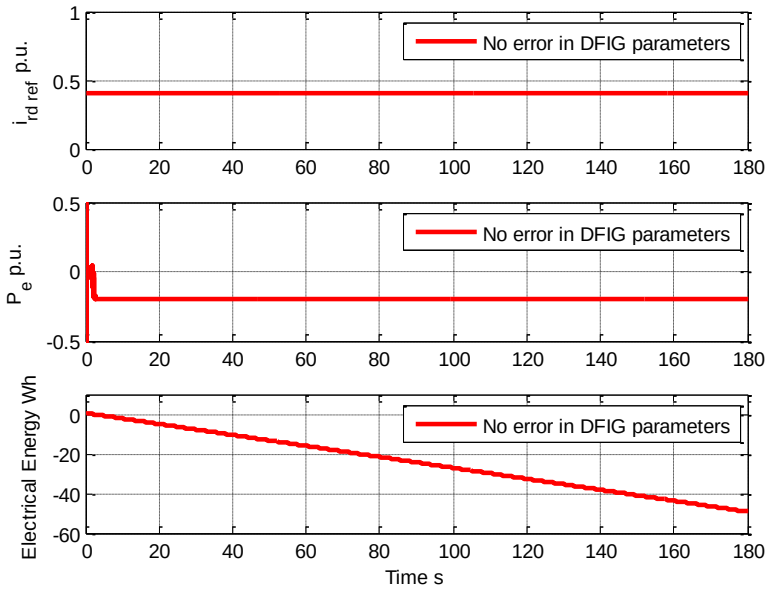

Figure 5.4: WECS dynamic response controlled by the traditional MBLC for constant wind speed 6 m/s with no error in estimation of DFIG parameters: r_s, r_r, $L_{\sigma s}$ and L_m

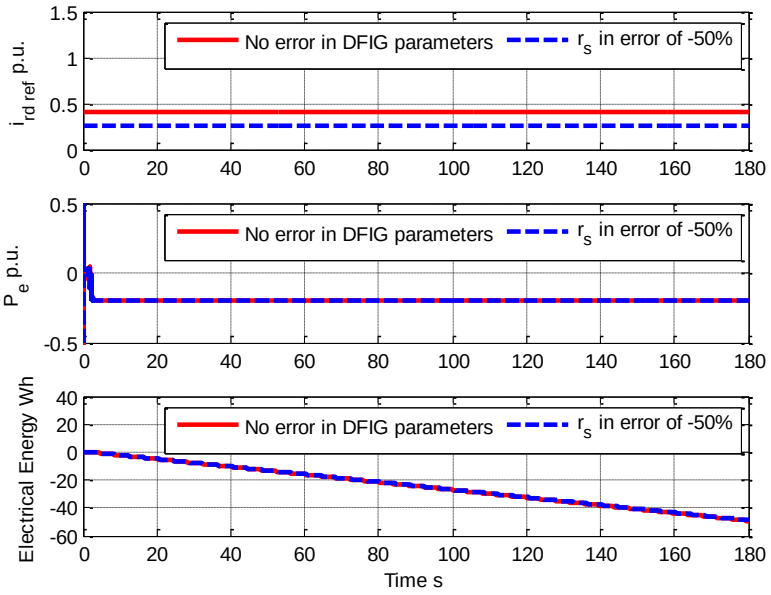

Figure 5.5: WECS dynamic response controlled by the traditional MBLC for constant wind speed 6 m/s with error in estimation of r_s of -50%

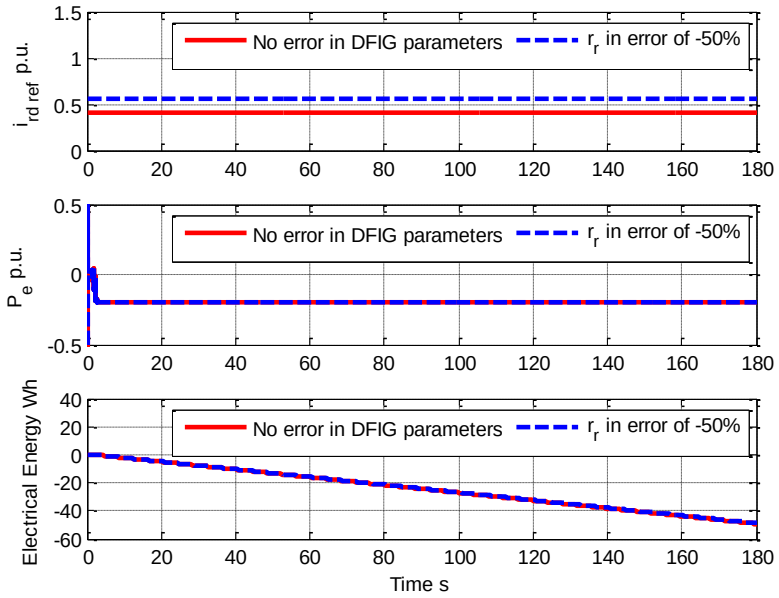

Figure 5.6: WECS dynamic response controlled by the traditional MBLC for constant wind speed 6 m/s with error in estimation of r_r of -50%

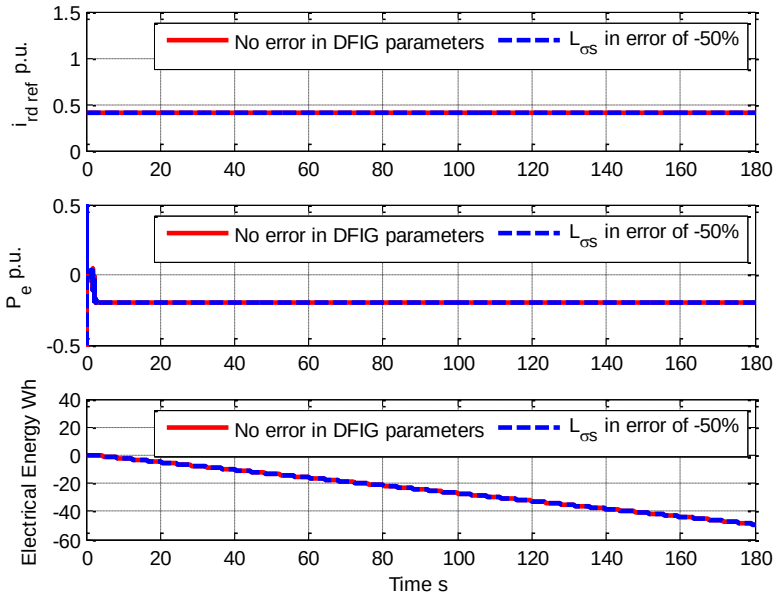

Figure 5.7: WECS dynamic response controlled by the traditional MBLC for constant wind speed 6 m/s with error in estimation of $L_{\sigma s}$ of -50%

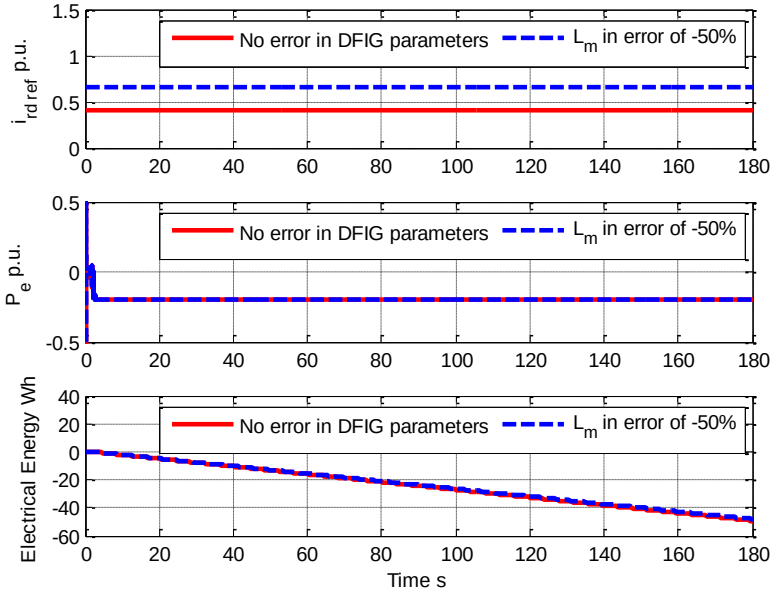

Figure 5.8: WECS dynamic response controlled by the traditional MBLC for constant wind speed 6 m/s with error in estimation of L_m of -50%

Figure 5.4 shows the reference case when there is no error. The traditional MBLC provides a reference for i_{rd} of 2.84 A, corresponding to the minimum copper loss operating point referred to control law (2.54). The electrical energy generated by the WECS is 49.15 Wh over a period of 3 minutes.

It can be seen that the traditional MBLC method can give high performance for tracking accurate determination of minimum loss condition when the DFIG parameters used in control law of the traditional MBLC method are exactly known.

Figure 5.5 shows the dynamic response when the estimation on the stator resistance, r_s, has an error of -50% of its nominal value. Under this uncertain condition, i_{rd} reference provided by the traditional MBLC method changes from 2.842 A to 1.842 A (-35.19%). Therefore, the total electrical energy generated reduces by 0.39 Wh (-0.79%).

Figure 5.6 shows the dynamic response when the estimation on the rotor resistance, r_r, has an error of -50% of its nominal value. i_{rd} reference changes from 2.842 to 3.900 A, (+37.23%). The electrical energy reduces by 0.38 Wh (-0.77%).

Figure 5.7 shows the dynamic response when the estimation on the stator leakage inductance, $L_{\sigma s}$, has an error of -50% of its nominal value. The i_{rd} reference changes from 2.842 to 2.941 A, (+3.48%). The electrical energy generated does not have any measurable change.

Figure 5.8 shows the dynamic response when the estimation on mutual inductance, L_m, has an error of -50% of its nominal value. The i_{rd} reference changes from 2.842 to 5.307 A (+86.73%). The electrical energy reduces by 2.13 Wh (-4.33%).

The influence on the error in the estimation of r_s, r_r, $L_{\sigma s}$ and L_m for finding the minimum DFIG loss operating point of the MBLC method has been analysed in Table 5.1-5.4, respectively for various level of error of the parameters. It can be seen that the error on the estimation of L_m has the highest impact in the efficiency in the MBLC method. However, this is a situation hardly occurring in practice as the value of L_m is usually overestimated for the presence of saturation of the magnetic circuits of the machine

Table 5.1: Electrical energy decrease in WECS controlled by traditional MBLC with an error in the estimation of r_s for a simulation of 3 minutes for wind speed 6 m/s

Estimation error of r_s from its nominal value	**i_{rdref} estimation**	**Electrical energy (Wh)**	**Loss energy of MBLC**
-50%	1.842 A	-48.76	-0.79%
-30%	2.305 A	-49.03	-0.24%
-10%	2.680 A	-49.14	-0.02%
0%	2.842 A	-49.15	0.00%
+10%	2.989 A	-49.14	-0.02%
+30%	3.248 A	-49.10	-0.10%
+50%	3.469 A	-49.02	-0.26%

Table 5.2: Electrical energy decrease in WECS controlled by traditional MBLC with an error in the estimation of r_r for a simulation of 3 minutes for wind speed 6 m/s

Estimation error of r_r from its nominal value	**i_{rdref} estimation**	**Electrical energy (Wh)**	**Loss energy of MBLC**
-50%	3.900 A	-48.77	-0.77%
-30%	3.394 A	-49.05	-0.20%
-10%	3.005 A	-49.14	-0.02%
0%	2.842 A	-49.15	0.00%
+10%	2.695 A	-49.14	-0.02%
+30%	2.444 A	-49.08	-0.14%
+50%	2.235 A	-49.00	-0.31%

Table 5.3: Electrical energy decrease in WECS controlled by traditional MBLC with an error in the estimation of $L_{\sigma s}$ for a simulation of 3 minutes for wind speed 6 m/s

Estimation error of $L_{\sigma s}$ from its nominal value	**i_{rdref} estimation**	**Electrical energy (Wh)**	**Loss energy of MBLC**
-50%	2.941 A	-49.15	0.00%
-30%	2.901 A	-49.15	0.00%
-10%	2.861 A	-49.15	0.00%
0%	2.842 A	-49.15	0.00%
+10%	2.822 A	-49.15	0.00%
+30%	2.784 A	-49.15	0.00%
+50%	2.746 A	-49.14	-0.02%

Table 5.4: Electrical energy decrease in WECS controlled by traditional MBLC with an error in the estimation of L_m for a simulation of 3 minutes for wind speed 6 m/s

Estimation error of L_m from its nominal value	**i_{rdref} estimation**	**Electrical energy (Wh)**	**Loss energy of MBLC**
-50%	5.307 A	-47.02	-4.33%
-30%	3.942 A	-48.74	-0.83%
-10%	3.133 A	-49.13	-0.04%
0%	2.842 A	-49.15	0.00%
+10%	2.599 A	-49.12	-0.06%
+30%	2.221 A	-48.99	-0.33%
+50%	1.938 A	-48.83	-0.65%

5.3 Online Parameter Estimation of DFIG by using Kalman Filter Method

Generally, the basic concept of online parameter estimation is that a process plant model is run in parallel with parameterisation of the plant model which has the same structure as the process model with the same input and, then an estimator algorithm generates and updates the estimated parameters until the output of parameterised plant model, $\hat{y}(t)$ approaches the actual output of the system, *y(t)*.

5.3.1 Parameterisation of Plant Model of DFIG

The dynamic model of the DFIG in the *dq* reference frame can be rearranged to create the parameterisation of the plant model as:

$$\begin{cases} v_{sd} = r_s i_{sd} + \dfrac{d\psi_{sd}}{dt} - \omega_s \psi_{sq} \\ v_{sq} = r_s i_{sq} + \dfrac{d\psi_{sq}}{dt} + \omega_s \psi_{sd} \\ v_{rd} = r_r i_{rd} + \dfrac{d\psi_{rd}}{dt} - (\omega_s - p\omega_m)\psi_{rq} \\ v_{rq} = r_r i_{rq} + \dfrac{d\psi_{rq}}{dt} + (\omega_s - p\omega_m)\psi_{rd} \end{cases} \tag{5.11}$$

$$\begin{cases} \psi_{sd} = L_s i_{sd} + L_m i_{rd} \\ \psi_{sq} = L_s i_{sq} + L_m i_{rq} \\ \psi_{rd} = L_m i_{sd} + L_r i_{rd} \\ \psi_{rq} = L_m i_{sq} + L_r i_{rq} \end{cases} \tag{5.12}$$

Substituting (5.12) into (5.11), the model of the DFIG becomes:

$$\begin{bmatrix} v_{sd} \\ v_{sq} \\ v_{rd} \\ v_{rq} \end{bmatrix} = \begin{bmatrix} r_s + L_s \dfrac{d}{dt} & -\omega_s L_s & L_m \dfrac{d}{dt} & -\omega_s L_m \\ \omega_s L_s & r_s + L_s \dfrac{d}{dt} & \omega_s L_m & L_m \dfrac{d}{dt} \\ L_m \dfrac{d}{dt} & -(\omega_s - p\omega_m)L_m & r_r + L_r \dfrac{d}{dt} & -(\omega_s - p\omega_m)L_r \\ (\omega_s - p\omega_m)L_m & L_m \dfrac{d}{dt} & (\omega_s - p\omega_m)L_r & r_r + L_r \dfrac{d}{dt} \end{bmatrix} \begin{bmatrix} i_{sd} \\ i_{sq} \\ i_{rd} \\ i_{rq} \end{bmatrix} \tag{5.13}$$

A general form of the dynamic model for the parameter estimation can be expressed as follows [114]:

$$y(t) = \Phi^T(t)\theta(t) \tag{5.14}$$

The matrix form of (5.14) can be written as:

$$\begin{bmatrix} y_1(t) \\ y_2(t) \\ . \\ . \\ y_n(t) \end{bmatrix} = \begin{bmatrix} \Phi_{11} & \Phi_{12} & . & . & \Phi_{1m} \\ \Phi_{21} & \Phi_{22} & . & . & \Phi_{2m} \\ . & & & & \\ . & & & & \\ \Phi_{n1} & \Phi_{n2} & . & . & \Phi_{nm} \end{bmatrix} \begin{bmatrix} \theta_1(t) \\ \theta_2(t) \\ . \\ . \\ \theta_m(t) \end{bmatrix} \tag{5.15}$$

where $y(t)$ is the measured output variable of the dynamic model, $\Phi(t)$ is the observation vector measured from the dynamic model and $\theta(t)$ is the parameter variables to be estimated. In this thesis, the parameters of the DFIG to estimate are r_s, r_r, $L_{\sigma s}$, $L_{\sigma r}$ and L_m. Hence, the estimated parameter vector of the DFIG can be written as:

$$\theta = [r_s \;\; r_r \;\; L_{\sigma s} \;\; L_{\sigma r} \;\; L_m]^T \tag{5.16}$$

The measured output vector $y(t)$ is the stator and rotor voltages in the *dq* reference frame. The vector form can be written by:

$$y = [v_{sd} \;\; v_{sq} \;\; v_{rd} \;\; v_{rq}]^T \tag{5.17}$$

Rearranging (5.13) to (5.15), the parameterised plant model can be expressed as follows:

$$\begin{bmatrix} v_{sd} \\ v_{sq} \\ v_{rd} \\ v_{rq} \end{bmatrix} = \begin{bmatrix} i_{sd} & 0 & \dfrac{di_{sd}}{dt} - \omega_s i_{sq} & 0 & \dfrac{di_{sd}}{dt} + \dfrac{di_{rd}}{dt} - \omega_s (i_{sq} + i_{rq}) \\ i_{sq} & 0 & \dfrac{di_{sq}}{dt} - \omega_s i_{sd} & 0 & \dfrac{di_{sq}}{dt} + \dfrac{di_{rq}}{dt} + \omega_s (i_{sd} + i_{rd}) \\ 0 & i_{rd} & 0 & \dfrac{di_{rd}}{dt} - (\omega_s - p\omega_m) i_{rq} & \dfrac{di_{rd}}{dt} + \dfrac{di_{sd}}{dt} - (\omega_s - p\omega_m)(i_{rq} + i_{sq}) \\ 0 & i_{rq} & 0 & \dfrac{di_{rq}}{dt} - (\omega_s - p\omega_m) i_{rd} & \dfrac{di_{rq}}{dt} + \dfrac{di_{sq}}{dt} + (\omega_s - p\omega_m)(i_{rd} + i_{sd}) \end{bmatrix} \begin{bmatrix} r_s \\ r_r \\ L_{\sigma s} \\ L_{\sigma r} \\ L_m \end{bmatrix} \tag{5.18}$$

The parameterised plant model in discrete time can be obtained as follows:

$$\begin{bmatrix} v_{sd}(k) \\ v_{sq}(k) \\ v_{rd}(k) \\ v_{rq}(k) \end{bmatrix} = \begin{bmatrix} i_{sd}(k) & 0 & \frac{\Delta i_{sd}(k)}{\Delta t} - \omega_s(k) i_{sq}(k) & 0 & \frac{\Delta i_{sd}(k)}{\Delta t} + \frac{\Delta i_{rd}}{\Delta t} - \omega_s(k)(i_{sq}(k) + i_{rq}(k)) \\ i_{sq}(k) & 0 & \frac{\Delta i_{sq}(k)}{\Delta t} - \omega_s(k) i_{sd}(k) & 0 & \frac{\Delta i_{sq}(k)}{\Delta t} + \frac{\Delta i_{rq}(k)}{\Delta t} + \omega_s(k)(i_{sd}(k) + i_{rd}(k)) \\ 0 & i_{rd}(k) & 0 & \frac{\Delta i_{rd}(k)}{\Delta t} - (\omega_s(k) - p\omega_m(k)) i_{rq}(k) & \frac{\Delta i_{rd}(k)}{\Delta t} + \frac{\Delta i_{sd}(k)}{\Delta t} - (\omega_s(k) - p\omega_m(k))(i_{rq}(k) + i_{sq}(k)) \\ 0 & i_{rq}(k) & 0 & \frac{\Delta i_{rq}(k)}{\Delta t} - (\omega_s(k) - p\omega_m(k)) i_{rd}(k) & \frac{\Delta i_{rq}(k)}{\Delta t} + \frac{\Delta i_{sq}(k)}{\Delta t} + (\omega_s(k) - p\omega_m(k))(i_{rd}(k) + i_{sd}(k)) \end{bmatrix} \begin{bmatrix} r_s(k) \\ r_r(k) \\ L_{\sigma s}(k) \\ L_{\sigma r}(k) \\ L_m(k) \end{bmatrix}$$

(5.19)

To decrease the complication of the online parameter estimation, the stator leakage inductance, $L_{\sigma s}$, and the rotor leakage inductance, $L_{\sigma r}$, are assumed to be equal. Hence, the estimated parameter vector of the DFIG can be written by:

$$\theta = [r_s \;\; r_r \;\; L_{\sigma s} \;\; L_m]^T \tag{5.20}$$

And, the dynamic model for the parameter estimation can be expressed as follows

$$\begin{bmatrix} v_{sd}(k) \\ v_{sq}(k) \\ v_{rd}(k) \\ v_{rq}(k) \end{bmatrix} = \begin{bmatrix} i_{sd}(k) & 0 & \frac{\Delta i_{sd}(k)}{\Delta t} - \omega_s(k) i_{sq}(k) & \frac{\Delta i_{sd}(k)}{\Delta t} + \frac{\Delta i_{rd}(k)}{\Delta t} - \omega_s(k)(i_{sq}(k) + i_{rq}(k)) \\ i_{sq}(k) & 0 & \frac{\Delta i_{sq}(k)}{\Delta t} + \omega_s(k) i_{sd}(k) & \frac{\Delta i_{sq}(k)}{\Delta t} + \frac{\Delta i_{rq}(k)}{\Delta t} + \omega_s(k)(i_{sd}(k) + i_{rd}(k)) \\ 0 & i_{rd}(k) & \frac{\Delta i_{rd}(k)}{\Delta t} - (\omega_s(k) - p\omega_m(k)) i_{rq}(k) & \frac{\Delta i_{rd}(k)}{\Delta t} + \frac{\Delta i_{sd}(k)}{\Delta t} - (\omega_s(k) - p\omega_m(k))(i_{rq}(k) + i_{sq}(k)) \\ 0 & i_{rq}(k) & \frac{\Delta i_{rq}(k)}{\Delta t} + (\omega_s(k) - p\omega_m(k)) i_{rd}(k) & \frac{\Delta i_{rq}(k)}{\Delta t} + \frac{\Delta i_{sq}(k)}{\Delta t} + (\omega_s(k) - p\omega_m(k))(i_{rd}(k) + i_{sd}(k)) \end{bmatrix} \begin{bmatrix} r_s(k) \\ r_r(k) \\ L_{\sigma s}(k) \\ L_m(k) \end{bmatrix}$$

(5.21)

5.3.2 Kalman Filter Estimation Algorithm

The parameter estimation using Kalman filter is implemented in the discrete time. The linear state space model of the parameterised plant model in (5.21) can be expressed as [114]:

$$\begin{cases} \theta(k+1) = \theta(k) + \Delta\theta(k) \\ y(k) = \Phi^T(k)\theta(k) + w(k) \end{cases} \tag{5.22}$$

The algorithms of the online parameter estimation by using Kalman filter can be expressed following steps [114]:

1. Initial condition: when $k = 0$, the initialisation of the online parameter estimation by using Kalman filter is defined as:

$$\begin{cases} \hat{\theta}(0) = \theta_{init} \\ P(0) = P_{init} \end{cases} \tag{5.23}$$

where θ_{init} is the initial parameter estimation and P_{init} is the initial error covariance.

2. Prediction step: when $k > 0$, the recursion of the online parameter estimation by using Kalman filter is started in the prediction step as follow:

$$\hat{y}(k) = \Phi^T(k)\hat{\theta}(k-1) \tag{5.24}$$

3. Correction step: the correction step can be calculated after the prediction step as:

$$K(k) = \frac{P(k-1)\Phi(k)}{\Phi^T(k)P(k-1)\Phi(k) + R} \tag{5.25}$$

$$\hat{\theta}(k) = \hat{\theta}(k-1) + K(k)(y(k) - \hat{y}(k)) \tag{5.26}$$

$$P(k) = P(k-1) - K(k)\Phi^T(k)P(k-1) + Q \tag{5.27}$$

where K is the Kalman filter gain, R is the measurement noise covariance; $E(w(k)w^T(k))$ and Q is the process noise covariance; $E(\Delta\theta(k)\Delta\theta^T(k))$. The prediction and correction steps are recursively computed to adapt the estimated parameters of the DFIG approaching the accurate value.

Figure 5.9 shows the general block diagram of DFIG parameter estimation by using the Kalman filter algorithm in discrete time. The output error received from the comparison between the DFIG and DFIG parameterised model is used to update the estimated DFIG parameters by the Kalman filter algorithm in the correction step, then, these estimated DFIG parameters are used to update the estimated output via DFIG parameterised model. The estimated DFIG parameters are updated for minimal error between measured output and estimated output. As the Kalman filter is implemented in the recursive algorithm, it can work well in real time applications[73].

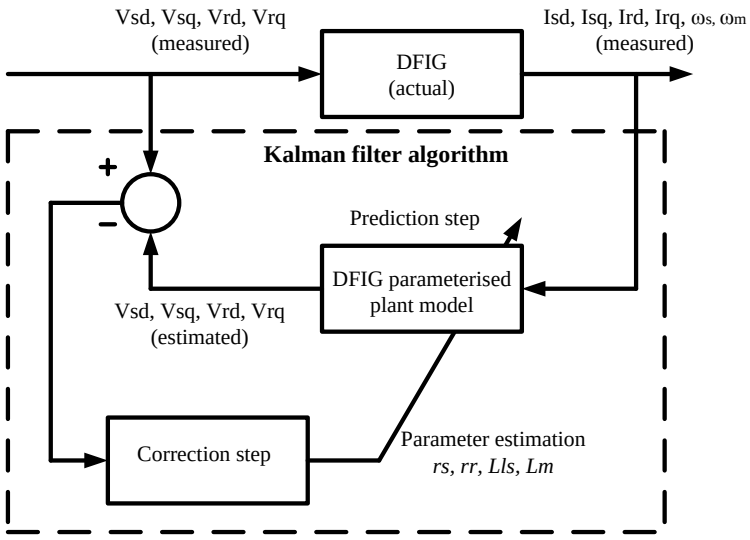

Figure 5.9: Block diagram for DFIG parameter estimation by Kalman filter algorithm

To test the performance of the parameter estimation of the DFIG in the WECS by using the Kalman filter method, The simulation is performed with a 5kW DFIG where r_s = 0.72 Ω, r_r = 0.75 Ω, $L_{\sigma s}$ = $L_{\sigma r}$ = 0.0058 H and L_m = 0.858 H. From Figure 5.9, the generator speed, measured voltages and measured currents in *dq* coordinate of the DFIG are fed to the Kalman filter estimator. The estimated voltages of the DFIG can be calculated by using (5.21). The Kalman filter algorithm adapts the estimated parameters of the DFIG. The error between the estimated voltages $\hat{y}(t)$ and the actual voltage *y(t)* gets close to zero as $t \rightarrow \infty$.

The guidelines for defining the measurement noise covariance, *R*, and the process noise covariance, *Q*, are indicated in [115]. The initial values of the parameters and the noise covariance are given by:

$$\begin{cases} \hat{\theta}(0) = [0.02\ 0.02\ 0.02\ 0.02]^T \\ P(0) = 10^3 \cdot diag([1\ 1\ 1\ 1]) \\ Q = 10^{-7} \cdot diag([1\ 1\ 1\ 1]) \\ R = 1 \cdot diag([2\ \ 2\ \ 2\ \ 2]) \end{cases} \tag{5.28}$$

The proposed online parameter estimation was simulated in Matlab/Simulink, initially for a constant wind speed of 6 m/s.

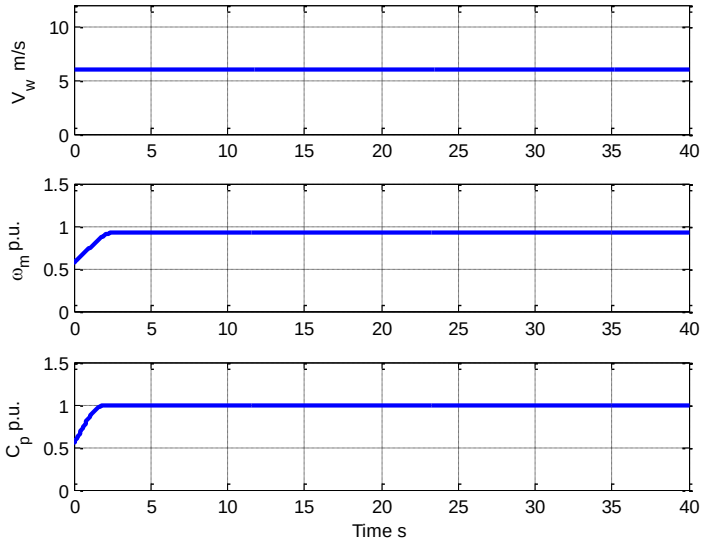

(a)

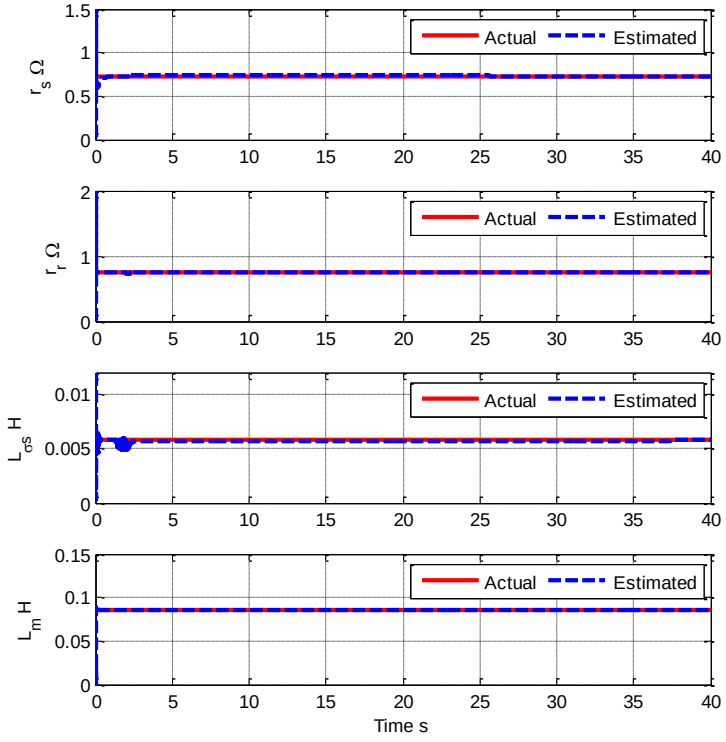

(b)

Figure 5.10: DFIG parameter estimation in WECS controlled by fuzzy controller based SIRM for constant wind speed 6 m/s

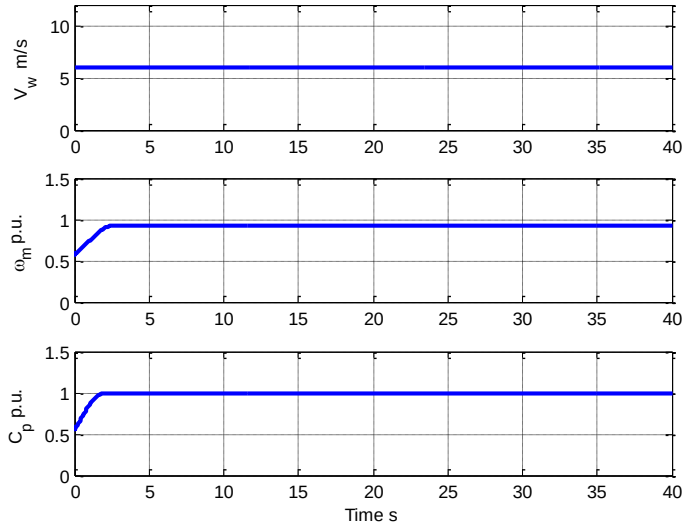

(a)

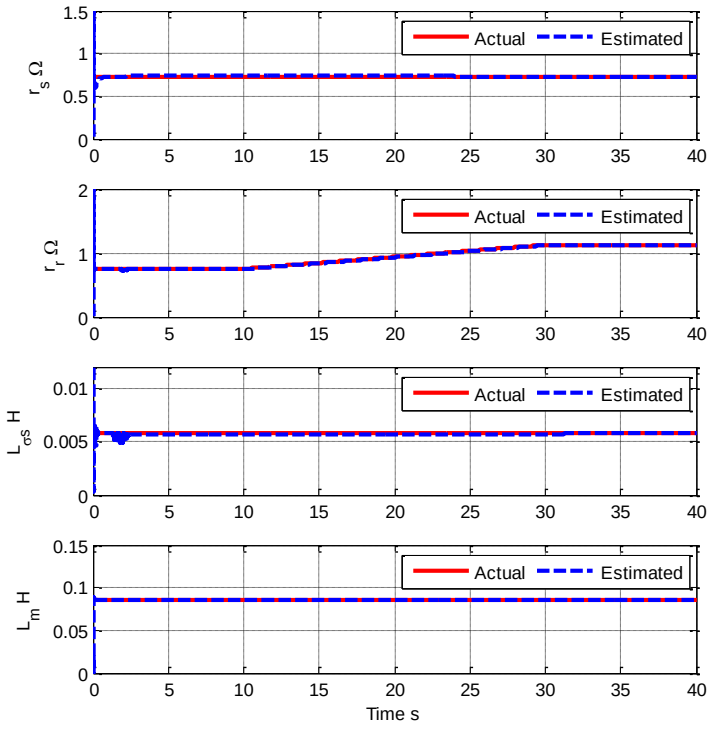

(b)

Figure 5.11: DFIG parameter estimation under r_r variation in WECS controlled by fuzzy controller based SIRM for constant wind speed 6 m/s

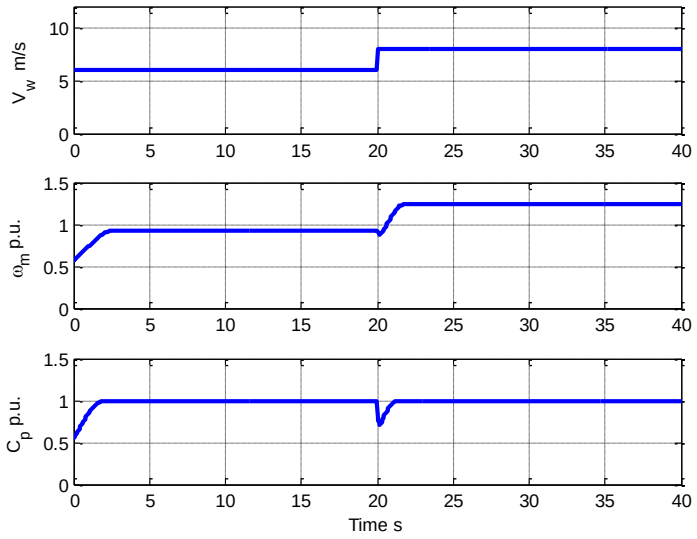

(a)

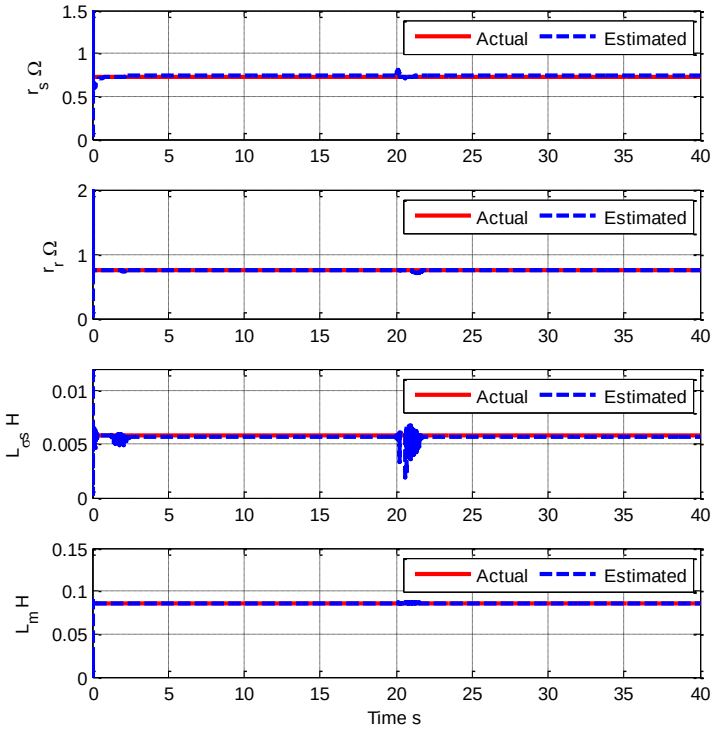

(b)

Figure 5.12: DFIG parameter estimation in WECS controlled by fuzzy controller based SIRM for step-changing wind speed from 6 to 8 m/s

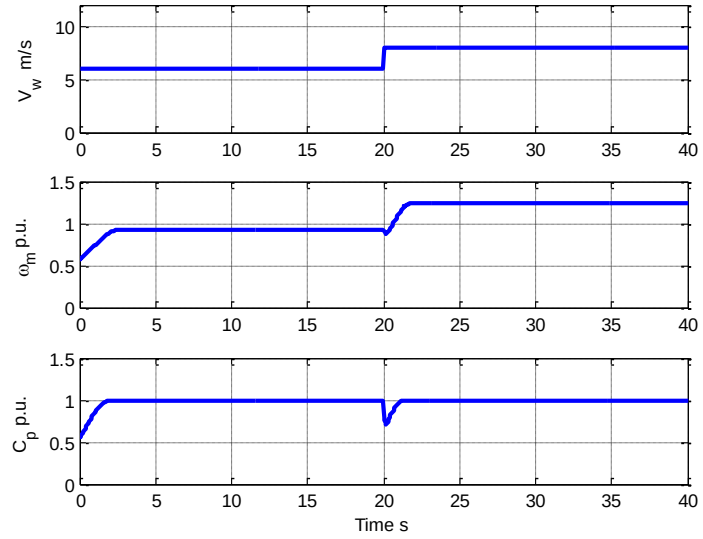

(a)

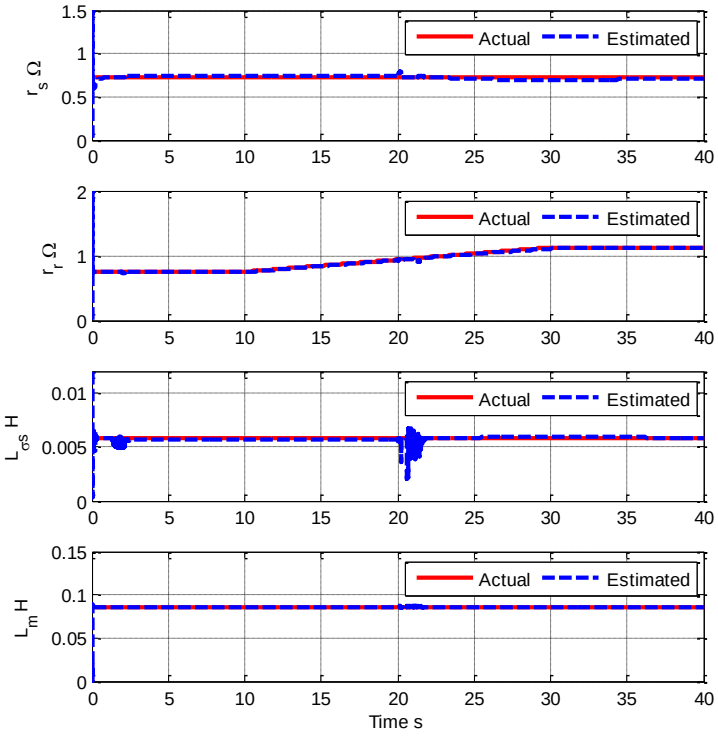

(b)

Figure 5.13: DFIG parameter estimation under r_r variation in WECS controlled by fuzzy controller based SIRM for step-changing wind speed from 6 to 8 m/s

Figure 5.10 shows the performance of the online Kalman filter estimator with constant DFIG parameters. The corrected estimation of the DFIG parameters is completed within 2 seconds, as shown in Figure 5.10(b).

Figure 5.11 shows the Kalman filter response for a dynamic variation of r_r due to a temperature change. The estimation of the DFIG parameter can track the actual value of r_r with a good performance also in this case, as shown in Figure 5.11(b).

Figure 5.12 shows the case of wind speed changing as a step from 6 to 8 m/s but with DFIG parameters unchanged. It can be seen that the Kalman filter reacts quite well to the disturbance and re-estimate the parameters correctly within 2 seconds. It is worth noting that the most sensitive parameters also have the least deviation after the disturbance, evidencing the appropriateness of the algorithm proposed.

Figure 5.13 shows the performance of the online DFIG parameter estimation by using Kalman filter in the WECS controlled by the fuzzy controller based on SIRM for step-changing wind speed from 6 to 8 m/s under condition of no change parameter and change of the parameter, respectively.

Under the fuzzy controller based SIRM, the DFIG operates with 146.2 rad/s and 194.9 rad/s in the MPPT control mode as shown in Figure 5.12(a) and 5.13(a). It can be seen that the proposed online DFIG parameter estimation can reach near the actual value very fast in the beginning and track the actual value of r_r in changing from 0.75 to 1.125 Ω with a good performance as shown in Figure 5.12(b) and 5.13(b). However, the estimation of $L_{\sigma s}$ gave transient instability under rapid wind speed variation because the

online DFIG parameter estimation using Kalman filter was operated under rapid variation of measured currents and rotational speed of the DFIG.

Table 5.5: Online parameter estimation of the DFIG by using Kalman filter for constant wind speed 6 m/s

DFIG Parameter	Actual value	Estimated value	%Error
r_s (Ω)	0.72	0.7276	1.05
r_r (Ω)	0.75	0.7493	-0.09
$L_{\sigma s}$ (H)	0.0058	0.00575	-0.86
L_m (H)	0.0858	0.08583	0.03

Table 5.5 shows the estimated parameters of the DFIG in the WECS when operates under constant wind speed 6 m/s.

5.4 Performance Analysis of the Enhanced MBLC with Online Parameter Estimation

The block diagram of the enhanced MBLC for VSFP wind turbines is shown in Figure 5.14. The enhanced MBLC generates the optimal i_{rd} reference to the vector control on the rotor-side converter for minimising the copper losses of the DFIG in the WECS. The advantage of the enhanced MBLC is that the control law as i_{rd} reference can adapt itself when the parameters of the DFIG change due to temperature or magnetic saturation. Therefore, the operation of the system at the optimum operating point, corresponding to minimum copper losses, is not affected by parameter uncertainties.

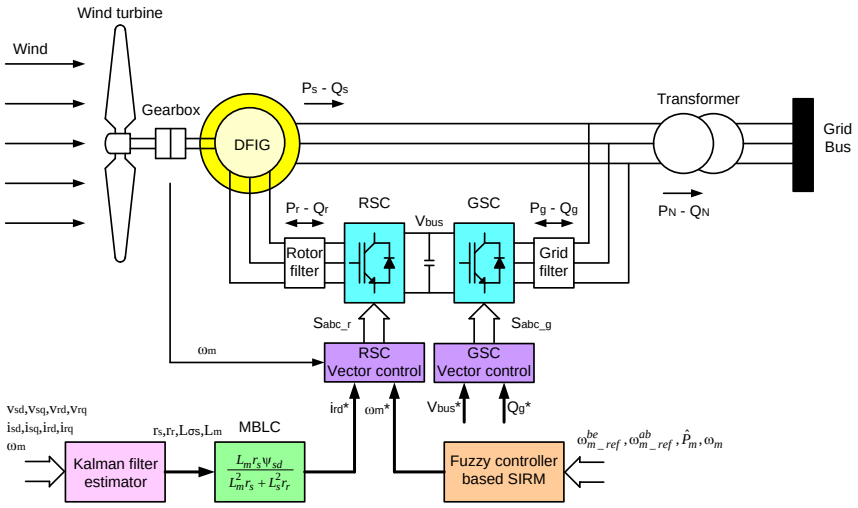

Figure 5.14: Block diagram of enhanced MBLC for WECS

5.4.1 Simulation Results

The simulation results based on the Matlab/Simulink have been used to compare the performance of traditional and enhanced MBLC methods. The efficiency of the two loss minimisation control methods will be compared by measuring the electrical energy generated by the DFIG for the same external condition and the identical SIRM-based fuzzy controller.

Figure 5.15 and 5.16 show the for a constant wind speed of 6 m/s, assuming for r_s an error of +30% and L_m an error of -50%. Section (a) of the figure shows the online DFIG parameter estimation of r_s, r_r, $L_{\sigma s}$ and L_m by using a Kalman filter in comparison with the actual values. Section (b) of the figures shows the wind speed 6 m/s, the *d*-axis rotor current reference, i_{rdref}, the extracted electrical power from the DFIG, P_e and the extracted electrical energy in Wh from the DFIG.

Figure 5.15 shows the WECS performance when the actual values of DFIG parameters do not change during operation. The proposed online parameter estimation return correct estimated values of the parameters in 5 seconds. Therefore, the enhanced MBLC generates the optimal i_{rd} reference of 2.842 A. On the contrary, the traditional MBLC method generates a constant i_{rd} reference of 6.116 A. As a result, in 2 minutes the enhanced MBLC method extracts 2.50 Wh more electrical energy than the traditional MBLC method (+8.31%), i.e. 1,800 Wh/day extra.

Figure 5.16 shows the WECS performance when r_r changes during operation. The proposed online parameter estimation can track the actual value of r_r with a good performance. Similarly to the previous case, the enhanced MBLC method extracts 3.16 Wh electrical energy more than the traditional MBLC method in 2 minutes (+10.82%) , i.e. 2,275 Wh/day extra.

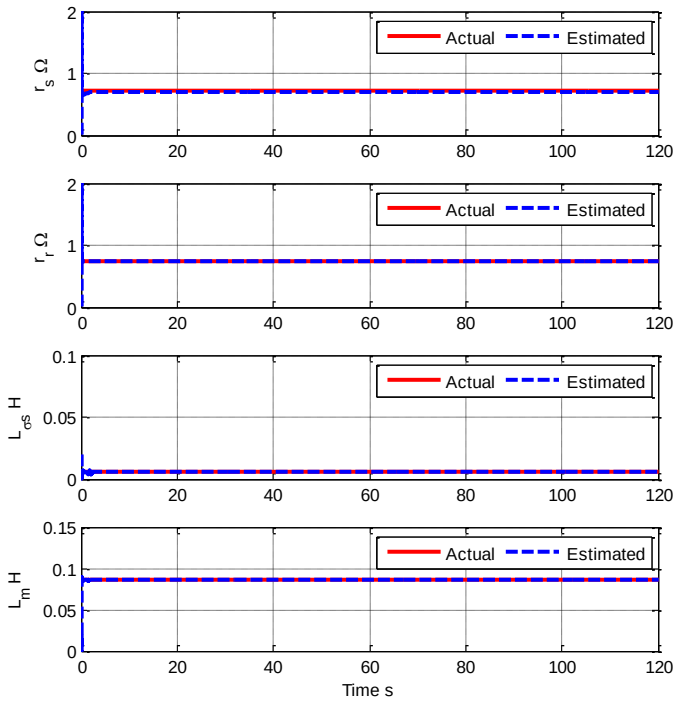

(a)

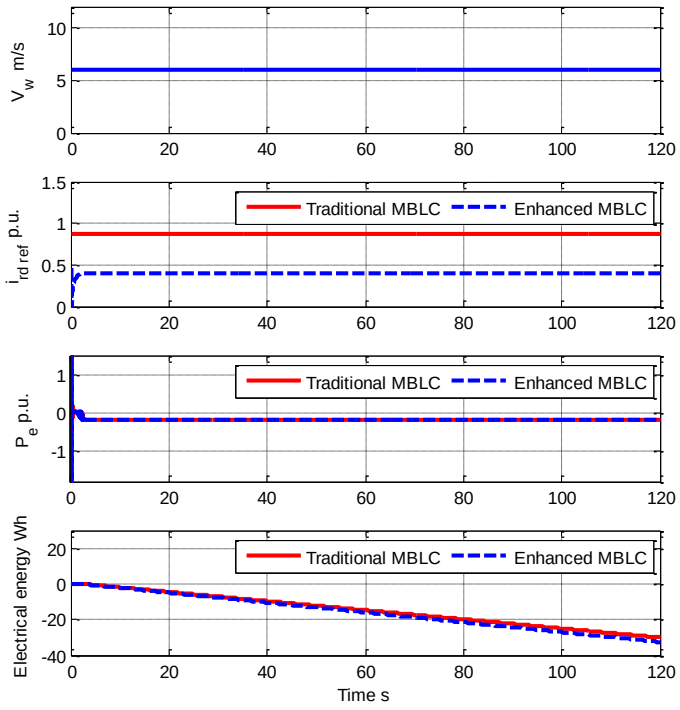

(b)

Figure 5.15: WECS dynamic response controlled by the traditional MBLC and the enhanced MBLC for constant wind speed 6 m/s

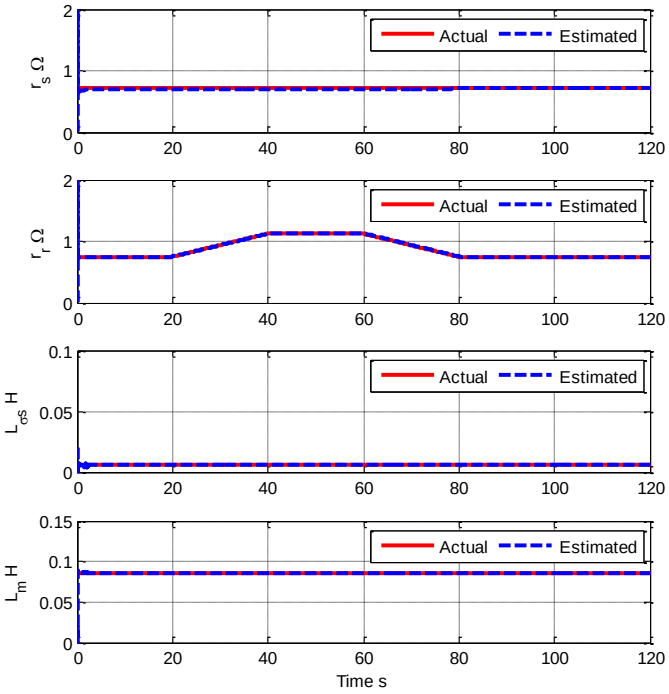

(a)

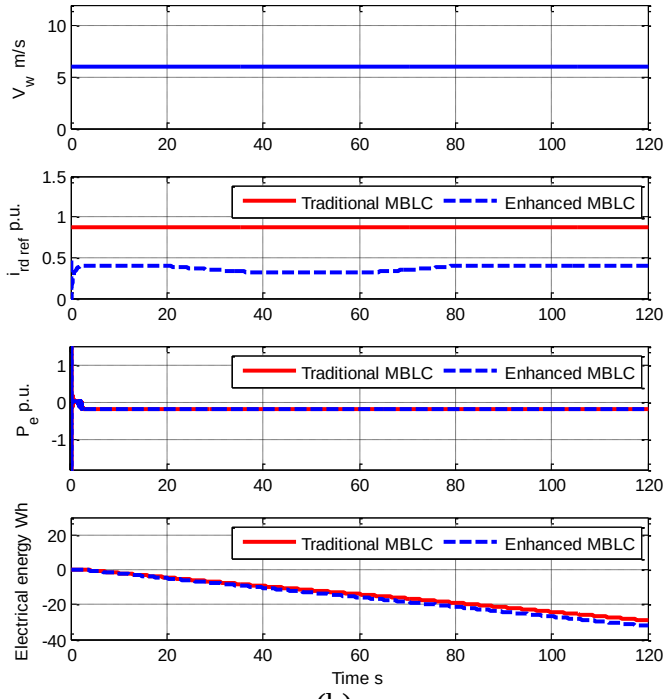

(b)

Figure 5.16: WECS dynamic response controlled by the traditional MBLC and the enhanced MBLC for constant wind speed 6 m/s under r_r variation

Figure 5.17 and 5.18 show the dynamic response with a step-change of the wind speed from 6 to 8 m/s, assuming for r_s an error of +30% and L_m an error of -50%. In this scenario, the fuzzy controller based on SIRM has generated an optimal speed reference of 146.2 and 194.9 rad/s after the step change, respectively.

Figure 5.17 shows the WECS performance when the actual values of the DFIG parameters do not change during operation. The proposed online parameter estimation can reach the actual values very fast and is insensitive to the wind speed step, as shown in Figure 5.17 (a). Therefore, the enhanced MBLC generates the correct optimal i_{rd} reference. As a consequence, the enhanced MBLC method extracts 2.49 Wh more electrical energy than the traditional MBLC method in 2 minutes (+4.66%).

Figure 5.18 shows the WECS performance when r_r changes during operation. The estimator works quite well also in this case, as shown in Figure 5.18 (a). It can be seen that the enhanced MBLC method can extract more electrical energy than the traditional MBLC method by 3.14 Wh in 2 minutes (+5.98%).

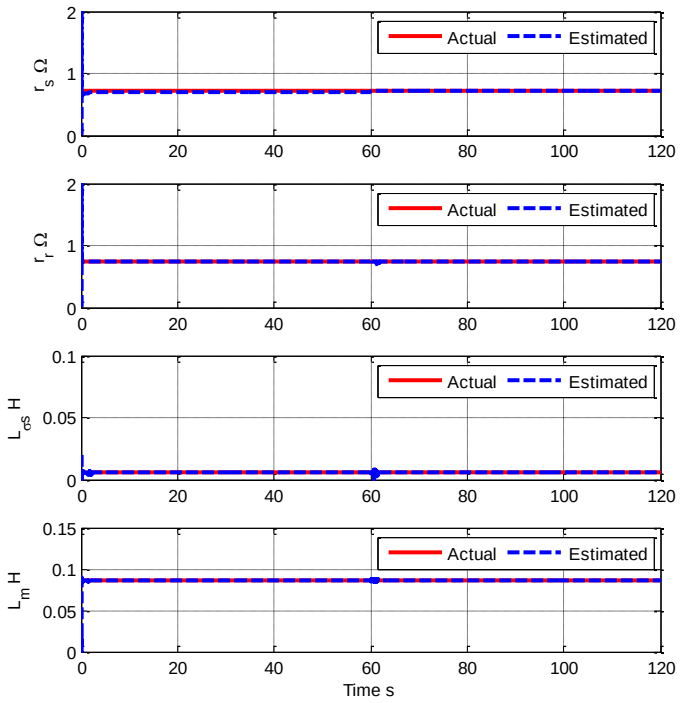

(a)

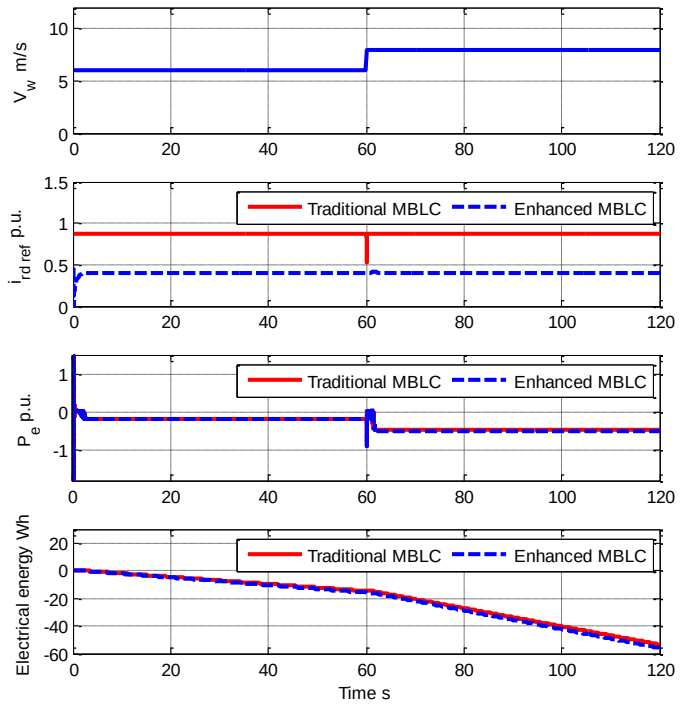

(b)

Figure 5.17: WECS dynamic response controlled by the traditional MBLC and the enhanced MBLC for step-changing wind speed

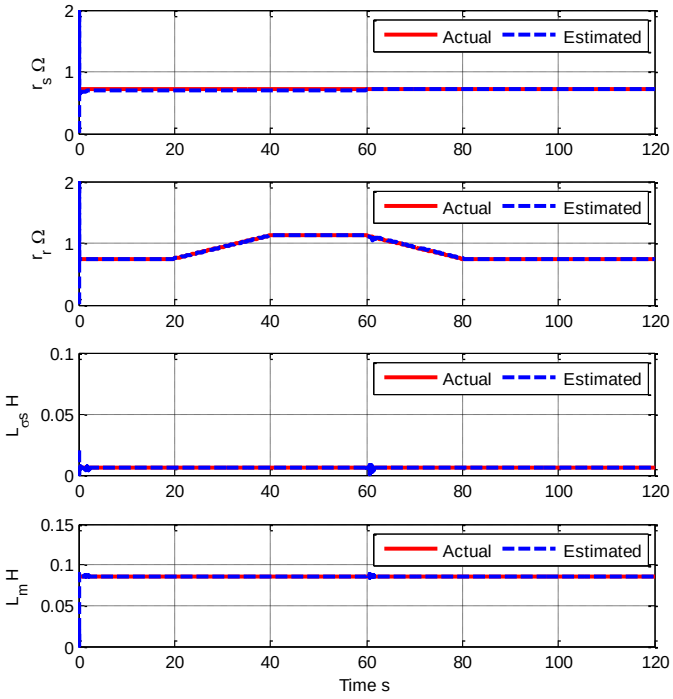

(a)

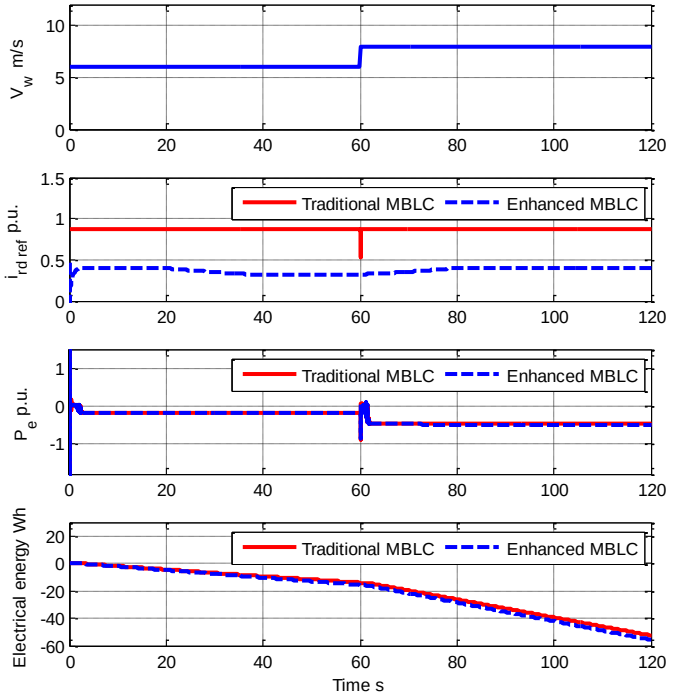

(b)

Figure 5.18: WECS dynamic response controlled by the traditional MBLC and the enhanced MBLC for step-changing wind speed 6 m/s under r_r variation

Figure 5.19 and 5.20 show the dynamic response for variable wind speed with an average $\bar{v}_w$ = 6 m/s, assuming same errors again for r_s and L_m.

Figure 5.19 shows the WECS performance when the actual values of the DFIG parameter do not change during operation. It can be seen that the parameters estimated are now affected by a small noise due to the continuously changing wind conditions, but the tracking is substantially satisfactory as the variation is within 40% of the average estimated value. This also means that the i_{rd} reference is correctly assigned. On the contrary; the traditional MBLC method does not have any adaptation features. As a consequence, the enhanced MBLC method extracts 2.30 Wh more electrical energy than the traditional MBLC method in 2 minutes (+7.21%).

Figure 5.20 shows the WECS performance when the r_r of DFIG parameter changes during operation. The simulation shows that the estimator is not affected by simultaneous variation of the wind speed and the DFIG parameters. In this scenario, the enhanced MBLC method can extract 3.02 Wh more electrical energy than the traditional MBLC method in 2 minutes (+9.75%).

For cases of variable wind speed, the i_{rd} reference of the standard MBLC method is decreased from 6.116 A by the current reference limitation to keep rotor current space vector of two components: i_{rd} reference and i_{rq} reference at its nominal value.

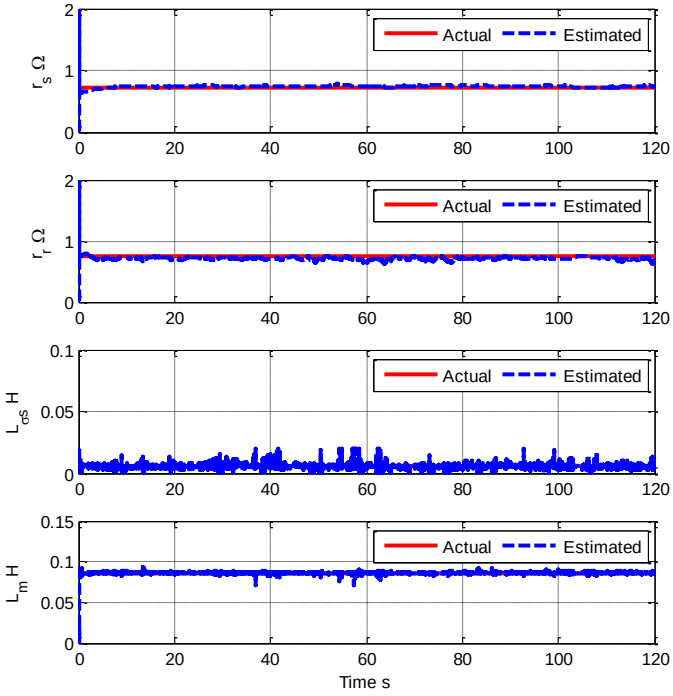

(a)

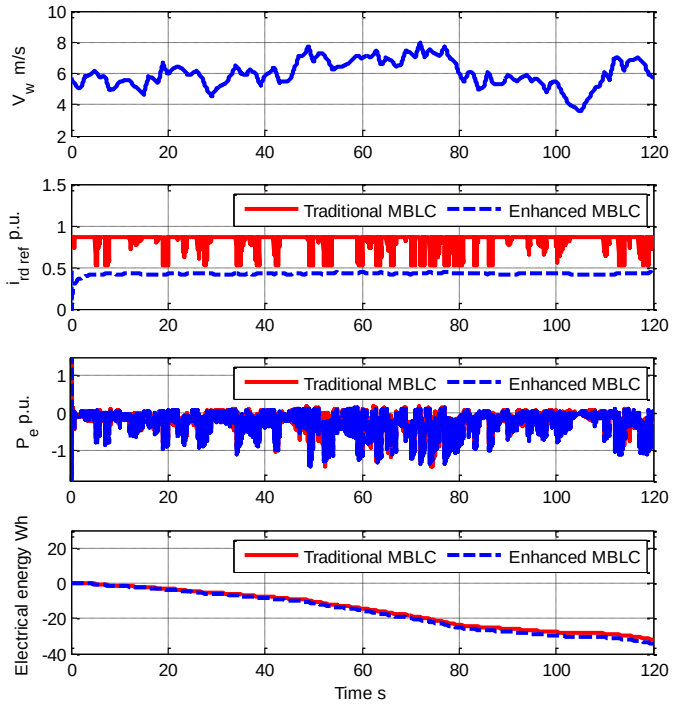

(b)

Figure 5.19: WECS dynamic response controlled by the traditional MBLC and the enhanced MBLC for realistic wind speed

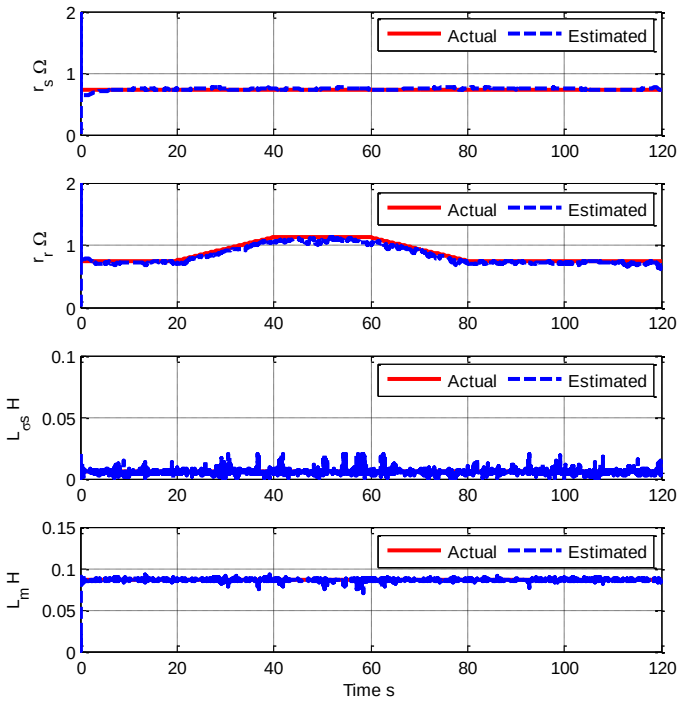

(a)

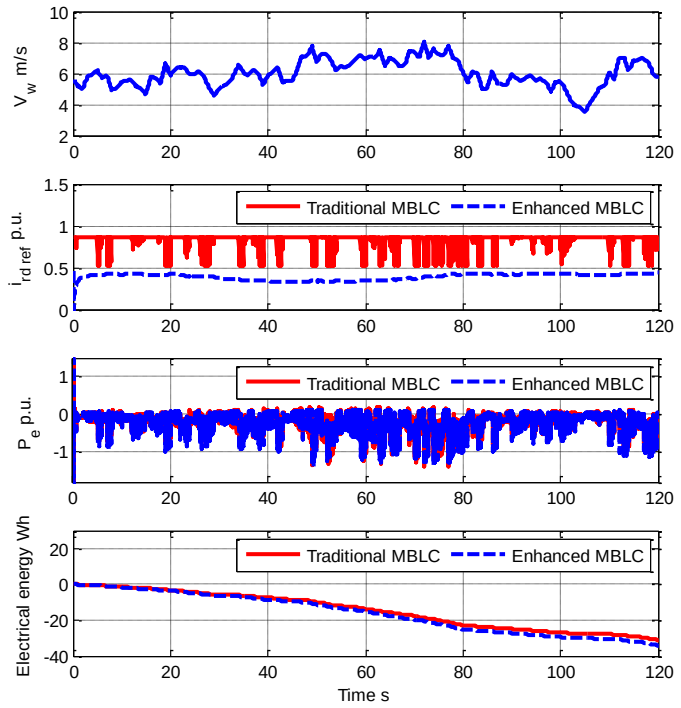

(b)

Figure 5.20: WECS dynamic response controlled by the traditional MBLC and the enhanced MBLC for realistic wind speed 6 m/s under r_r variation

5.5 Summary

This chapter has investigated how the control of the rotor current can be used to minimise DFIG copper losses. Copper loss minimisation control is used to generate the optimal i_{rd} command to manage the reactive power flow and reduce losses, but its efficacy is dependent on the accuracy of the knowledge of machine parameters.

An enhanced MBLC method has been proposed in this chapter to address this problem using an online Kalman filter parameter estimator. The filter operation and performance have been validated by a large number of simulations under various profiles of wind speed and error in the estimation of the DFIG parameters. The results have proven that the enhanced MBLC provides strong robustness against parameter uncertainty and, hence, correct determination of the rotor current reference for copper losses minimisation.

Chapter 6 Performance Analysis of the Proposed Controller

6.1 Introduction

This chapter analyses the performance of the WECS for a VSFP wind turbine controlled simultaneously by the SIRM-based fuzzy control and the enhanced MBLC. The performance of the SIRM-based fuzzy control with errors in the estimation of the wind turbine parameters is analysed in section 6.2. Next, the performance of the enhanced MBLC with errors in the estimation of the DFIG parameters is analysed in section 6.3. Finally, section 6.4 focusses on the prediction of the annual extra electrical energy that can be generated in practice with the proposed controller taking into account the Weibull wind speed distribution.

6.2 Performance Analysis of SIRM-Based Fuzzy Controller

In this section, the SIRM-based fuzzy controller has been compared with the traditional power control technique described in section 2.5.1.3. Figure 6.1 shows that the generator speed reference is provided by the fuzzy SIRM-based controller, while the i_{rd} reference is generated by the traditional MBLC. The dynamic performances of the WECS are tested using a wind speed profile with a step-change and a randomly variable wind speed profile. It has been assumed that the parameters ρ and λ_i are uncertain and

varying between -20% and +20% of their nominal value. Table 6.1 outlines the seven conditions for the air density ρ and λ_i used for the testing.

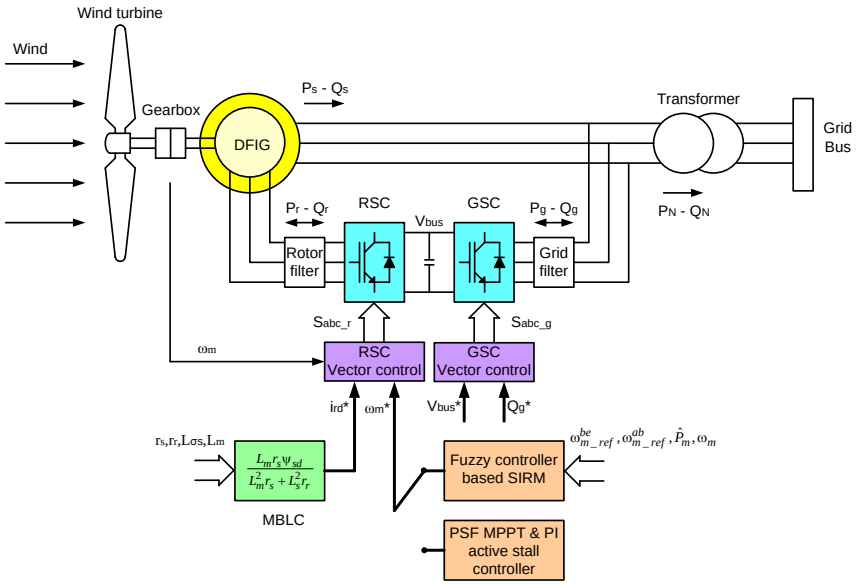

Figure 6.1: Structure of a DFIG WECS controlled by two power control and MBLC

Table 6.1: Study case of error in estimation of ρ and λ_i for performance analysis of both power control systems

Case study	Estimation error of ρ of its nominal value	Estimation error of λ_i of its nominal value
1	0%	0%
2	0%	-20%
3	0%	+20%
4	-20%	0%
5	+20%	0%
6	-20%	-20%
7	+20%	+20%

The simulation study has covered all the seven cases indicated above in Table 6.1. However, for brevity, only the figures referring to cases 1 and 2 have been reported in this chapter, while the other cases are shown in Appendix B.

6.2.1 Constant Wind Speed with Step-Changes

In these tests, it has been assumed that the wind speed is constant, but it changes as a step at certain instants, namely from 5 to 8 m/s at t = 60 sec. and then from 8 to 12 m/s at t = 120 sec. In particular, the second step involves a transition from MPPT to power limitation control using the active stall control. The quantities shown in the figures are the wind speed, V_w, the generator speed, ω_m, the magnitude of stator current, i_s, the magnitude of rotor current, i_r, the electromagnetic torque, T_{em}, the mechanical power extracted from the turbine, P_m, the power coefficient, C_p and the electrical energy.

Figure 6.2 shows the dynamic response of the system with the two controllers when the estimation on the air density and λ_i have no errors. The traditional control and the SIRM-based fuzzy controller can generate optimal speed reference from 121.8 rad/s (or 121.8/157 = 0.775 p.u.) to 194.9 rad/s (or 194.9/157 = 1.241 p.u.) that corresponds to the maximum power coefficient, C_{pmax} of the wind turbine of 0.48 when wind speed steps from 5 to 8 m/s. When wind speed changes up from 8 to 12 m/s at t = 120 sec, which is above the rated wind speed of 10 m/s, the two control systems can generate the speed reference from 194.9 rad/s to 184.9 rad/s (or 1.177 p.u.) that corresponds to the rated power point of the wind turbine of 5 kW (or 1 p.u.). The two electrical energies generated by the DFIG give the same value around 127.6 Wh. It can be seen that the

SIRM-based fuzzy controller gives the same performance as the traditional control in both steady state and dynamic response.

Figure 6.3 shows the example dynamic response for an error in the estimation of λ_i of -20%. The traditional power control based on PSF MPPT cannot generate the correct speed reference corresponding to the maximum power coefficient, C_{pmax} of 0.48. On the contrary, the SIRM-based fuzzy controller can still generate the optimal speed reference, hence, produces more electrical energy than the traditional power control. When wind speed is above the rated wind speed, the two control systems work well and in similar way.

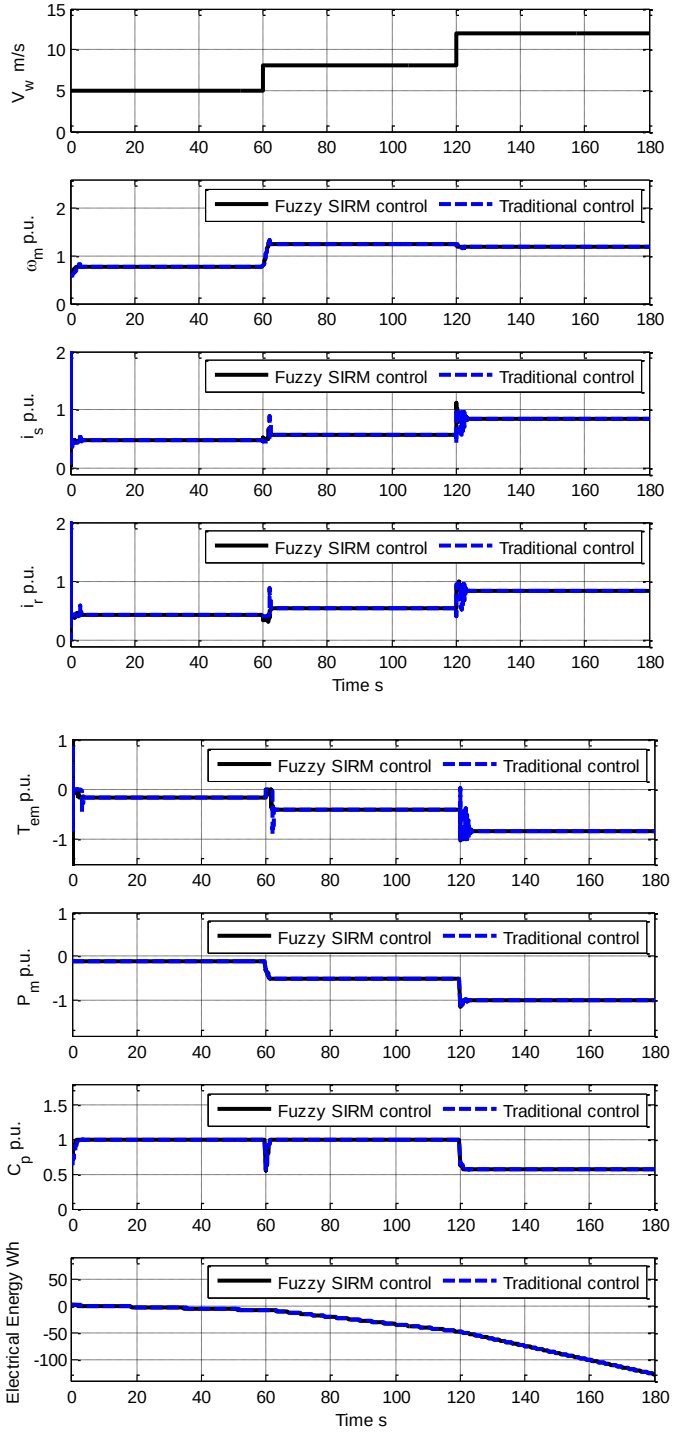

Figure 6.2: WECS dynamic response controlled by the traditional power control and the SIRM-based fuzzy controller for step-up-changing wind speed with no error on the estimation of air density and λ_i (case 1)

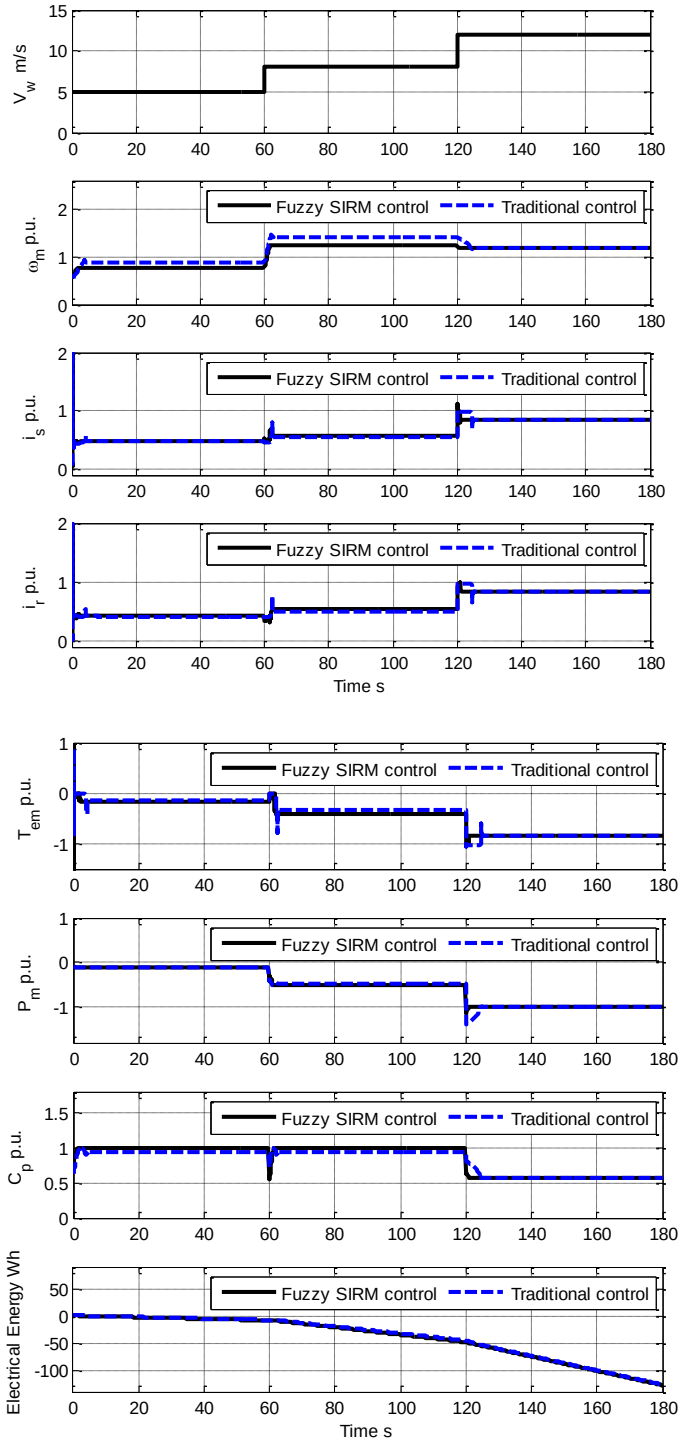

Figure 6.3: WECS dynamic response controlled by the traditional power control and the SIRM-based fuzzy controller for step-up-changing wind speed with estimating of λ_i in error of -20% (case 2)

Table 6.2: Energy generated by the DFIG in WECS of proposed power control in comparison with a traditional power control with the estimation of ρ and λ_i in 3 minutes under the step-changing wind speed from 5 to 8 m/s and the 8 to 12 m/s

Case study	k_{opt} calculation PSF MPPT	DFIG energy traditional power control (Wh)	DFIG energy proposed power control (Wh)	Extra energy from proposed power control
1	0.1186	-127.6	-127.7	+0.08%
2	0.0754	-126.4	-127.7	+1.03%
3	0.1750	-123.6	-127.7	+3.32%
4	0.0945	-127.3	-127.7	+0.95%
5	0.1418	-126.6	-127.7	+0.31%
6	0.0603	-126.1	-127.7	+1.27%
7	0.2100	-118.6	-127.7	+7.67%

The different cases of Table 6.1 have been analysed in similar way and the figures are not shown in this thesis. However, Table 6.2 reports the difference in the amount of electrical energy generated in comparison with the traditional control.

6.2.2 Randomly Variable Wind Speed

The performances of the two control systems have been then compared using a realistic wind speed profile described in Chapter 4 for the uncertain aerodynamic conditions of Table 6.1. Tests have been repeated for low wind speed for which $\bar{v}_w$ value is between 4 and 6 m/s, medium wind speed for which $\bar{v}_w$ value is between 7 and 10 m/s, and high wind speed for which $\bar{v}_w$ value is between 11 and 14 m/s, respectively.

Figure 6.4 and 6.5 show the dynamic response for the two controllers with low wind speed, initially with no error on the estimation of the air density and λ_i and then with an error of -20% on λ_i with randomly variable wind speed profile of $\bar{v}_w$ = 6 m/s.

For Figure 6.4, as the wind speed changes in practice between 4 and 8 m/s, the operations of the wind turbine are always below the rated wind speed. The traditional control and the SIRM-based fuzzy controller attempt to generate optimal speed reference that corresponds to the maximum power operating point of the wind turbine according to wind speed between 320W. (or 320/5000 = 0.064 p.u.) to 2561W. (or 2561/5000 = -0.512 p.u.). The power coefficient, C_p of the wind turbine reaches near the maximum value of 0.48 for all wind speed profiles. It can be observed that the traditional control can extract more mechanical power than the SIRM-based fuzzy controller and it generates 0.69% more electrical energy the period of 3 minutes. This is because the continuous variation of the wind speed influences the estimation of the optimal speed reference, which oscillates slightly more than the traditional controller, which is instead not affected by it.

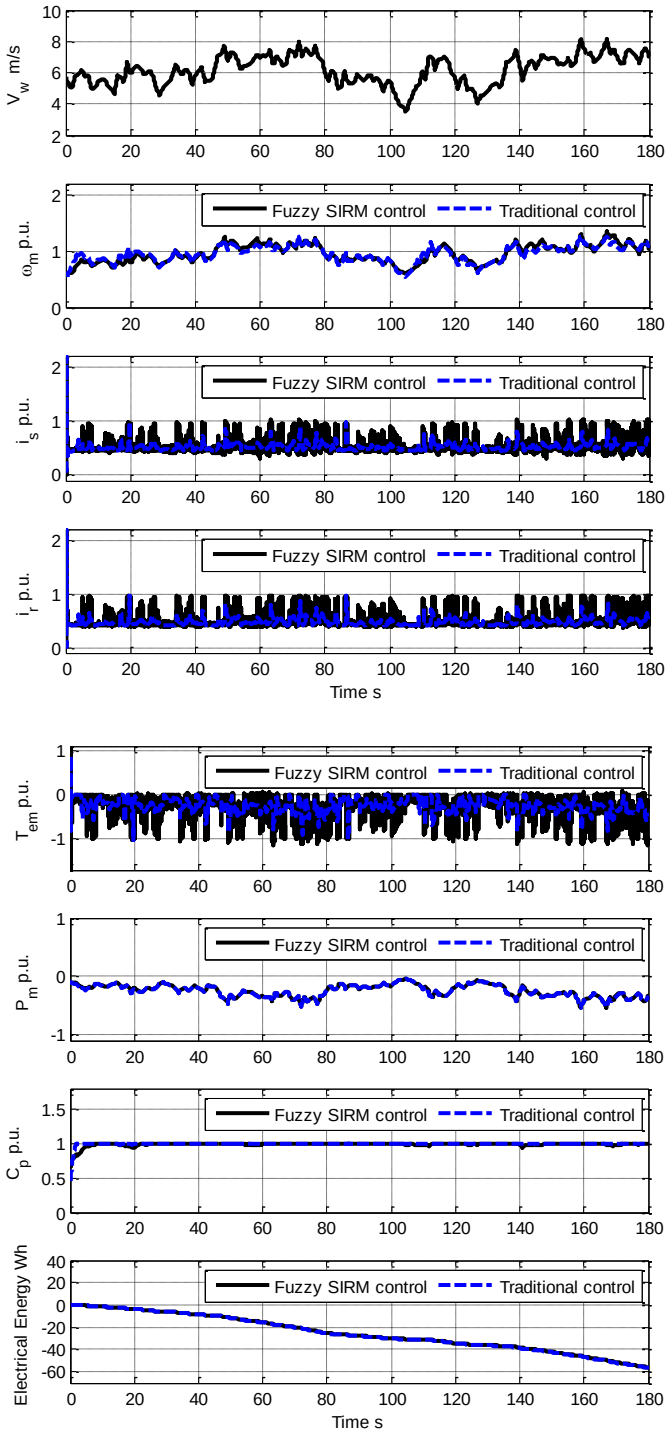

Figure 6.4: WECS dynamic response controlled by the traditional power control and the SIRM-based fuzzy controller for low real wind speed profile ($\bar{v}_w$ = 6 m/s) with no error on the estimation of air density and λ_i (case 1)

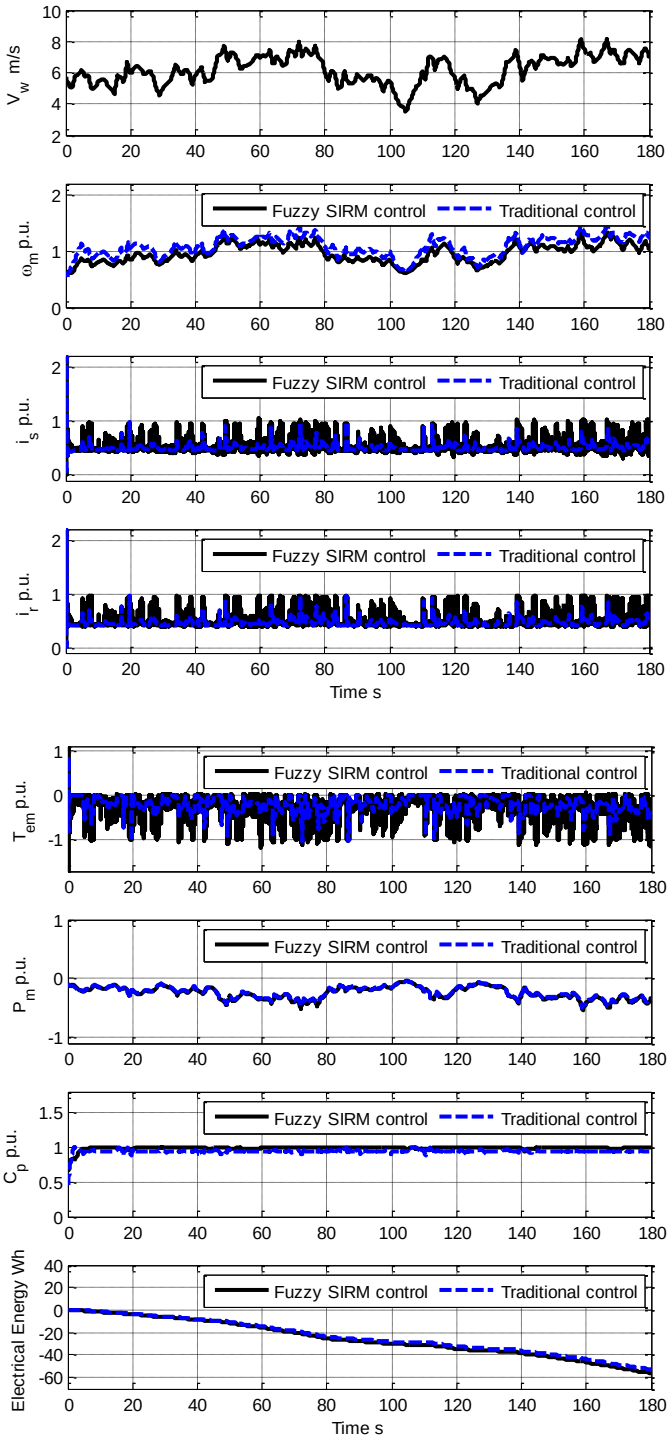

Figure 6.5: WECS dynamic response controlled by the traditional power control and the SIRM-based fuzzy controller for low real wind speed profile ($\bar{v}_w$ = 6 m/s) with estimating of λ_i in error of -20% (case 2)

Figure 6.5 shows the dynamic response when there is an error of -20% on λ_i. The error in the estimation of λ_i affects the MPPT efficiency of the PSF method because k_{opt} is different from the maximum power of wind turbine condition of 0.1186.

The SIRM-based fuzzy controller can instead correctly identify the maximum power point and, as a result, it generates 6.13% more electrical energy than the traditional power control over a period of 3 minutes.

Table 6.3: Energy generated by the DFIG in WECS of proposed power control in comparison with a traditional power control with the estimation of ρ and λ_i in 3 minutes under the low real wind speed profile ($\bar{v}_w$ = 6 m/s)

Case study	k_{opt} calculation PSF MPPT	DFIG energy traditional power control (Wh)	DFIG energy proposed power control (Wh)	Extra energy from proposed power control
1	0.1186	-56.57	-56.18	+0.69%
2	0.0754	-53.02	-56.27	+6.13%
3	0.1750	-52.12	-56.12	+6.65%
4	0.0945	-55.59	-56.18	+1.06%
5	0.1418	-55.82	-56.15	+0.59%
6	0.0603	-49.45	-56.26	+13.77%
7	0.2100	-47.05	-56.22	+19.49%

The simulations have been repeated for all the other conditions, and the summary of the results is reported in Table 6.3. The efficiency of the traditional MPPT is reduced when the k_{opt} is moved from the maximum operating point by error in the estimation of ρ and

λ_i. It can be seen that the error in the estimation of λ_i makes a much more influence in MPPT efficiency than the error in ρ. The traditional MPPT with an error of +20% on λ_i (case 3) and an error of +20% in ρ (case 5) generate 7.87% and 1.33% less energy than no error in case 1. The SIRM-based fuzzy controller has provided an adaptive control which can find the maximum power point under the error of λ_i and ρ. Therefore, the proposed control can extract more energy than the traditional control. For example, in case of an error of +20% in the estimation of λ_i and ρ, the SIRM-based fuzzy controller generates 19.49% more electrical energy than the traditional power control over a period of 3 minutes.

Figure 6.6 shows the case of an average wind speed $\bar{v}_w$ = 8 m/s. The wind speed profile varies between 6 to 10 m/s, which means that the operations are below the rated wind speed. Similarly to the previous case, the traditional control extracts more mechanical power than the SIRM-based fuzzy controller if there are no errors in the estimation of the parameters and it generates 0.88% more electrical energy.

Figure 6.7 shows the dynamic response with an error of -20% in the estimation of λ_i. It is evident that the PSF method is not capable of tracking the optimal speed reference correctly and, hence, the power coefficient is less than the maximum. The SIRM-based fuzzy controller tracks the optimal reference speed correctly and, hence, produces more extracted mechanical power and hence 3.75% more generated electrical energy than the traditional power control.

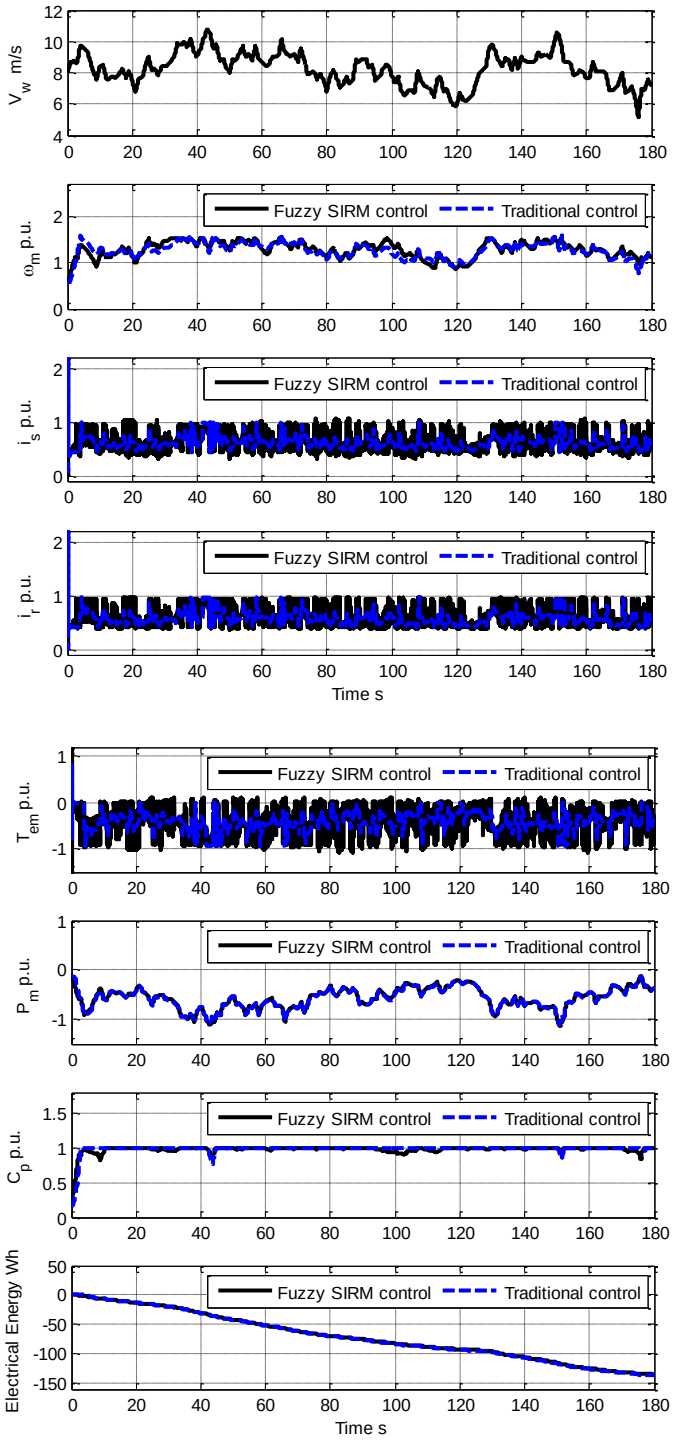

Figure 6.6: WECS dynamic response controlled by the traditional power control and the SIRM-based fuzzy controller for medium real wind speed profile ($\bar{v}_w$ = 8 m/s) with no error on the estimation of air density and λ_i (case 1)

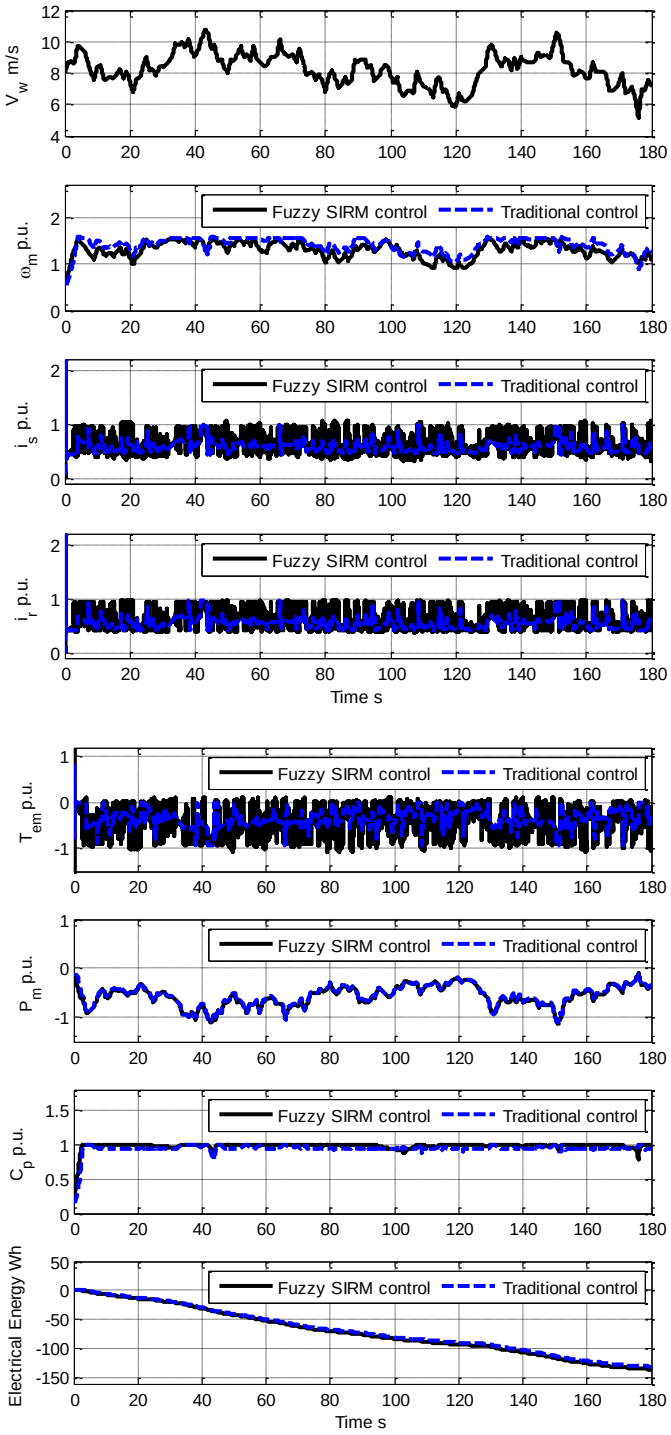

Figure 6.7: WECS dynamic response controlled by the traditional power control and the SIRM-based fuzzy controller for medium real wind speed profile ($\bar{v}_w$ = 8 m/s) with estimating of λ_i in error of -20% (case 2)

Table 6.4: Energy generated by the DFIG in WECS of proposed power control in comparison with a traditional power control with the estimation of ρ and λ_i in 3 minutes under the medium real wind speed profile ($\bar{v}_w$ = 8 m/s)

Case study	k_{opt} calculation PSF MPPT	DFIG energy traditional power control (Wh)	DFIG energy proposed power control (Wh)	Extra energy from proposed power control
1	0.1186	-136.3	-135.1	-0.88%
2	0.0754	-130.8	-135.7	+3.75%
3	0.1750	-126.7	-135.7	+7.10%
4	0.0945	-134.7	-135.4	+0.52%
5	0.1418	-134.2	-135.3	+0.82%
6	0.0603	-127.0	-135.4	+6.61%
7	0.2100	-113.6	-135.8	+19.54%

Table 6.4 shows the performance of the SIRM-based fuzzy controller and the traditional power control in the DFIG wind-energy generation for tracking maximum operating point with the error in the estimation of ρ and λ_i for the cases 1-7 in Table 6.1. The performance of the proposed control algorithm applied medium real wind speed profile ($\bar{v}_w$ = 8 m/s) gives a similar trend compared with low real wind speed profile ($\bar{v}_w$ = 6 m/s).

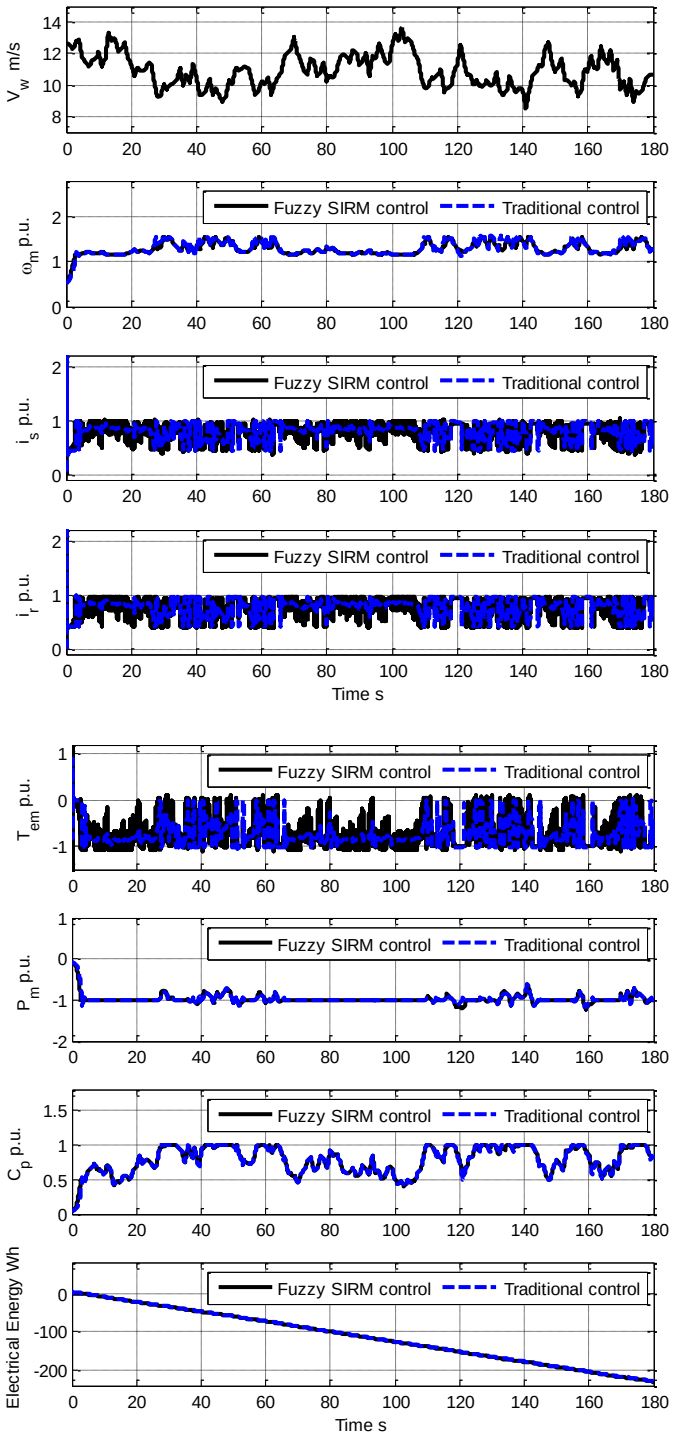

Figure 6.8: WECS dynamic response controlled by the traditional power control and the SIRM-based fuzzy controller for high real wind speed profile ($\bar{v}_w$ = 11 m/s) with no error on the estimation of air density and λ_i (case 1)

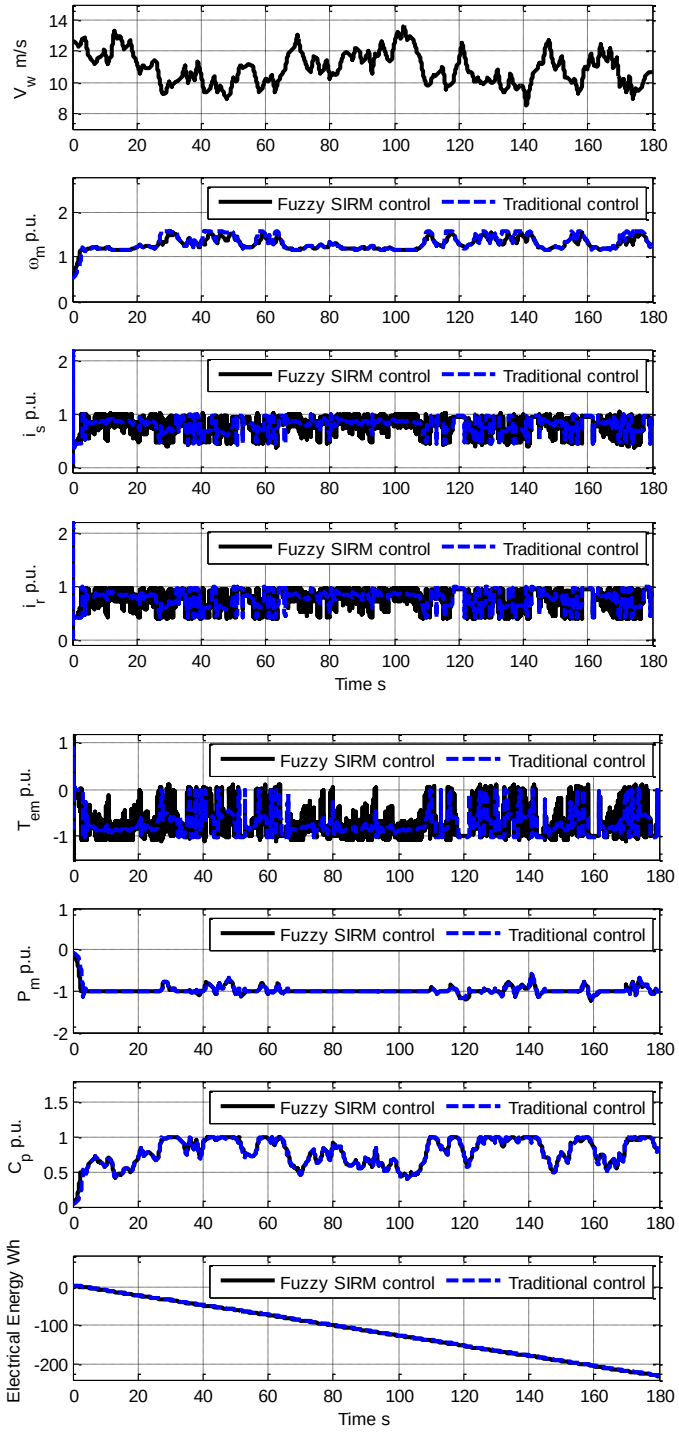

Figure 6.9: WECS dynamic response controlled by the traditional power control and the SIRM-based fuzzy controller for high real wind speed profile ($\bar{v}_w$ = 11 m/s) with estimating of λ_i in error of -20% (case 2)

Figure 6.8 shows the dynamic response for high wind speed ($\bar{v}_w$ = 11 m/s) which features frequent transitions of the rated wind speed and, hence, it involves two different operating modes of the wind turbine. Similar to the previous cases, the traditional control operates better if there are no estimation errors. However, it can be seen that the SIRM-based fuzzy control gives more mechanical power than the traditional power control below the rated wind speed when λ_i has an error of -20%, while both power controls have a similar response above the rated wind speed as shown in Figure 6.9.

The various curves have been analysed, and the results have been summarised in Table 6.5.

Table 6.5: Energy generated by the DFIG in WECS of proposed power control in comparison with a traditional power control with the estimation of ρ and λ_i in 3 minutes under the high real wind speed profile ($\bar{v}_w$ = 11 m/s)

Case study	**k_{opt} calculation PSF MPPT**	**DFIG energy traditional power control (Wh)**	**DFIG energy proposed power control (Wh)**	**Extra energy from proposed power control**
1	0.1186	-229.1	-230.1	+0.44%
2	0.0754	-229.4	-230.4	+0.44%
3	0.1750	-223.4	-230.3	+3.09%
4	0.0945	-229.5	-230.4	+0.39%
5	0.1418	-227.4	-230.0	+1.14%
6	0.0603	-229.4	-230.4	+0.44%
7	0.2100	-214.9	-230.3	+7.17%

6.3 Performance Analysis of the Enhanced MBLC

This section compares the performance of the enhanced MBLC and the traditional MBLC. From Figure 6.10, the optimal i_{rd} reference was provided by the enhanced MBLC and the traditional MBLC while the generator speed reference was generated by the fuzzy controller based on SIRM. To test the dynamic performance of the WECS controller by the two loss minimisation algorithms, the wind speed profile has been changed in steps and with a random distribution using various errors in the estimation of the DFIG parameters.

Table 6.6: Study case of error in estimation of r_s, r_r, $L_{\sigma s}$ and L_m

Case study	Variation of r_s from nominal value	Variation of r_r from nominal value	Variation of $L_{\sigma s}$ from nominal value	Variation of L_m from nominal value
1	0%	0%	0%	0%
2	+50%	0%	0%	0%
3	-50%	0%	0%	0%
4	0%	+50%	0%	0%
5	0%	-50%	0%	0%
6	0%	0%	+50%	0%
7	0%	0%	-50%	0%
8	0%	0%	0%	+50%
9	0%	0%	0%	-50%
10	0%	-50%	0%	-50%

6.3.1 Wind Speed Changing with Fixed Steps

To test the dynamic of the WECS controlled by the two loss minimisation control, step-changing wind speed is applied under uncertain DFIG parameters in Table 6.6.

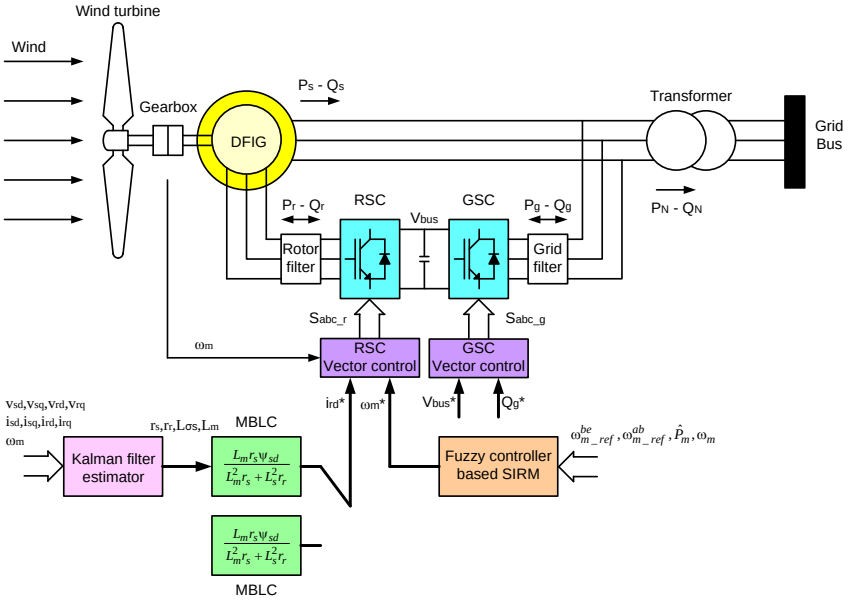

Figure 6.10: Structure of a DFIG WECS controlled by two loss minimisation and fuzzy control based SIRM

Figure 6.11 shows the dynamic response without error on the estimation of the parameters r_s, r_r, $L_{\sigma s}$ and L_m. Figure 6.12 shows instead the response in case the stator resistance r_s is affected by an error of +50%. The other figures are not shown and reported in Appendix B.

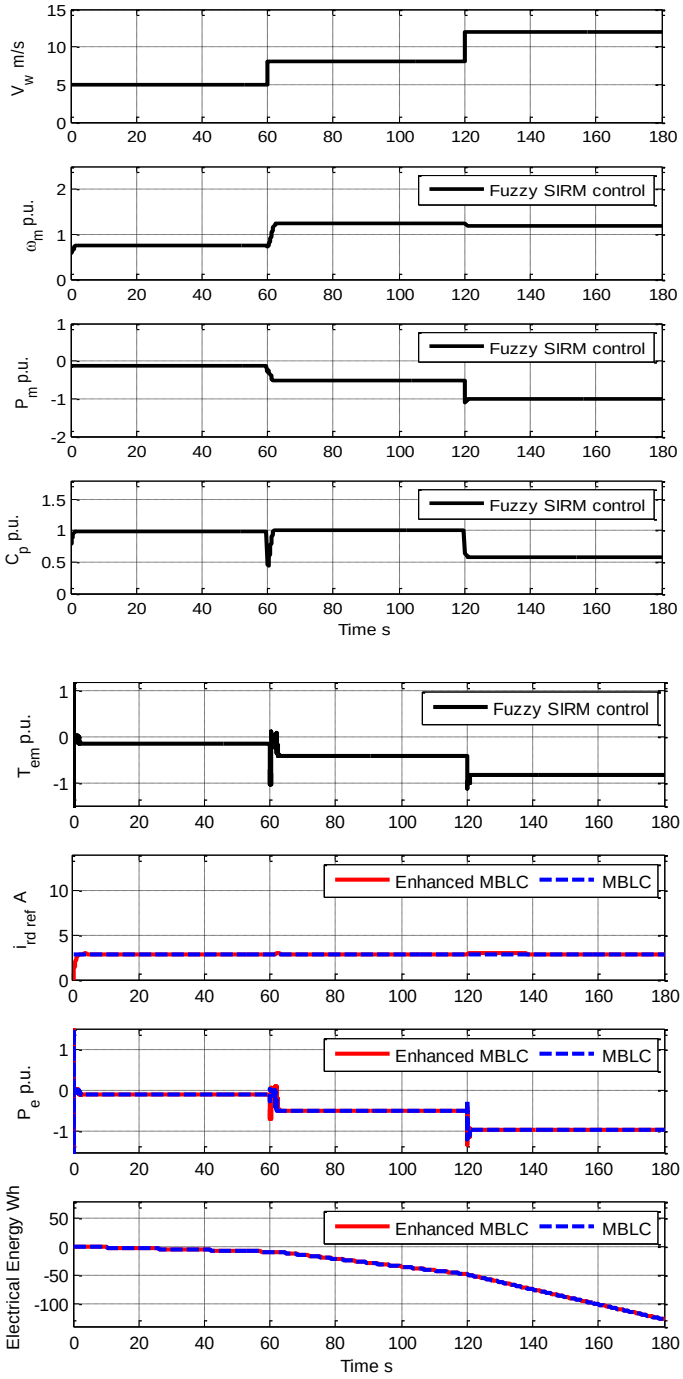

Figure 6.11: WECS dynamic response controlled by the traditional MBLC and the enhanced MBLC for step-up-changing wind speed with no error on the estimation of r_s, r_r, $L_{\sigma s}$ and L_m (case 1)

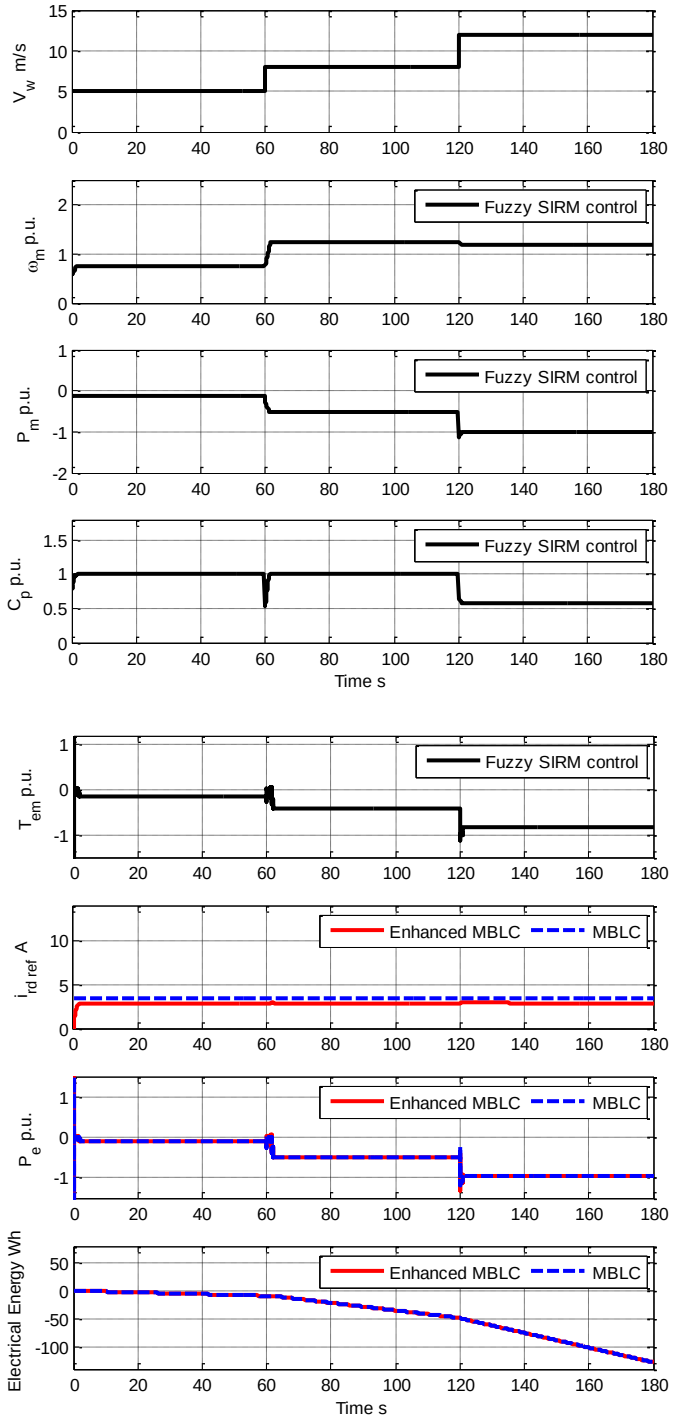

Figure 6.12: WECS dynamic response controlled by the traditional MBLC and the enhanced MBLC for step-up-changing wind speed with error in estimation r_s of +50%, r_r of 0%, $L_{\sigma s}$ of 0% and L_m of 0% (case 2)

Table 6.7: Energy generated by the DFIG in WECS of enhanced MBLC in comparison with MBLC under the estimation of r_s, r_r, $L_{\sigma s}$ and L_m in 3 minutes under the step-changing wind speed from 5 to 8 m/s and the 8 to 12 m/s

Case study	i_{rd_ref} calculation MBLC (A)	DFIG energy MBLC (Wh)	DFIG energy enhanced MBLC (Wh)	Extra energy from enhanced MBLC
1	2.842	-127.5	-127.5	+0.00%
2	3.469	-127.5	-127.5	+0.00%
3	1.842	-127.3	-127.5	+0.16%
4	2.235	-127.5	-127.5	+0.00%
5	3.900	-127.2	-127.5	+0.24%
6	2.746	-127.5	-127.5	+0.00%
7	2.941	-127.5	-127.5	+0.00%
8	1.938	-127.3	-127.5	+0.16%
9	5.307	-125.5	-127.5	+1.60%
10	7.438	-123.3	-127.5	+3.41%

The various curves have been analysed, and the results have been summarised in Table 6.7. The efficiency of the traditional MBLC is deteriorated because the control law, i_{rd} reference, from (2.54) cannot keep an accurate determination of the minimum loss condition, causing the error in estimation of r_s, r_r, $L_{\sigma s}$ and L_m. The analysis from Table 6.7 shows that the parameter of the DFIG mostly affecting the efficiency in the MBLC method is L_m. The traditional MBLC with an error of -50% on L_m produces 1.60% less electrical energy than the case of no error in 3 minutes. The enhanced MBLC can adapt itself the control law for the minimum loss condition by the online

parameter estimation. Therefore, the enhanced MBLC can extract more electrical energy than the traditional MBLC when the parameters of the DFIG change.

6.3.2 Randomly Variable Wind Speed

The tests have been repeated with randomly variable wind speed and, specifically, for the low, medium and high average wind defined in the previous sections.

As an example, Figure 6.13 shows the dynamic response for low wind and no error, while Figure 6.14 shows the response for the same wind for error of +50 % on the stator resistance.

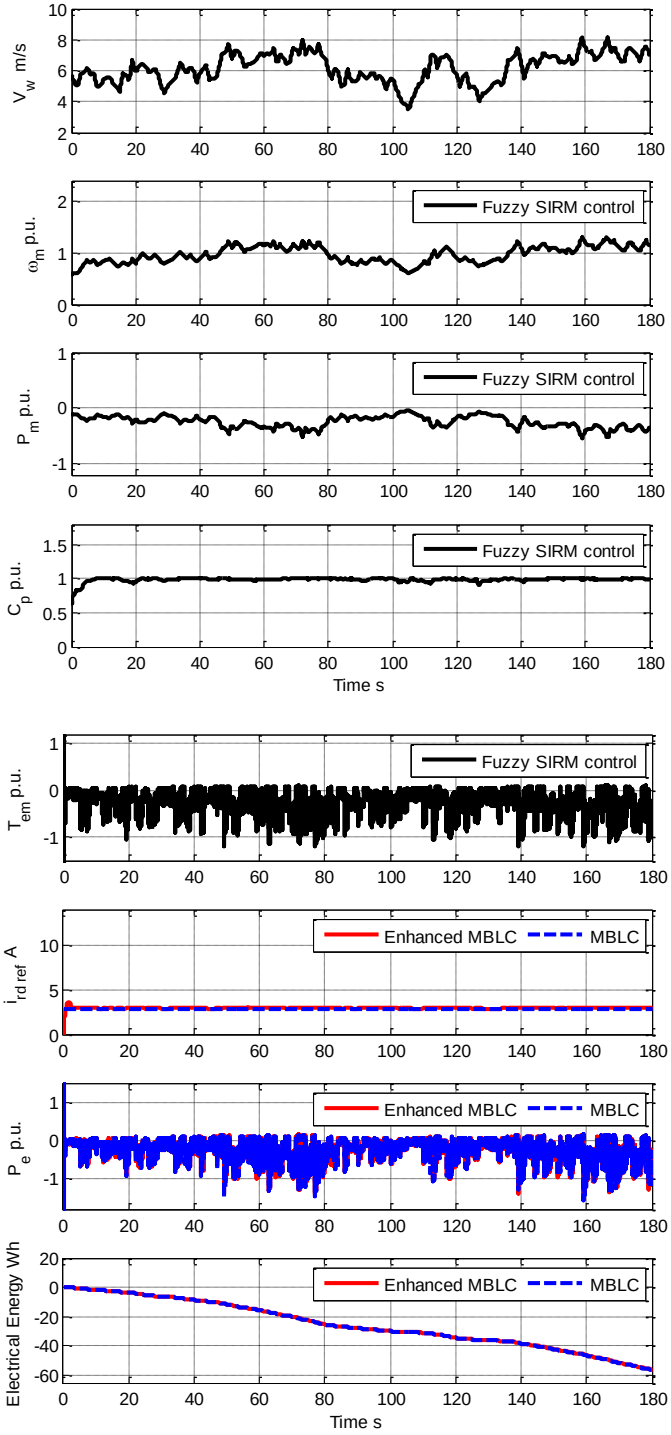

Figure 6.13: WECS dynamic response controlled by the traditional MBLC and the enhanced MBLC for low real wind speed profile ($\bar{v}_w$ = 6 m/s) with no error on the estimation of r_s, r_r, $L_{\sigma s}$ and L_m (case 1)

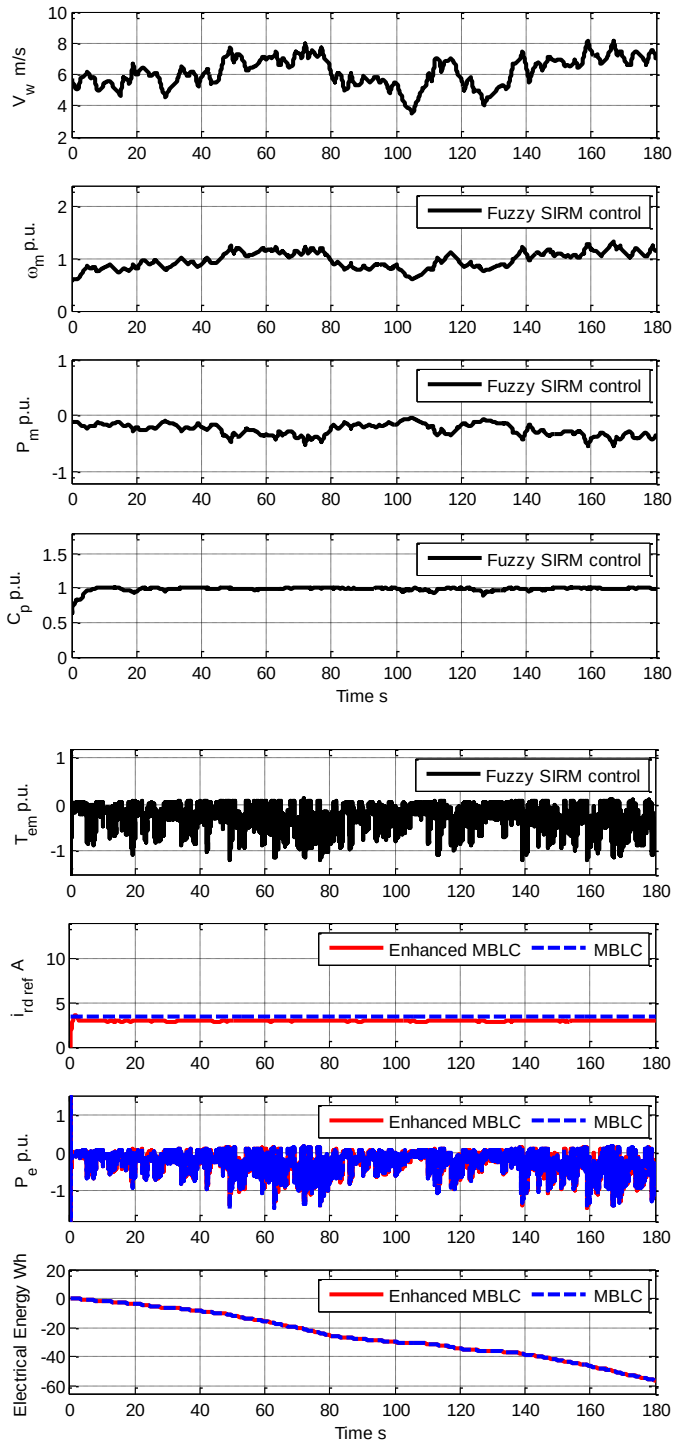

Figure 6.14: WECS dynamic response controlled by the traditional MBLC and the enhanced MBLC for low real wind speed profile ($\bar{v}_w$ = 6 m/s) with error in estimation r_s of +50%, r_r of 0%, $L_{\sigma s}$ of 0% and L_m of 0% (case 2)

The results of the simulations are summarised in Table. 6.8. As can be seen from the table, the performance of the enhanced MBLC method applied low real wind speed profile ($\bar{v}_w$ = 6 m/s) gives a similar trend compared with step-changing wind speed from 5 to 8 m/s and the 8 to 12 m/s.

Table 6.8: Energy generated by the DFIG in WECS of an enhanced MBLC in comparison with a MBLC with the estimation of r_s, r_r, $L_{\sigma s}$ and L_m in 3 minutes under the low real wind speed profile ($\bar{v}_w$ = 6 m/s)

Case study	**i_{rd_ref} calculation MBLC (A)**	**DFIG energy MBLC (Wh)**	**DFIG energy enhanced MBLC (Wh)**	**Extra energy from enhanced MBLC**
1	2.845	-56.12	-56.03	-0.16%
2	3.469	-55.98	-56.01	+0.05%
3	1.842	-55.78	-56.12	+0.61%
4	2.235	-56.00	-56.09	+0.16%
5	3.900	-55.71	-56.01	+0.54%
6	2.746	-56.13	-56.11	-0.04%
7	2.941	-56.11	-56.09	-0.04%
8	1.938	-55.82	-56.14	+0.57%
9	5.307	-53.98	-56.10	+3.93%
10	7.438	-50.40	-56.15	+11.41%

Table 6.7 and Table 6.8 show that the error in the estimation of L_m produces the most influence in loss minimisation control efficiency in comparison on r_s, r_r,and $L_{\sigma s}$. In case of an error of -50% in the estimation r_r, and L_m, the enhanced MBLC generates 3.14% and 11.41% more electrical energy from the DFIG than the traditional MBLC in 3 minutes length under step wind speed and real wind speed, respectively. The key of the enhanced MBLC method is that the parameters of DFIG can estimate online through the Kalman filter method. Therefore, the enhanced MBLC method can find the minimum copper loss operating point of the DFIG under uncertainties of DFIG parameters. The proposed algorithm gives higher performance than the traditional MBLC method.

6.4 Long-Term Estimation of Annual Energy Production

In this section, the annual electrical energy generation of the DFIG wind energy conversion system for a VSFP wind turbine by using the optimal control is analysed. To investigate the extra annual energy yield obtained from using the proposed control, it is necessary to know the probability density distribution of the wind speed for a specific site. The structure of the WECS controlled by the optimal control algorithm using the SIRM-based fuzzy controller and the enhanced MBLC and the traditional control algorithm using the traditional power control and the standard MBLC is shown in Figure 6.15.

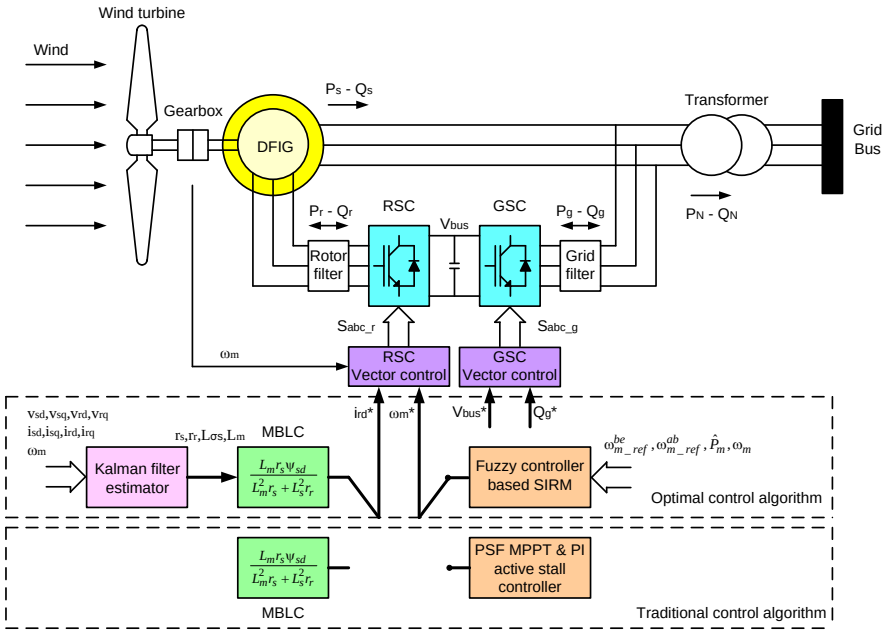

Figure 6.15: Structure of a DFIG WECS controlled optimal control (fuzzy controller based SIRM & enhanced MBLC) and traditional control (PSF MPPT & active stall & MBLC)

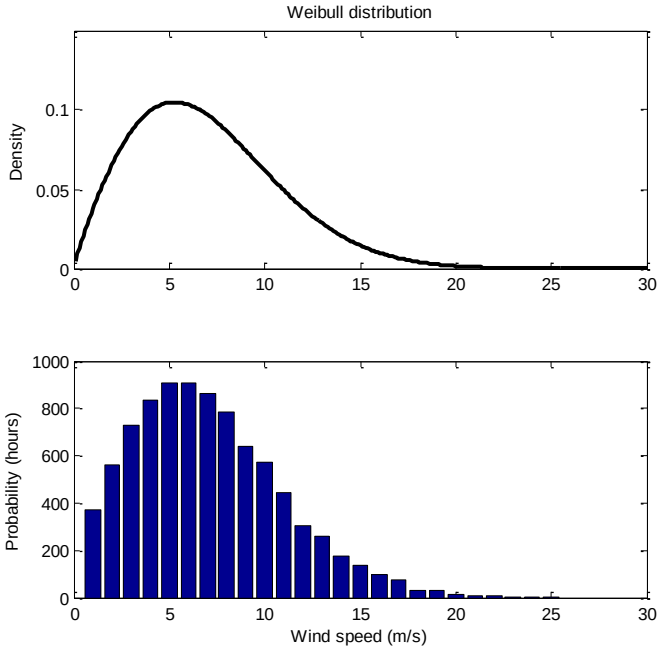

Figure 6.16: Weibull wind speed distribution with mean wind speed = 7.5 m/s

The annual energy produced by the WECS station is a function of wind speed which is presented by a Weibull distribution function [116]. The Weibull distribution is used to calculate number of hours at any wind speed per year. The Weibull function can be expressed as follows:

$$f(v_w) = \frac{k}{c}\left(\frac{v_w}{c}\right)^{k-1} \exp\left[-\left(\frac{v_w}{c}\right)^k\right] \tag{7.1}$$

where k is shape factor and c is scale factor. $f(v_w)$ denotes a probability density distribution function of wind speed, v_w.

In this thesis, the wind speed data was taken from the weather stations of Plymouth, UK for the year 2005 which the mean wind speed for the whole year = 7.5 m/s and the standard deviation = 3.9 m/s[117]. The information above is used for calculating the shape factor and scale factor to fit the Weibull distribution with Matlab software in (7.1). Therefore, the wind speed distribution of Plymouth can be represented as in Figure 6.16. The histogram shows the frequency of the different hourly wind speed from 1 to 30 m/s for a year-long simulation using the above-defined Weibull distribution. From this Figure, it has been calculated in Table 6.9 the number of hours for each wind speed for one year.

Table 6.9: Number of hours of wind speed per year

Wind speed (m/s)	**Frequency (hours)**	**Wind speed (m/s)**	**Frequency (hours)**
0.1-1.0	371	**15.1-16.0**	97
1.1-2.0	562	**16.1-17.0**	77
2.1-3.0	728	**17.1-18.0**	33
3.1-4.0	833	**18.1-19.0**	32
4.1-5.0	909	**19.1-20.0**	15
5.1-6.0	906	**20.1-21.0**	8
6.1-7.0	864	**21.1-22.0**	6
7.1-8.0	786	**22.1-23.0**	2
8.1-9.0	638	**23.1-24.0**	1
9.1-10.0	571	**24.1-25.0**	1
10.1-11.0	445	**25.1-26.0**	0
11.1-12.0	306	**26.1-27.0**	0
12.1-13.0	258	**27.0-28.0**	0
13.1-14.0	174	**28.1-29.0**	0
14.1-15.0	137	**29.1-30.0**	0

A number of tests with the above indicated average wind speeds have been conducted to estimate the yearly production of electrical energy with the proposed algorithm compared to the traditional power control. It has been assumed that the parameter λ_i and ρ is 20% larger than the nominal value and that L_m is 50% lower than the nominal value. The result of each simulation, whose diagrams are similar to those shown in the previous chapters, is then multiplied by the number of hours shown in Table 6.9.

Table 6.10: Electrical energy increase of the optimal control algorithm with the Weibull distribution account in comparison with the traditional control algorithm for estimating of λ_i and ρ in error of +20% and L_m in error of -50%

Wind speed (m/s)	% increase in 3 minutes	Electrical energy increase per hour (Wh)	Annual electrical energy increase (kWh)
5	28.60%	166.6	151.44
6	25.03%	224.8	203.67
7	23.05%	334.8	289.27
8	21.33%	476.0	374.14
9	19.83%	522.0	333.03
10	13.90%	490.0	279.79
11	7.82%	334.0	148.63
12	2.09%	96.0	29.37
13	1.08%	50.0	12.9

The results of this analysis have been reported in Table 6.10 for some values of the average wind speed. The table shows that the optimal control can give more electrical energy than the traditional control. Considering the difference for each wind speed and their relative weight in terms of hours of occurrence, it can be concluded that the optimal control algorithm can produce around 1822.24 kWh more energy than the traditional control algorithm per year or increase by 14.53%.

Another set of simulations have been carried out for an error of +20% on ρ and +50% on r_s. The results, summarised in Table 6.11, shows that in this case, the optimal control algorithm can produce around 118.62 kWh more energy than the traditional control algorithm per year or increase by 0.83%. It is therefore evident that an error on these

parameters is much less sensitive than the error on λ_i and L_m, although the increase of electrical energy is still considerable.

Table 6.11: Electrical energy increase of the optimal control algorithm with the Weibull distribution account in comparison with the traditional control algorithm for estimating of ρ in error of +20% and r_s in error of +50%

Wind speed (m/s)	% increase in 3 minutes	Electrical energy increase per hour (Wh)	Annual electrical energy increase (kWh)
5	0.83%	6.2	5.63
6	0.74%	8.2	7.43
7	0.86%	13.2	13.13
8	0.97%	26.0	20.44
9	0.57%	18.0	11.48
10	0.85%	34.0	19.42
11	1.23%	56.0	24.92
12	0.77%	36.0	11.01
13	0.43%	20.0	5.16

6.5 Summary

This chapter has compared the performance of the SIRM-base fuzzy logic control with enhanced MBLC with the traditional MPPT control in the presence of uncertainties of aerodynamic and electrical parameters.

A number of case studies have been analysed to investigate the difference of the electrical energy generated by the two algorithms and evaluate which parameter affects most the generation of electrical power. The simulations, undertaken for various wind

speed profiles and various errors in the knowledge of parameters, has shown that the two most important parameters are the coefficient λ_i and the parameter L_m.

Then, the analysis has been extended to predict the annual energy yield taking into account that the wind average speed changes according to a Weibull distribution and, hence, the frequency of each average speed is different in a year. It has been shown that, depending on the level of uncertainty and the type of parameter affected by the error, the difference in the electrical energy generated can be from 118.62 to 1822.24 kWh per year.

Chapter 7 Conclusion and Future Works

7.1 Conclusion

In this thesis, a new optimal control algorithm for a DFIG-based wind generation system with a VSFP wind turbine has been presented. The advantage of VSFP wind turbine is that it can produce the optimal mechanical power for the full range of the wind speed by using only the generator speed control. Without a mechanism of the pitch angle control system, the WECS coupled with a VSFP wind turbine gives much more reliability than the variable-pitch wind turbines. Hence, this wind turbine has a low maintenance cost because it does not require the pitch angle control for limiting the extracted mechanical power.

The proposed control algorithm provides the maximum efficiency of the DFIG-based wind generation system with fixed-pitch wind turbines using the adaptation feature for tracking maximum power extracted of the wind turbine and minimum copper losses of the DFIG which compensates with the uncertainties of the wind turbine and DFIG parameters. Therefore, the proposed control algorithm can give more electrical energy in comparison with the traditional methods of MPPT control and MBLC, which have difficulty in identifying accurate operating points under parameter changes. The new control algorithm does not require a wind speed sensor and also gives more electrical energy without modifying the hardware.

This research work explored the control of a well-consolidated DFIG WECS topology having the stator terminals of the DFIG directly connected to the constant frequency and amplitude voltage power grid and the rotor terminals connected to the power grid through a back-to-back converter consisting of a RSC and a GSC. With this configuration, there are two degrees of freedom to optimise the performance of the system that have been selected as the direct and quadrature component of the rotor current in the rotating reference frame.

The equations of the model have shown that is it possible to find optimal references for these two components, which can be successfully tracked using appropriate current regulators for the control of the RSC. It has also been found that the optimal condition depends on the level of the wind speed and separate algorithms are needed when the speed is below and above the rated wind speed. This is because in the first case it is desired to maximise the mechanical power available from the wind, whereas in the second case it is desired to limit the mechanical power to the maximum level sustainable by the WECS. However, these optimal references are dependent on a number of aerodynamic, mechanical and electrical parameters of the WECS.

The investigation on suitable control technique for WECS under parameter uncertainty has led to the development of a new fuzzy controller based on a SIRMs connected fuzzy inference model. The proposed fuzzy controller has seven SIRMs according to input variable generating from the hybrid MPPT control and the active stall regulation. The dynamic importance degrees in the hybrid MPPT control are designed that the P&O MPPT is active after the speed reference has the same direction from as the PSF MPPT.

Moreover, others dynamic importance degrees are designed that the hybrid MPPT controls have higher priority than the active stall regulation when the observed mechanical power is less than its rated power. The main advantages of the fuzzy control based SIRM is that the number of fuzzy rules is reduced in comparison with the conventional fuzzy inference method and fuzzy rules can be designed easily. From the simulation results in section 6.2, at below-rated wind speed, the fuzzy control based SIRM gives better performance regarding the robustness and produces more electrical energy from the DFIG than the PSF MPPT control when the wind turbine parameters have errors. The proposed control based on the hybrid MPPT can give the correct direction of the optimal speed reference to the maximum power point during rapid wind variation, as it combines the quick response of PSF with the adaptive feature of fuzzy controller. At above-rated wind speed, the fuzzy control based SIRM can decrease the speed reference to the stall region to limit power at its rated value. The proposed control gives smooth speed reference trajectory in the transition between the MPPT and the active stall control because both controllers are constructed of SIRM-based fuzzy controller and weighted by the fuzzy set of dynamic importance degree according to control situations.

The problem of improving the efficiency of DFIGs has been tackled by introducing an enhanced MBLC to generate the optimal i_{rd} reference corresponding to the minimum copper loss. The proposed control overcomes the limitation of traditional MBLC that cannot change the control law corresponding to the condition of minimum DFIG losses when the estimation of DFIG parameters from the experimental test is not infinitely accurate. The key novelty of the enhanced MBLC is that the parameters of DFIG are

obtained from an online estimation through the Kalman filter method. The work on the design of the online parameter estimation has proven that the proposed Kalman filter returns a fast-tracking response which is suitable for variable wind speed condition. To achieve this, a good adjustment was required between the precision of the Kalman filter and the response time, as continuously variable wind speeds affect the algorithm and produce a continuing small oscillation of the parameter estimation. Therefore, the i_{rd} reference generated from the enhanced MBLC leads to the accurate determination of the condition of minimum copper losses of the DFIG. From the simulation results in section 6.3, the enhanced MBLC gives the higher performance regarding adaptation of the control law and produces more electrical energy from the DFIG than the MBLC when the DFIG parameters are errors.

The optimal control algorithm provides the advantages of robustness of the control that deal with uncertainties on the parameters of the wind turbine and the DFIG.

The simulation study on the optimal control algorithm, combining both the fuzzy control based SIRM and the enhanced MBLC, has then demonstrated an improvement of the efficiency of the WECS for all the simulated conditions.

Furthermore, it has been estimated that for a typical year, the energy yield of the WECS with the proposed control can be higher than a traditional control, supporting the theoretical hypotheses of this work.

7.2 Future Works

The research work of this thesis can be continued in the following areas.

7.2.1 Experimental Verification in the Laboratory

The simulation study has predicted a substantial increase of the electrical energy generated by the DFIG with the proposed control. A demonstration on a scale model of a WECS would further support this result and give a more detailed insight into the real influence of power losses on the different components. The experimental simulator should include the DFIG, back-to-back PWM converter, DC link, speed sensor, DSP microcontrollers and wind turbine simulator set and gives further recommendations on the control performance which maybe gives some difference between experimental results and simulation results, causing operating properties of sensor, power electronic devices, DSP microcontroller and so on.

7.2.2 Study on Minimum Total Loss Control in DFIG Circuit

The thesis has focused only on the copper loss minimisation control for the DFIG in the WECS. From [29], It revealed that the copper loss is greater than the power converter loss. The analysis can be extended to include in loss of the back-to-back converter and the filter to develop new algorithm to the total loss minimisation control of the DFIG WECS. The new control will generate the optimal i_{rd} reference based on of the loss model of DFIG, filter and power converters.

7.2.3 Optimal Use of the Torque Available from the DFIG

In this thesis, it has been assumed that the torque of the DFIG generator is never positive, i.e., the machine is never motoring. However, this could be helpful to accelerate the rotor to reach the speed of the maximum power point quickly. A more detailed study would be devoted to understanding for which condition this is more convenient compared to the case of leaving the wind only to accelerate the rotor or any intermediate situation. Further work on the analysis of the control strategy for variable wind speeds, where the torque of the generator could be optimised to improve the dynamical response of the speed control will be investigated.

References

[1] P. Costa, A. Martins, and A. Carvalho, "Wind energy extraction and conversion: optimization through variable speed generators and nonlinear fuzzy control," in *EWEC'06*, 2006.

[2] F. D. Bianchi, H. De Battista, and R. J. Mantz, *Wind turbine control systems: principles, modeling and gain scheduling design*, Springer, 2007.

[3] R. Datta and V. T. Ranganathan, "A method of tracking the peak power points for a variable speed wind energy conversion system," *IEEE Transactions on Energy Conversion.*, vol. 18, pp. 163–168, 2003.

[4] H. Li, Z. Chen, and J. K. Pedersen, "Optimal power control strategy of maximizing wind energy tracking and conversion for VSCF doubly fed induction generator system," in *2006 CES/IEEE 5th International Power Electronics and Motion Control Conference*, vol. 3, pp. 1779–1784, 2007.

[5] G. M. Joselin Herbert, S. Iniyan, E. Sreevalsan, and S. Rajapandian, "A review of wind energy technologies," *Renewable and Sustainable Energy Reviews*, vol. 11, pp. 1117–1145, 2007.

[6] J. F. Manwell, J. G. McGowan, and A. L. Rogers, *Wind energy explained: theory, design and application*, 2nd ed, John Wiley & Son Ltd, 2010.

[7] G. Abad, J. Lopez, M. Rodriguez, L. Marroyo, and G. Iwanski, *Doubly fed induction machine: modeling and control for wind energy generation*. Wiley, 2011.

[8] R. Pena, J. C. Clare, and G. M. Asher, "Doubly fed induction generator using back-to-back PWM converters and its application to variable-speed wind-energy generation," *IEE Proceedings-Electric Power Applications*, vol. 143, pp. 231-241, 1996.

[9] "Wind turbine power calculations" [Online]. Available: https://www.raeng.org.uk/publications/other/23-wind-turbine.html. [Accessed: 19-Dec-2018].

[10] S. Janakiraman, "An adaptive sensorless control for maximum power point tracing in wind energy conversion system," MSc Thesis, Electrical and Computer Engineering, University of Houston, 2014.

[11] M. Ragheb and A. M. Ragheb, "Wind turbines theory - the betz equation and optimal rotor tip speed ratio," *Fundamental and Advanced Topics in Wind Power : InTech*, 2011.

[12] J. Zaragoza, J. Pou, A. Arias, C. Spiteri, E. Robles, and S. Ceballos, "Study and experimental verification of control tuning strategies in a variable speed wind energy conversion system," *Renewable Energy*, vol. 36, no. 5, pp. 1421–1430, 2011.

[13] M. Mansour, M. N. Mansouri, and M. F. Mmimouni, "Study and control of a variable-speed wind-energy system connected to the grid," *International Journal of Renewable Energy Research*, vol. 1, pp. 96-104, 2011.

[14] M. Cirrincione, M. Pucci, and G. Vitale, "Neural MPPT of variable-pitch wind generators with induction machines in a wide wind speed range," *IEEE Transactions on Industry Applications*, vol. 49, no. 2, pp. 942–953, 2013.

[15] S. Heier, *Grid integration of wind energy conversion systems*, 2nd ed, John Wiley and Sons Inc, 2006.

[16] J. Morren, J. Pierik, and S. W. H. de Haan, "Inertial response of variable speed wind turbines," *Electric Power Systems Research*, vol. 76, pp. 980-987, 2006.

[17] Q. Chen, M. Defourny, and O. Brüls, "Control and simulation of doubly fed induction generator for variable speed wind turbine systems based on an integrated finite element approach," in *European Wind Energy Conference and Exhibition*, 2011.

[18] B. Neammanee, S. Sirisumrannukul, and S. Chatratana, "Control strategies for variable-speed fixed-pitch wind turbines," *Wind Power: InTech*, pp. 209–232, 2010.

[19] Z. Xin-fang, X. Da-ping, and L. Yi-bing, "Adaptive optimal fuzzy control for variable speed fixed pitch wind turbines," in *Fifth World Congress on Intelligent Control and Automation*, vol. 3, pp. 2481–2485, 2004.

[20] C. Jiawei, W. Changyun, and S. Yongduan, "Power control strategy for variable-speed fixed-pitch wind turbines," in *2014 13th International Conerence on Control Automation Robotics & Vision(ICARCV)*, pp. 559-564, 2014.

[21] D. Kumar and K. Chatterjee, "A review of conventional and advanced MPPT algorithms for wind energy systems," *Renewable and Sustainable Energy Reviews*, vol. 55, pp. 957–970, 2016.

[22] X. Jing, "Modeling and control of a doubly-fed induction generator for wind turbine-generator systems," MSc Thesis, Faculty of Graduate School, Marquete University, 2009.

[23] H. Camblong, I. M. de Alegria, M. Rodriguez, and G. Abad, "Experimental evaluation of wind turbines maximum power point tracking controllers," *Energy Conversion and Management*, vol. 47, no. 18–19, pp. 2846–2858, 2006.

[24] A. D. Hansen, P. Sørensen, F. Iov, and F. Blaabjerg, "Control of variable speed wind turbines with doubly-fed induction generators," in Wind Engineering, vol. 28, no. 4, pp. 411–432, 2004.

[25] N. R. Babu and P. Arulmozhivarman, "Wind energy conversion systems - a technical review," *Journal of Engineering Science and Technology*, vol. 8, no. 4, pp. 493–507, School of Engineering, Taylor's University, 2013.

[26] J. Tamura, "Calculation method of losses and efficiency of wind generators," [Online]. Available: https://www.academia.edu/21626345/Calculation_Method_of_Losses_and_Efficiency_of_Wind_Generators.html. [Accessed: 19-Dec-2018].

[27] A. G. Abo-Khalil, H. G. Park, D. C. Lee, S. P. Ryu, and S. H. Lee, "Loss minimization control for doubly-fed induction generators in variable speed wind turbines," in *IECON 2007*-33rd *Annual Conference of the IEEE Industrial Electronics Society*, pp. 1109–1114, 2008.

[28] O. P. Mahela and A. G. Shaik, "Comprehensive overview of grid interfaced wind energy generation systems," *Renewable and Sustainable Energy Reviews*, vol. 57, pp. 260–281, 2016.

[29] R. Takahashi, H. Ichita, J. Tamura, M. Kimura, M. Ichinose, M. Futami, and K. Ide, "Efficiency calculation of wind turbine generation system with doubly-fed induction generator," in *XIX International Conference on Electrical Machines - ICEM 2010*, 2010.

[30] A. Mesemanolis, C. Mademlis, and I. Kioskeridis, "High-efficiency control for a wind energy conversion system with induction generator," *IEEE Transaction on Energy Conversion*, vol. 27, no. 4, pp. 958–967, 2012.

[31] A. Mesemanolis, C. Mademlis, and I. Kioskeridis, "Optimal efficiency control strategy in wind energy conversion system with induction generator," *IEEE Journal of Emerging and Selected Topics in Power Electronics*, vol. 1, no. 4, pp. 238–246, 2013.

[32] S. Rajendran and D. Jena, "Control of variable speed variable pitch wind turbine at above and below rated wind speed," *Journal of Wind Energy*, pp. 1-14, 2014.

[33] V. Lesic, M. Vasak, N. Peric, G. Joksimovic, and T. M. Wolbank, "Fault-tolerant control of a wind turbine with a squirrel-cage induction generator and stator inter-turn faults," in *The 12th International Workshop on Advanced Motion Control-AMC*, 2012.

[34] S. Arnaltes, J. L. Rodriguez-Amenedo, and M. E. Montilla-DJesus, "Control of variable speed wind turbines with doubly fed asynchronous generators for stand-alone applications," *Energies*, vol. 11, 2018.

[35] A. Hwas and R. Katebi, "Wind turbine control using PI pitch angle controller," *IFAC Proceedings Volumes*, vol. 45, no. 3, pp. 241-246, 2012.

[36] H. Vihriala, "Control of variable speed wind turbine," PhD Thesis, Tempere University of technology, 2002.

[37] S. Sahoo, B. Subudhi, and G. Panda, "Pitch angle control for variable speed wind turbine using fuzzy logic," in *2016 International Conference on Information Technology (ICIT)*, pp. 28–32, 2017.

[38] M. A. Abdullah, A. H. M. Yatim, and C. W. Tan, "A study of maximum power point tracking algorithms for wind energy system," in *2011 IEEE Conference on Clean Energy and Technology (CET)*, pp. 321–326, 2011.

[39] J. S. Thongam, and M. Ouhrouche, "MPPT control methods in wind energy conversion systems," *Fundamental and Advanced Topics in Wind Power : InTech*, pp. 339-360, 2011.

[40] A. Kadri, H. Marzougui, and F. Bacha, "MPPT control methods in wind energy conversion system using DFIG," in *2016 4th International Conference on Control Engineering & Information Technology (CEIT)*, pp. 16–18, 2016.

[41] S. M. Barakati, M. Kazerani, S. Member, and J. D. Aplevich, "Maximum power tracking control for a wind turbine system including a matrix converter," *IEEE Transactions on Energy Conversion*, vol. 24, no. 3, pp. 705–713, 2009.

[42] K. H. Kim, T. L. Van, D. C. Lee, S. H. Song, and E. H. Kim, "Maximum output power tracking control in variable-speed wind turbine systems considering rotor inertial power," *IEEE Transactions on Industrial Electros.*, vol. 60, no. 8, pp. 3207–3217, 2013.

[43] S. Morimoto, H. Nakayama, M. Sanada, and Y. Takeda, "Sensorless output maximization control for variable-speed wind generation system using IPMSG," *IEEE Transactions on Industry Applications*, vol. 41, no. 1, pp. 60–67, 2005.

[44] M. Nasiri, J. Milimonfared, and S. H. Fathi, "Modeling, analysis and comparison of TSR and OTC methods for MPPT and power smoothing in permanent magnet synchronous generator-based wind turbines," *Energy Conversion and Management*, vol. 86, pp. 892–900, 2014.

[45] Y. Daili, J. P. Gaubert, and L. Rahmani, "Implementation of a new maximum power point tracking control strategy for small wind energy conversion systems without mechanical sensors," *Energy Conversion and Management*, vol. 97, pp. 298–306, 2015.

[46] S. Cai and H. Wen, "Modeling and MPPT control of DFIG wind energy system," in *International Conference on Renewable Power Generation (RPG 2015)*, 2015.

[47] J. S. Thongam, P. Bouchard, R. Beguenane, A. F. Okou, and A. Merabet, "Control of variable speed wind energy conversion system using a wind speed sensorless optimum speed MPPT control method," *IECON 2011 - 37th Annual Conference of the IEEE Industrial Electronics Society*, pp. 855–860, 2011.

[48] A. Dahbi, M. Hachemi, N. Nait-Said, and M. S. Nait-Said, "Realization and control of a wind turbine connected to the grid by using PMSG," *Energy Conversion and Management*, vol. 84, pp. 346–353, 2014.

[49] K. Y. Oh, J. Y. Park, J. S. Lee, and J. K. Lee, "Implementation of a torque and a collective pitch controller in a wind turbine simulator to characterize the dynamics at three control regions," *Renewable Energy*, vol. 79, no. 1, pp. 150–160, 2015.

[50] A. E. Yaakoubi, A. Asselman, A. Djebli, and E. H. Aroudam, "A MPPT strategy based on fuzzy control for a wind energy conversion system," in *9th International Conference Interdisciplinarity in Engineering (INTER-ENG 2015)*, pp. 697–704, 2015.

[51] Q. Wang and L. Chan, "An independent maximum power extraction strategy for wind energy conversion systems," in *1999 IEEE Canadian Conference on Electrical and Computer Engineering*, vol. 2, pp. 1142–1147, 1999.

[52] C. Patsios, A. Chaniotis, M. Rotas, and A. G. Kladas, "A comparison of maximum-power-point tracking control techniques for low-power variable-speed wind generators," in *2009 8th International Symposium on Advanced Electromechanical Motion Systems and Electric Drives Joint Symposium*, pp. 1–6, 2009.

[53] A. G. Abo-Khalil, D. C. Lee, and J. K. Seok, "Variable speed wind power generation system based on fuzzy logic control for maximum output power tracking," in *2004 IEEE 35th Annual Power Electronics Speccialist Conference*, vol. 3, pp. 2039–2043, 2004.

[54] E. Adzic, Z. Ivanovic, M. Adzic, and V. Katic, "Optimum fuzzy logic control of induction generator in wind turbine application," in *2008 6th International Symposium on Intelligent Systems and Informatics*, pp. 3–7, 2008.

[55] Q. Zeng, L. Chang, and R. Shao, "Fuzzy-logic-based maximum power point tracking strategy for PMSG variable-speed wind turbine generation systems," in *2008 Canadian Conference on Electrical and Computer Engineering*, no. 1, pp. 405–409, 2008.

[56] X. Yao, C. Guo, Z Xing, Y Li, and S. Liu, "Variable speed wind turbine maximum power extraction based on fuzzy logic control," in *2009 International Conference on Intelligent Human-Machine Systems and Cybernetics (IHMSC 2009)*, vol. 2, pp. 202–205, 2009.

[57] M. Azzouz, A. L. Elshafei, and H. Emara, "Evaluation of fuzzy-based maximum power tracking in wind energy conversion systems (WECS)," *IET Renewable Power Generation*, vol. 5, no. 6, pp. 422–430, 2011.

[58] S. M. Raza Kazmi, H. Goto, H.-J. Guo, and O. Ichinokura, "A novel algorithm for fast and efficient speed-sensorless maximum power point tracking in wind energy conversion systems," *IEEE Transactions on Industrial Electronics*, vol. 58, no. 1, pp. 29–36, 2011.

[59] Ch. Patsios, A. Chaniotis, and A. Kladas, "A hybrid maximum power point tracking system for grid-connected variable speed wind-generators," in *2008 IEEE Power Electronics Specialist Conference*, vol. 94, no. 7, pp. 714–721, 2008.

[60] T. Takagi and M. Sugeno, "Fuzzy identification of systems and its applications to modeling and control," *IEEE Transactions on Systems, Man, and Cybernetics*, vol. SMC-15, no. 1, pp. 116–132, 1985.

[61] N. Yubazaki, J. Yi, M. Otani, and K. Hirota, "SIRM's connected fuzzy inference model and its applications to first-order lag systems and second-order lag systems," in *Soft Computing in Intelligent Systems and Information Processing*, pp. 545-550, 1996.

[62] J. Yi, N. Yubazaki, and K. Hirota, "SIRMs dynamidy connected fuzzy inference model applied to stabilization control of inverted pendulum and cart systems," in *Fuzzy and Information Processing*, pp. 771–775, 1999.

[63] J. Yi, N. Yubazaki, and K. Hirota, "Upswing and stabilization control of inverted pendulum and cart system by the SIRMs dynamically connected fuzzy inference model," in *1999 IEEE International Fuzzy Systems Conference Proceeding*, pp. 400–405, 1999.

[64] J. Yi and N. Yubazaki, "Stabilization fuzzy control of inverted pendulum systems," *Artificial Intelligence in Engineering*, vol. 14, no. 2, pp. 153–163, 2000.

[65] J. Yi, N. Yubazaki, and K. Hirota, "A proposal of SIRMs dynamically connected fuzzy inference model for plural input fuzzy control," *Fuzzy Sets and Systems*, vol. 125, no. 1, pp. 79–92, 2002.

[66] N. Yubazaki, J. Yi, M. Otani, N. Unemura, and K. Hirota, "Trajectory tracking control of unconstrained objects based on the SIRMs dynamically connected fuzzy inference model," in *Proceedings of 6th International Fuzzy Systems Conference*, pp. 609-614, 1997.

[67] K. Krajangpan, W. Sadara, and B. Neammanee, "Control strategies for maximum active power and minimum copper loss of doubly fed induction generator in wind turbine system," in *2010 International Conference on Power System Technology*, pp. 1–7, 2010.

[68] Y. Tang and L. Xu, "A flexible active and reactive power control strategy for a variable speed constant frequency generating system," *IEEE Transactions on Power Electronics*, vol. 10, no. 4, pp. 472–478, 1995.

[69] B. Zhang, W. Hu, and Z. Chen, "Loss minimizing operation of doubly fed induction generator based wind generation systems considering reactive power provision," in *IECON 2014-40th Annual Conference of the IEEE Industrial Electronics Society*, pp. 2146-2152, 2014.

[70] K. Kerrouche, A. Mezouar, and Kh. Belgacem, "Decoupled control of doubly fed induction generator by vector control for wind energy conversion system," *Energy Procedia*, vol. 42, pp. 239–248, 2013.

[71] M. G. S and N. A. Divya, "Rotor side converter control of DFIG based wind energy conversion system," *International Journal of Engineering Research & Technology (IJERT)*, vol. 4, no. 08, pp. 607–612, 2015.

[72] A. H. Kasem, E. F. El-Saadany, H. H. El- Tamaly, and M. A. A. Wahab, "Performance enhancement of DFIG-based wind turbines close to the rated operation," in *2008 40th North American Power Symposium*, pp. 1–6, 2008.

[73] L. Loron and G. Laliberté, "Application of the extended Kalman filter to parameters estimation of induction motors," in *1993 Fifth European Conference on Power Electronics and Applications*, pp. 85–90, 1993.

[74] H. A. Toliyat, E. Levi, and M. Raina, "A review of RFO induction motor parameter estimation techniques," *IEEE Transactions on Energy Conversion*, vol. 18, no. 2, pp. 271-283, 2003.

[75] P. A. Ioannou and J. Sun, *Robust adaptive control*, Prentice Hall, 1996.

[76] K. Belmokhtar, H. Ibrahim, and A. Merabet, "Online parameter identification for a DFIG driven wind turbine generator based on recursive least squares algorithm," in *2015 IEEE 28th Canadian Conference on Electrical and Computer Engineering (CCECE)*, pp. 965-969, 2015.

[77] S. O. Pepainas, "Adaptive control and parameter identification of a doubly-fed induction generator for wind power," MSc Thesis, Electrical Engineer, Naval Postgraduate School, 2011.

[78] S. Thomsen, K. Rothenhagen, and F. W. Fuchs, "Online parameter identification methods for doubly fed induction generators," in *2008 IEEE Power Electronics Specialists Conference*, pp. 2735–2741, 2008.

[79] C. M. Ong, *Dynamic simulation of electric machinery using Matlab/Simulink*, Prentice Hall, 1998.

[80] H. Abu-Rub, A. Iqbal, and J. Guzinski, *High perfermance control of AC drives with Matlab/Simulink Models*, Wiley, 2012.

[81] H. Abu-Rub, M. Malinowski, and K. Al-Haddad, *Power electronics for renewable energy systems, transportation and industrial applications*, Wiley, 2012.

[82] B. Subudhi and P. S. Ogeti, "Optimal preview stator voltage-oriented control of DFIG WECS," *IET Generation Transmission & Distribution*, vol. 12, no. 4, pp. 1004–1013, 2018.

[83] W. Srirattanawichaikul, S. Premrudeepreechacharn, and Y. Kumsuwan, "A comparative study of vector control strategies for rotor-side converter of DFIG wind energy systems," in *2016 13th International Conference on Electrical Engineering/Electronics,Computer,Telecommunications and Information Technology (ECTI-CON)*, 2016.

[84] G. Calderón, J. Mina, J. C. Rosas-Caro, M. Madrigal, A. Claudio, and A. López, "Simulation and comparative analysis of DFIG-based WECS using stator voltage and stator flux reference frames," *IEEE Latin America Transactions*, vol. 15, no. 6, pp. 1052–1059, 2017.

[85] S. Li, R. Challoo, and M. J. Nemmers, "Comparative study of DFIG power control using stator-voltage and stator-flux oriented frames," in *2009 IEEE Power & Energy Society General Meeting*, pp. 1–8, 2009.

[86] M. K. Bourdoulis and A. T. Alexandridis, "Rotor-side cascaded PI controller design and gain tuning for DFIG wind turbines," in *4th International Conference on Power Engineering, Energy and Electrical Drives*, pp. 733–738, 2013.

[87] B. Hopfensperger, D. J. Atkinson, and R. A. Lakin, "Stator-flux-oriented control of a doubly-fed induction machine with and without position encoder," *IEE Proceedings-Electric Power Applications*, vol. 147, no. 4, pp. 241-250, 2000.

[88] H. S. Ko, S. Bruey, J. Jatskevich, G. Dumont, and A. Moshref, "A PI control of DFIG-based wind farm for voltage regulation at remote location," in *2007 IEEE Power Engineering Society General Meeting*, pp. 1–6, 2007.

[89] F. Haugen, "Ziegler-Nichols ' closed-loop method," [Online] Available: http://techteach.no/publications/articles/zn_closed_loop_method/zn_closed_loop_method.pdf [Accessed: 19-Dec-2018].

[90] V. Bobal, J. Machacek, and R. Prokop, "Tuning of digital PID controllers based on Ziegler-Nichols method," *IFAC Proceedings Volumes*, vol. 30, no. 21, pp. 145–150, 1997.

[91] A. Karimi, D. Garcia, and R. Longchamp, "PID controller tuning using Bode's integrals," *IEEE Transctions on Control Systems Technology*, vol. 11,no. 6, pp. 812-821, 2003.

[92] L. Lei, "Doubly-fed induction generator wind turbine modelling, control and reliability," PhD Thesis, Faculty of Engineering and Physical Sciences, The University of Manchester, 2014.

[93] C. L. Phillips and R. D. Harbor, *Feedback control systems*, 4th ed, Prentice Hall, 2000.

[94] B. C. Kuo and D. C. Hanselman, *Matlab tools for control system analysis and design*, Englewood Cliffs, New Jersey: Prentice-Hall, 1994.

[95] W. Qiao, W. Zhou, J. M. Aller, and R. G. Harley, "Wind speed estimation based sensorless output maximization control for a wind turbine driving a DFIG," *IEEE Transactions on Power Electronics*, vol. 23, no. 3, pp. 1156-1169, 2008.

[96] Burmer. "Encoders and sensors for wind turbines smart solutions for every environment," Available: http://vt.baumer.com/fileadmin/user_upload/international/Downloads/BR-CT/Baumer_Wind-turbines_BR_EN_1505_11136232.pdf [Accessed: 19-Dec-2018].

[97] E. Muljadi, K. Pierce, and P. Migliore, "A conservative control strategy for variable-speed stall-regulated wind turbines," *19th American Society of Mechanical Engineering (ASME) Wind Energy Symposium*, pp. 1-8, 2000.

[98] K. Krajangpan, W. Sadara, and B. Neammanee, "Control strategies for maximum active power and minimum copper loss of doubly fed induction generator in wind turbine system," in *2010 International Conference on Power System Technology*, pp. 1–7, 2010.

[99] J. Chen, J. Chen, and C. Gong, "New overall power control strategy for variable-speed fixed-pitch wind turbines within the whole wind velocity range," *IEEE Transactions on Industrial Electronics*, vol. 60, no. 7, pp. 2652–2660, 2013.

[100] M. F. Tsai, C. S. Tseng, and Y. H. Hung, "A novel MPPT control design for wind-turbine generation systems using neural network compensator," *IECON 2012 – 38th Annual Conference on IEEE Industrial Electronics Society*, pp. 3521–3526, 2012.

[101] R. D. Shukla and R. K. Tripathi, "Maximum power extraction schemes & power control in wind energy conversion system," *International Journal of Scientific & Engineering Research*, vol. 3, no. 6, pp. 1–7, 2012.

[102] "How to calculate air density," [Online]. Available: https://www.brisbanehotairballooning.com.au/calculate-air-density.html, [Accessed: 12-Dec-2018].

[103] C. Nichita, D. Luca, B. Dakyo, and E. Ceanga, "Large band simulation of the wind speed for real time wind turbine simulators," *IEEE Transactions on Energy Conversion*, vol. 17, no. 4, pp. 523–529, 2002.

[104] A. Burlibasa and E. Ceanga, "Rotationally sampled spectrum approach for simulation of wind speed turbulence in large wind turbines," *Applied Energy*, vol. 111, pp. 624–635, 2013.

[105] M. G. Simões, B. K. Bose, and R. J. Spiegel, "Design and performance evaluation of a fuzzy-logic-based variable-speed wind generation system," *IEEE Transactions on Industry Applications*, vol. 33, no. 4, pp. 956–965, 1997.

[106] S. M. Mirhassani, S. Z. M. Golroodbari, S. M. M. Golroodbari, and S. Mekhilef, "An improved particle swarm optimization based maximum power point tracking strategy with variable sampling time," *International Journal of Electrical Power & Energy Systems*, vol. 64, pp. 761–770, 2015.

[107] H. Seki, F. Mizuguchi, S. Watanabe, H. Ishii, and M. Mizumoto, "SIRMs connected fuzzy inference method using kernel method," in *2008 IEEE International Conference on Systems, Man, and Cybernetics*, pp. 1776–1781, 2008.

[108] M. Mizumoto, "Product-sum-gravity method=fuzzy singleton-type reasoning method=simplified fuzzy reasoning method," in *Proceedings of IEEE 5th International Fuzzy Systems*, pp. 2098–2102, 1996.

[109] C. L. Cheng, C. T. Hsieh, and S. N. Wang, "Analysis of the fuzzy logic controller using product-sum-gravity inference method," in *Soft Computing in Intelligent Systems and Information Processing*, pp. 206–211, 1996.

[110] E. Welfonder, R. Neifer, and M. Spanner, "Development and experimental identification of dynamic models for wind turbines," *Control Engineering Practice*, vol. 5, no. 1, pp. 63–73, 1997.

[111] B. Fan, Z. Yang, W. Xu, and X. Wang, "Rotor resistance online identification of vector controlled induction motor based on neural network," *Mathematical Problems in Engineering*, pp. 1-10, 2014.

[112] E. Bounadja, A. Djahbar, M. O. Mahmoudi, and M. Matallah "Direct torque control of saturated doubly-fed induction generator using high order sliding mode controllers," *International Journal of Advanced Computer Science and Applications*, vol. 7, no. 7, pp. 55-61, 2016.

[113] H. M. Jabr and N. C. Kar, "Effects of main and leakage flux saturation on the transient performances of doubly-fed wind driven induction generator," *Electric Power Systems Research*, vol. 77, no. 8, pp. 1019–1027, 2007.

[114] L. Ljung, *System identification-theory for the user*, PTR Prenti. Prentice Hall, 1999.

[115] S. Bolognani, L. Tubiana, and M. Zigliotto, "Extended kalman filter tuning in sensorless PMSM Drives," *IEEE Transactions on Industry Applications*, vol. 39, no. 6, pp. 1741–1747, 2003.

[116] S. Heier, *Grid integration of wind energy conversion systems*, 2nd ed, John Wiley and Sons Inc, 2006.

[117] "Wind Power Program." [Online]. Available: http://www.wind-power-program.com. [Accessed: 19-Dec-2018].

Appendix A: DFIG and Wind Turbine Characteristics

Table A. 1: DFIG characteristics

Characteristics	**Value**	**Unit**
Synchronous speed	1500	rpm
Rated power	5	kW
Rated line-to-line stator voltage	380	V_{rms}
Rate stator current	8.36	A_{rms}
Rated torque	31.8	Nm
Stator connection	Star	-
Number of pole pairs of DFIG (p)	2	-
Rated line-to-line rotor voltage	705	V_{rms}
Stator-rotor turns ratio (u)	0.54	-
Stator resistance (r_s)	720	mΩ
Stator leakage inductance ($L_{\sigma s}$)	5.8	mH
Mutual inductance (L_m)	85.8	mH
Rotor resistance referred to the stator (r_r)	750	mΩ
Rotor leakage inductance referred to the stator ($L_{\sigma s}$)	6	mH
Inertia of DFIG (J_G)	0.024	$kg.m^2$

Table A. 2: Wind turbine characteristics

Characteristics	**Value**	**Unit**
Power	5	kW
Blade radius (R)	2.327	m
Gearbox ratio (G)	7	-
Rated wind speed (V_{rated})	10	m/s
Cut-in wind speed ($V_{cut\text{-}in}$)	4	m/s
Cut-out wind speed ($V_{cut\text{-}out}$)	14	m/s
Maximum power coefficient (C_{pmax})	0.48	-
Optimal tip speed ratio (λ_{opt})	8.1	
Inertia of wind turbine(J_T)	13.5	$kg.m^2$

Appendix B: Additional Results

The WECS dynamic responses controlled by the traditional power control and the SIRM-based fuzzy controller for the step-up-changing wind speed in different cases of Table 6.1 are shown in Figure B.1 to B.5.

The WECS dynamic response controlled by the traditional power control and the SIRM-based fuzzy controller for the low real wind speed profile ($\bar{v}_w$ = 6 m/s) in different cases of Table 6.1 are shown in Figure B.6 to B.10.

The WECS dynamic response controlled by the traditional power control and the SIRM-based fuzzy controller for the medium real wind speed profile ($\bar{v}_w$ = 8 m/s) in different cases of Table 6.1 are shown in Figure B.11 to B.15.

The WECS dynamic response controlled by the traditional power control and the SIRM-based fuzzy controller for the high real wind speed profile ($\bar{v}_w$ = 11 m/s) in different cases of Table 6.1 are shown in Figure B.16 to B.20.

The WECS dynamic response controlled by the traditional MBLC and the enhanced MBLC for the step-up-changing wind speed in different cases of Table 6.6 are shown in Figure B.21 to B.28.

The WECS dynamic response controlled by the traditional MBLC and the enhanced MBLC for the low real wind speed profile ($\bar{v}_w$ = 6 m/s) in different cases of Table 6.6 are shown in Figure B.29 to B.36.

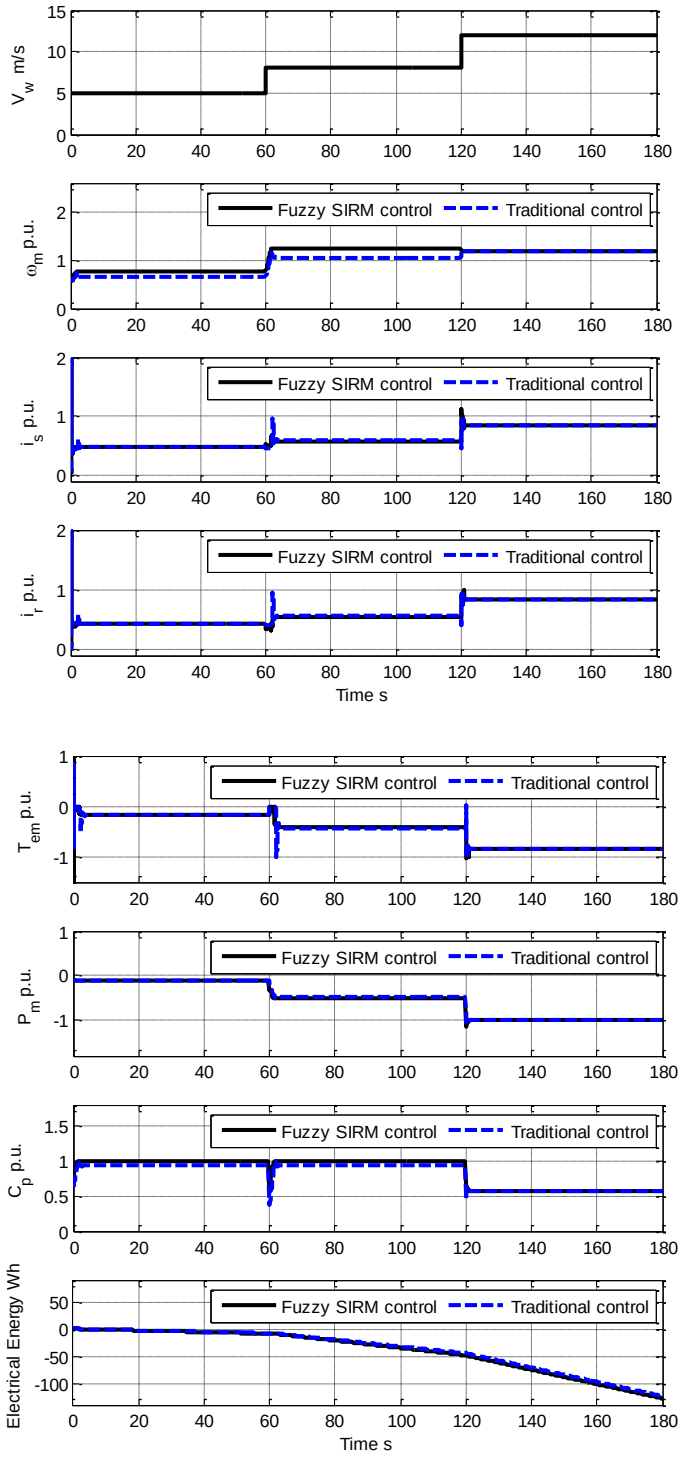

Figure B.1: WECS dynamic response controlled by the traditional power control and the SIRM-based fuzzy controller for step-up-changing wind speed with estimating of λ_i in error of +20% (case 3)

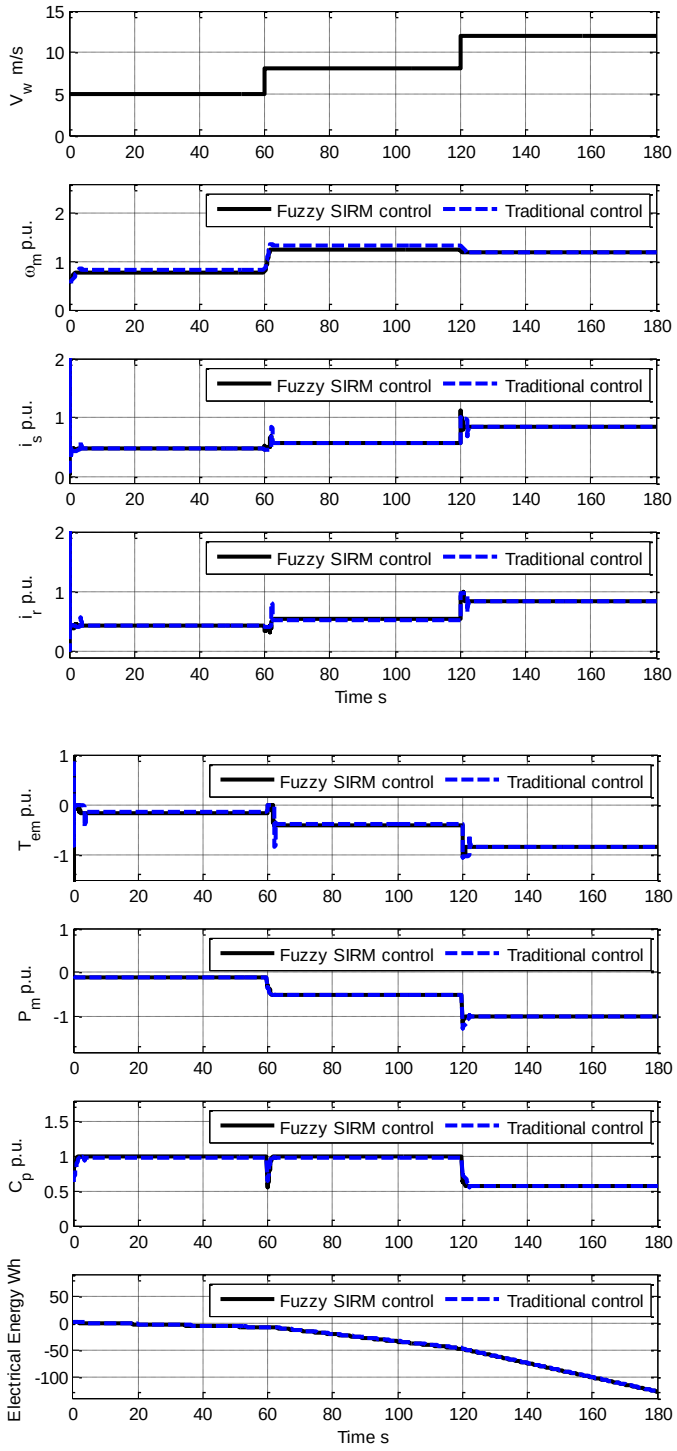

Figure B.2: WECS dynamic response controlled by the traditional power control and the SIRM-based fuzzy controller for step-up-changing wind speed with estimating of air density in error of -20% (case 4)

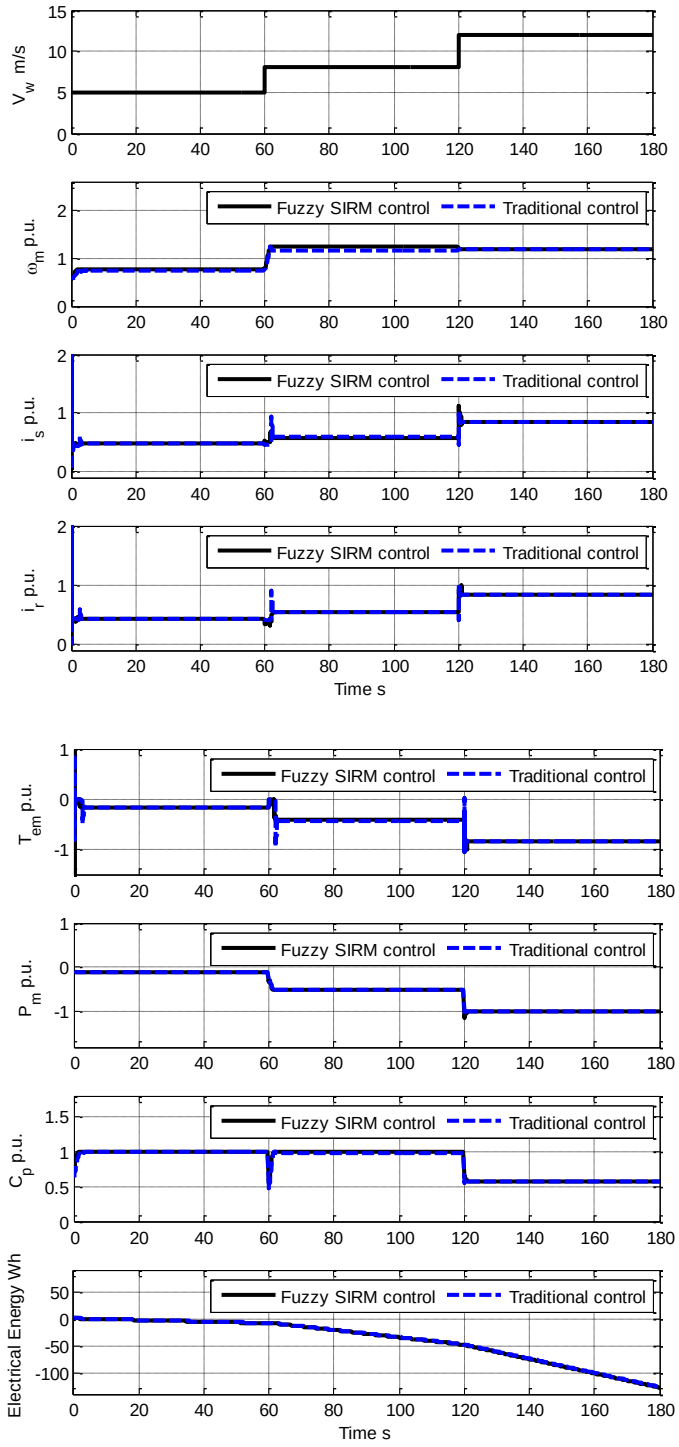

Figure B.3: WECS dynamic response controlled by the traditional power control and the SIRM-based fuzzy controller for step-up-changing wind speed with estimating of air density in error of +20% (case 5)

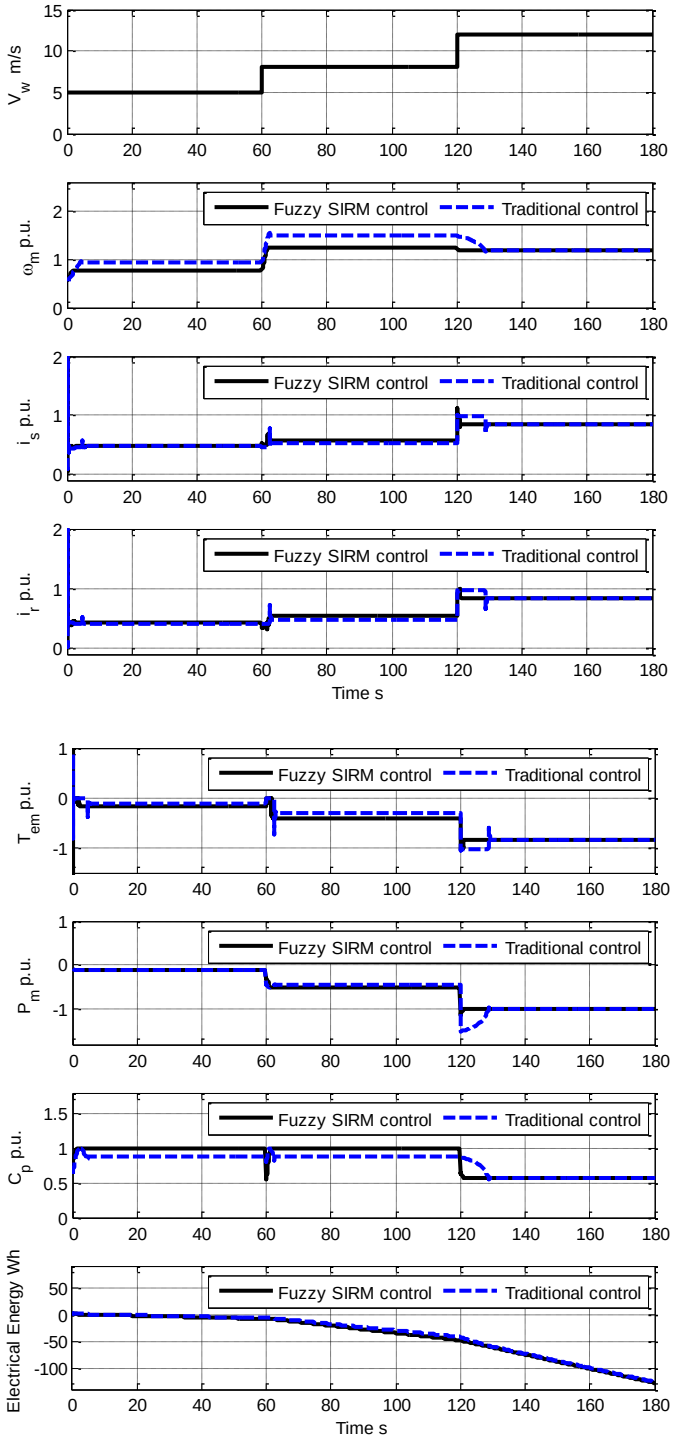

Figure B.4: WECS dynamic response controlled by the traditional power control and the SIRM-based fuzzy controller for step-up-changing wind speed with estimating of λ_i and air density in error of -20% and -20%, respectively (case 6)

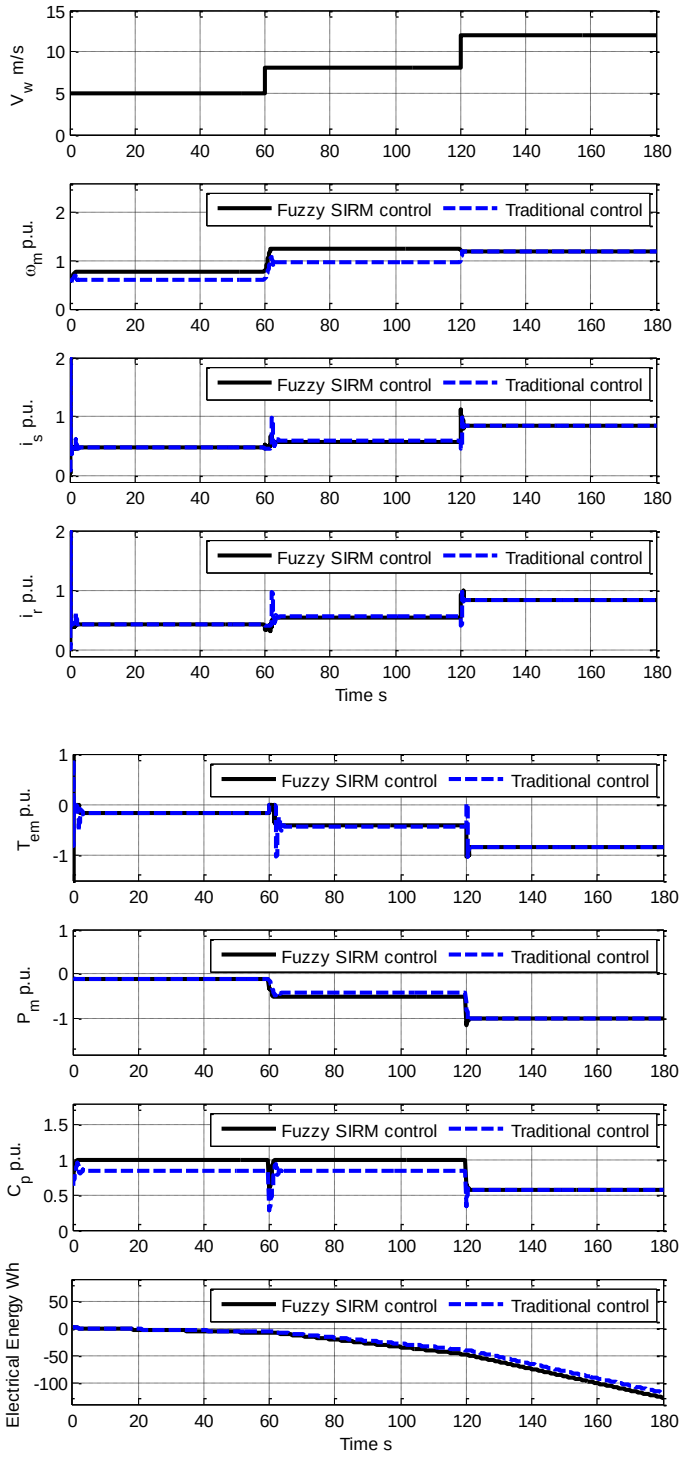

Figure B.5: WECS dynamic response controlled by the traditional power control and the SIRM-based fuzzy controller for step-up-changing wind speed with estimating of λ_i and air density in error of +20% and +20%, respectively (case 7)

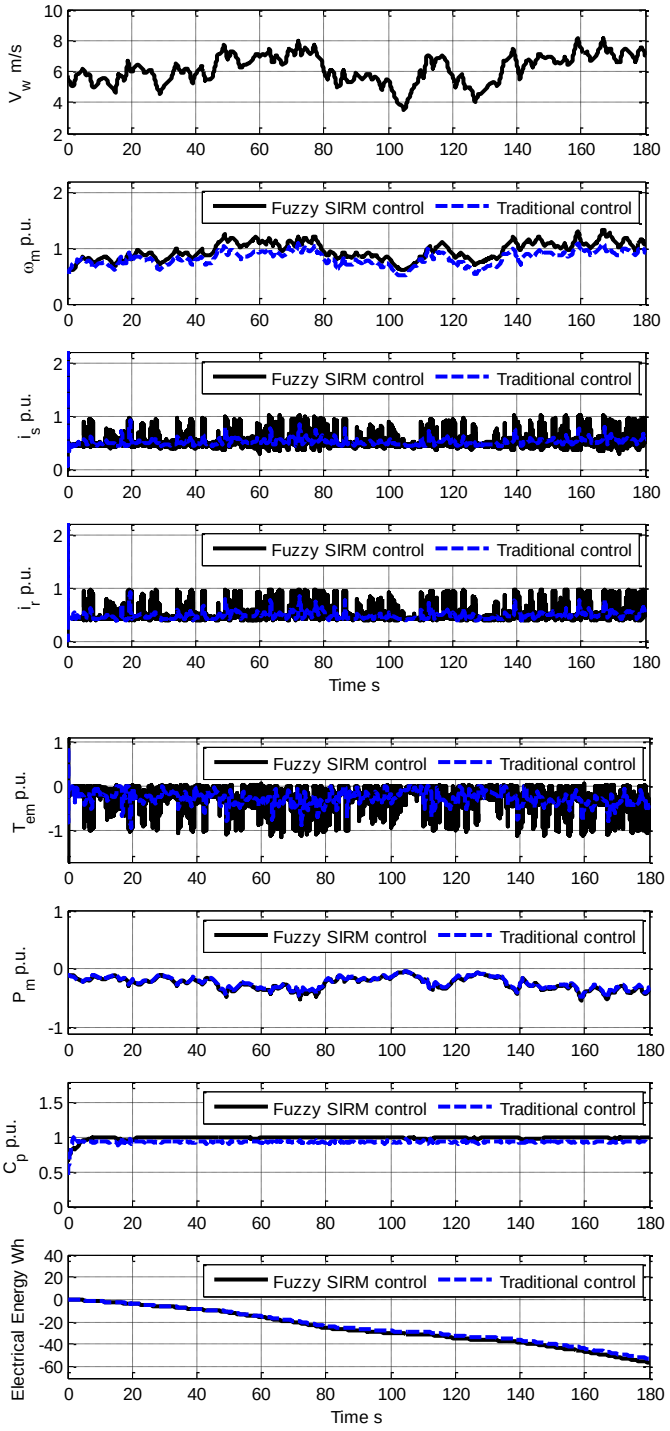

Figure B.6: WECS dynamic response controlled by the traditional power control and the SIRM-based fuzzy controller for low real wind speed profile ($\bar{v}_w$ = 6 m/s) with estimating of λ_i in error of +20% (case 3)

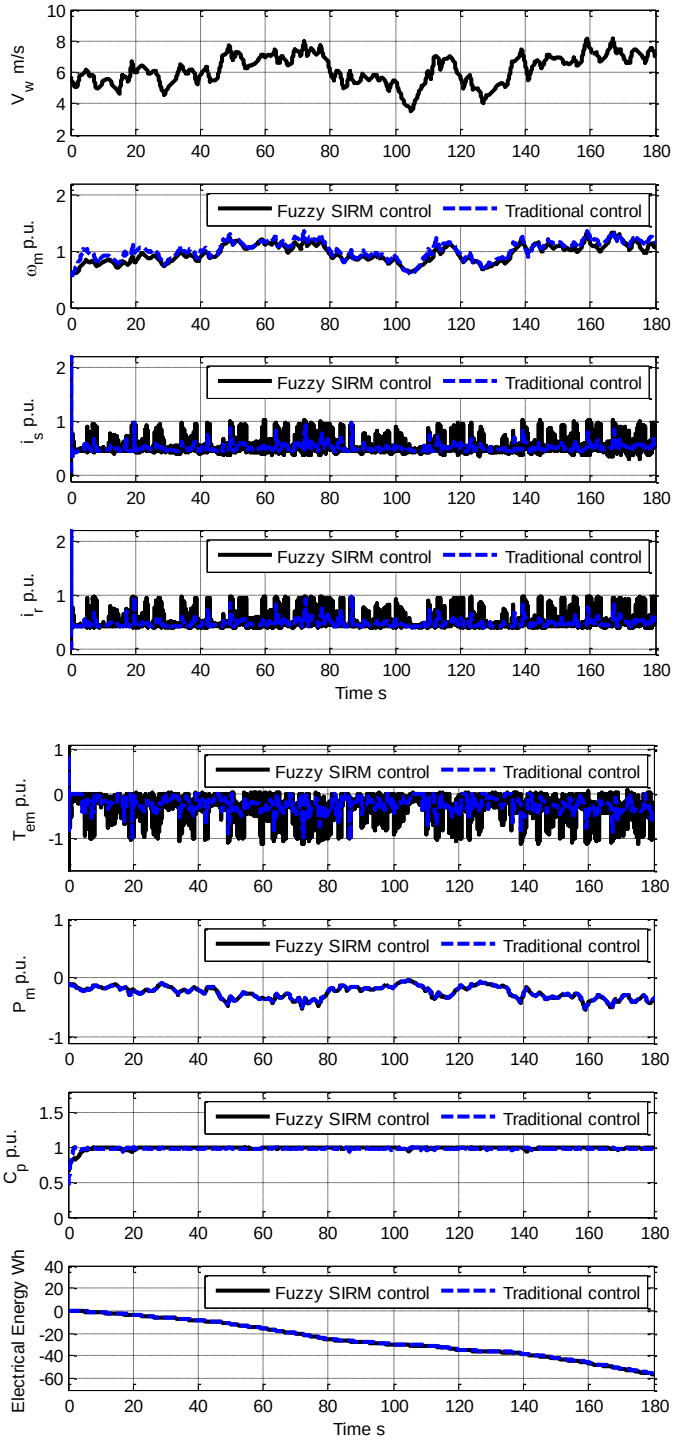

Figure B.7: WECS dynamic response controlled by the traditional power control and the SIRM-based fuzzy controller for low real wind speed profile ($\bar{v}_w$ = 6 m/s) with estimating of air density in error of -20% (case 4)

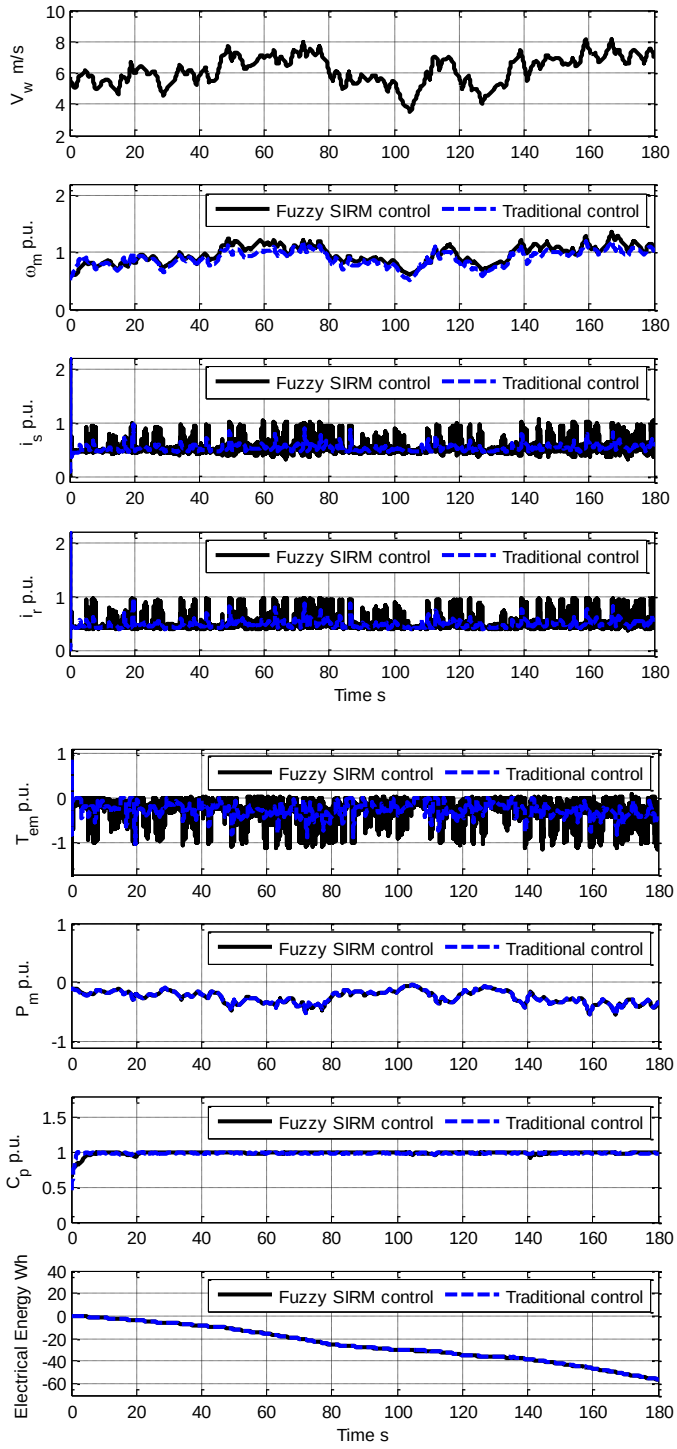

Figure B.8: WECS dynamic response controlled by the traditional power control and the SIRM-based fuzzy controller for low real wind speed profile ($\bar{v}_w$ = 6 m/s) with estimating of air density in error of +20% (case 5)

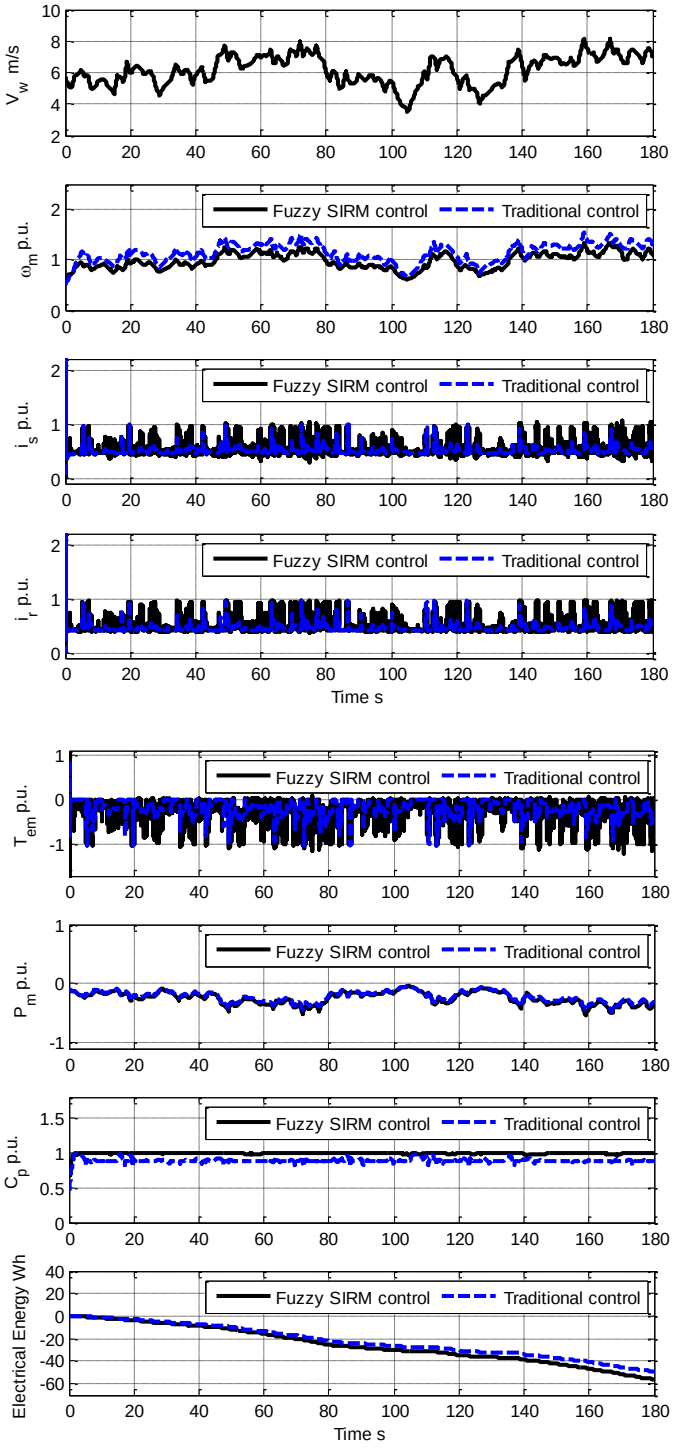

Figure B.9: WECS dynamic response controlled by the traditional power control and the SIRM-based fuzzy controller for low real wind speed profile ($\bar{v}_w$ = 6 m/s) with estimating of λ_i and air density in error of -20% and -20%, respectively (case 6)

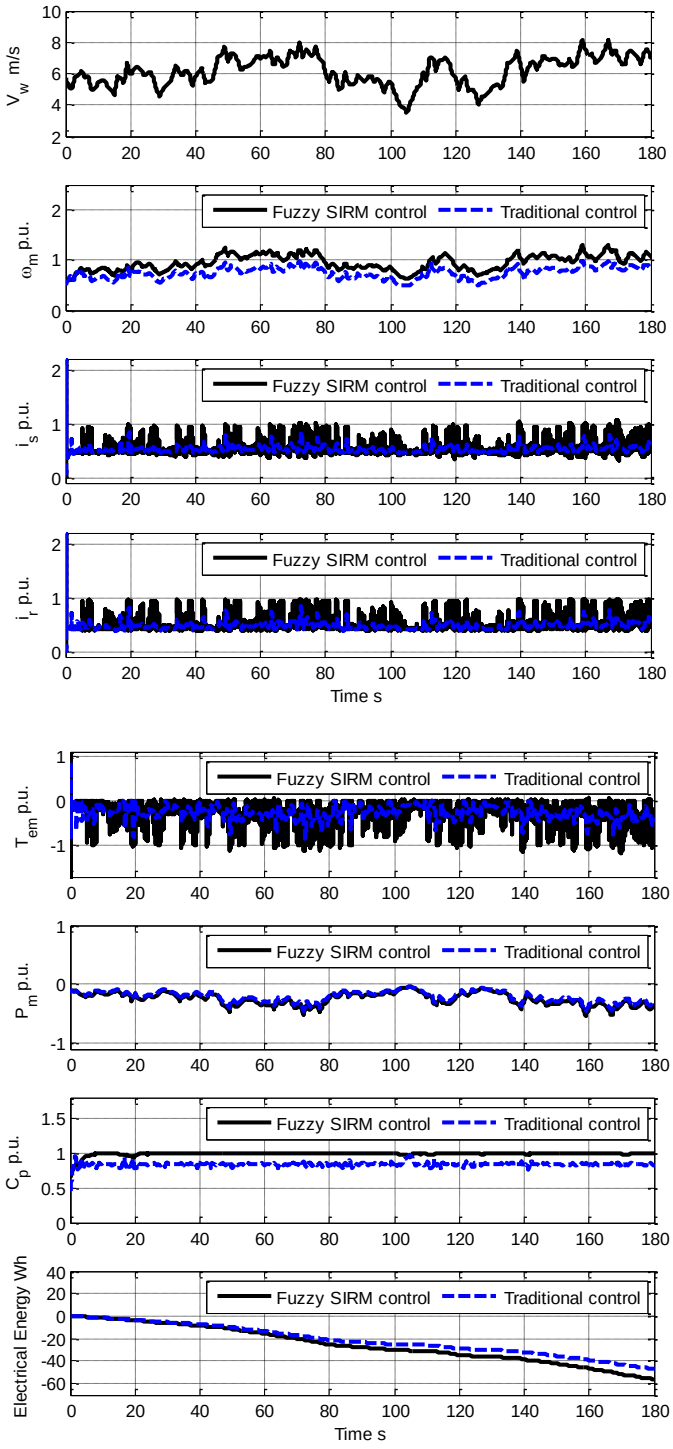

Figure B.10: WECS dynamic response controlled by the traditional power control and the SIRM-based fuzzy controller for low real wind speed profile ($\bar{v}_w$ = 6 m/s) with estimating of λ_i and air density in error of +20% and +20%, respectively (case 7)

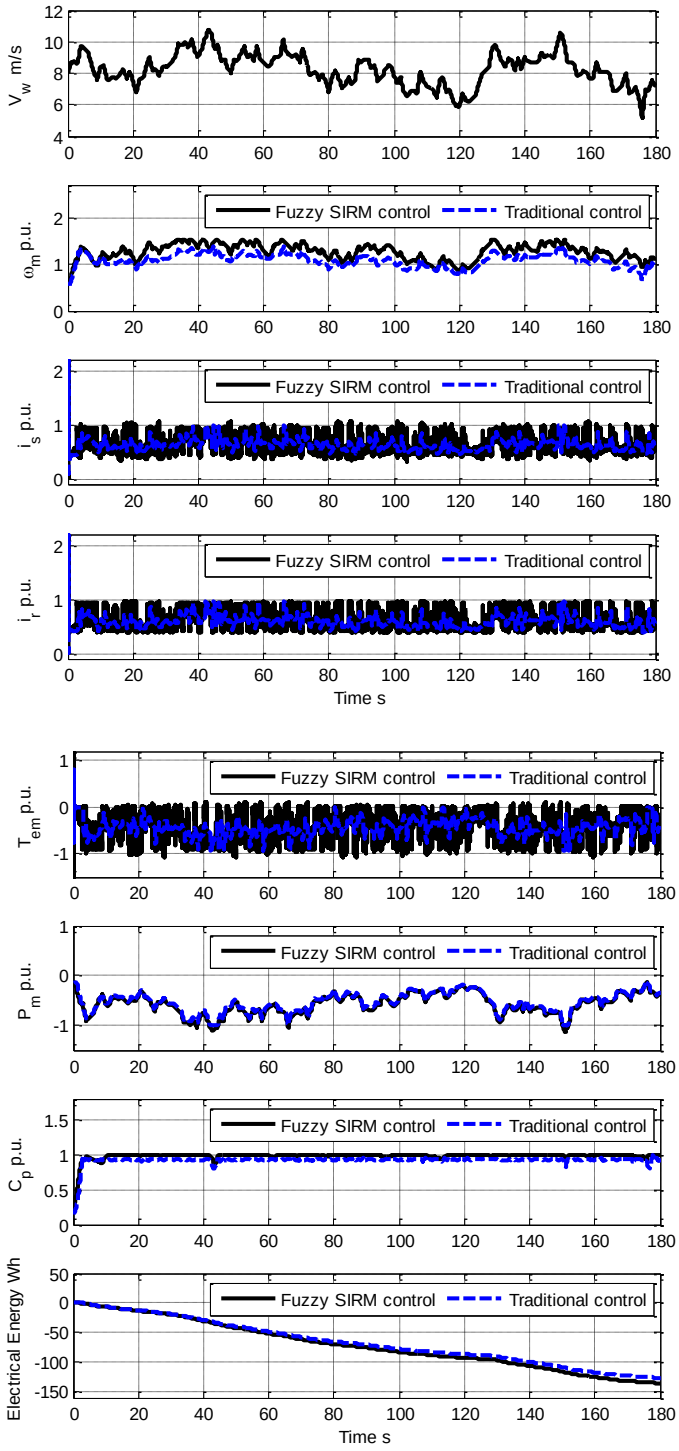

Figure B.11: WECS dynamic response controlled by the traditional power control and the SIRM-based fuzzy controller for medium real wind speed profile ($\bar{v}_w$ = 8 m/s) with estimating of λ_i in error of +20% (case 3)

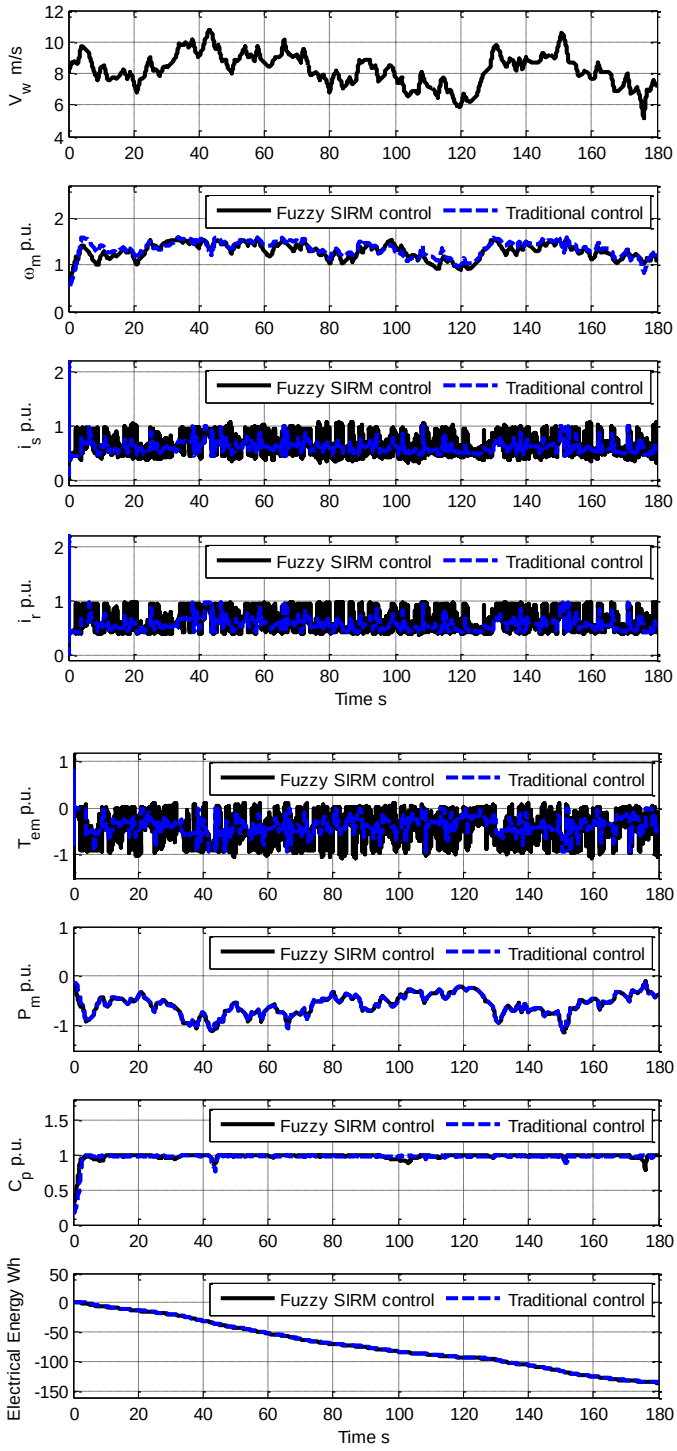

Figure B.12: WECS dynamic response controlled by the traditional power control and the SIRM-based fuzzy controller for medium real wind speed profile ($\bar{v}_w$ = 8 m/s) with estimating of air density in error of -20% (case 4)

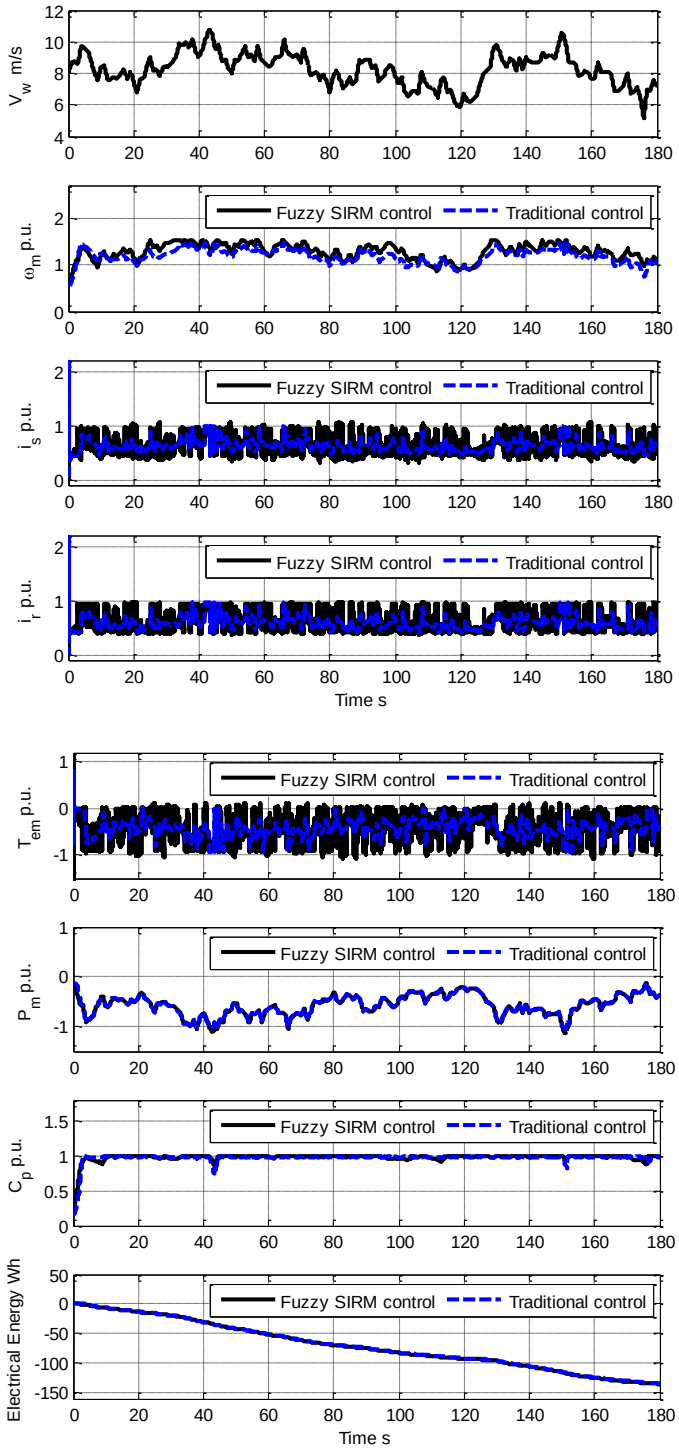

Figure B.13: WECS dynamic response controlled by the traditional power control and the SIRM-based fuzzy controller for medium real wind speed profile ($\bar{v}_w$ = 8 m/s) with estimating of air density in error of +20% (case 5)

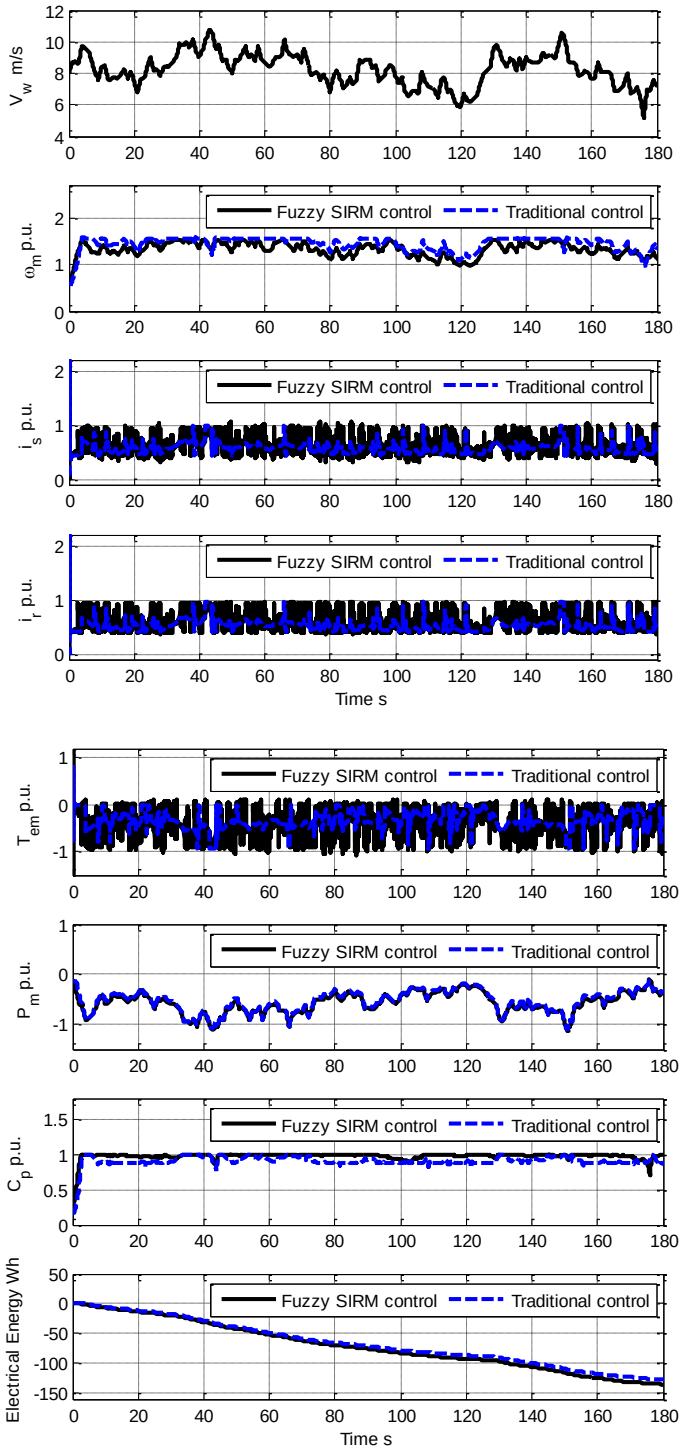

Figure B.14: WECS dynamic response controlled by the traditional power control and the SIRM-based fuzzy controller for medium real wind speed profile ($\bar{v}_w$ = 8 m/s) with estimating of λ_i and air density in error of -20% and -20%, respectively (case 6)

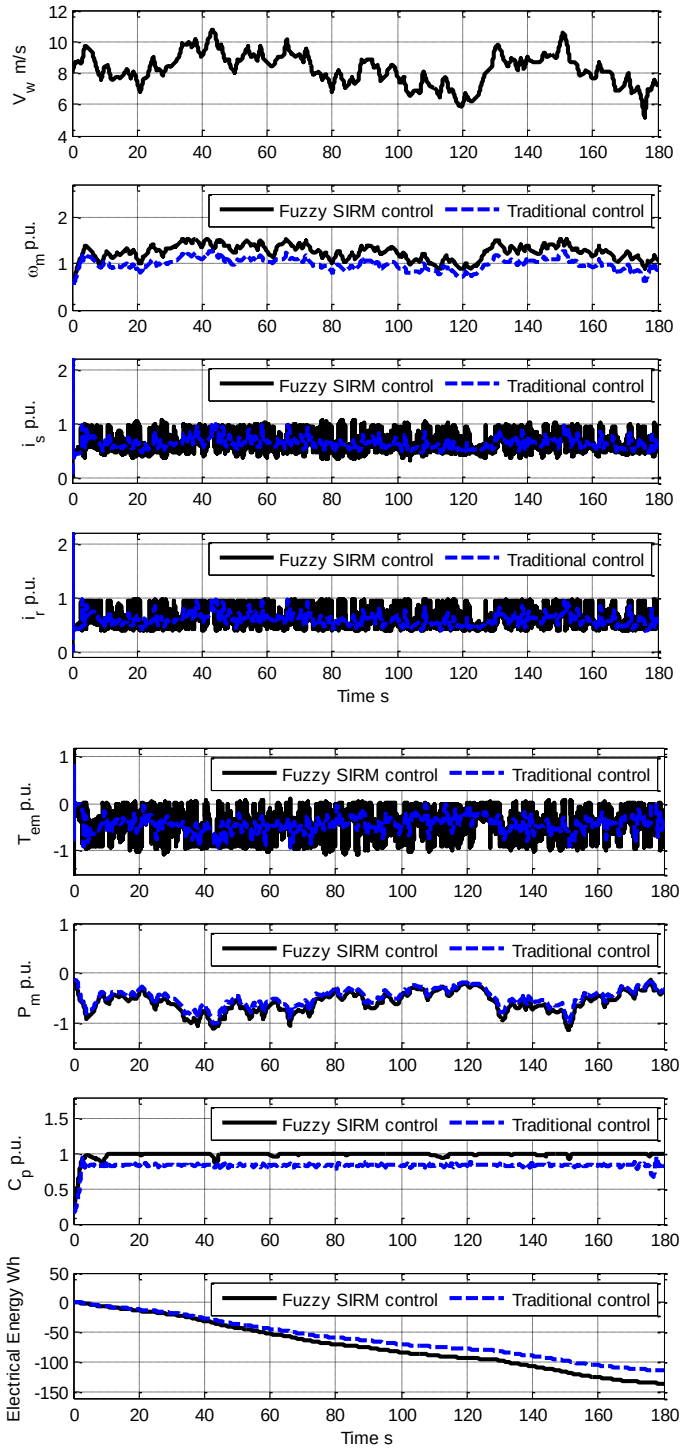

Figure B.15: WECS dynamic response controlled by the traditional power control and the SIRM-based fuzzy controller for medium real wind speed profile ($\bar{v}_w$ = 8 m/s) with estimating of λ_i and air density in error of +20% and +20%, respectively (case 7)

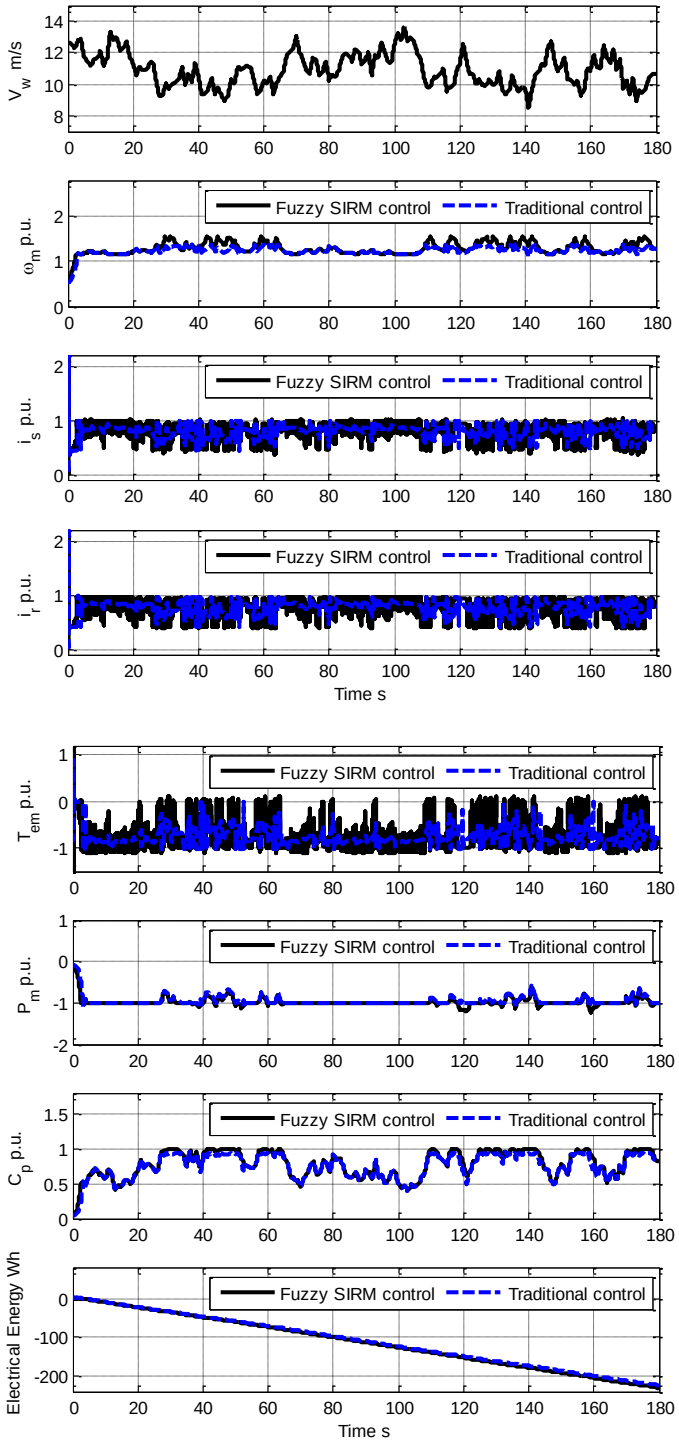

Figure B.16: WECS dynamic response controlled by the traditional power control the SIRM-based fuzzy controller for high real wind speed profile ($\bar{v}_w$ = 11 m/s) with estimating of λ_i in error of +20% (case 3)

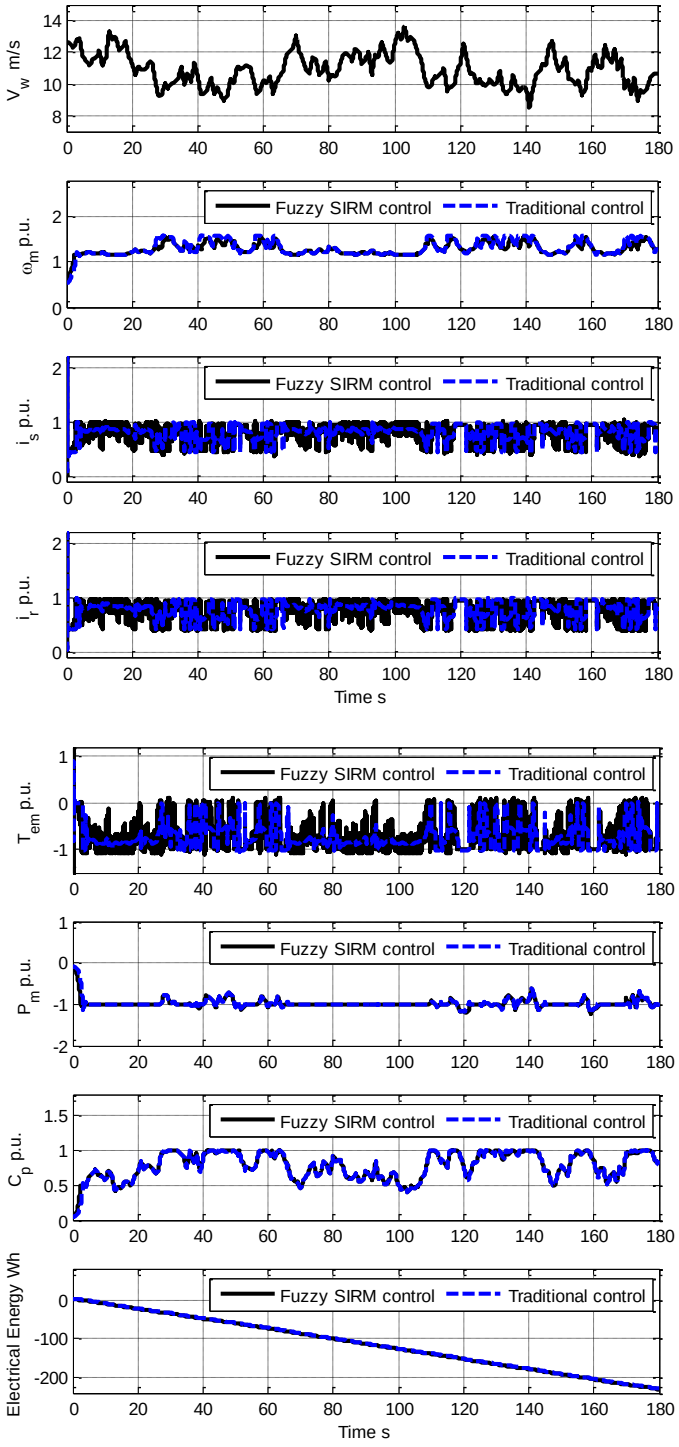

Figure B.17: WECS dynamic response controlled by the traditional power control and the SIRM-based fuzzy controller for high real wind speed profile ($\bar{v}_w$ = 11 m/s) with estimating of air density in error of -20% (case 4)

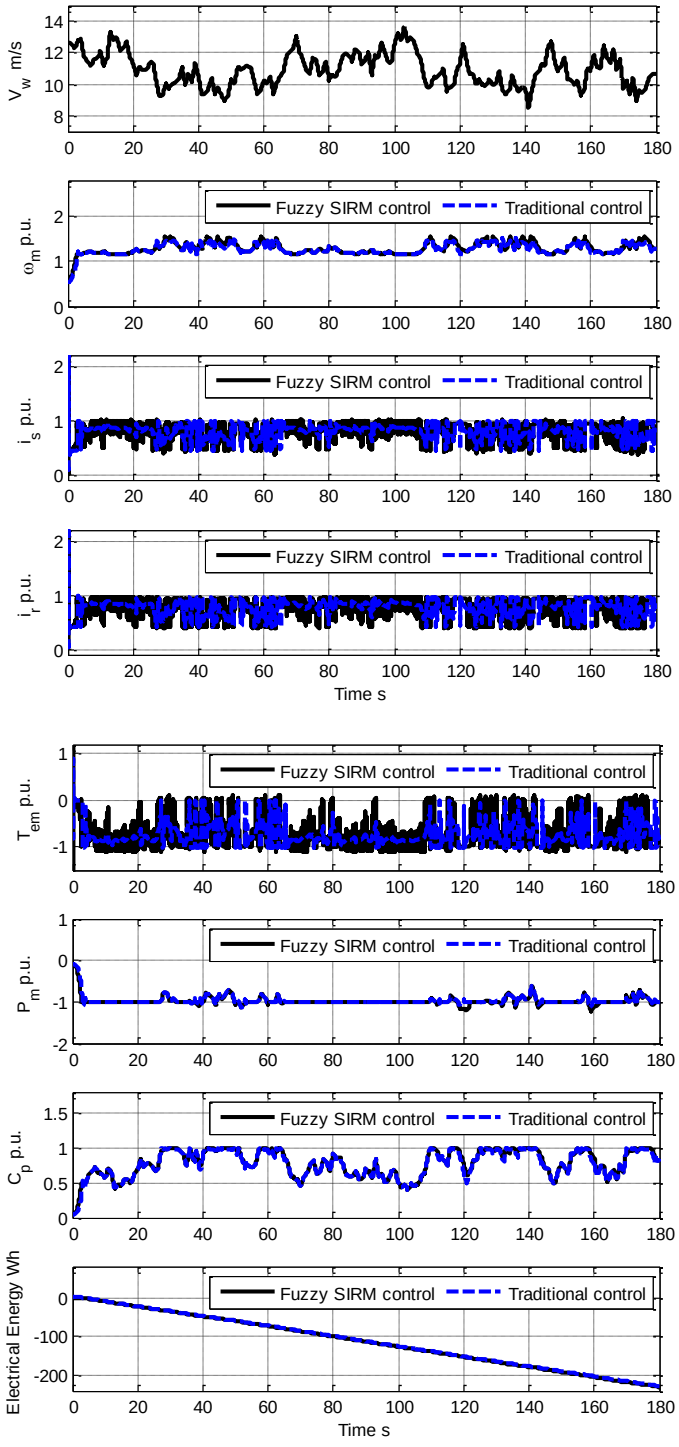

Figure B.18: WECS dynamic response controlled by the traditional power control and the SIRM-based fuzzy controller for high real wind speed profile ($\bar{v}_w$ = 11 m/s) with estimating of air density in error of +20% (case 5)

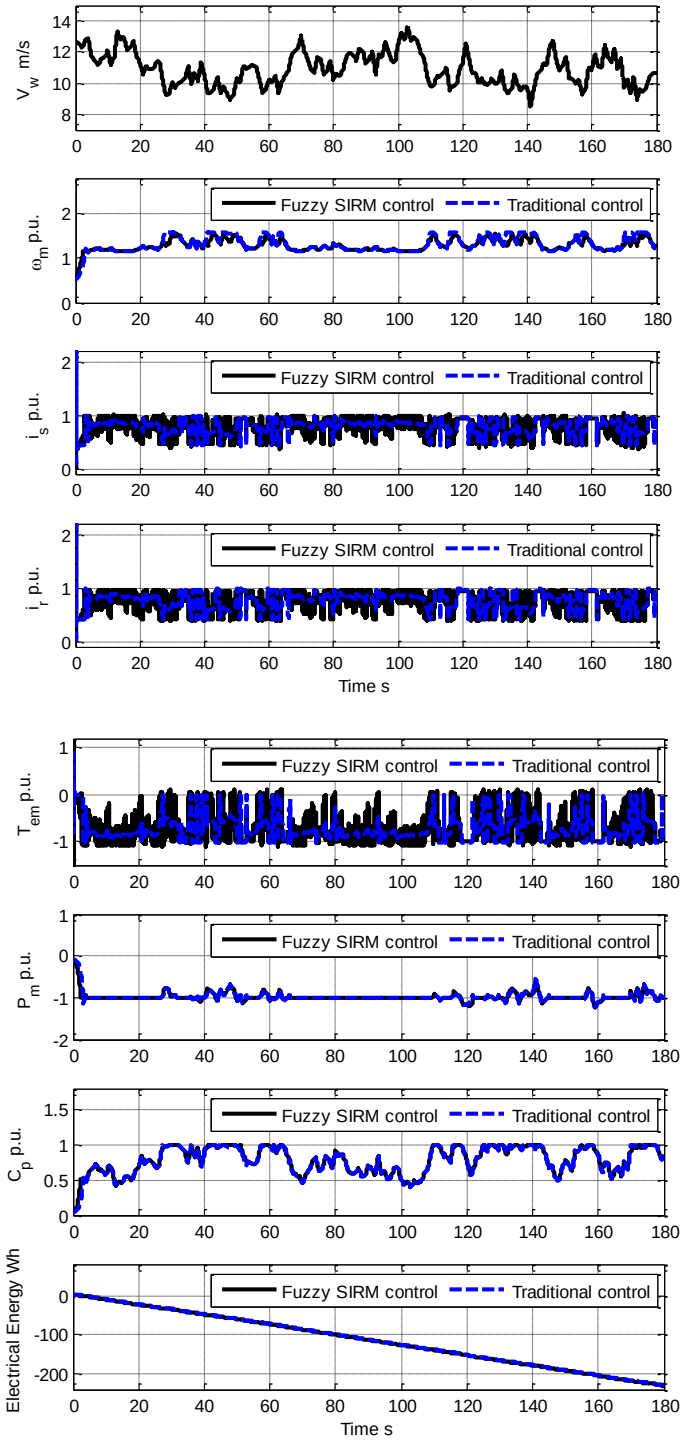

Figure B.19: WECS dynamic response controlled by the traditional power control and the SIRM-based fuzzy controller for high real wind speed profile ($\bar{v}_w$ = 11 m/s) with estimating of λ_i and air density in error of -20% and -20%, respectively (case 6)

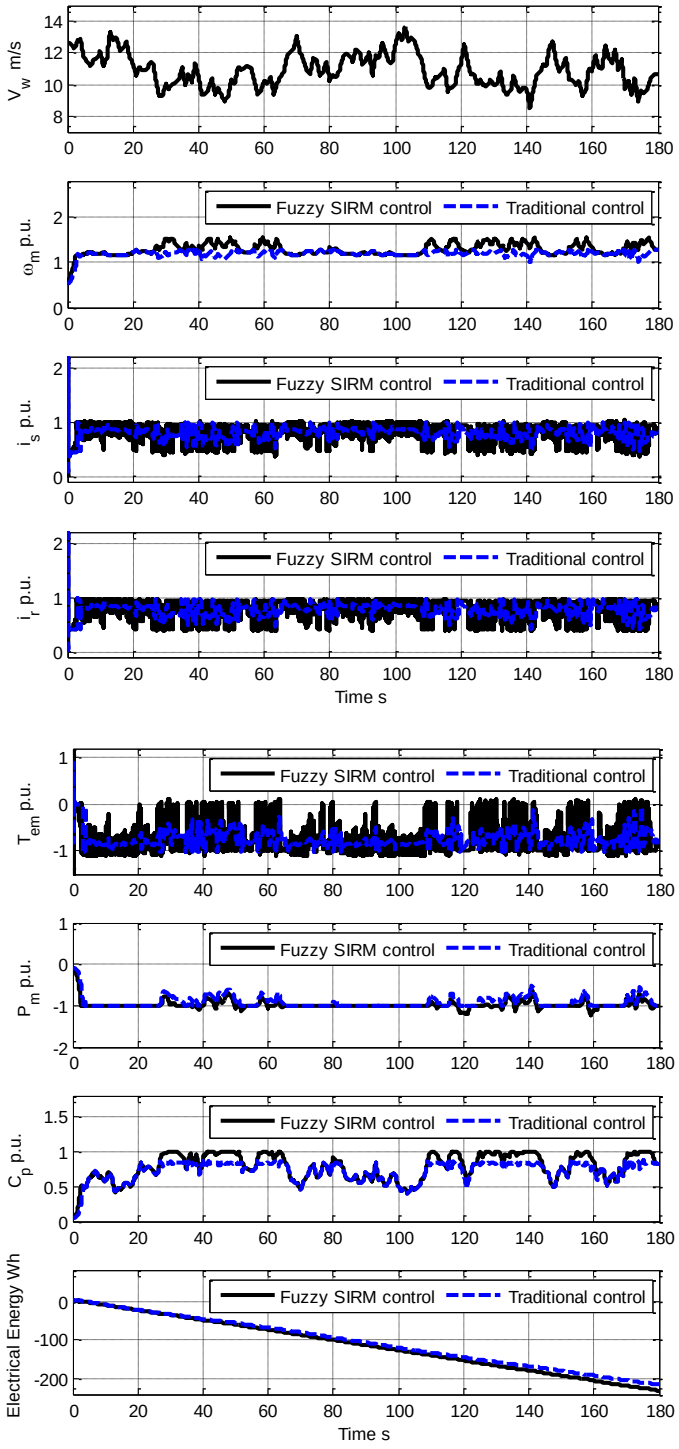

Figure B.20: WECS dynamic response controlled by the traditional power control and the SIRM-based fuzzy controller for high real wind speed profile ($\bar{v}_w$ = 11 m/s) with estimating of λ_i and air density in error of +20% and +20%, respectively (case 7)

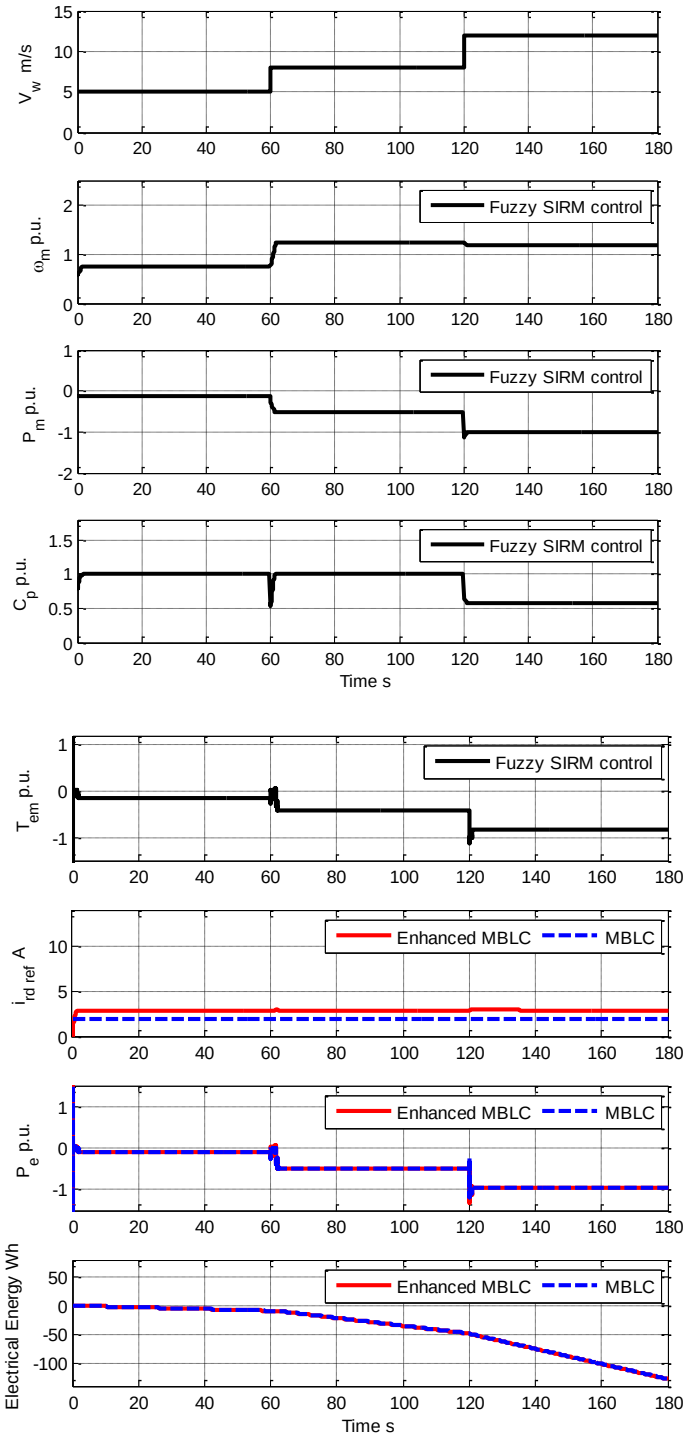

Figure B.21: WECS dynamic response controlled by the traditional MBLC and the enhanced MBLC for step-up-changing wind speed with error in estimation r_s of -50%, r_r of 0%, $L_{\sigma s}$ of 0% and L_m of 0% (case 3)

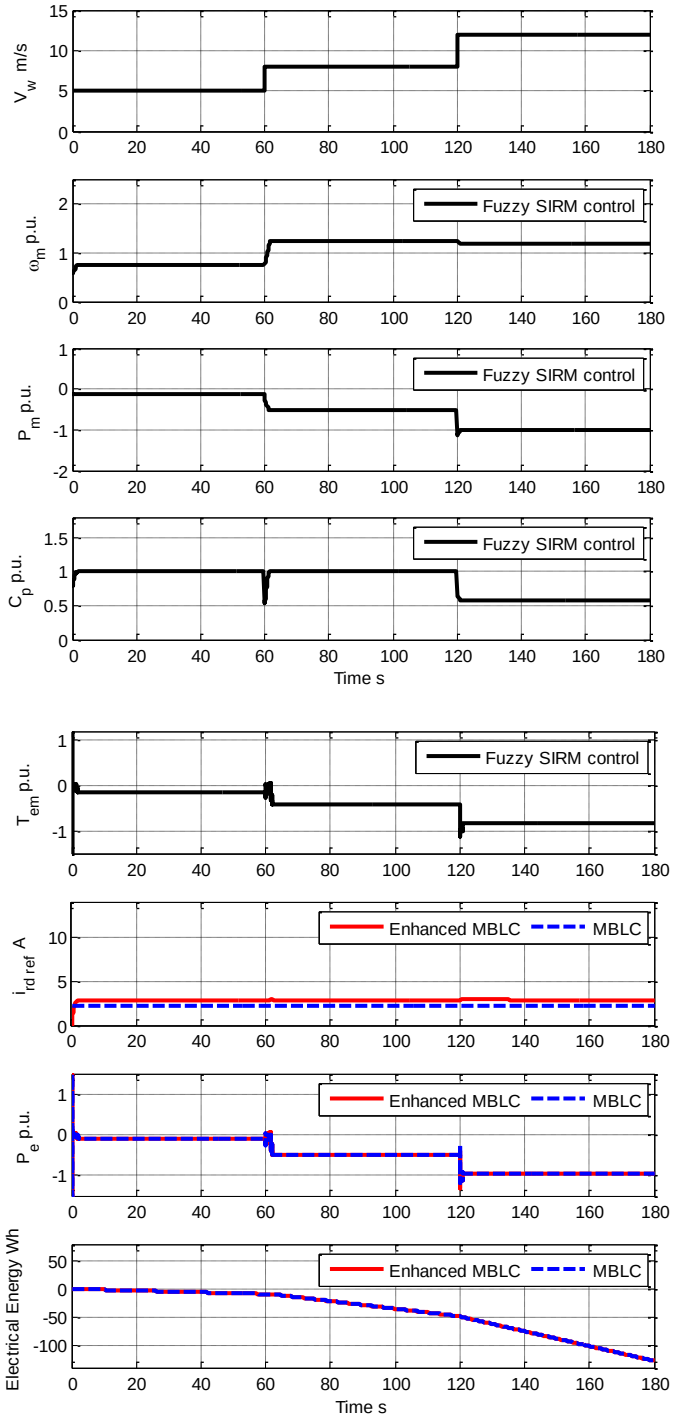

Figure B.22: WECS dynamic response controlled by the traditional MBLC and the enhanced MBLC for step-up-changing wind speed with error in estimation r_s of 0%, r_r of +50%, $L_{\sigma s}$ of 0% and L_m of 0% (case 4)

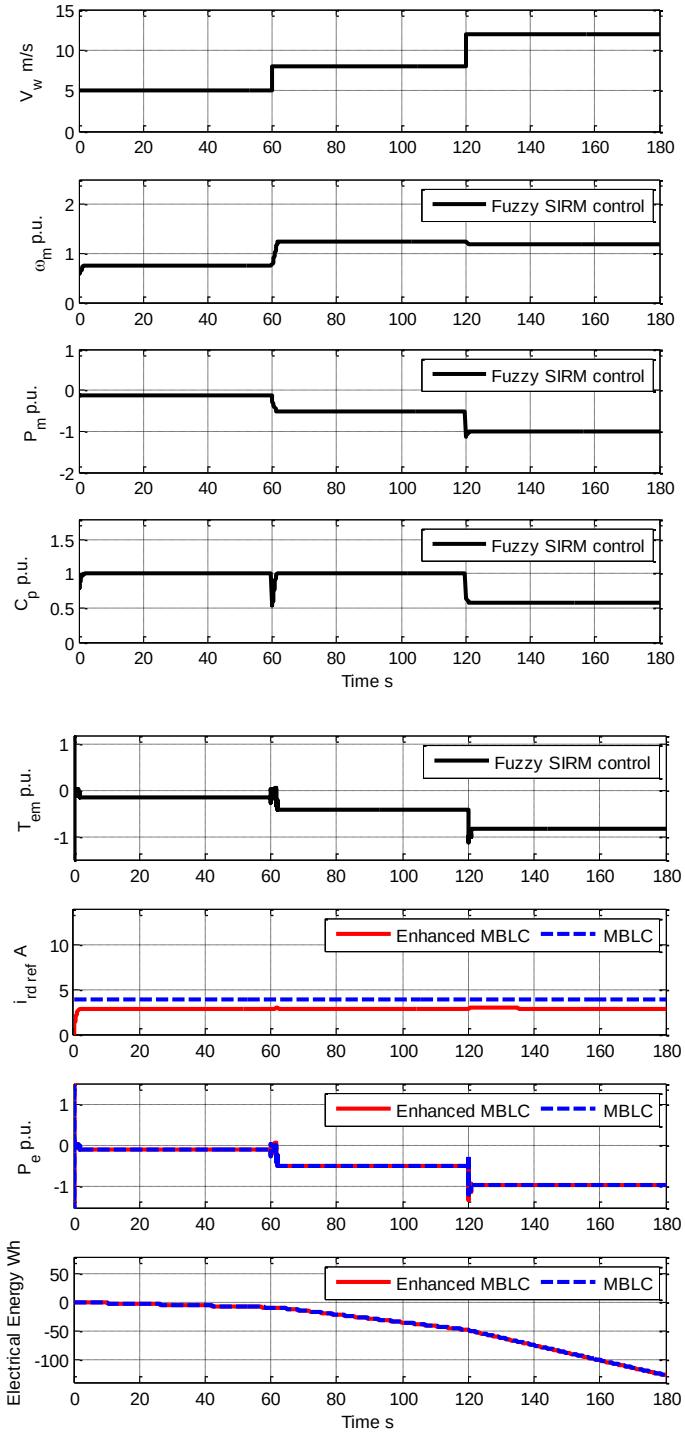

Figure B.23: WECS dynamic response controlled by the traditional MBLC and the enhanced MBLC for step-up-changing wind speed with error in estimation r_s of 0%, r_r of -50%, $L_{\sigma s}$ of 0% and L_m of 0% (case 5)

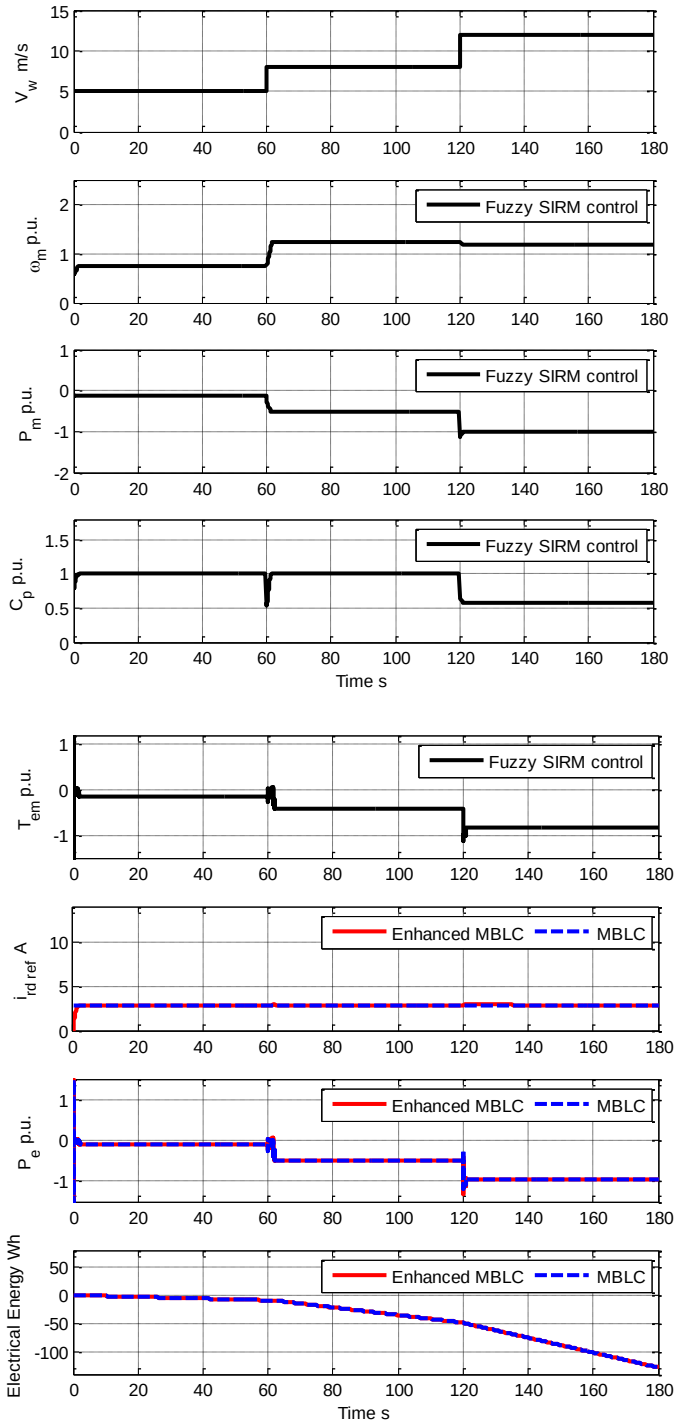

Figure B.24: WECS dynamic response controlled by the traditional MBLC and the enhanced MBLC for step-up-changing wind speed with error in estimation r_s of 0%, r_r of 0%, $L_{\sigma s}$ of +50% and L_m of 0% (case 6)

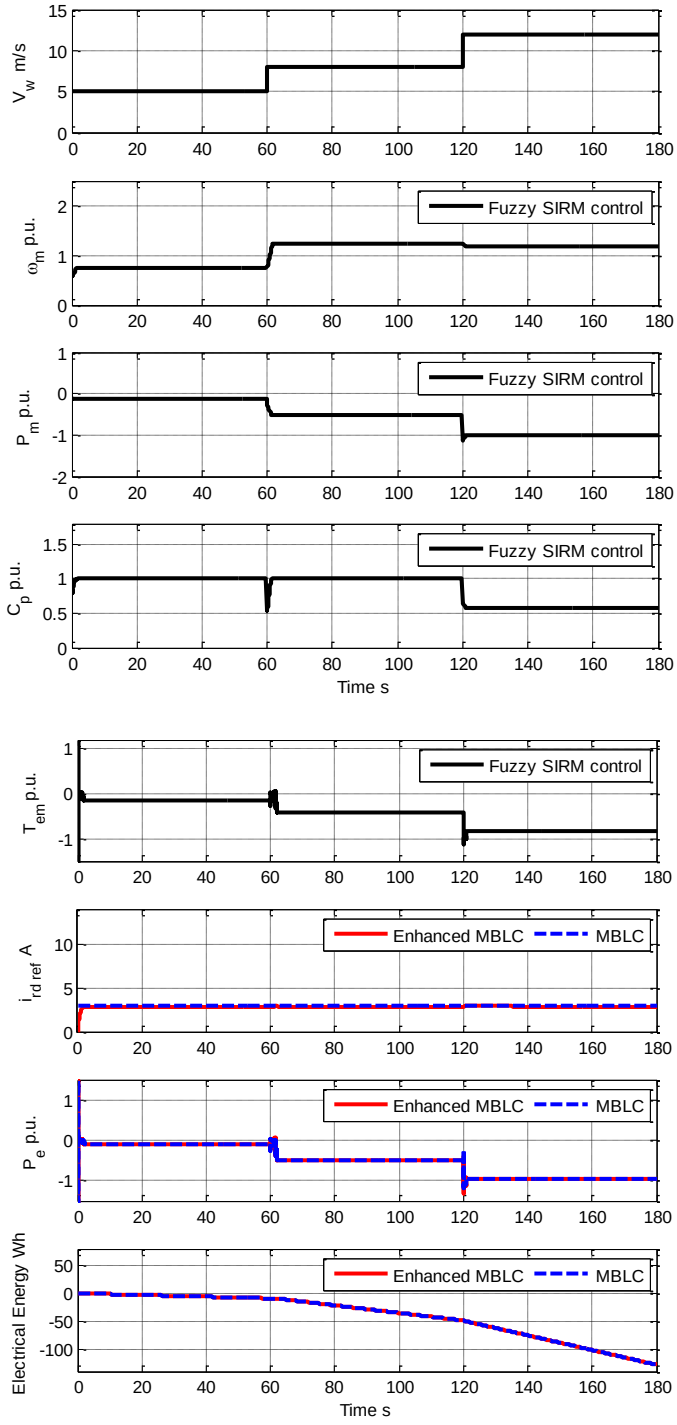

Figure B.25: WECS dynamic response controlled by the traditional MBLC and the enhanced MBLC for step-up-changing wind speed with error in estimation r_s of 0%, r_r of 0%, $L_{\sigma s}$ of -50% and L_m of 0% (case 7)

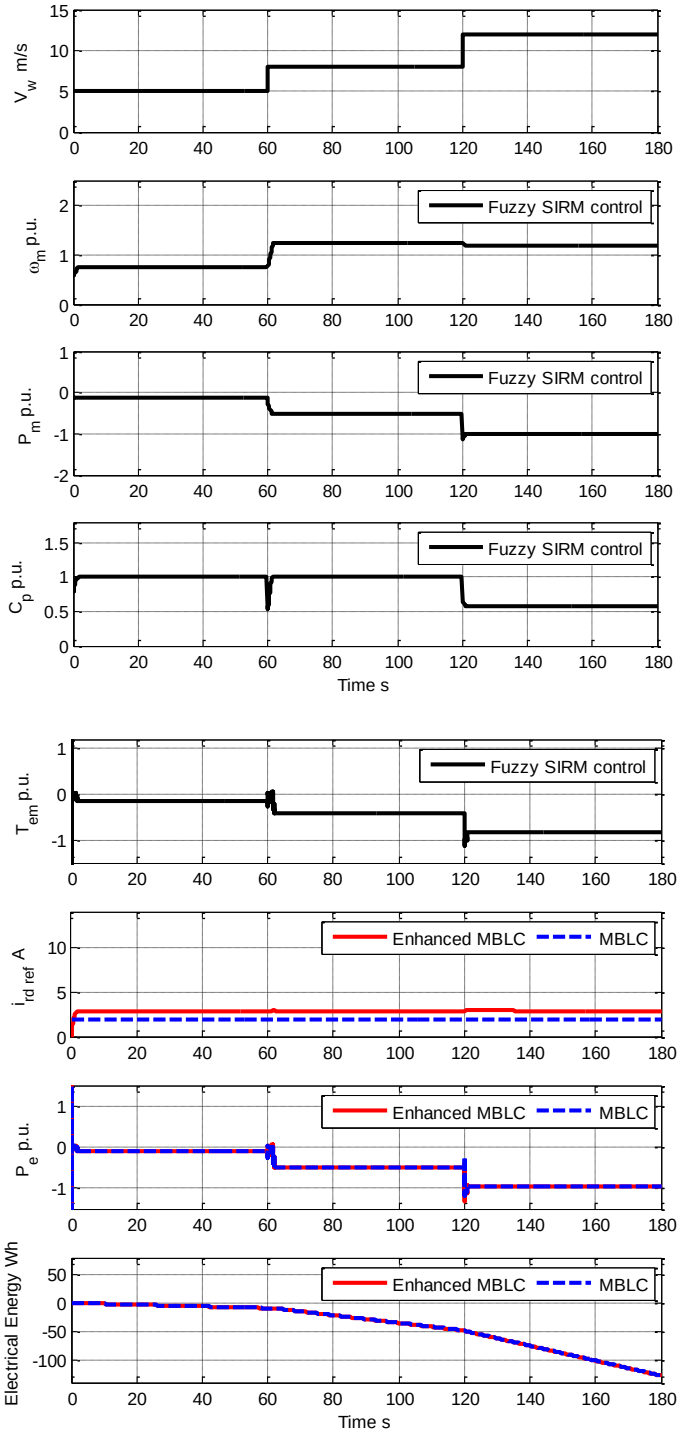

Figure B.26: WECS dynamic response controlled by the traditional MBLC and the enhanced MBLC for step-up-changing wind speed with error in estimation r_s of 0%, r_r of 0%, $L_{\sigma s}$ of 0% and L_m of +50% (case 8)

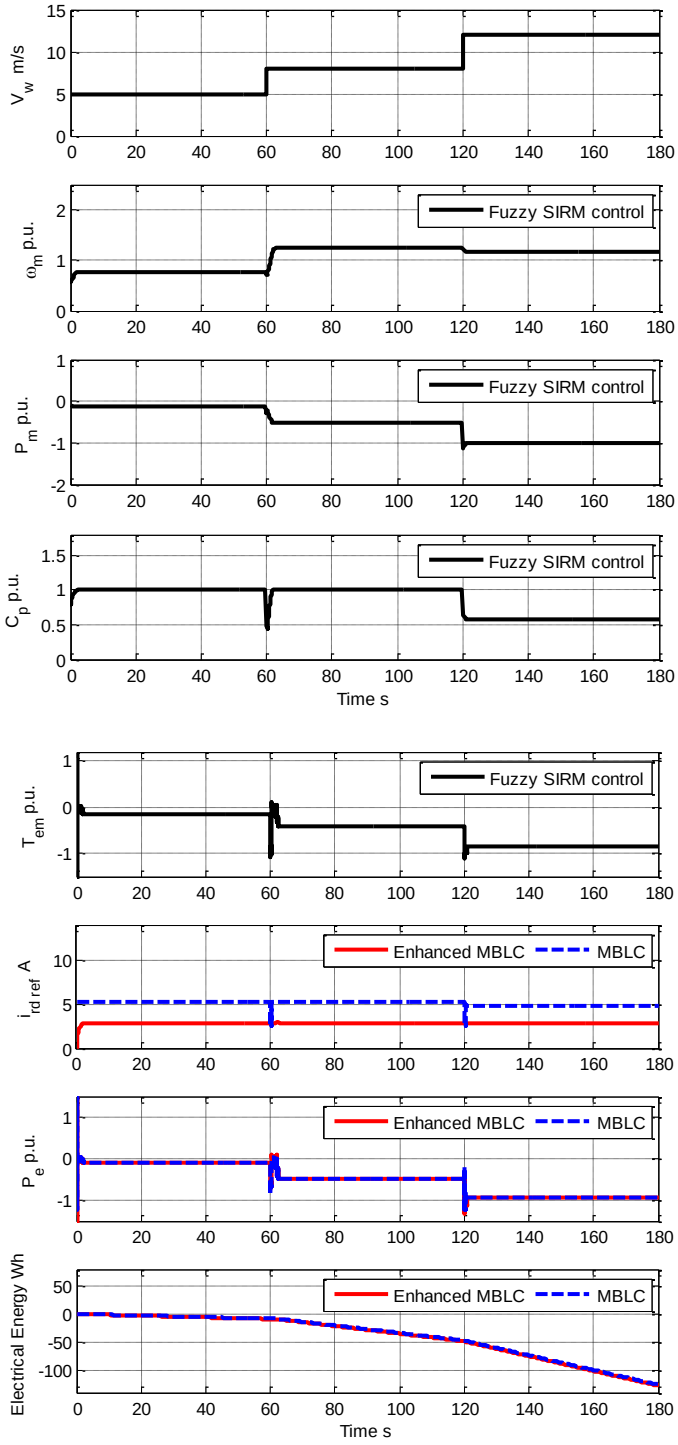

Figure B.27: WECS dynamic response controlled by the traditional MBLC and the enhanced MBLC for step-up-changing wind speed with error in estimation r_s of 0%, r_r of 0%, $L_{\sigma s}$ of 0% and L_m of -50% (case 9)

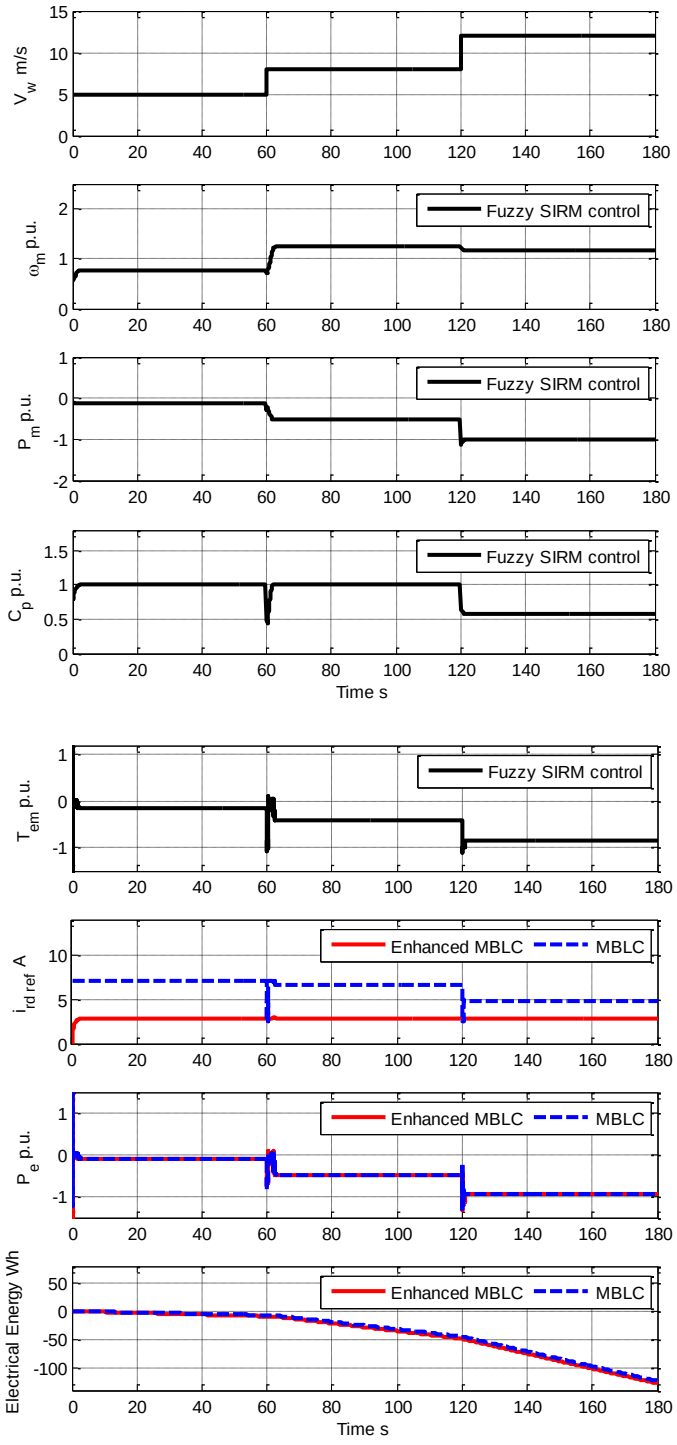

Figure B.28: WECS dynamic response controlled by the traditional MBLC and the enhanced MBLC for step-up-changing wind speed with error in estimation r_s of 0%, r_r of -50%, $L_{\sigma s}$ of 0% and L_m of -50% (case 10)

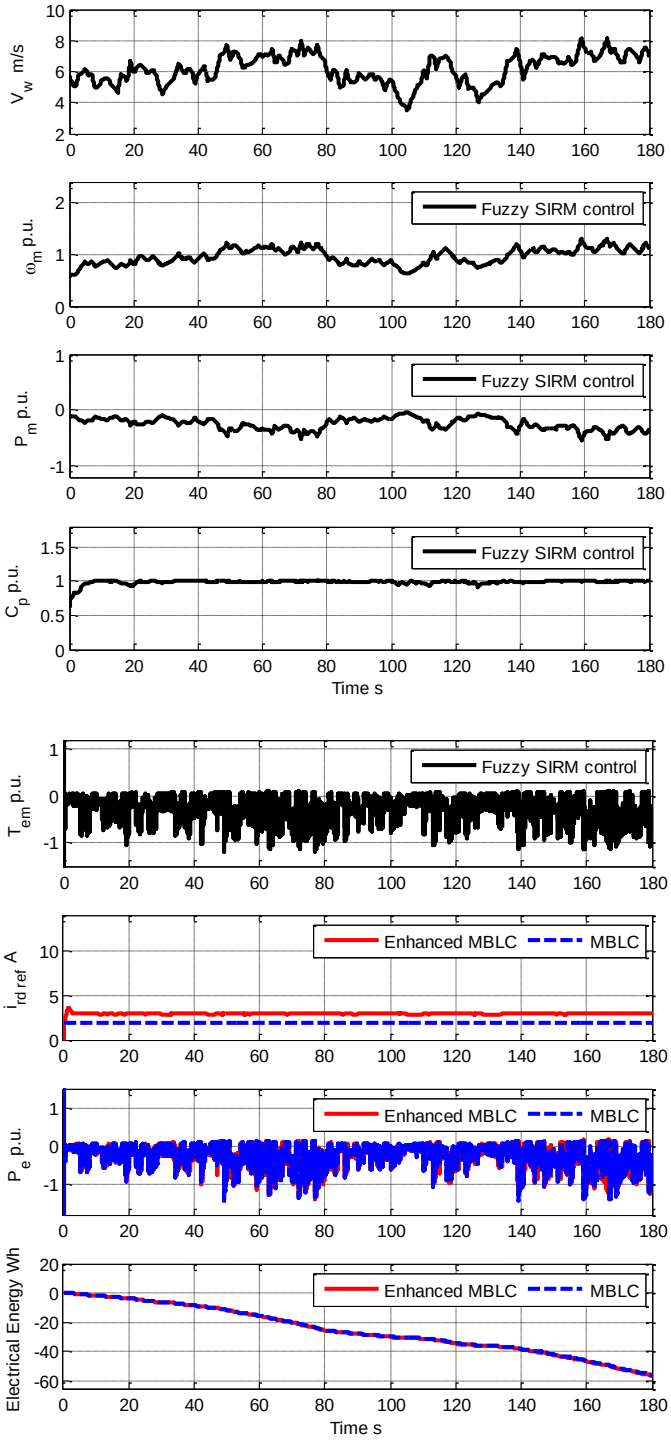

Figure B.29: WECS dynamic response controlled by the traditional MBLC and the enhanced MBLC for low real wind speed profile ($\bar{v}_w$ = 6 m/s) with error in estimation r_s of -50%, r_r of 0%, $L_{\sigma s}$ of 0% and L_m of 0% (case 3)

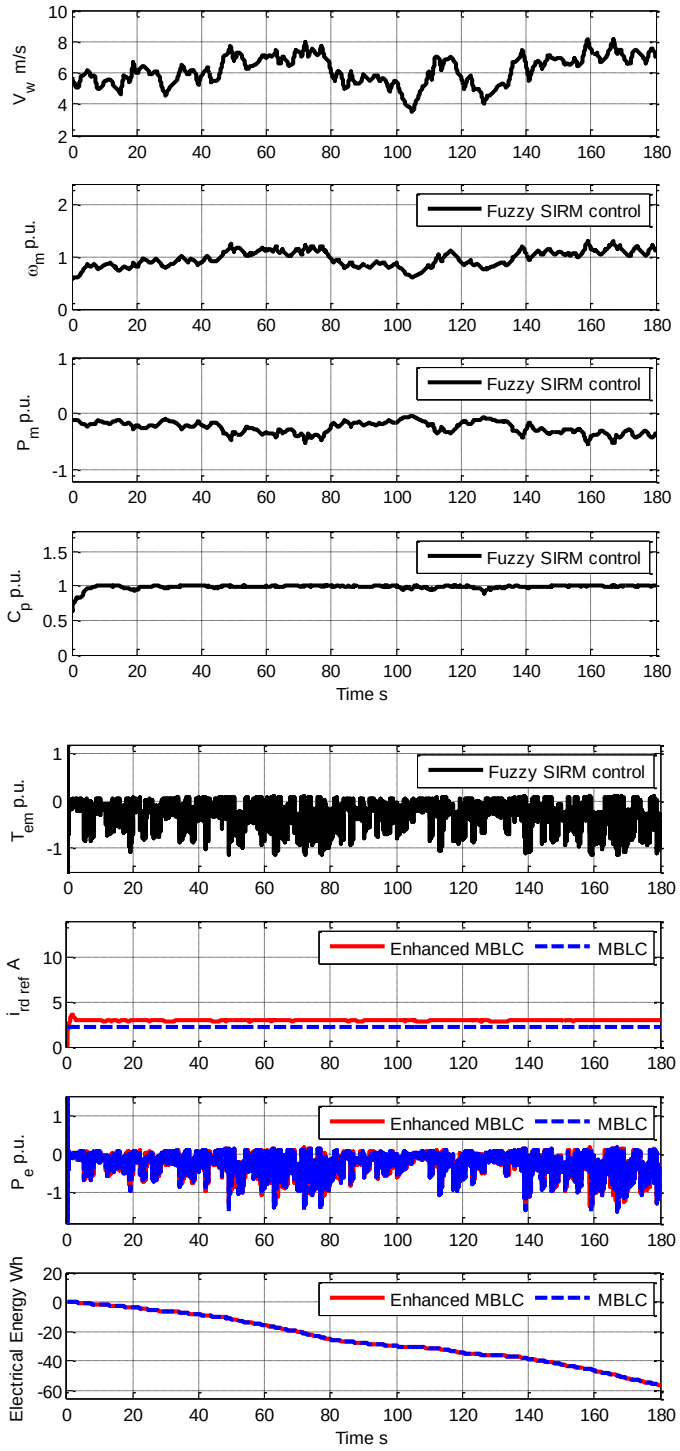

Figure B.30: WECS dynamic response controlled by the traditional MBLC and the enhanced MBLC for low real wind speed profile ($\bar{v}_w$ = 6 m/s) with error in estimation r_s of 0%, r_r of +50%, $L_{\sigma s}$ of 0% and L_m of 0% (case 4)

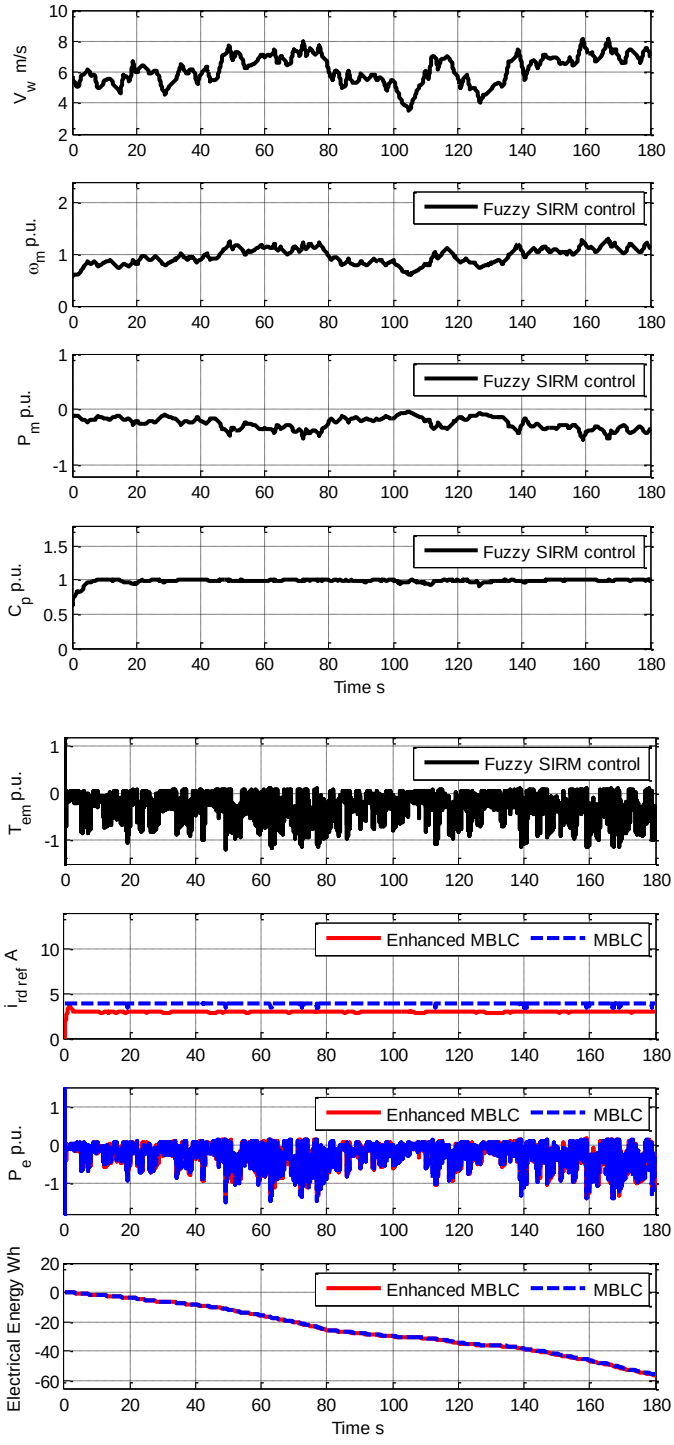

Figure B.31: WECS dynamic response controlled by the traditional MBLC and the enhanced MBLC for low real wind speed profile ($\bar{v}_w$ = 6 m/s) with error in estimation r_s of 0%, r_r of -50%, $L_{\sigma s}$ of 0% and L_m of 0% (case 5)

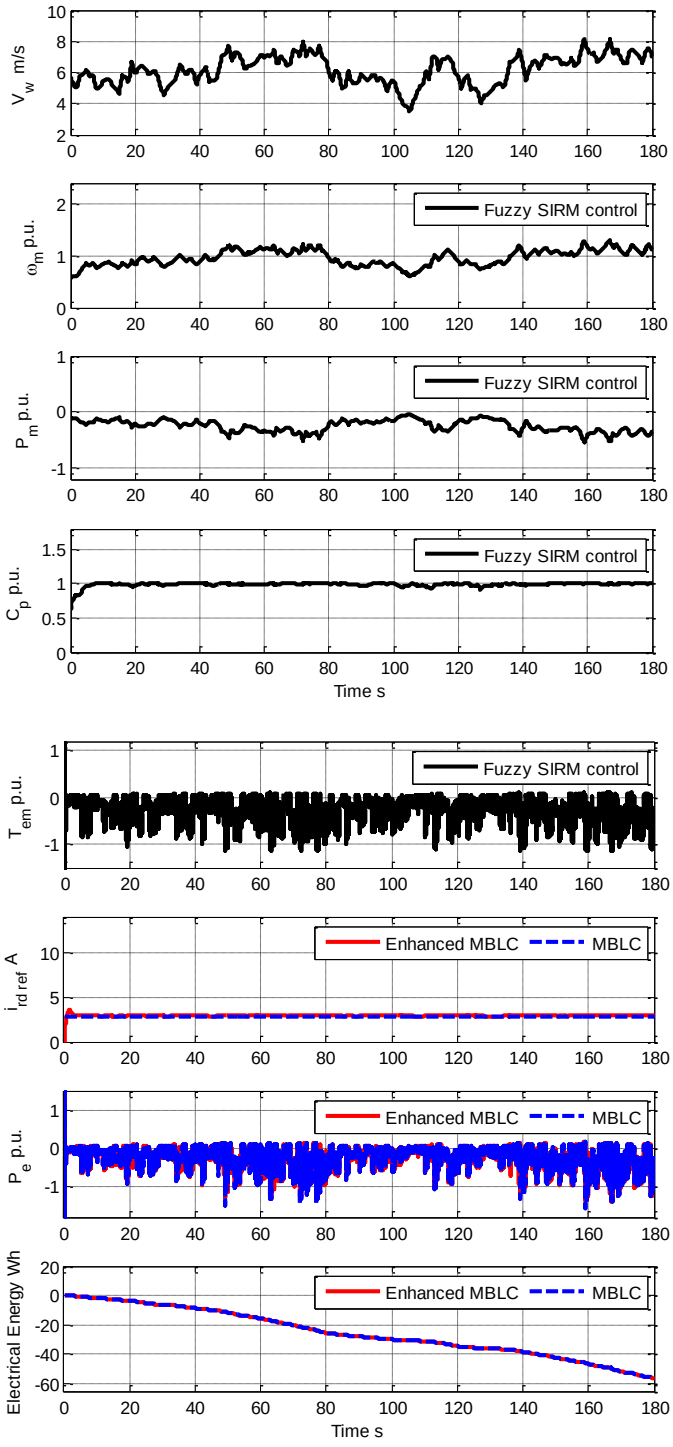

Figure B.32: WECS dynamic response controlled by the traditional MBLC and the enhanced MBLC for low real wind speed profile ($\bar{v}_w$ = 6 m/s) with error in estimation r_s of 0%, r_r of 0%, $L_{\sigma s}$ of +50% and L_m of 0% (case 6)

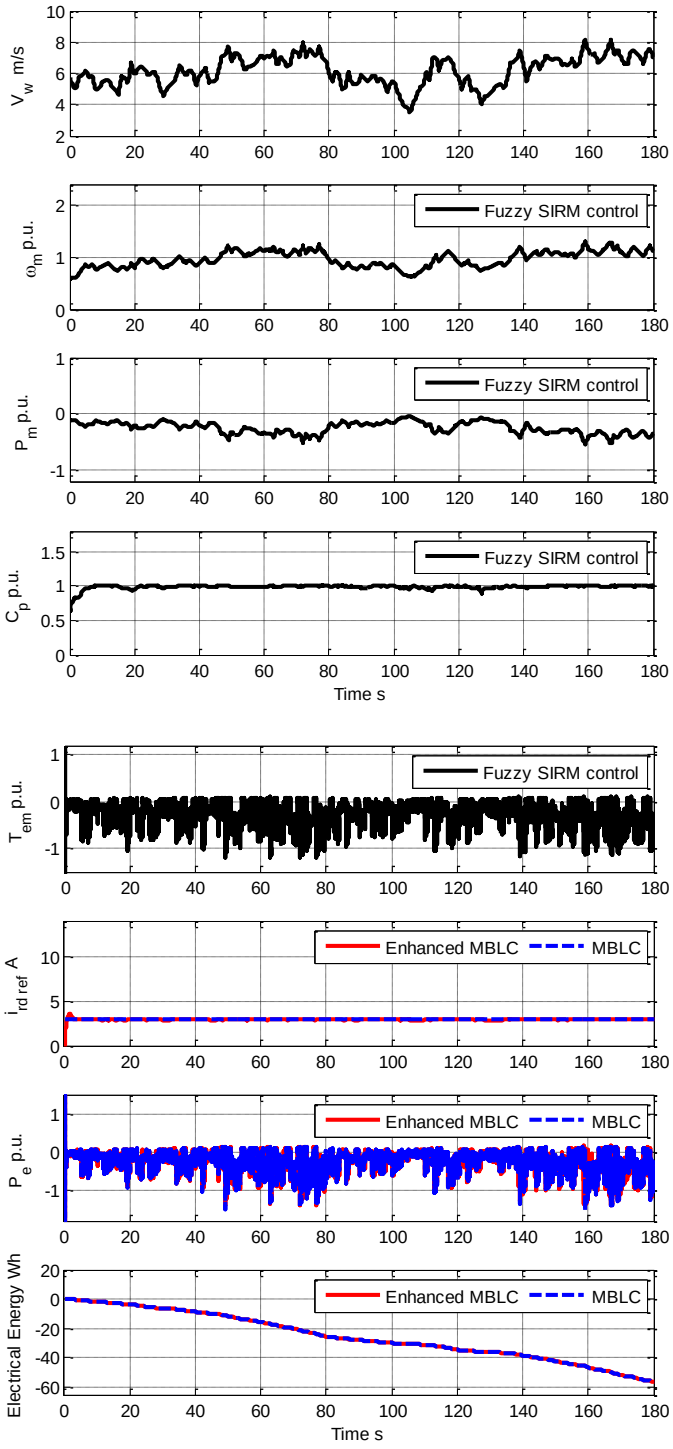

Figure B.33: WECS dynamic response controlled by the traditional MBLC and the enhanced MBLC for low real wind speed profile ($\bar{v}_w$ = 6 m/s) with error in estimation r_s of 0%, r_r of 0%, $L_{\sigma s}$ of -50% and L_m of 0% (case 7)

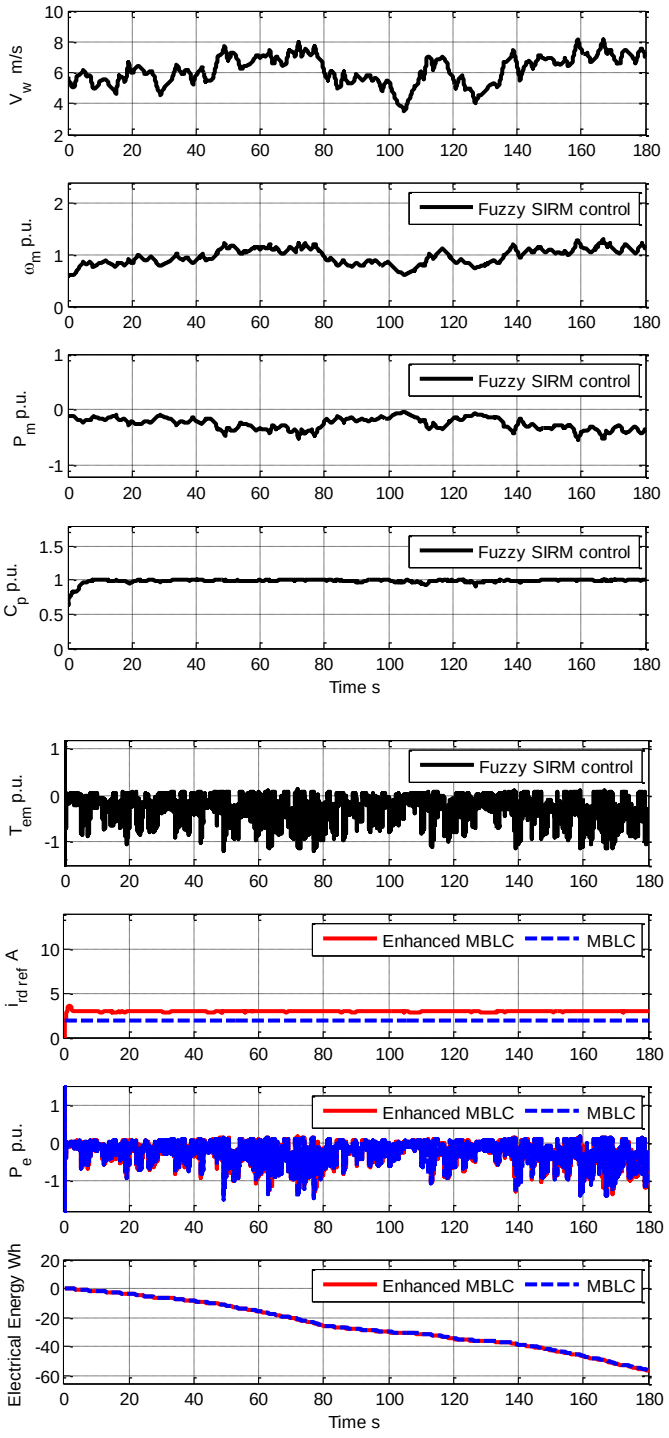

Figure B.34: WECS dynamic response controlled by the traditional MBLC and the enhanced MBLC for low real wind speed profile ($\bar{v}_w$ = 6 m/s) with error in estimation r_s of 0%, r_r of 0%, $L_{\sigma s}$ of 0% and L_m of +50% (case 8)

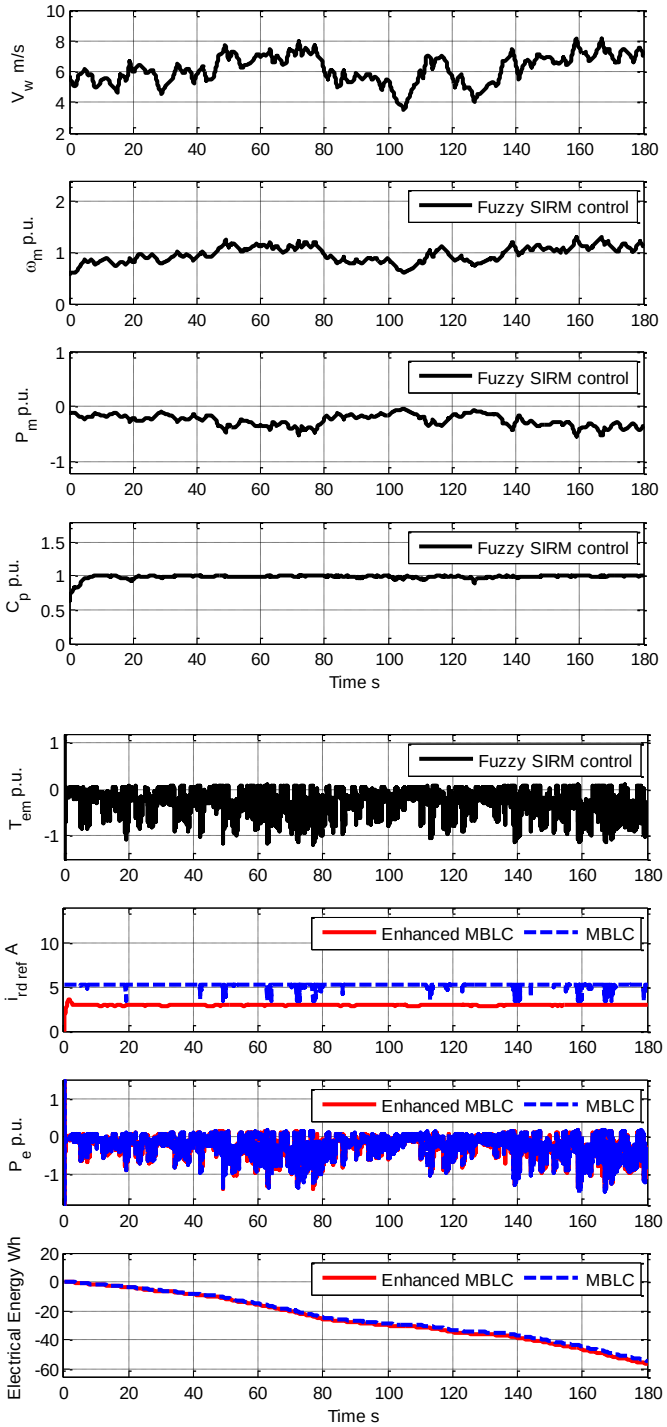

Figure B.35: WECS dynamic response controlled by the traditional MBLC and the enhanced MBLC for low real wind speed profile ($\bar{v}_w$ = 6 m/s) with error in estimation r_s of 0%, r_r of 0%, $L_{\sigma s}$ of 0% and L_m of -50% (case 9)

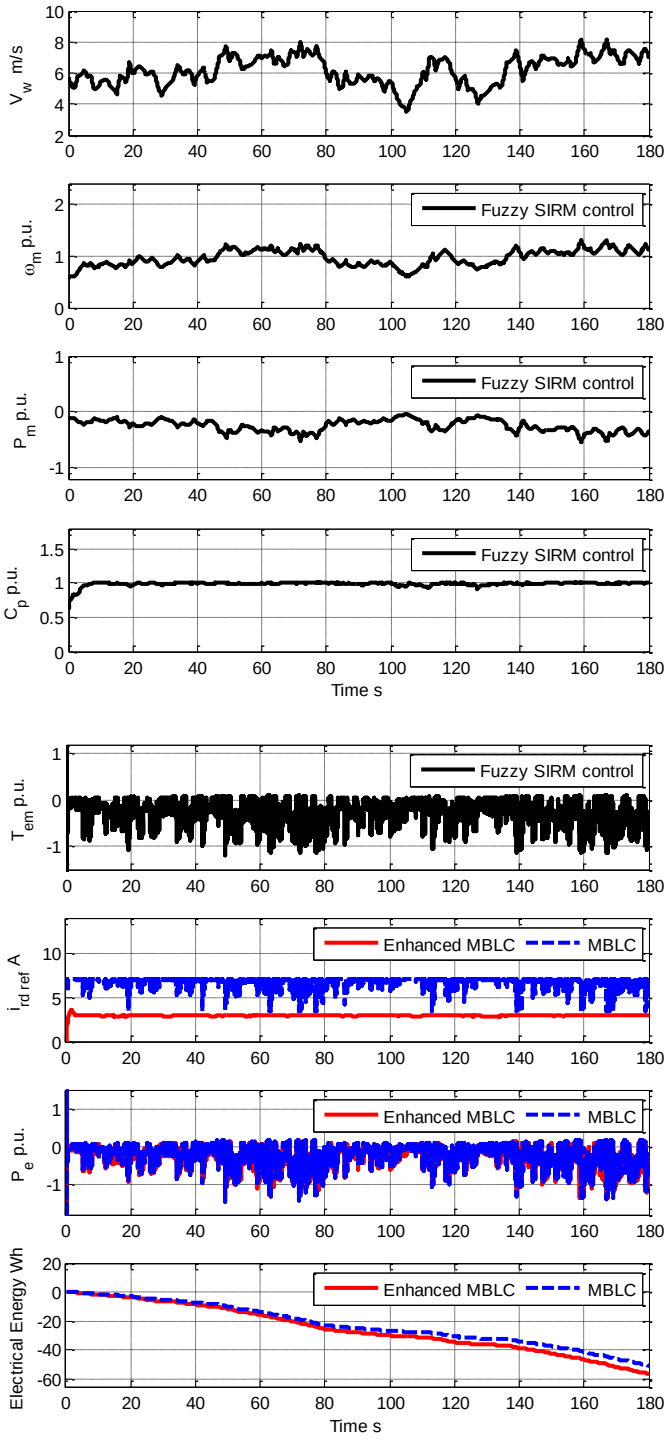

Figure B.36: WECS dynamic response controlled by the traditional MBLC and the enhanced MBLC for low real wind speed profile ($\bar{v}_w$ = 6 m/s) with error in estimation r_s of 0%, r_r of -50%, $L_{\sigma s}$ of 0% and L_m of -50% (case 10)

Appendix C: Publications

1. C Sompracha, D Jayaweera and, P Tricoli, "A novel particle swarm optimisation technique to improve energy efficiency of doubly-fed induction generators for wind turbines," 7th International Conference on Renewable Power Generation, Copenhagen, Denmark, 26-27 Sep 2018.